

Machine Learning Beyond Point Predictions: Uncertainty Quantification



Rafael Izbicki

Machine Learning

Beyond Point Predictions:

Uncertainty Quantification

1st Edition

Title: Machine Learning learning beyond point predictions: uncertainty quantification. First Edition. Version from January 13, 2025.

Author: Rafael Izbicki.

Cover: This cover was created with the help of AI. Special thanks to Lea Veras, Luben M. C. Cabezas, Michel Helcias Montoril, and Tiago Mendonça for their valuable suggestions and help with editing it.

ISBN: 978-65-01-20272-3

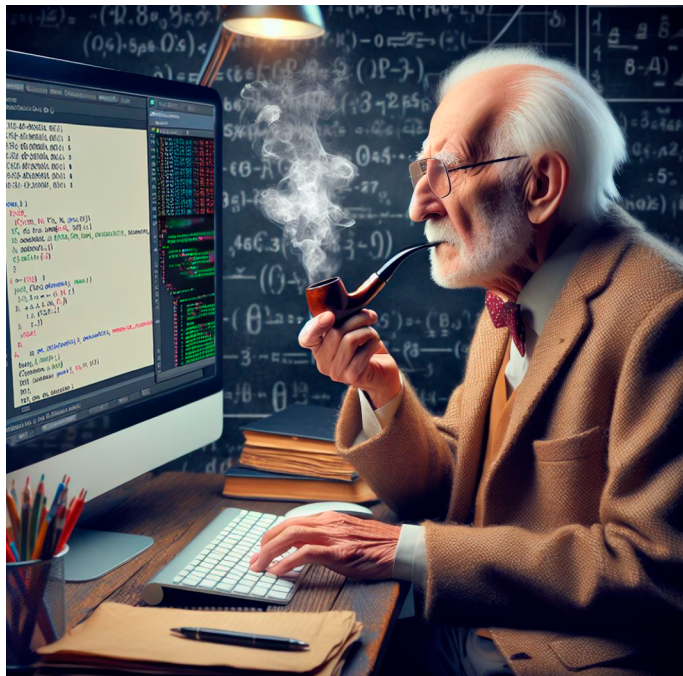


This work is licensed under a Creative Commons Attribution-NonCommercial-NoDerivatives 4.0 International License. To view a copy of this license, visit <https://creativecommons.org/licenses/by-nc-nd/4.0/>.

Rafael Izbicki

Machine Learning

Beyond Point Predictions: Uncertainty Quantification



Solum certum nihil esse certi.

The only certain thing is that
nothing is certain.

Pliny the Elder

To all of those who deeply shaped the way I
think:

My teachers
My students
My family

Contents

1	Introduction	1
1.1	Motivating Example: Life Expectancy and GDP	2
1.2	Aleatoric and Epistemic Uncertainty	3
1.3	Applications of UQ in ML	5
1.4	Outline of the Book	8
I	Foundations of Uncertainty Quantification in ML	11
2	Review of Supervised Learning	13
2.1	Notation and Assumptions	14
2.2	Loss Functions and Risk	15
2.2.1	Optimal Solutions for Different Loss Functions	16
2.3	Model Selection: Overfitting and Underfitting	18
2.3.1	Data Splitting and Cross-Validation	19
2.4	Bias and Variance Tradeoff	22
2.5	Tuning Parameters	25
2.6	Methods to Create Prediction Functions	25
2.6.1	Parametric Methods	25
2.6.2	K-Nearest Neighbors	28
2.6.3	Trees	29
2.6.4	Bagging and Random Forests	32
2.6.5	Boosting	34
2.6.6	Artificial Neural Networks	35
2.7	The Myth of Imbalanced Data	42

2.8	Summary	43
3	Quantifying Aleatoric Uncertainty with Conditional Densities	45
3.1	Loss Functions	46
3.1.1	The L_2 loss and the Brier Score	47
3.1.2	The Cross-Entropy Loss (or the Negative Loglikelihood)	48
3.1.3	Continuous Ranked Probability Score (CRPS)	50
3.1.4	Accuracy, F1-scores and Related metrics: Improper Metrics for Probabilistic Classification	52
3.2	Probabilistic Classifiers	54
3.3	Parametric Approaches	54
3.4	FlexCode	56
3.4.1	Normalization and Spurious Bumps	58
3.4.2	Variable Importance	58
3.4.3	Theory	59
3.5	Mixture Models and Networks	60
3.6	Normalizing Flows	62
3.7	The Ratio Trick	64
3.8	Other Conditional Density Estimators	65
3.9	Quantile Regression	67
3.9.1	Pinball Loss	67
	3.9.1.1 Estimation the Quantile Function	68
3.10	Simulated Example: Gaussian Distribution	71
3.11	Example: Twitter Location Prediction	72
3.12	Summary	73
4	Diagnostics and Recalibration	75
4.1	PIT Values: Evaluating Calibration in Regression	76
4.1.1	Probabilistic Calibration and Recalibration	79
4.1.2	Simulated Example: Gaussian Distribution Revisited	80
4.2	Conditional PIT values	81
4.2.1	Diagnostics	84
4.2.2	Monotonic Neural Networks to Estimate the Regression Function	84
4.2.3	Handling Multivariate Responses	85

4.2.4	Example: Neural Density Inference for Galaxy Images	87
4.3	Calibration of Classification Models	89
4.3.1	Evaluating Marginal Calibration	89
4.3.2	Recalibration of Probabilistic Classifiers	91
4.3.3	Limitations of Marginal Calibration	92
4.3.4	Example	93
4.4	Summary	95
5	From Conditional Densities to Prediction Regions	97
5.1	Optimal Prediction Regions	98
5.1.1	Tuning Parameters and Notions of Coverage	102
5.2	Plug-in Prediction Regions	102
5.3	Conformal Regions	103
5.3.1	A Different Perspective on Conformal Regions: Tolerance Regions	109
5.3.2	Comparison to Prediction Sets from Linear Models	111
5.3.3	Achieving Asymptotic Conditional Coverage	114
5.3.3.1	Label-Conditional Conformal Regions	116
5.3.4	Local Conformal Regions	117
5.3.5	Conformal Sets for Classification	119
5.3.6	Example: Photometric Redshift Prediction	120
5.4	Comparing Linear, Bayesian, Conformal Methods, and Plug-in Approaches	122
5.5	Summary	124
6	Capturing Epistemic Uncertainty through Bayesian and Ensemble Techniques	127
6.1	Bayesian Models	128
6.1.1	Aleatoric vs. Epistemic Uncertainty Revisited	131
6.1.2	Bayesian-Optimal Prediction Regions	132
6.2	Gaussian Process Regression	133
6.2.1	Feature Space Perspective	133
6.2.2	Kernel Perspective	134
6.2.3	Bayesian Optimization and Gaussian Processes	138
6.3	Bayesian Additive Regression Trees (BART)	142

6.4	Monte Carlo Dropout	145
6.5	Batch Normalization	147
6.6	Deep Ensembles	148
6.7	The Bootstrap	149
6.8	Summary	151
II	Applications	153
7	Photometric Redshift Prediction	155
7.1	Vera C. Rubin Observatory	156
7.2	Southern Photometric Local Universe Survey (S-PLUS)	159
8	Disease Surveillance: Dengue and COVID-19	163
8.1	Dengue Nowcasting	164
8.1.1	Prediction Model	164
8.1.2	Uncertainty Quantification for the Number of Cases	165
8.1.3	Results	166
8.2	COVID-19 Hospitalizations and Vaccination Impact	169
8.2.1	Prediction Model for Avoided Hospitalizations	169
8.2.2	Results	171
9	Likelihood-Free Inference (LFI)	173
9.1	Approximate Bayesian Computation via Conditional Density Estimation (ABC-CDE)	175
9.1.1	Estimating the Posterior Density via CDE	175
9.1.2	Method Selection: Comparing Different Estimators of the Posterior	176
9.1.3	Summary Statistics Selection	179
9.2	Examples	180
9.2.1	Examples with Known Posteriors	180
9.2.1.1	CDE and Method Selection	181
9.2.1.2	Summary Statistic Selection	181
9.2.2	Application: Estimating a Galaxy's Dark Matter Density Profile	183
9.3	Likelihood Free Frequentist Inference (LF2I)	186

9.3.1	Confidence Sets via Neyman Inversion	186
9.3.2	Choosing a Test Statistic	187
9.3.2.1	Likelihood-Based Statistics	188
9.3.2.2	Waldo	189
9.3.3	Calibrating the Cutoffs	190
9.3.4	Evaluating Coverage and UQ over the Confidence Sets	192
9.3.5	Example: Two Moons	193
9.3.6	Nuisance Parameters	194
9.3.7	Example: Muon energy estimation	196
9.4	Summary	197
10	Optimizing Construction Schedules: Mitigating Weather-Related Delays	199
10.1	Estimating the Distribution	202
10.2	Model Selection	203
10.2.1	CDE loss	204
10.2.2	Weighted pinball loss	204
10.3	Example	205
11	Closing Thoughts	207
11.1	Summary of Key Concepts	208
11.2	Limitations of UQ Approaches	210
11.2.1	Assumptions and Ontological Uncertainties	210
11.2.2	Overconfidence	211
11.2.3	Uncertainty Cannot Address All Risks	211
11.3	Practical Recommendations for Using UQ in Machine Learning	212

Foreword

This book. Over the past few decades, Machine Learning has achieved remarkable success in generating accurate predictions across diverse domains. However, point predictions alone are often insufficient; understanding and effectively representing the uncertainties in these predictions is crucial for informed decision-making in real-world applications. As a result, there has been a surge in research focused on developing methods to quantify this uncertainty. This book aims to explore some of these techniques, with a particular emphasis on approaches that I find compelling and to which I have contributed through my research.

The role of the two cultures in uncertainty quantification. Breiman (2001a) distinguishes between two key cultures in statistical modeling: the *data modeling culture*, which dominates traditional statistics, and the *algorithmic modeling culture*, prevalent in machine learning. The data modeling culture emphasizes the interpretation of model parameters, operating under the assumption that the model accurately reflects the underlying data-generating mechanism. This leads to a focus on goodness-of-fit tests to ensure the model's validity. In contrast, the algorithmic modeling culture prioritizes prediction accuracy, where models are evaluated based on their predictive performance using loss functions, rather than an assumption of correctness.

Integrating these approaches is particularly advantageous for uncertainty quantification. While loss functions are effective for comparing models, they provide only a relative measure of performance and do not assess the model's overall adequacy. Consequently, they fall short of answering critical questions such as, "Should we continue searching for better estimates, or is our current

model fit sufficient?" Goodness-of-fit techniques, however, can address this gap by evaluating model adequacy and suggesting potential improvements. Thus, combining these cultures enables a more comprehensive model evaluation. This integrated approach is emphasized in Chapter 4, which focuses on using goodness-of-fit methods to assess the adequacy of density models, thereby enriching the model evaluation process with practical insights.

Theory. This book presents theoretical results about some of the techniques we explore. Good theory is not an abstract exercise; it provides a different perspective on problems, complementing what we learn from practical applications and simulations. While some sections discuss more advanced mathematics to deepen your understanding, you can still grasp the book's core concepts even if you choose to skip these parts, especially if you're focused on an introductory overview of uncertainty quantification.

Prerequisites. We assume that the reader is familiar with the foundations of probability and statistical inference. An excellent introduction to the topic at the desired level is provided by Schervish and DeGroot (2014). Readers will also benefit from having taken an introductory class on machine learning or regression analysis. James et al. (2013) offer a great introduction to these topics.

Research Papers. Parts of this book are based on the following research papers:

- Izbicki, R., & Lee, A. B. (2017). Converting high-dimensional regression to high-dimensional conditional density estimation. *Electronic Journal of Statistics*, 11(2), 2800–2831
- Izbicki, R., Lee, A. B., & Pospisil, T. (2019). ABC-CDE: Toward approximate bayesian computation with complex high-dimensional data and limited simulations. *Journal of Computational and Graphical Statistics*, 28(3), 481–492
- Izbicki, R., Shimizu, G. T., & Stern, R. B. (2020). Distribution-free conditional predictive bands using density estimators. *Proceedings of Machine Learning Research (AISTATS Track)*

- Dalmasso, N., Pospisil, T., Lee, A. B., Izbicki, R., Freeman, P. E., & Malz, A. I. (2020b). Conditional density estimation tools in Python and R with applications to photometric redshifts and likelihood-free cosmological inference. *Astronomy and Computing*, 100362
- Dalmasso, N., Izbicki, R., & Lee, A. (2020a). Confidence sets and hypothesis testing in a likelihood-free inference setting. *International Conference on Machine Learning*, 2323–2334
- Schmidt, S. J., Malz, A. I., Soo, J. Y. H., Almosallam, I. A., Brescia, M., Cavuoti, S., Cohen-Tanugi, J., Connolly, A. J., DeRose, J., Freeman, P. E., Graham, M. L., Iyer, K. G., Jarvis, M. J., Kalmbach, J. B., Kovacs, E., Lee, A. B., Longo, G., Morrison, C. B., Newman, J. A., . . . LSST Dark Energy Science Collaboration. (2020). Evaluation of probabilistic photometric redshift estimation approaches for The Rubin Observatory Legacy Survey of Space and Time (LSST). *Monthly Notices of the Royal Astronomical Society*, 499(2), 1587–1606
- Izbicki, R., Bastos, L. S., Izbicki, M., Lopes, H. F., & Santos, T. M. d. (2021). How many hospitalizations has the COVID-19 vaccination already prevented in São Paulo? *Clinics*, 76, e3250
- Zhao, D., Dalmasso, N., Izbicki, R., & Lee, A. B. (2021). Diagnostics for conditional density models and bayesian inference algorithms. *Uncertainty in Artificial Intelligence*, 1830–1840
- Dey, B., Zhao, D., Newman, J. A., Andrews, B. H., Izbicki, R., & Lee, A. B. (2022). Calibrated predictive distributions via diagnostics for conditional coverage. *arXiv:2205.14568*
- Izbicki, R., Shimizu, G., & Stern, R. B. (2022). CD-split and HPD-split: Efficient conformal regions in high dimensions. *Journal of Machine Learning Research*
- Masserano, L., Dorigo, T., Izbicki, R., Kuusela, M., & Lee, A. (2023). Simulator-based inference with waldo: Confidence regions by leveraging prediction algorithms and posterior estimators for inverse problems. *International Conference on Artificial Intelligence and Statistics*, 2960–2974

- Nakazono, L., R Valen  a, R., Soares, G., Izbicki, R., Ivezi  ,   ., R Lima, E., T Hirata, N., Sodr   Jr, L., Overzier, R., Almeida-Fernandes, F., et al. (2024). The quasar catalogue for s-plus dr4 (qucats) and the estimation of photometric redshifts. *Monthly Notices of the Royal Astronomical Society*, 531(1), 327–339
- Xiao, Y., Soares, G., Bastos, L., Izbicki, R., & Moraga, P. (2024). Dengue nowcasting in brazil by combining official surveillance data and google trends information. *medRxiv*. <https://doi.org/10.1101/2024.09.02.24312934>
- Dalmasso, N., Masserano, L., Zhao, D., Izbicki, R., & Lee, A. B. (2024). Likelihood-free frequentist inference: Bridging classical statistics and machine learning for reliable simulator-based inference. *Electronic Journal of Statistics*, 18(2), 5045–5090
- Cabezas, L. M. C., Soares, G. P., Ramos, T. R., Stern, R. B., & Izbicki, R. (2024). Distribution-free calibration of statistical confidence sets. *arXiv preprint arXiv:2411.19368*. <https://arxiv.org/pdf/2411.19368.pdf>
- Cabezas, L. M., Otto, M. P., Izbicki, R., & Stern, R. B. (2025). Regression trees for fast and adaptive prediction intervals. *Information Sciences*, 121369
- Comito, M. B., Izbicki, R., do Canto Hubert Junior, P., & Moura, F. (2025). Improving decision-making in construction: Nonparametric modeling of weather-induced delays [in prep.]

Code and Data. Notebooks for reproducing some of the analyses presented in this book are available at <https://github.com/rizbicki/UQ4ML>. These notebooks are referenced throughout the book for further exploration. For additional resources, including details about the book and purchasing a printed version, visit the official website at <https://rafaelizbicki.com/UQ4ML>.

Errors. This book certainly contains many errors. If you encounter any mistakes, whether grammatical or related to mathematics, or if you have additional suggestions, please email them to rafaelizbicki (at) gmail.com.

Acknowledgments. I am deeply grateful to my long-term collaborators, Ann B. Lee and Rafael B. Stern, whose significant contributions were crucial in developing much of the research that forms the foundation of this book. Their insights have been invaluable, and this work would not have been possible without their partnership.

I am also grateful to Brett Andrews, Leonardo Soares Bastos, Luben Miguel Cruz Cabezas, Mateus Borges Comito, Victor Coscrito, Biprateep Dey, Nic Dal-masso, Tomasso Dorigo, Marco Henrique de Almeida Inacio, Meyer Izicki, Paulo do Canto Hubert Junior, Mikael Kuusela, Hedibert Freita Lopes, Alex Malz, Luca Masserano, Filipe Moura, Lilianne Nakazono, Jeff Newman, Mateus Piovezan Otto, Taylor Pospisil, Thiago Rodrigo Ramos, Hellen Geremias dos Santos, Tiago Mendonça dos Santos, Paula Moraga, Gilson Shimizu, Gabriela Soares, Guilherme Pedrilho Soares, Raquel Ruiz Valença, Yang Xiao, and David Zhao for their exceptional contributions as co-authors.

I gratefully acknowledge the São Paulo Research Foundation (FAPESP), the Brazilian National Council for Scientific and Technological Development (CNPq), the Coordination for the Improvement of Higher Education Personnel (CAPES), and the Federal University of São Carlos (UFSCar). Their support was essential in making this project possible.

Finally, I am deeply thankful to Deborah, Meyer, Sarah, Lea, Bianca, and Lila for their constant support and understanding.

Chapter 1

Introduction



The Fortune Teller. Georges de La Tour, 1630s, The Metropolitan Museum of Art, New York.

1.1. Motivating Example: Life Expectancy and GDP

Maturity is the capacity to endure uncertainty.

John Huston Finley

Machine learning (ML) has seen significant progress in recent years, driven by larger datasets, improved computing capabilities, and more advanced algorithms. These advancements have enhanced the accuracy of predictions across a variety of fields, from healthcare diagnostics to market trend forecasting. However, despite these improvements, the relationship between the inputs to a machine learning model, represented by x , and the target variable, y , often involves significant uncertainty. This uncertainty can stem not only from the limitations of the model but also from the inherent unpredictability of the phenomena being studied, given the available features x .

The central goal of this book is to provide practical tools and theoretical insights for enhancing the reliability of machine learning predictions by incorporating uncertainty quantification. We focus on developing methods that go beyond simple point predictions to offer a more nuanced understanding of the uncertainty inherent in various prediction problems, enabling more informed decision-making across diverse applications.

1.1 Motivating Example: Life Expectancy and GDP

To illustrate the challenges of uncertainty in prediction, consider the relationship between GDP per capita (x) and life expectancy (y) in 211 countries in 2012, as shown in Figure 1.1. GDP per capita is often used as a proxy for a country’s wealth or development, and it generally correlates with better health outcomes, including longer life expectancy. However, no machine learning model that outputs a single y for each x can perfectly predict life expectancy across all countries using GDP alone. This is because GDP per capita, while informative, is not the sole determinant of life expectancy. Other factors, such as healthcare quality, education, and lifestyle, contribute to the observed outcomes, leading to variability even among countries with similar GDPs.

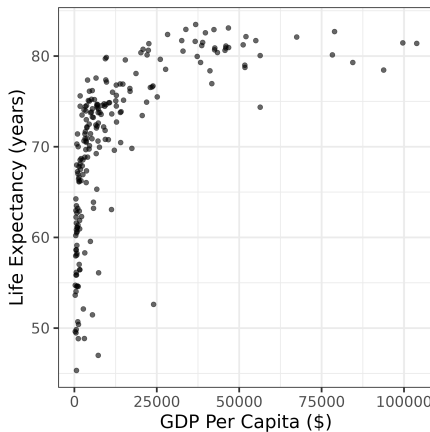


Figure 1.1: Life expectancy (y) versus GDP per Capita (x) of 211 countries. It is impossible to give perfect predictions for y using x only. Moreover, countries with a GDP per capita of $\approx \$1000$ have much greater variability in their life expectancy than countries with a GDP per capita of $\approx \$80000$.

Even with infinite data, perfect predictions are impossible here. This is because x does not uniquely determine y , so inherent variability limits the precision of point predictions, often making them insufficient for decision-making. For example, countries with a GDP per capita around \$1000 show much more variability in life expectancy than those around \$80000, making predictions for the former far less reliable. This highlights the need for models that not only predict likely outcomes but also communicate the uncertainty surrounding them.

1.2 Aleatoric and Epistemic Uncertainty

The uncertainty associated with predicting a new label Y given features x can be divided into two main categories¹:

- **Aleatoric Uncertainty:** This type of uncertainty arises when the same feature vector x corresponds to different possible labels y . It captures

¹There are several nuances in this classification; see Hüllermeier and Waegeman (2021) and references therein for a thorough discussion.

1.2. Aleatoric and Epistemic Uncertainty

the inherent variability in the distribution of Y conditional on \mathbf{x} , which we denote by $f(y|\mathbf{x})$. For example, in the case of GDP and life expectancy, two countries with the same GDP per capita may have different life expectancies due to factors such as healthcare or education. Aleatoric uncertainty can be measured by the conditional distribution of Y given \mathbf{x} . Figure 1.2 illustrates this concept: the green and blue curves represent the conditional densities $f(y|\mathbf{x}_a)$ and $f(y|\mathbf{x}_b)$, showing that while the optimal point predictions for \mathbf{x}_a and \mathbf{x}_b (given by the true regression functions $\mathbb{E}[Y|\mathbf{x}_a]$ and $\mathbb{E}[Y|\mathbf{x}_b]$; see Chapter 2 for a mathematical explanation) are identical, the associated uncertainties differ. This reflects the inherent variability in the output for each input. In the context of classification (that is, a prediction problem where Y is a qualitative label), $f(y|\mathbf{x})$ is the probability of the label given the features, $\mathbb{P}(Y = y|\mathbf{x})$.

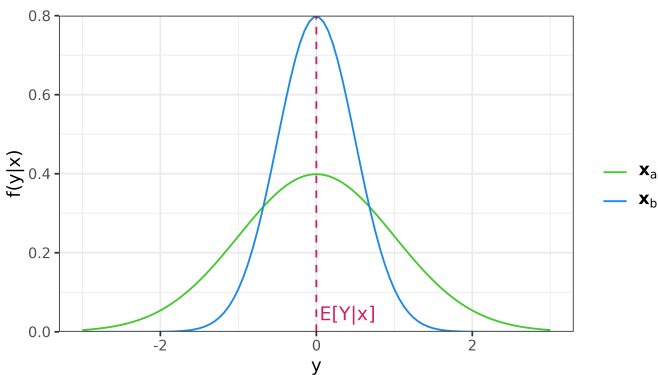


Figure 1.2: Conditional densities $f(y|\mathbf{x})$ for inputs $\mathbf{x} = \mathbf{x}_a$ (green) and $\mathbf{x} = \mathbf{x}_b$ (blue), showing identical optimal point predictions but different uncertainties. The dashed line marks the optimal point prediction $r(\mathbf{x}) = \mathbb{E}[Y|\mathbf{x}]$.

- **Epistemic Uncertainty:** This uncertainty is due to a lack of knowledge about the true data generating process (that is, the true distribution of $Y|\mathbf{x}$). Increasing the size of the dataset can help reduce epistemic uncertainty, but it does not affect aleatoric uncertainty. Epistemic uncertainty is particularly important in scenarios with limited data. Figure 1.3 illustrates epistemic uncertainty: the first plot shows three regression models that are compatible with the same dataset, each producing dif-

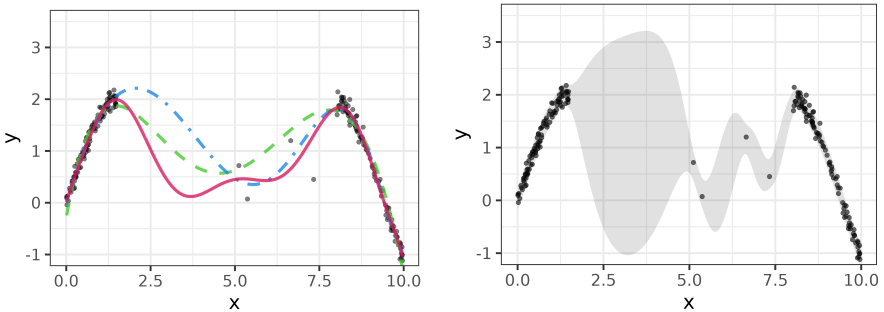


Figure 1.3: Illustration of epistemic uncertainty. Left: Comparison of three regression models, each producing very different predictions due to sparse data in certain regions. Right: Gaussian process regression with uncertainty bands, where the shaded area represents epistemic uncertainty.

ferent predictions due to sparse data in certain regions, highlighting the uncertainty that arises from the lack of data. The second plot shows the epistemic uncertainty associated to the regression function as measured by a Gaussian process fit to the same data (see Section 6.2 for Gaussian processes). These bands visually depict epistemic uncertainty, showing greater uncertainty in areas with fewer data points and more confidence in regions with denser data.

In many prediction problems, it is important to distinguish between these two types of uncertainty, as they require different treatment. While epistemic uncertainty can be mitigated by gathering larger datasets or improving the model, aleatoric uncertainty can only be reduced by measuring additional covariates.

In the next section, we will briefly explore real-world machine learning problems where quantifying uncertainty is important.

1.3 Applications of UQ in ML

Uncertainty Quantification (UQ) techniques play an essential role in improving the reliability and utility of predictive models in many fields. By

1.3. Applications of UQ in ML

offering insights into the limitations and confidence of model predictions, UQ aids in decision-making and enhances risk assessment. Here are some examples of applications of UQ in machine learning:

- **Medical Image Segmentation:** UQ is essential for addressing inherent ambiguities in medical image segmentation, such as variations in anatomical definitions and partial volumes. Traditional deep learning models often rely on point estimates, which may fail to capture the full spectrum of plausible segmentations. UQ techniques enable the inference of distributions over possible segmentations, providing a more comprehensive quantification of uncertainty – crucial in clinical settings where inter-rater variability and consensus-based decisions are common (Csillag et al., 2023; Selvan et al., 2020).
- **Fault Diagnosis:** UQ is crucial for fault diagnosis because it provides a measure of confidence in the diagnostic outcomes, which is essential for making informed decisions in critical systems. UQ allows engineers and system operators to understand not just what the diagnosis indicates, but also how reliable that diagnosis is. This is particularly important in scenarios where false positives or negatives can lead to significant consequences, such as unnecessary maintenance actions or undetected failures (Mian et al., 2024).
- **Residential Load Forecasting:** Accurate residential load forecasting is critical for efficient energy management, yet traditional probabilistic methods often struggle with the inherent uncertainty in household electricity consumption patterns. UQ techniques provide a more complete probabilistic representation of future consumption, which is essential for informed decision-making in modern power systems (Afrasiabi et al., 2020).
- **Astronomy:** UQ is indispensable in astronomy, particularly for estimating distances to galaxies (photo-z estimation; see Chapter 7 for details) and performing likelihood-free cosmological inference (Chapter 9). While traditional methods typically offer single-point estimates, UQ methods deliver a more nuanced picture, enabling more accurate infer-

ences in scenarios where multiple redshifts or cosmological parameter values align with the observed data.

- **Validating Soil Property Predictions:** When ML models are used as a replacement or supplement to traditional soil laboratory analysis, rigorous uncertainty assessment becomes indispensable. Without a clear understanding of the model's confidence in its predictions, it is difficult to gauge their reliability for critical applications such as digital soil mapping or soil carbon accounting (Bejani and Ghatee, 2021; England and Viscarra Rossel, 2018; Padarian et al., 2022; Searle et al., 2021). UQ also facilitates the integration of predictions from various models or sensors, as understanding the uncertainty associated with each prediction is crucial for appropriately weighting different sources (Horta et al., 2015).
- **Land-Use Land-Cover (LULC) Classification:** UQ enhances the reliability of LULC maps by identifying areas with high classification uncertainty, which is critical for accurate environmental and ecological analysis. This ensures that users are aware of the confidence levels in different regions of the map, improving the robustness of downstream applications (Valle et al., 2024b; Valle et al., 2023).
- **Forest Biomass Estimation:** UQ improves reliability in biomass predictions by addressing uncertainty in multistep upscaling approaches using sensors like LiDAR and Landsat. Conformal prediction ensures well-calibrated intervals, aiding applications like carbon accounting and forest management (Valle et al., 2024a).
- **Cancer Risk Assessment:** In the context of cancer risk assessment, uncertainty quantification helps in providing more accurate and personalized predictions, reducing the number of unnecessary biopsies while maintaining high sensitivity for cancer detection. This enhances decision-making in clinical settings by offering clearer insights into the confidence level of each diagnosis (Clark et al., 2024; Fröhlich et al., 2024; Vazquez and Facelli, 2022).
- **Robotics Motion Planning:** UQ can be used in robotics for ensuring safe and effective motion planning, particularly when robots operate in

1.4. Outline of the Book

unfamiliar environments. For instance, it can be used to enable robots to create prediction regions in real-time, ensuring that their movements remain safe even under changing conditions (Marques and Berenson, 2024).

- **Autonomous Vehicles:** Uncertainty quantification plays a critical role in the safety and reliability of autonomous vehicles by providing confidence measures for the vehicle's perception and decision-making systems. It helps in identifying scenarios where the model's predictions are uncertain, allowing the system to take precautionary actions, such as slowing down or handing control back to a human driver (McAllister et al., 2017).
- **Predicting Infectious Disease Waves:** UQ plays a crucial role in predicting waves of infectious diseases, such as dengue, COVID-19, and Influenza. By quantifying uncertainty in real-time models, UQ enhances the reliability of forecasts, enabling better preparation and response to potential outbreaks (Codeço et al., 2016; Ray and Reich, 2018; Wu et al., 2020); see also Chapter 8.
- **Natural Language Processing (NLP):** UQ enhances reliability in NLP by addressing challenges like hallucinations, biases, and poor calibration in large language models (LLMs). It is applicable to tasks such as text classification, natural language generation, part-of-speech tagging, and multilabel classification (Campos et al., 2024; Cherian et al., 2024).

Some of these examples will be explored in greater depth throughout the book.

1.4 Outline of the Book

In this book, we explore various methods for estimating uncertainties in prediction problems. The structure of this book is as follows:

The first part covers the statistical foundations of uncertainty quantification in machine learning. It starts with Chapter 2, which reviews supervised learning for classification and regression. Chapter 3 then covers methods to estimate conditional densities, modeling the aleatoric uncertainty of the target

Y given the input \mathbf{x} . Chapter 4 introduces tools to evaluate whether these estimates are good. Chapter 5 explains how to compute prediction bands for Y from estimated densities and discusses alternative methods based on conformal inference. Some of these take into account both the aleatoric and the epistemic uncertainties. Chapter 6 then provides an overview of techniques that directly model both the aleatoric and the epistemic uncertainty on Y .

The second part of the book contains applications of the tools introduced in previous chapters. Chapter 7 applies some of the UQ techniques to the photo-z problem from cosmology, while Chapter 8 applies them to dengue epidemic nowcasting and to evaluate the impact of vaccination in COVID-19. Chapter 9 applies the techniques to likelihood-free inference problems, where the goal is to infer parameters θ of a statistical model in which a tractable likelihood function is unavailable. Finally, Chapter 10 demonstrates how to predict the duration of construction projects by incorporating weather-related delays using historical meteorological data.

Chapter 11 concludes the book by summarizing the key topics explored and briefly discussing further challenges in UQ.

1.4. Outline of the Book

Part I

Foundations of Uncertainty Quantification in ML

Chapter 2

Review of Supervised Learning



A Philosopher Lecturing on the Orrery. Joseph Wright of Derby, 1766, Derby Museum and Art Gallery, Derby.

2.1. Notation and Assumptions

Forecasting is the art of saying
what will happen and then
explaining why it didn't.

Unknown Author

The main objective of a supervised model is to predict the value of a random variable $Y \in \mathcal{Y}$ using information from a vector $\mathbf{x} = (x_1, \dots, x_d) \in \mathbb{R}^d := \mathcal{X}$. Depending on the nature of Y , the problem can be categorized as follows:

- **Regression:** When Y is a quantitative variable, the task involves predicting a continuous value.
- **Classification:** When Y is a qualitative variable, the task involves assigning the input to one of several predefined categories.

To achieve this goal, we assume access to a *labeled dataset*:

$$(\mathbf{X}_1, Y_1), \dots, (\mathbf{X}_n, Y_n)$$

where both the \mathbf{x} 's and y 's are known.

2.1 Notation and Assumptions

Independence is happiness.

Susan B. Anthony

The variable Y is often called the response variable, dependent variable, target, label, or outcome variable. On the other hand, the observations contained in $\mathbf{x} = (x_1, \dots, x_d)$ are generally referred to as explanatory variables, independent variables, features, attributes, predictors, covariates, or input variables.

Throughout the book, unless stated otherwise, we assume that the labeled dataset is independent and identically distributed (i.i.d.) to (\mathbf{X}, Y) . See the notation used in Table 2.1.

Table 2.1: Notation used in the book.

Response	Covariates			
Y_1	$X_{1,1}$...	$X_{1,d}$	($= \mathbf{X}_1$)
\vdots	\vdots	..	\vdots	\vdots
Y_n	$X_{n,1}$...	$X_{n,d}$	($= \mathbf{X}_n$)

The goal of a supervised model is to create a function

$$g : \mathbb{R}^d \longrightarrow \mathcal{Y}$$

that has good predictive power. That is, g must be such that, given *new* i.i.d. observations $(\mathbf{X}_{n+1}, Y_{n+1}), \dots, (\mathbf{X}_{n+m}, Y_{n+m})$, we have

$$g(\mathbf{x}_{n+1}) \approx y_{n+1}, \dots, g(\mathbf{x}_{n+m}) \approx y_{n+m}.$$

In a regression problem, we assume that $\mathcal{Y} \subset \mathbb{R}$, while in a classification problem, we assume without loss of generalization that $\mathcal{Y} = \{0, 1, \dots, K - 1\}$ for some $K > 1$.

2.2 Loss Functions and Risk

In supervised learning, constructing a good prediction function $g : \mathbb{R}^d \longrightarrow \mathcal{Y}$ requires a criterion to measure its performance. This is typically done using a *loss function*, which quantifies the error in a prediction and provides a way to guide the learning process.

A loss function is defined as

$$\begin{aligned} L : \mathcal{Y} \times \mathcal{Y} &\rightarrow \mathbb{R}, \\ (g(\mathbf{x}), y) &\mapsto L(g(\mathbf{x}), y), \end{aligned}$$

where $g(\mathbf{x})$ is the predicted value and y is the true label. The loss function evaluates how well the prediction $g(\mathbf{x})$ matches the true outcome y . The choice of a loss function depends on the nature of the task, with typical examples being:

2.2. Loss Functions and Risk

- In **regression tasks**, a commonly used loss function is the quadratic loss:

$$L(g(\mathbf{x}), y) = (y - g(\mathbf{x}))^2, \quad (2.1)$$

which penalizes larger deviations between the prediction and the actual outcome more heavily.

- For **classification**, the loss function $L(g(\mathbf{x}), y)$ is often designed so that $L(k, k) = 0$ for every $k \in \mathcal{Y}$. Here, $L(k, j)$ represents the penalty for predicting class j when the true class is k . A common choice is the zero-one loss, $L(k, j) = \mathbb{I}(k \neq j)$, which assigns an equal penalty to all misclassifications, even though this assumption may not be appropriate in many real-world applications (see Section 2.7).

The performance of a prediction function g is then assessed through the *risk*, which is the expected loss over new, unseen data:

$$R(g) = \mathbb{E}[L(g(\mathbf{X}), Y)],$$

here (\mathbf{X}, Y) represents a random variable drawn from the same distribution as the training data. The risk measures how well the function g performs on average, with lower risk indicating better performance.

In classification problems, the risk under the zero-one loss becomes

$$R(g) = \mathbb{E}[\mathbb{I}(Y \neq g(\mathbf{X}))] = \mathbb{P}(Y \neq g(\mathbf{X})), \quad (2.2)$$

which represents the probability that the classifier misclassifies a new sample. A more intuitive and commonly used measure is the classifier's *accuracy*, given by $1 - R(g) = \mathbb{P}(Y = g(\mathbf{X}))$. Minimizing the risk is equivalent to maximizing the accuracy. However, it is important to note some limitations of this metric when the goal is to quantify uncertainties (see Section 3.1.4).

2.2.1 Optimal Solutions for Different Loss Functions

Different choices of loss functions lead to different optimal prediction functions. For instance:

Theorem 1 (Regression function). *In a regression problem, the function g that minimizes the risk $R(g) = \mathbb{E}[(Y - g(\mathbf{X}))^2]$ is the regression function, which is the conditional expectation:*

$$r(\mathbf{x}) = \mathbb{E}[Y|\mathbf{x}].$$

This result indicates that, under quadratic loss, the best prediction function is the one that outputs the average value of Y given \mathbf{x} . While $r(\mathbf{x})$ is generally unknown in practical scenarios, this insight suggests that regression problems can be tackled by estimating the regression function $r(\mathbf{x})$.

Theorem 2 (Bayes classifier). *In classification, the function g that minimizes the risk is called the Bayes classifier. It is defined as:*

$$g_{\text{Bayes}}(\mathbf{x}) := \arg \min_{j \in \mathcal{Y}} \sum_{k \in \mathcal{Y}} L(k, j) \mathbb{P}(Y = k|\mathbf{x}). \quad (2.3)$$

In the binary classification case (that is, $K = 2$) with $L(k, k) = 0$ for all $k \in \mathcal{Y}$, this reduces to the decision rule:

$$g_{\text{Bayes}}(\mathbf{x}) = \begin{cases} 1, & \text{if } \mathbb{P}(Y = 1|\mathbf{x}) \geq \frac{L(0,1)}{L(0,1) + L(1,0)}, \\ 0, & \text{otherwise.} \end{cases} \quad (2.4)$$

Under the zero-one loss, this further simplifies to:

$$g_{\text{Bayes}}(\mathbf{x}) = \begin{cases} 1, & \text{if } \mathbb{P}(Y = 1|\mathbf{x}) \geq \frac{1}{2}, \\ 0, & \text{otherwise.} \end{cases}$$

In the general classification case with a zero-one loss, the Bayes classifier becomes:

$$g_{\text{Bayes}}(\mathbf{x}) = \arg \max_{j \in \mathcal{Y}} \mathbb{P}(Y = j|\mathbf{x}).$$

As in the regression case, $\mathbb{P}(Y = k|\mathbf{x})$ cannot be computed in real-world problems. However, this theorem suggests that classification problems can be solved by estimating such probabilities.

The objective of supervised learning is, therefore, to develop methods that estimate these functions effectively, ensuring low risk and therefore reliable predictions.

2.3. Model Selection: Overfitting and Underfitting

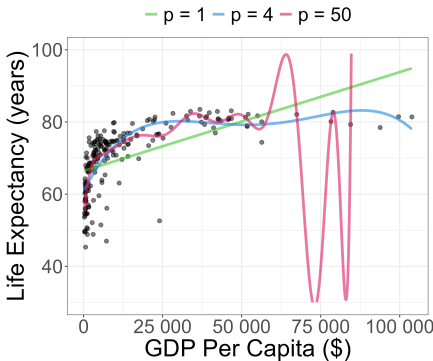


Figure 2.1: GDP per Capita and Life Expectancy in 211 countries and the fitted prediction models g . Each g is a polynomial with p degrees.

2.3 Model Selection: Overfitting and Underfitting

The best preparation for tomorrow
is doing your best today.

H. Jackson Brown Jr

In practical problems, it is common to fit multiple models to $g(\mathbf{x})$ and search for the one with the best predictive power, that is, the one with the lowest risk. This is exemplified below in a regression context.

Exemple 2.1. [Life Expectancy and Per Capita GDP] Recall the example from Section 1.1. The challenge is to utilize this data to predict the life expectancy of countries where the GDP per Capita is known but life expectancy is not. To achieve this, one can estimate $\mathbb{E}[Y|\mathbf{x}]$, where Y is the life expectancy in a given country, and \mathbf{x} is its GDP per Capita. Figure 2.1 shows the fitting of three different models for the prediction function:

$$g(x) = \beta_0 + \sum_{i=1}^p \beta_i x^i, \text{ for } p \in \{1, 4, 50\}.$$

In other words, we fit three polynomial regressions: one of degree 1, one of degree 4, and one of degree 50. The fits were performed (that is, β_i were estimated) using the least squares method (Section 2.6.1). While the degree-1

model is too simplistic for the data, the model with $p = 50$ (that is, 50th-degree) is too complex and seems to provide a function g that will not make good predictions on new observations. The model with $p = 4$ seems to be the most reasonable in this case. We say that the model with $p = 1$ suffers from *underfitting*, while the model with $p = 50$ suffers from *overfitting* – it over-adapts to this specific sample but has low generalization power. The goal of this section is to describe methods for choosing the best predictive model among those that were fitted, that is, the model with the highest predictive power. In this example, we want a method that automatically chooses $p = 4$.

□

The goal of a model selection method is to identify a function g from a candidate class \mathbb{G} that has good predictive performance, characterized by low risk. Because the true risk $R(g)$ is unknown, it must be estimated to assess the predictive ability of any given $g \in \mathbb{G}$. In the next section, we introduce methods for estimating this risk.

2.3.1 Data Splitting and Cross-Validation

The *observed risk* (also known as the *training error*, or the *training risk*), defined by

$$\frac{1}{n} \sum_{i=1}^n L(g(\mathbf{X}_i), Y_i), \quad (2.5)$$

is a very optimistic estimator of the true risk. If used for model selection, it leads to overfitting. This happens because g was chosen to fit well $(\mathbf{X}_1, Y_1), \dots, (\mathbf{X}_n, Y_n)$.

One way to solve this problem is to divide the dataset into two parts: *training* and *validation*:

$$\overbrace{(\mathbf{X}_1, Y_1), (\mathbf{X}_2, Y_2), \dots, (\mathbf{X}_s, Y_s)}^{\text{Training (e.g., 70\%)}}, \overbrace{(\mathbf{X}_{s+1}, Y_{s+1}), \dots, (\mathbf{X}_n, Y_n)}^{\text{Validation (e.g., 30\%)}}.$$

We use the training set exclusively to estimate g (e.g., estimate the coefficients of the linear regression), and the validation set *only to estimate $R(g)$*

2.3. Model Selection: Overfitting and Underfitting

via

$$\hat{R}(g) = \frac{1}{n-s} \sum_{i=s+1}^n L(g(\mathbf{X}_i), Y_i) =: \hat{R}(g), \quad (2.6)$$

that is, we evaluate the error on the validation set.

A good practice for choosing which samples will be used for the training set and which will be used for the validation set is to do it randomly. Thus, a random number generator is used to choose which samples will be used for training and which will be used for validation. This procedure avoids problems when the dataset is previously sorted according to some covariate (e.g., the person who collected the data may have ordered the observations according to some variable).

Since the validation set was not used to estimate the parameters of g , the estimator from Equation 2.6 is consistent by the law of large numbers.

The procedure of dividing the data into two parts and using one part to estimate the risk is called *data splitting*. A variation of this method is *cross-validation*, which uses the entire sample. For example, in *leave-one-out cross-validation* (LOOCV) (Stone, 1974), the estimator used is given by

$$\hat{R}(g) = \frac{1}{n} \sum_{i=1}^n L(g_{-i}(\mathbf{X}_i); Y_i),$$

where g_{-i} is fitted using all observations except the i -th one, that is, using

$$(\mathbf{X}_1, Y_1), \dots, (\mathbf{X}_{i-1}, Y_{i-1}), (\mathbf{X}_{i+1}, Y_{i+1}), \dots, (\mathbf{X}_n, Y_n).$$

Alternatively, we can use *k-fold cross-validation*. In this approach, we randomly divide the data into k disjoint *folds* of approximately the same size. Let $L_1, \dots, L_k \subset \{1, \dots, n\}$ be the indices associated with each of the folds. The idea of *k-fold cross-validation* is to create k estimators of the regression function using the same method, $\hat{g}_{-1}, \dots, \hat{g}_{-k}$, where \hat{g}_{-j} is created using all observations in the dataset except those in fold L_j . The estimator of the risk is given by

$$\hat{R}(g) = \frac{1}{n} \sum_{j=1}^k \sum_{i \in L_j} L(g_{-j}(\mathbf{X}_i); Y_i).$$

Note that when $k = n$, we get LOOCV. For more details, see Wasserman (2006).

Training vs. Validation vs. Test. Just like the error on the training set is very optimistic because each $g \in \mathbb{G}$ is chosen to (approximately) minimize it, the error on the validation set *evaluated on the $g \in \mathbb{G}$ with the lowest error on the validation set* is also optimistic, especially if many prediction methods are evaluated on the validation set, that is, if $|\mathbb{G}|$ is large. This can lead to overfitting to the validation set, that is, it may lead to choosing a function g that performs well on the validation set but not on new observations. One way to circumvent this problem is to split the original dataset into three parts: training, validation, and test. The training and validation sets are used as described above. The test set is used to estimate the error of the best prediction function determined using the validation set. This way, we can know if the risk of the best g found using the validation set is indeed small.

Several variations of these ideas can be used. For example, suppose we want to compare a polynomial regression with a lasso (Section 2.6.1). A reasonable procedure is: (i) choose the best polynomial degree and the lasso *tuning parameter* λ using *data splitting* within the training set (that is, dividing the training set into two parts: training and validation), and (ii) compare the performance of the best polynomial regression with the best lasso (according to criterion (i)) on the test set. This way, the test will be used to compare only two models. Alternatively, we can replace (i) with cross-validation within the training set.

Cross-validation or data-splitting over a fine grid of tuning parameters can be computationally expensive, particularly when dealing with numerous tuning parameters or models that are slow to fit, such as certain boosting algorithms or neural networks. A more efficient alternative is Bayesian optimization (Section 6.2.3).

Confidence Intervals for Risk. Using the test set, we can also create a confidence interval for the risk. Let $(\tilde{\mathbf{X}}_1, \tilde{Y}_1), \dots, (\tilde{\mathbf{X}}_m, \tilde{Y}_m)$ be the elements of the test set (that is, they were not used for training or validation of the model). An unbiased estimator for the risk of g , obtained using the training

2.4. Bias and Variance Tradeoff

and validation sets, is given by

$$\widehat{R}(g) = \frac{1}{m} \sum_{k=1}^m \underbrace{L(g(\tilde{\mathbf{X}}_k); \tilde{Y}_k)}_{W_k}.$$

Since $\widehat{R}(g)$ is an average of i.i.d. random variables, the Central Limit Theorem implies that

$$\widehat{R}(g) \approx \text{Normal}\left(R(g), \frac{1}{m} \mathbb{V}[W_1]\right).$$

Moreover, we can estimate $\mathbb{V}[W_1]$ with

$$\widehat{\sigma^2} = \frac{1}{m} \sum_{k=1}^m (W_k - \bar{W})^2,$$

where $\bar{W} = \frac{1}{m} \sum_{k=1}^m W_k$. Thus, an approximate 95% confidence interval for $R(g)$ is given by

$$\widehat{R}(g) \pm 2\sqrt{\frac{1}{m} \widehat{\sigma^2}}. \quad (2.7)$$

Equation 2.7 also provides insight into how to choose the size of the division between training and validation. We can choose the smallest m such that the size of the confidence interval for the risk is as small as we want. This idea is especially interesting when the sample size is large. In this case, the size of the validation set can be much smaller than the training set, since estimating the risk is a much easier task than creating a prediction function.

2.4 Bias and Variance Tradeoff

Simplicity is an exact medium
between too little and too much.

Sir Joshua Reynolds

The quadratic loss function of Equation 2.1 is such that its risk can be

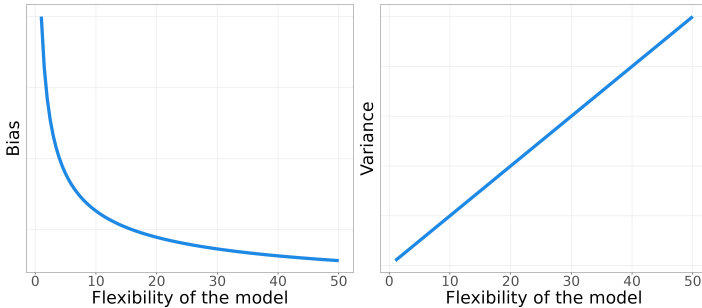


Figure 2.2: Typical behaviour of the bias and the variance of a model as a function of its complexity.

decomposed as¹

$$R(g) = \int \mathbb{V}[Y|\mathbf{X} = \mathbf{x}] d\mathbb{P}(\mathbf{x}) + \int (r(\mathbf{x}) - \mathbb{E}[g(\mathbf{X})|\mathbf{X} = \mathbf{x}])^2 d\mathbb{P}(\mathbf{x}) \\ + \int \mathbb{V}[g(\mathbf{X})|\mathbf{X} = \mathbf{x}] d\mathbb{P}(\mathbf{x}).$$

This decomposition has the following three key components:

- $\mathbb{V}[Y|\mathbf{X} = \mathbf{x}]$, which is the *intrinsic variance* of the response variable, which does not depend on the chosen function g and thus cannot be reduced;
- $(r(\mathbf{x}) - \mathbb{E}[g(\mathbf{X})|\mathbf{X} = \mathbf{x}])^2$ is the square of the estimator g bias; and
- $\mathbb{V}[g(\mathbf{X})|\mathbf{X} = \mathbf{x}]$ is the variance of the estimator g .

The values of the last two items can be reduced if we choose an appropriate g . Roughly speaking, complex models (e.g. models with many parameters) have low bias but high variance since they are hard to estimate. In contrast, models that are less flexible have low variance but very high bias as they are too simplistic to describe the data-generating model. Therefore, to achieve good predictive power, one should choose the model that has the right amount of complexity. Figure 2.2 illustrates the trade-off between bias and variance.

¹Notice that in this decomposition, the expectation associated with the risk also integrates over the randomness inherent to g , reflecting that g itself is an estimated quantity.

2.4. Bias and Variance Tradeoff

Exemple 2.2. We revisit the GPD vs Life Expectancy problem of Example 2.1. Here our goal is to select the best estimator within the class

$$\mathbb{G} = \left\{ g(x) : g(x) = \beta_0 + \sum_{i=1}^p \beta_i x^i, \text{ for } p \in \{1, 2, \dots, 50\} \right\}.$$

Figure 2.3 (left panel) displays the quadratic error, estimated via cross validation, for each $g \in \mathbb{G}$. As the risks for $p > 12$ are excessively high, we only show the behavior for $p \leq 12$. Figure 2.1 (right panel) demonstrates that, indeed, minimizing the error on the validation set leads to a good fit.

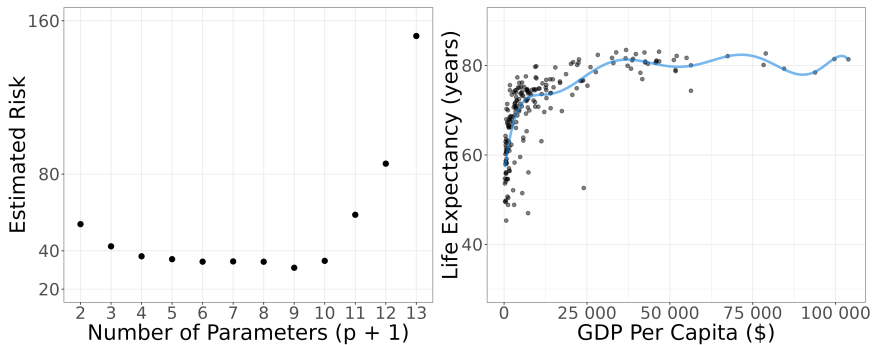


Figure 2.3: Estimated risk as a function of the number of parameters in polynomial regression for predicting Life Expectancy based on GDP per Capita. The panel on the right illustrates the best-performing model, selected through data-splitting.

□

The bias-variance tradeoff also occurs for other loss functions. However, the details are somewhat different. Suppose \mathbb{G} is a class of prediction functions (for example, all classifiers based on logistic regression),

$$R_{or} := \inf_{g \in \mathbb{G}} R(g)$$

is the best risk (that is, the oracle risk) that can be achieved using prediction functions from \mathbb{G} , and

$$R_* := \inf_{g: \mathcal{X} \rightarrow \mathcal{Y}} R(g)$$

is the risk of the best prediction function among all prediction functions. Then, for all $g \in \mathbb{G}$,

$$R(g) = R_* + T_1 + T_2,$$

where R_* is the risk of the best prediction function (a general version of the intrinsic variance), $T_1 = R_{or} - R_*$ is the approximation error (a general version of the bias), and $T_2 = R(g) - R_{or}$ is the estimation error (a general version of the variance). Thus, \mathbb{G} cannot be too large or too small.

2.5 Tuning Parameters

The role of the parameter p (degree of the polynomial) in Example 2.1 is to control the trade-off between bias and variance. The optimal value of p depends on n and $r(\mathbf{x})$. The parameter p is called a *tuning parameter*. Other examples of tuning parameters include λ in the lasso, the number of neighbors k in k -nearest neighbors, the depth of a decision tree in tree-based models, and the learning rate η in gradient boosting or neural networks.

Several regression methods have one or more *tuning parameters*. In this book, we will always choose them through cross-validation or *data splitting*, although these are not the only ways to do this (see, for example, Wasserman 2006).

2.6 Methods to Create Prediction Functions

Next, we investigate several approaches to estimate regression functions and perform classification.

2.6.1 Parametric Methods

Nature is pleased with simplicity.
And nature is no dummy.

Sir Isaac Newton

One way to create a prediction function g is to (i) parameterize it (that is, assume it belongs to a class of functions that can be described by a finite

2.6. Methods to Create Prediction Functions

number of parameters), (ii) find parameter values for the parameters that lead to a function that has good fit. In practice, step (ii) is done by designing and optimizing a loss function.

Some examples of methods that fall into this framework are:

- **[Linear regression via least squares]** Linear regression uses a linear form for the prediction function, meaning that the prediction function used can be written as

$$g(\mathbf{x}) = \boldsymbol{\beta}^\top \mathbf{x} = \beta_0 x_0 + \beta_1 x_1 + \dots + \beta_d x_d, \quad (2.8)$$

where we adopt the convention $x_0 \equiv 1$, and where $\boldsymbol{\beta} = (\beta_0, \dots, \beta_d)$. Note that x_i is not necessarily the i -th original variable; we can create new covariates that are functions of the original ones (e.g., $x_i^2, x_i x_j$, etc.; see Example 2.1). One way to estimate the coefficients $\boldsymbol{\beta}$ of linear regression is by using the method of least squares, which consists of finding the solution to

$$\hat{\boldsymbol{\beta}} = \arg \min_{\boldsymbol{\beta}} \frac{1}{n} \sum_{i=1}^n (Y_i - \beta_0 - \beta_1 x_{i,1} - \dots - \beta_d x_{i,d})^2, \quad (2.9)$$

which mimics the squared loss function. The prediction function is then given by $g(\mathbf{x}) = \hat{\boldsymbol{\beta}}^\top \mathbf{x}$.

- **[Lasso and Ridge Regression]** The lasso (Tibshirani, 1996) also assumes a linear form for the regression function. However, it instead minimizes the function

$$\frac{1}{n} \sum_{i=1}^n (Y_i - \beta_0 - \beta_1 x_{i,1} - \dots - \beta_d x_{i,d})^2 + \lambda \sum_{j=1}^d |\beta_j|, \quad (2.10)$$

where λ is a tuning parameter. The L_1 penalty $\sum_{j=1}^d |\beta_j|$ decreases the variance of the least-squares solution, thus leading to a smaller risk if there is not much increase in the bias. This is the case when several covariates are not useful to predict Y and therefore have small coefficients β_j . The solution induced by Equation 2.10 has many zeros (that is, the vector $\hat{\boldsymbol{\beta}}$ is sparse). Therefore, the resulting model is also easy to interpret.

An alternative to the lasso is ridge regression (Hoerl and Kennard, 1970), which instead minimizes the function

$$\frac{1}{n} \sum_{i=1}^n (Y_i - \beta_0 - \beta_1 x_{i,1} - \dots - \beta_d x_{i,d})^2 + \lambda \sum_{j=1}^d \beta_j^2, \quad (2.11)$$

that is, an L_2 penalty is used. Unlike the lasso, ridge regression shrinks the coefficients (and thus reduces the variance of the least squares solution) without forcing them to zero. Additionally, ridge regression offers a closed-form solution for the coefficients, which can be computationally advantageous.

- [Logistic Regression] In a binary classification problem (that is, $K = 2$), a logistic regression assumes that

$$\mathbb{P}(Y = 1 | \mathbf{x}) = \frac{e^{\beta_0 + \sum_{i=1}^d \beta_i x_i}}{1 + e^{\beta_0 + \sum_{i=1}^d \beta_i x_i}}.$$

The coefficients β are often estimated by maximizing the log-likelihood function

$$\sum_{k=1}^n \log \left[\left(\frac{e^{\beta_0 + \sum_{i=1}^d \beta_i x_{k,i}}}{1 + e^{\beta_0 + \sum_{i=1}^d \beta_i x_{k,i}}} \right)^{y_k} \left(\frac{1}{1 + e^{\beta_0 + \sum_{i=1}^d \beta_i x_{k,i}}} \right)^{1-y_k} \right].$$

This corresponds to minimizing the cross-entropy between the vector (y_1, \dots, y_n) and the estimated probabilities. Similarly to the lasso, a penalty that decreases the variance of this estimator may be introduced.

Once the probabilities are estimated, a classifier can be chosen via

$$g(\mathbf{x}) = \mathbb{I}(\widehat{\mathbb{P}}(Y = 1 | \mathbf{x}) > K),$$

which mimics the Bayes classifier (Theorem 2) and K is given by the loss function. Alternatively, other metrics for classification can be used to choose K , such as the sensitivity and the specificity.

Although a parametric model may be incorrect in the sense that the best pre-

2.6. Methods to Create Prediction Functions

diction function does not precisely align with the specified parametric shape, it can still yield good predictions. This is primarily because the parametric assumption substantially reduces the estimation error (as discussed in Section 2.4) of the model.

2.6.2 K-Nearest Neighbors

We're neighbors and we're going
to pull together.

Rick Perry

The k -nearest neighbors (KNN) (Benedetti, 1977; Stone, 1977) is a nonparametric approach to create prediction functions. As the name implies, KNN constructs a prediction function, denoted as $g(\mathbf{x})$, by considering the labels of the closest neighbors to a given point \mathbf{x} within the training dataset. Specifically, in the context of regression, the KNN estimate for the regression function is defined as

$$g(\mathbf{x}) = \frac{1}{k} \sum_{i \in \mathcal{N}_{\mathbf{x}}} y_i, \quad (2.12)$$

where $\mathcal{N}_{\mathbf{x}}$ is the set of the k observations closest to \mathbf{x} , that is,

$$\mathcal{N}_{\mathbf{x}} = \left\{ i \in \{1, \dots, n\} : d(\mathbf{x}_i, \mathbf{x}) \leq d_{\mathbf{x}}^k \right\},$$

and $d_{\mathbf{x}}^k$ is the distance from the k -th nearest neighbor of \mathbf{x} to \mathbf{x} . In other words, the regression function evaluated at \mathbf{x} is estimated using a local average of the responses of the k nearest neighbors to \mathbf{x} in the covariate space.

The tuning parameter k can be chosen through cross-validation. A high value of k leads to a very simple model (approaching a constant as $k \rightarrow \infty$), resulting in high bias but low variance. Conversely, a low value of k leads to an estimator with high variance but low bias.

In a classification context, Equation 2.12 can be replaced by a majority voting mechanism. Specifically, the predicted class label $\hat{y}(\mathbf{x})$ for a given point \mathbf{x} is determined by the most frequent class among its k nearest neighbors.

Formally, this can be expressed as:

$$g(\mathbf{x}) = \arg \max_{c \in \mathcal{Y}} \sum_{i \in \mathcal{N}_{\mathbf{x}}} \mathbb{I}(y_i = c).$$

Alternatively, probabilities of each class can be estimated by calculating the proportion of neighbors that belong to each class. This probabilistic version of KNN assigns a probability to each class label based on the relative frequency of that label among the k nearest neighbors. Formally, the estimated probability that a point \mathbf{x} belongs to class c is given by:

$$\hat{\mathbb{P}}(Y = c | \mathbf{x}) = \frac{1}{k} \sum_{i \in \mathcal{N}_{\mathbf{x}}} \mathbb{I}(y_i = c).$$

2.6.3 Trees

Trees are a non-parametric approach that provides highly interpretable results. They are built by recursively partitioning the covariate space, where each division forms a node, and each endpoint represents a leaf; see Figure 2.4 for an example.

To predict a new observation, we start at the top of the tree and evaluate the condition at the root node. If the condition is met, we proceed left; if not, we go right. This process repeats at each node until reaching a leaf.

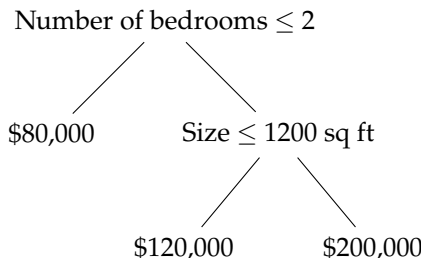


Figure 2.4: Regression tree that predicts the price of an apartment.

Formally, a tree creates a partition of the covariate space into distinct and disjoint regions: R_1, \dots, R_j . In a regression context, the prediction for the

2.6. Methods to Create Prediction Functions

response Y of an observation with covariates \mathbf{x} that are in R_k is given by

$$g(\mathbf{x}) = \frac{1}{|\{i : \mathbf{x}_i \in R_k\}|} \sum_{i:\mathbf{x}_i \in R_k} y_i. \quad (2.13)$$

To predict the response value for \mathbf{x} , we identify the region to which \mathbf{x} belongs and calculate the average of the response variable values for the training samples within this region. In classification, this aggregation can instead use the mode of the Y values that fall within R_k , for example.

The construction of a tree structure involves two main steps: (i) growing a fully developed, complex tree, and (ii) pruning it to avoid overfitting.

In step (i), the objective is to form "pure" partitions, where the values of Y in each leaf's training observations are as homogeneous as possible. Achieving this requires defining a measure of leaf homogeneity for a tree T . In regression tasks, the mean squared error is often used:

$$\mathcal{P}(T) = \sum_R \sum_{i:\mathbf{x}_i \in R} \frac{(y_i - \hat{y}_R)^2}{n},$$

where \hat{y}_R is the predicted response value for observations within region R . For classification tasks, the Gini index is frequently applied:

$$\sum_R \sum_{c \in \mathcal{Y}} \hat{p}_{R,c} (1 - \hat{p}_{R,c}),$$

where $\hat{p}_{R,c}$ denotes the proportion of observations in region R classified as belonging to category c .

Finding the optimal tree T to minimize $\mathcal{P}(T)$ is practically infeasible due to computational complexity. Instead, we use a heuristic approach to construct a tree with high homogeneity by making recursive binary splits, as shown in Figure 2.5.

The algorithm begins by dividing the covariate space into two distinct regions, illustrated in Figure 2.5(a). To determine the first partition (R_1, R_2), we systematically explore all combinations of covariates x_i and potential cut points t_1 , selecting the combination that maximizes homogeneity within each

region. Thus, we define

$$R_1 = \{\mathbf{x} : x_i < t_1\} \text{ and } R_2 = \{\mathbf{x} : x_i \geq t_1\}.$$

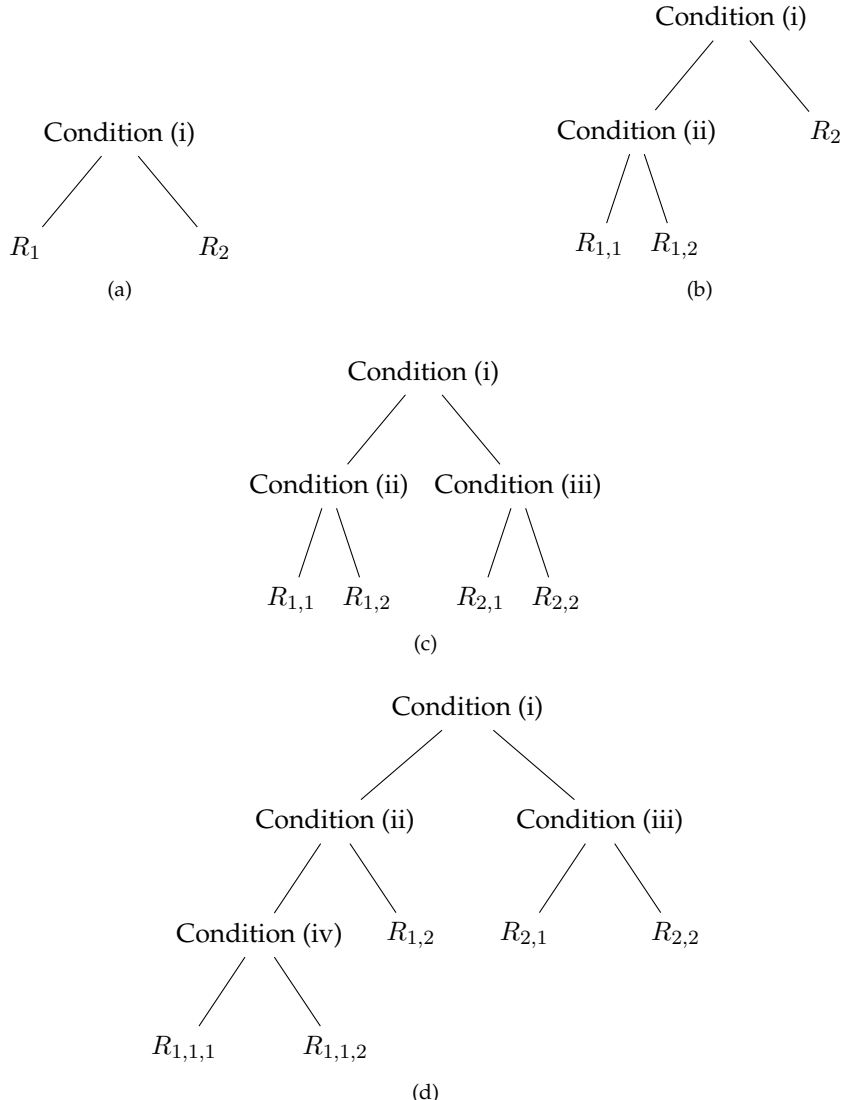


Figure 2.5: Recursively growing a tree.

2.6. Methods to Create Prediction Functions

After establishing these initial regions, the root node of the tree is set. In the next step, we aim to further split either R_1 or R_2 , as shown in Figure 2.5(b). To identify the optimal new split, we apply the same strategy: exploring all combinations of covariates x_i and cut points t_2 to find the configuration that maximizes homogeneity. At this stage, we must also choose which region to split, either R_1 or R_2 . Suppose we opt to partition R_1 using covariate x_j and cut point t_2 . This results in the subregions $\{R_{1,1}, R_{1,2}\}$, illustrated in Figure 2.5(b). Thus, we define

$$R_{1,1} = \{\mathbf{x} : x_i < t_1, x_j < t_2\}, \quad R_{1,2} = \{\mathbf{x} : x_i < t_1, x_j \geq t_2\}, \text{ and} \\ R_2 = \{\mathbf{x} : x_i \geq t_1\}.$$

This recursive procedure continues, as illustrated in Figures 2.5(c) and (d), until the tree reaches a stage where each leaf node contains only a small, predetermined number of observations. For instance, the process may be halted once all leaf nodes contain fewer than five observations.

The tree generated by this process performs well on the training set, but it tends to overfit, resulting in poor predictive performance on new observations. To address this, we proceed to step (ii), known as pruning. The aim here is to reduce the tree's size and complexity, thus lowering the variance of the estimator. During pruning, nodes are removed one at a time, and the prediction error on a validation set is evaluated. Based on these results, decisions are made regarding which nodes should remain in the tree.

2.6.4 Bagging and Random Forests

Regression trees are highly interpretable, but they often have lower predictive power compared to other estimators. Bagging and random forests (Breiman, 2001b) address this limitation by combining multiple trees to improve predictions for the same problem.

To illustrate this approach, imagine a regression scenario where we have two prediction functions for Y , $g_1(\mathbf{x})$ and $g_2(\mathbf{x})$. The risks associated with these (conditional on \mathbf{x}) are given by

$$\mathbb{E}[(Y - g_1(\mathbf{x}))^2 | \mathbf{x}] \quad \text{and} \quad \mathbb{E}[(Y - g_2(\mathbf{x}))^2 | \mathbf{x}],$$

respectively. Now, consider the combined estimator $g(\mathbf{x}) = \frac{g_1(\mathbf{x}) + g_2(\mathbf{x})}{2}$. Then we have

$$\begin{aligned}\mathbb{E}[(Y - g(\mathbf{x}))^2 | \mathbf{x}] &= \mathbb{V}[Y | \mathbf{x}] + \frac{1}{4}\mathbb{V}[g_1(\mathbf{x}) + g_2(\mathbf{x}) | \mathbf{x}] + \\ &\quad \left(\mathbb{E}[Y | \mathbf{x}] - \frac{\mathbb{E}[g_1(\mathbf{x}) | \mathbf{x}] + \mathbb{E}[g_2(\mathbf{x}) | \mathbf{x}]}{2} \right)^2.\end{aligned}$$

If $g_1(\mathbf{x})$ and $g_2(\mathbf{x})$ are uncorrelated (that is, $\text{Cor}(g_1(\mathbf{x}), g_2(\mathbf{x}) | \mathbf{x}) = 0$), unbiased (that is, $\mathbb{E}[g_1(\mathbf{x}) | \mathbf{x}] = \mathbb{E}[g_2(\mathbf{x}) | \mathbf{x}] = r(\mathbf{x})$), and have equal variance (that is, $\mathbb{V}[g_1(\mathbf{x}) | \mathbf{x}] = \mathbb{V}[g_2(\mathbf{x}) | \mathbf{x}]$), then

$$\mathbb{E}[(Y - g(\mathbf{x}))^2 | \mathbf{x}] = \mathbb{V}[Y | \mathbf{x}] + \frac{1}{2}\mathbb{V}[g_i(\mathbf{x}) | \mathbf{x}] \leq \mathbb{E}[(Y - g_i(\mathbf{x}))^2 | \mathbf{x}] \quad (2.14)$$

for $i = 1, 2$. This shows that it is preferable to use the combined estimator $g(\mathbf{x})$ over either $g_1(\mathbf{x})$ or $g_2(\mathbf{x})$ alone. Although this example considers only two estimators, the same principle applies when combining any number B of estimators.

Building on this concept, bagging – short for "bootstrap aggregating" – works by generating B distinct trees from B bootstrap samples of the original dataset². Each tree is constructed following the steps in Section 2.6.3 but without pruning, allowing each tree to grow fully. After building the trees, bagging combines their predictions to produce a more stable estimator. In regression, the aggregated prediction function is

$$g(\mathbf{x}) = \frac{1}{B} \sum_{b=1}^B g_b(\mathbf{x}),$$

where $g_b(\mathbf{x})$ represents the prediction from the b -th tree. In classification, the final prediction is obtained by taking the majority vote across all trees.

Random forests extend the concept of bagging by introducing extra randomness into the tree-building process. In addition to using bootstrap samples, random forests select a random subset of features at each node split, which decreases the correlation between trees and improves predictive accuracy over

²A bootstrap sample is a random sample with replacement that matches the original sample size.

2.6. Methods to Create Prediction Functions

bagging alone. Specifically, instead of considering all d covariates at each node, a random subset of $m < d$ covariates is chosen for each split. These m covariates are randomly drawn from the full set, with a new subset selected at each node as the tree expands. In classification tasks, a common choice is to select \sqrt{p} features from a total of p features at each split, while in regression, typically $p/3$ features are used.

2.6.5 Boosting

Like random forests and bagging, boosting aggregates multiple prediction functions, but it combines them in a distinct manner. Boosting iteratively builds new models to correct errors made by previous ones, refining predictions with each step. Various implementations and variations of boosting exist; here, we will focus on a single approach in the regression context.

In boosting, the estimator $g(\mathbf{x})$ is built incrementally. Initially, we set $g(\mathbf{x}) \equiv 0$, resulting in an estimator with high bias but minimal variance (specifically, zero). At each step, we adjust g to reduce bias while carefully managing an increase in variance. This is achieved by adding a function that predicts the residuals $r_i = Y_i - g(\mathbf{x}_i)$. A common choice for this function is a regression tree, but to prevent overfitting, this tree is typically shallow. Furthermore, instead of adding this function directly, we multiply it by a factor λ , known as the "learning rate," which takes a value between 0 and 1 to further guard against overfitting. Formally, this version of boosting follows the following algorithm:

1. Define $g(\mathbf{x}) \equiv 0$ and $r_i = y_i \forall i = 1, \dots, n$.
2. For $b = 1, \dots, B$:
 - (a) Fit a tree with p leaves to $(\mathbf{x}_1, r_1), \dots, (\mathbf{x}_n, r_n)$. Let $g^b(\mathbf{x})$ be its respective prediction function.
 - (b) Update g and the residuals: $g(\mathbf{x}) \leftarrow g(\mathbf{x}) + \lambda g^b(\mathbf{x})$ and $r_i \leftarrow Y_i - g(\mathbf{x})$.
3. Return the final model $g(\mathbf{x})$.

In this version of boosting, the key tuning parameters are B , p , and λ . Unlike random forests, large values of B can lead to overfitting, so B is typically selected through data splitting.

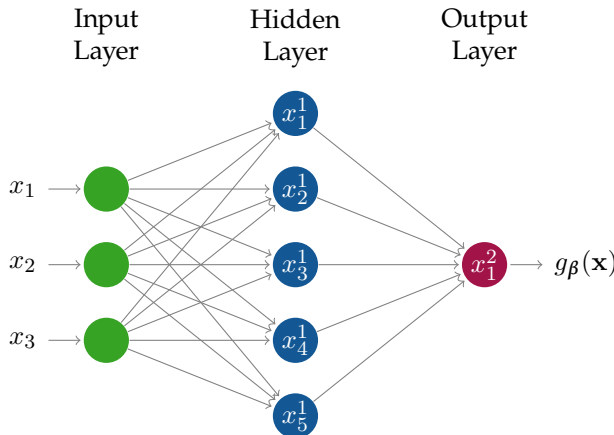


Figure 2.6: Example of a neural network with one hidden layer.

Modern boosting implementations, such as XGBoost (Chen and Guestrin, 2016), LightGBM (Ke et al., 2017), and CatBoost (Prokhorenkova et al., 2018), have enhanced the method with optimizations like gradient-based learning, regularization, parallel processing, and efficient handling of categorical variables. These advancements make boosting more accurate and scalable.

2.6.6 Artificial Neural Networks

With four parameters I can fit an elephant, and with five I can make him wiggle his trunk.

John von Neumann

Artificial neural networks are a well-established concept in artificial intelligence and dates back to the 1940's (McCulloch and Pitts, 1943; Rosenblatt, 1958).

Structure. Neural networks parametrize the function that is being estimated. In the context of regression, they function as a non-linear estimator of $r(\mathbf{x})$ and can be visually represented by a structure similar to that shown in Figure 2.6.

The nodes on the left side of the figure represent the network inputs,

2.6. Methods to Create Prediction Functions

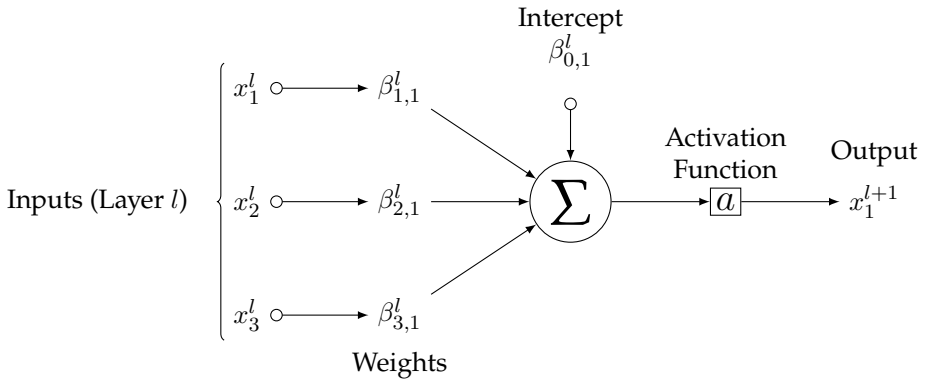


Figure 2.7: Example of the processing that occurs within a neuron located in layer $l + 1$. The output x_1^{l+1} is given by $a \left(\beta_{0,j}^l + \sum_{i=1}^3 \beta_{i,1}^l x_i^l \right)$.

corresponding to the dataset covariates (three in this example). The nodes in the second layer, called hidden layer nodes, apply transformations to the inputs from the previous layer. Each arrow represents a weight β (a parameter in statistical terms) associated with a connection. These weights control how each node in the hidden layer combines the inputs from the previous layer.

For this network, if $\mathbf{x} = (x_1, x_2, x_3)$ is the input vector, the output of a neuron j in the hidden layer is computed as

$$x_j^1 := a \left(\beta_{0,j}^0 + \sum_{i=1}^3 \beta_{i,j}^0 x_i^0 \right), \quad \text{where } x_i^0 = x_i \text{ for } i = 1, 2, 3,$$

with a representing a user-defined function called the *activation function*. The superscript indicates the layer in the network. Once all x_j^1 values for neurons j in the hidden layer are computed, the model output can be calculated. In this example, the output is given by

$$x_1^2 := a \left(\beta_{0,1}^1 + \sum_{i=1}^3 \beta_{i,1}^1 x_i^1 \right) =: g_{\beta}(\mathbf{x}).$$

This process is illustrated in detail in Figure 2.7.

Some common choices for the activation function are:

- **Identity:** $a(z) = z$
- **Logistic:** $a(z) = \frac{1}{1+e^{-z}}$
- **Hyperbolic Tangent:** $a(z) = \frac{e^z - e^{-z}}{e^z + e^{-z}}$
- **ReLU (Rectified Linear Unit):** $a(z) = \max\{0, z\}$
- **Leaky ReLU:** $a(z) = \begin{cases} 0.01z & \text{if } z < 0 \\ z & \text{if } z \geq 0 \end{cases}$

In general, a neural network can have multiple hidden layers and a different number of neurons in each layer. These are choices made by the user. Figure 2.8 presents a schematic of a neural network with four hidden layers, each with six neurons.

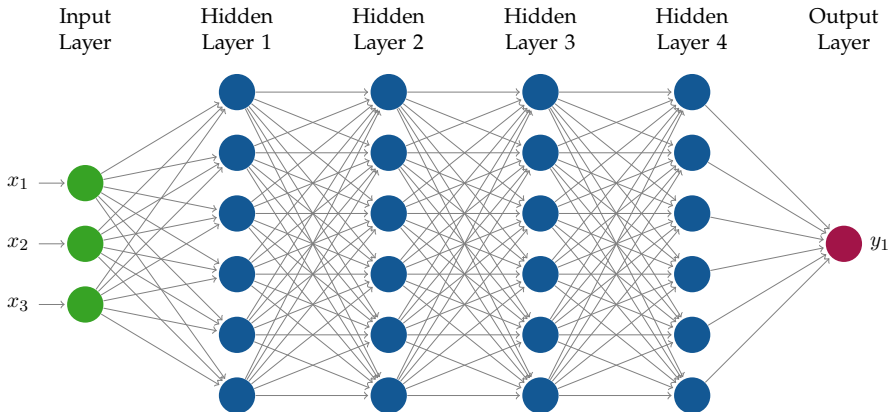


Figure 2.8: Example of a feed-forward neural network.

The propagation of input covariates in the neural network is done sequentially through these layers. Consider a network with H hidden layers, each with d_h neurons ($h = 1, \dots, H$), and let $\beta_{i,j}^l$ be the weight assigned to the connection between input i in layer l and output j in layer $l+1$, $l = 0, \dots, H$. Here, $h = 0$ denotes the input layer, and $H+1$ denotes the output layer. The estimator

2.6. Methods to Create Prediction Functions

of an artificial neural network for the regression function takes the form

$$g(\mathbf{x}) = x_1^{H+1} = a \left(\beta_{0,1}^H + \sum_{i=1}^{d_H} \beta_{i,1}^H x_i^H \right) \quad (2.15)$$

where, for all $l = 1, \dots, H$ and $j = 1, \dots, d_{l+1}$,

$$x_j^{l+1} = a \left(\beta_{0,j}^l + \sum_{i=1}^{d_l} \beta_{i,j}^l x_i^l \right).$$

Notice that if $a(z) = z$ and there are no hidden layers, a neural network represents a regular linear regression. Indeed, as a linear regression, a neural network also parametrizes g . However, such parametrization is typically more complex, and the architecture of the network (and therefore its parametrization) is usually taylored for each dataset.

Another way to represent a neural network is through matrix notation. For $l = 0, \dots, H$, let

$$\mathbb{H}_l = \begin{pmatrix} \beta_{0,1}^l & \beta_{1,1}^l & \cdots & \beta_{d_l,1}^l \\ \vdots & \vdots & \ddots & \vdots \\ \beta_{0,d_{l+1}}^l & \beta_{1,d_{l+1}}^l & \cdots & \beta_{d_l,d_{l+1}}^l \end{pmatrix}$$

be the collection of all weights associated to the l -th layer of a network. In this case, $d_0 = d$ is the number of neurons in the input layer, and d_{H+1} is the number of neurons in the output layer. The estimator of Equation 2.15 can be written as the following composition of functions:

$$g(\mathbf{x}) = a \circ \mathbb{H}_H \dots \tilde{a} \circ \mathbb{H}_1 \cdot \tilde{a} \circ \mathbb{H}_0 \cdot \tilde{\mathbf{x}},$$

where $\tilde{\mathbf{x}} = (1, \mathbf{x})$ and $\tilde{a}(\mathbf{y}) = (1, a(\mathbf{y}))$.

The structure of neural networks discussed here can be highly generalized. For example, each function a applied at each layer may differ, and the network's output need not be limited to a single real number. Neural networks can also accommodate more complex architectures, such as feedback loops, where outputs from neurons are fed back into earlier layers.

In classification tasks, the network's output typically consists of K values:

$$g_0(\mathbf{x}), \dots, g_{K-1}(\mathbf{x}),$$

representing estimates of the probabilities $\mathbb{P}(Y = i|\mathbf{x})$ for $i = 0, \dots, K-1$. Figure 2.9 provides an illustration of a typical classification network architecture.

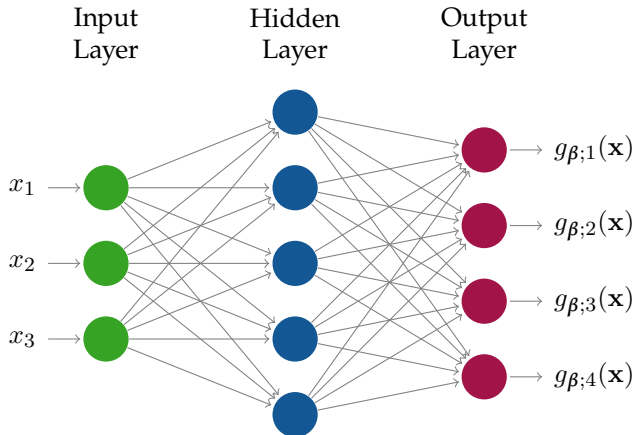


Figure 2.9: Example of a classification neural network with one hidden layer in the case where Y takes four possible values.

To produce these probability estimates, the *softmax* function is commonly used as the activation function in the final layer. The softmax function is defined as:

$$a_i(\mathbf{z}) = \frac{e^{z_i}}{\sum_{j=0}^{K-1} e^{z_j}},$$

where \mathbf{z} represents the vector of inputs in the last layer, and a_i is the activation applied to the i -th neuron in the output layer. This function ensures that all output values fall within the range of zero to one and that the outputs sum to one, making them interpretable as probabilities. The softmax function can be seen as a generalization of the logistic function to multiple classes.

Estimation. To estimate the parameters of a neural network, a differentiable loss function must first be defined. In regression tasks, the mean squared error

2.6. Methods to Create Prediction Functions

is commonly used:

$$\text{MSE}(g_{\beta}) = \frac{1}{n} \sum_{i=1}^n (g_{\beta}(\mathbf{x}_i) - y_i)^2,$$

where β represents all the network parameters, encompassing the collection of matrices $\mathbb{H}_0, \dots, \mathbb{H}_H$.

For classification tasks, the cross-entropy loss is typically used:

$$\text{CE}(g_{\beta,0}, \dots, g_{\beta,K-1}) = -\frac{1}{n} \sum_{i=1}^n \sum_{j=0}^{K-1} \mathbb{I}(y_i = j) \log(g_{\beta;j}(\mathbf{x}_i)).$$

In this case, $g_{\beta;j}(\mathbf{x}_i)$ represents the estimated probability for class j given input \mathbf{x}_i , and $\mathbb{I}(y_i = j)$ is an indicator function that equals 1 if $y_i = j$ and 0 otherwise.

Once the loss function is defined, the next step is to minimize it with respect to the parameters β of the neural network. This is typically done using gradient-based optimization methods, such as gradient descent or its variants (e.g., stochastic gradient descent, Adam). The gradient of the loss function with respect to the parameters β is computed using backpropagation, which efficiently applies the chain rule to propagate the error backward through the network layers.

The optimization process iteratively updates the parameters β in the direction that decreases the loss function, aiming to reach a minimum. However, reaching the true global minimum of the loss function may not be desirable. For instance, consider the behavior of the 50-degree polynomial fit used to minimize the MSE in Example 2.1. Such a fit, while minimizing the training error, can lead to overfitting. Therefore, in practice regularization needs to be performed to ensure that the resulting estimated function is smooth and generalizes effectively to new, unseen data.

Early stopping is one such technique used to prevent overfitting. It halts the training process before the model fully converges to the minimum of the loss function, stopping when the validation loss stops improving, which signals the onset of overfitting. The best model parameters (those that resulted in the lowest validation loss) are then used as the final model. Figure 2.10 illustrates early stopping.



Figure 2.10: Training and validation loss over iterations during the training process of a neural network. The training loss decreases as the model learns, while the validation loss initially declines but later rises due to overfitting. The dashed vertical line indicates the epoch where early stopping is implemented, halting training to prevent overfitting.

In addition to early stopping, the choice of optimization method plays a crucial role in preventing poor generalization. One of the most commonly used methods is stochastic gradient descent (SGD). Unlike batch gradient descent, which computes gradients using the entire training set, SGD updates the model parameters based on gradients computed from a single training sample point or a small mini-batch $B \subset \{(\mathbf{X}_1, Y_1), \dots, (\mathbf{X}_n, Y_n)\}$. The batch being used changes at each iteration. This prevents the model from settling into sharp minima – often associated with overfitting – and encourages finding flatter minima that give better predictions.

Another widely used technique to prevent overfitting in neural networks is dropout. Dropout is a regularization method where, during each training iteration, a random subset of neurons in the network is "dropped out," or temporarily removed from the network (that is, set to zero). This forces the network to learn more robust features that are not reliant on specific neurons, as different subsets of neurons are active at different times. At test time, dropout is turned off, and the full network is used, but with the weights scaled down to account for the dropped neurons during training. In Section 6.4 we discuss how dropout can also be used for UQ.

2.7. The Myth of Imbalanced Data

For a more in-depth exploration of neural networks, we recommend referring to Goodfellow et al. (2016) and Zhang et al. (2021).

2.7 The Myth of Imbalanced Data

Myths which are believed in tend
to become true.

George Orwell

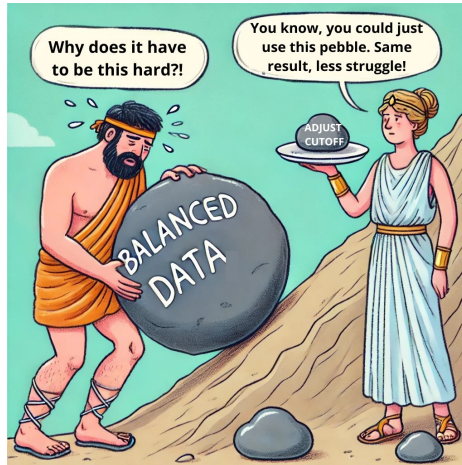
Imbalanced data is often considered problematic in binary classification because the classifier frequently defaults to a trivial classifier. A trivial classifier is one that always predicts the majority class, regardless of the input features. This can happen because, when using a cutoff of 0.5 (which is the default choice in most implementations) in the plugin classifier

$$g(\mathbf{x}) = \begin{cases} 1, & \text{if } \widehat{\mathbb{P}}(Y = 1 | \mathbf{x}) \geq 0.5, \\ 0, & \text{otherwise,} \end{cases}$$

the model will always predict the majority class in highly imbalanced datasets. For example, if the probability of $Y = 1$ is very low, say 0.01, the classifier will often predict $Y = 0$, leading to the trivial classifier $g(\mathbf{x}) \equiv 0$ (always predicting 0) when there is not too much information in the covariates to distinguish between classes.

However, the real issue of the problem is not imbalanced. Instead, the issue is that the choice 0.5 implicitly assumes equal costs for classification errors (Theorem 2), which is rarely true in practice. For instance, in medical diagnostics for a rare disease, misclassifying a sick patient ($Y = 1$) as healthy ($Y = 0$) is far more costly than the reverse. In such cases, relying on the 0.5 threshold leads to an overly conservative classifier that frequently misses true positives, especially when the disease is rare.

The misconception that imbalanced data itself is the core issue arises because, when the data is imbalanced, the triviality of the classifier makes the problem evident. However, the real problem lies with the zero-one loss function that does not capture the asymmetric nature of the problem.



A common solution to this problem is oversampling, which artificially balances the dataset by increasing the representation of the minority class. However, oversampling merely repeats the same data and therefore does not add new information. Instead, a better and faster solution lies in adjusting the loss function or modifying the decision cutoff to reflect the actual costs of misclassification. In fact, as shown in Assunção et al. (2024), oversampling is essentially equivalent to adjusting the decision threshold to $C = \mathbb{P}(Y = 1)$. The cutoff approach however is more general and allows for other costs. Assunção et al. (2024) also discuss other data augmentation techniques that, in some cases, can be more effective than oversampling because they introduce additional information rather than simply repeating existing data.

Despite these issues, hundreds of posts on platforms like Towards Data Science and Medium continue to advocate oversampling as the primary solution, overlooking the fact that the real issue lies in the inadequacy of the zero-one loss function and the inappropriate use of the 0.5 threshold, not the class imbalance itself.

2.8 Summary

In this chapter, we reviewed the fundamentals of supervised learning, where the goal is to predict a target variable (label) Y using a set of input

2.8. Summary

variables (features) \mathbf{x} . We saw that this task can be categorized as regression when Y is quantitative and classification when Y is qualitative.

We explored the concepts of loss functions and risk, emphasizing that different loss functions lead to different optimal solutions, such as the regression function in regression problems and the Bayes classifier in classification problems. We discussed the importance of model selection and saw how challenges like overfitting and underfitting can impact model performance. Techniques like data splitting, cross-validation, and understanding the bias-variance trade-off were introduced as essential tools for improving model selection and predictive accuracy.

The chapter also introduced various supervised learning methods. We saw examples of parametric methods, like linear regression, lasso, and logistic regression, which involve specific assumptions about the form of the prediction function. These methods generally have low variance but high bias. On the other hand, non-parametric methods, such as k -nearest neighbors and decision trees, were discussed for their flexibility in modeling data due to their low bias. These however have high variance, and thus generally require larger sample sizes. We also explored non-parametric ensemble methods like bagging, random forests, and boosting, which combine multiple models to enhance predictive performance. Lastly, we examined neural networks, highlighting their ability to capture complex relationships through highly flexible, parameterized functions, with the parametrization determined by the network's architecture.

Chapter 3

Quantifying Aleatoric Uncertainty with Conditional Densities



Under the Wave off Kanagawa. Katsushika Hokusai, 1831, The Metropolitan Museum of Art, New York.

3.1. Loss Functions

Prediction is very difficult,
especially if it is about the future.

Niels Bohr

Instead of focusing on a single point prediction $g(\mathbf{x})$ for Y , it is often more useful to understand the uncertainty around Y . This chapter focuses on estimating the conditional density $f(y|\mathbf{x})$, which captures the aleatoric uncertainty in Y for both discrete and continuous labels. Chapters 5 and 6 will explore epistemic uncertainty.

In classification problems, for example, $f(y|\mathbf{x}) = \mathbb{P}(Y = y|\mathbf{x})$ allows us to answer questions like, "What is the probability that the predicted label is correct?" This probability is $\mathbb{P}(Y = g(\mathbf{X})|\mathbf{x}) = f(g(\mathbf{x})|\mathbf{x})$.

The density $f(y|\mathbf{x})$ gives the full distribution of $Y|\mathbf{x}$ and can also be used to derive quantities like the regression function $\mathbb{E}[Y|\mathbf{x}] = \int y f(y|\mathbf{x}) dy$, which can be estimated using $\hat{f}(y|\mathbf{x})$. Quantiles of $Y|\mathbf{x}$ can also be directly estimated from $\hat{f}(y|\mathbf{x})$.

We begin by introducing loss functions for evaluating conditional density estimators. Next, we cover methods for estimating $f(y|\mathbf{x})$ in classification and regression settings. Finally, we discuss ways to directly estimate quantiles of $f(y|\mathbf{x})$.

3.1 Loss Functions

Similar to the standard supervised learning approach (Chapter 2), when it comes to comparing and fine-tuning different Conditional Density Estimators (CDEs), it is essential to define a suitable loss function. In this chapter, we define a loss function as a mapping

$$L: \mathcal{F} \times \mathcal{X} \times \mathcal{Y} \rightarrow \mathbb{R}$$
$$(\hat{f}, \mathbf{x}, y) \mapsto L(\hat{f}; \mathbf{x}, y),$$

where \hat{f} is an estimate of f and \mathcal{F} denotes the class of all conditional density estimates.

Typically, loss functions for conditional density estimation are required to be proper - their implied risk must be minimized by the true conditional density $f(y|\mathbf{x})$:

Definition 1 (Proper loss function). *A CDE loss function L is proper if, and only if,*

$$f = \arg \min_{\hat{f} \in \mathcal{F}} \mathbb{E} \left[L(\hat{f}; \mathbf{X}, Y) \right],$$

where f denotes the true conditional density of $Y|\mathbf{x}$.

For a loss function to be useful, it must not only be proper but also have a risk that is easy to estimate. In the next sections, we explore some examples of loss functions with these characteristics.

3.1.1 The L_2 loss and the Brier Score

The L_2 -loss is given by

$$L_2(\hat{f}; \mathbf{x}, y) = \int \left(\hat{f}(y'|\mathbf{x}) - f(y'|\mathbf{x}) \right)^2 dy',$$

where the integral is a summation for classification problems.

The L_2 -risk is therefore given by

$$\begin{aligned} \mathbb{E} \left[L_2(\hat{f}; \mathbf{X}, Y) \right] &= \iint \left(\hat{f}(y|\mathbf{x}) - f(y|\mathbf{x}) \right)^2 dP(\mathbf{x}) dy \\ &= \iint \hat{f}^2(y|\mathbf{x}) dP(\mathbf{x}) dy - 2 \iint \hat{f}(y|\mathbf{x}) dP(\mathbf{x}, y) + C, \end{aligned} \quad (3.1)$$

where C is a constant that does not depend on the estimator and $P(\mathbf{x}, y)$ is the joint distribution of (\mathbf{X}, Y) . It is easy to see from Equation 3.1 that the L_2 loss is proper.

Given a validation sample $(\mathbf{X}'_1, Y'_1), \dots, (\mathbf{X}'_m, Y'_m)$, the L_2 -risk can be estimated (up to C , which is not required for model selection and parameter tuning) by

$$\frac{1}{m} \sum_{i=1}^m \int \hat{f}^2(y|\mathbf{x}'_i) dy - 2 \frac{1}{m} \sum_{i=1}^m \hat{f}(y'_i|\mathbf{x}'_i).$$

3.1. Loss Functions

Notice that, in the classification problem, this estimate can be rewritten as

$$\begin{aligned}
& \frac{1}{m} \sum_{i=1}^m \sum_{j=0}^{k-1} \hat{f}^2(j|\mathbf{x}'_i) - 2 \frac{1}{m} \sum_{i=1}^m \sum_{j=0}^{k-1} \hat{f}(j|\mathbf{x}'_i) \mathbb{I}(y'_i = j) \\
&= \frac{1}{m} \sum_{i=1}^m \sum_{j=0}^{k-1} \left(\hat{f}(j|\mathbf{x}'_i) - \mathbb{I}(y'_i = j) \right)^2 - \frac{1}{m} \sum_{i=1}^m \sum_{j=0}^{k-1} \mathbb{I}(y'_i = j) \\
&= \frac{1}{m} \sum_{i=1}^m \sum_{j=0}^{k-1} \left(\hat{f}(j|\mathbf{x}'_i) - \mathbb{I}(y'_i = j) \right)^2 - 1.
\end{aligned}$$

It follows that minimizing the estimate of the L_2 -risk is equivalent to minimizing

$$\frac{1}{m} \sum_{i=1}^m \sum_{j=0}^{k-1} \left(\hat{f}(j|\mathbf{x}'_i) - \mathbb{I}(y'_i = j) \right)^2, \quad (3.2)$$

which is known as the Brier score (Brier, 1950).

3.1.2 The Cross-Entropy Loss (or the Negative Loglikelihood)

Only entropy comes easy.

Anton Chekhov

The cross-entropy loss is defined as

$$L_{\text{CE}}(\hat{f}; \mathbf{x}, y) = -\log \left(\hat{f}(y|\mathbf{x}) \right), \quad (3.3)$$

and therefore the CE-risk is given by

$$\mathbb{E} \left[L_{\text{CE}}(\hat{f}; \mathbf{X}, Y) \right] = -\mathbb{E} \left[\log \left(\hat{f}(Y|\mathbf{X}) \right) \right].$$

This risk can be estimated by the observed negative log-likelihood of a validation sample

$$-\frac{1}{m} \sum_{i=1}^m \log \left(\hat{f}(y'_i|\mathbf{x}'_i) \right),$$

which, in the case of classification, is often written as

$$-\frac{1}{m} \sum_{i=1}^m \sum_{j=0}^{k-1} \mathbb{I}(y'_i = j) \log(\hat{f}(j|\mathbf{x}'_i)).$$

The reason the cross-entropy loss has this name is that its associated risk is the expected cross-entropy between f and \hat{f} :

$$\begin{aligned}\mathbb{E}[L_{\text{CE}}(\hat{f}; \mathbf{X}, Y)] &= \mathbb{E}\left[\mathbb{E}\left[L_{\text{CE}}(\hat{f}; \mathbf{X}, Y) | \mathbf{X}\right]\right] \\ &= \mathbb{E}\left[H(f(\cdot|\mathbf{X}), \hat{f}(\cdot|\mathbf{X}))\right],\end{aligned}$$

where $H(p, q) = -\int p(y) \log(q(y)) dy$ denotes the cross-entropy between distributions p and q . Because $H(p, q)$ is minimized when $p = q$, it follows that the cross-entropy loss is also proper.

The cross-entropy loss can also be characterized in terms of the Kullback-Leibler divergence. Indeed,

$$H(f(\cdot|\mathbf{x}), \hat{f}(\cdot|\mathbf{x})) = H(f(\cdot|\mathbf{x})) + D_{\text{KL}}(f(\cdot|\mathbf{x}) \| \hat{f}(\cdot|\mathbf{x})),$$

where $H(f(\cdot|\mathbf{x})) = -\int f(y|\mathbf{x}) \log f(y|\mathbf{x}) dy$ is the entropy of the true distribution f , and

$$D_{\text{KL}}(f(\cdot|\mathbf{x}) \| \hat{f}(\cdot|\mathbf{x})) = \int f(y|\mathbf{x}) \log \frac{f(y|\mathbf{x})}{\hat{f}(y|\mathbf{x})} dy,$$

is the Kullback-Leibler divergence between f and \hat{f} . As $H(f(\cdot|\mathbf{X}))$ does not depend on \hat{f} , this shows that

$$\arg \min_{\hat{f} \in \mathcal{G}} \mathbb{E}[L_{\text{CE}}(\hat{f}; \mathbf{X}, Y)] = \arg \min_{\hat{f} \in \mathcal{G}} \mathbb{E}\left[D_{\text{KL}}(f(\cdot|\mathbf{X}) \| \hat{f}(\cdot|\mathbf{X}))\right],$$

where \mathcal{G} is any set of estimated densities. That is, minimizing the expected cross-entropy loss corresponds to minimizing the expected Kullback-Leibler divergence between f and \hat{f} .

The cross-entropy loss is sensitive to the tails of the estimated distribution because it penalizes small predicted probabilities heavily. When the true outcome y has a low predicted probability $\hat{f}(y|\mathbf{x})$, the logarithm of this small value leads to a large loss. This means that even a few low-probability events

3.1. Loss Functions

can significantly increase the overall loss, pushing the model to give more weight to rare or extreme outcomes. While this helps capture infrequent events, it also makes the model more sensitive to outliers and noise (Bowman, 1985; Hall, 1987).

3.1.3 Continuous Ranked Probability Score (CRPS)

The Continuous Ranked Probability Score (CRPS) is a proper scoring rule often used to evaluate probabilistic predictions, particularly when dealing with continuous variables (Gneiting and Katzfuss, 2014; Matheson and Winkler, 1976). CRPS measures the accuracy of an estimated conditional density \hat{f} through its cumulative distribution function (CDF), \hat{F} . In the context of conditional density estimation, the CRPS loss is defined as

$$L_{\text{CRPS}}(\hat{f}; \mathbf{x}, y) = \int_{-\infty}^{\infty} \left(\hat{F}(t|\mathbf{x}) - \mathbb{I}(y \leq t) \right)^2 dt,$$

where $\hat{F}(t|\mathbf{x}) = \int_{-\infty}^t \hat{f}(y|\mathbf{x}) dy$ is the estimated CDF for the conditional distribution of Y given \mathbf{x} . In simple terms, CRPS represents the squared difference between the predicted and empirical cumulative distributions.

Matheson and Winkler (1976) show that¹

$$L_{\text{CRPS}}(\hat{f}; \mathbf{x}, y) = \mathbb{E}[|Y - y| \mid \mathbf{x}] - \frac{1}{2} \mathbb{E}[|Y - Y'| \mid \mathbf{x}],$$

where Y and Y' are independent random variables with distribution $\hat{F}(\cdot|\mathbf{x})$, and both expectations are taken with respect to $\hat{F}(\cdot|\mathbf{x})$. This leads to two key observations:

- (i) If, for each \mathbf{x} , $\hat{f}(\cdot|\mathbf{x})$ is degenerate at a point prediction $y_0(\mathbf{x})$, then

$$L_{\text{CRPS}}(\hat{f}; \mathbf{x}, y) = |y_0(\mathbf{x}) - y|,$$

showing that CRPS generalizes the absolute error used in point predictions to density estimators. This property makes CRPS particularly useful for comparing density estimators with point estimators.

¹While the original definitions and proofs for CRPS are for unconditional distributions, they naturally extend to conditional distributions.

(ii) $L_{\text{CRPS}}(\hat{f}; \mathbf{x}, y)$ is in the same units as Y .

The next theorem shows that CRPS is proper.

Theorem 3. *The loss $L_{\text{CRPS}}(\hat{f}; \mathbf{X}, Y)$ is proper.*

Proof. Let $F(y|\mathbf{x})$ denote the true CDF of $Y|\mathbf{x}$. We begin by considering the expected CRPS loss conditioned on a fixed $\mathbf{X} = \mathbf{x}$:

$$\mathbb{E} [L_{\text{CRPS}}(\hat{f}; \mathbf{X}, Y) | \mathbf{x}] = \mathbb{E} \left[\int_{-\infty}^{\infty} (\hat{F}(t|\mathbf{x}) - F(t|\mathbf{x}) + F(t|\mathbf{x}) - \mathbb{I}(Y \leq t))^2 dt \middle| \mathbf{x} \right].$$

Expanding the square and changing the order of expectation and integration, we have:

$$\begin{aligned} \mathbb{E} [L_{\text{CRPS}}(\hat{f}; \mathbf{X}, Y) | \mathbf{x}] &= \mathbb{E} \left[\int_{-\infty}^{\infty} (\hat{F}(t|\mathbf{x}) - F(t|\mathbf{x}))^2 dt \middle| \mathbf{x} \right] \\ &\quad + 2 \int_{-\infty}^{\infty} (\hat{F}(t|\mathbf{x}) - F(t|\mathbf{x})) \mathbb{E} [(F(t|\mathbf{x}) - \mathbb{I}(Y \leq t)) dt] \middle| \mathbf{x} \\ &\quad + \int_{-\infty}^{\infty} \mathbb{E} [(F(t|\mathbf{x}) - \mathbb{I}(Y \leq t))^2] \middle| \mathbf{x} dt. \end{aligned}$$

Now, notice that

- The first term represents the squared distance between \hat{F} and F and is minimized when $\hat{F}(\cdot|\mathbf{x}) = F(\cdot|\mathbf{x})$.
- The second term equals zero. This follows from the fact that

$$\mathbb{E} [F(t|\mathbf{x}) - \mathbb{I}(Y \leq t) | \mathbf{x}] = F(t|\mathbf{x}) - \mathbb{E} [\mathbb{I}(Y \leq t) | \mathbf{x}] = F(t|\mathbf{x}) - F(t|\mathbf{x}) = 0.$$

- The third term does not depend on \hat{F} .

Therefore, minimizing $\mathbb{E} [L_{\text{CRPS}}(\hat{f}; \mathbf{X}, Y) | \mathbf{x}]$ reduces to minimizing the first term, which occurs when $\hat{F}(\cdot|\mathbf{x}) = F(\cdot|\mathbf{x})$. Since this holds for every fixed $\mathbf{x} \in \mathcal{X}$, the proof is complete. \square

The derivation of Theorem 3 offers an additional insight. The risk associated with L_{CRPS} , up to a constant K independent of \hat{f} , corresponds to

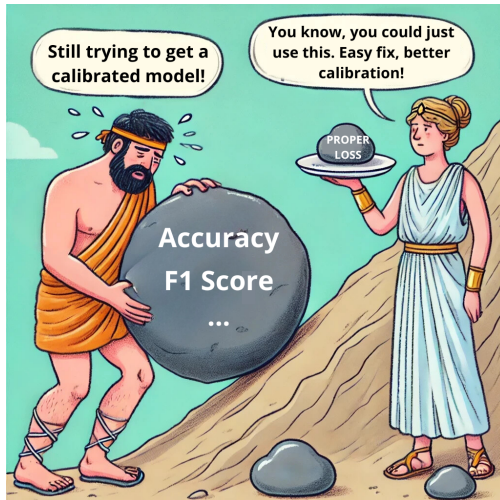
3.1. Loss Functions

the Harald Cramér distance between $\hat{F}(\cdot|\mathbf{x})$ and $F(\cdot|\mathbf{x})$, d_{HC} , averaged over \mathbf{x} (Cramér, 1928):

$$\begin{aligned}\mathbb{E} \left[L_{\text{CRPS}}(\hat{f}; \mathbf{X}, Y) \right] &= \int_{-\infty}^{\infty} \left(\hat{F}(t|\mathbf{x}) - F(t|\mathbf{x}) \right)^2 dt dP(\mathbf{x}) + K \\ &= \int d_{\text{HC}}^2 \left(\hat{F}(\cdot|\mathbf{x}), F(\cdot|\mathbf{x}) \right) dP(\mathbf{x}) + K,\end{aligned}$$

which is also equivalent to the energy distance between $\hat{F}(\cdot|\mathbf{x})$ and $F(\cdot|\mathbf{x})$ (Székely and Rizzo, 2013; Székely, 2003).

3.1.4 Accuracy, F1-scores and Related metrics: Improper Metrics for Probabilistic Classification



Accuracy, defined as $1 - \mathbb{P}(Y \neq g(\mathbf{X}))$ (Section 2.2), is widely used to tune hyperparameters in many machine learning frameworks and libraries. For example, in Python's scikit-learn, accuracy is often the default evaluation metric for probabilistic classification models, particularly in functions like GridSearchCV and RandomizedSearchCV. Until recently, this was also true for XGBoost's eval_metric parameter, which now defaults to logloss. However, the default scoring method for XGBoost remains accuracy, meaning that functions like GridSearchCV still rely on accuracy when tuning XGBoost.

models.

Although accuracy can yield reasonable results for classification tasks, using it to tune parameters can lead to suboptimal models when uncertainty quantification is important. This occurs because accuracy is an improper metric for probabilistic models.

To demonstrate this, consider two probabilistic models. The first, $\hat{\mathbb{P}}(Y = y|\mathbf{x})$, perfectly estimates the class probabilities, meaning $\hat{\mathbb{P}}(Y = y|\mathbf{x}) = \mathbb{P}(Y = y|\mathbf{x})$. The second model, $\hat{\mathbb{P}}'(Y = y|\mathbf{x})$, distorts the true probabilities by pushing them closer to 0.5 when they are near 0 or 1, and moving them further from 0.5 when they are close to it. Specifically, the model is defined as (see Figure 3.1):

$$\hat{\mathbb{P}}'(Y = y|\mathbf{x}) = \begin{cases} \frac{3}{2} - \mathbb{P}(Y = y|\mathbf{x}), & \text{if } \mathbb{P}(Y = y|\mathbf{x}) > \frac{1}{2} \\ \frac{1}{2} - \mathbb{P}(Y = y|\mathbf{x}), & \text{otherwise} \end{cases}$$

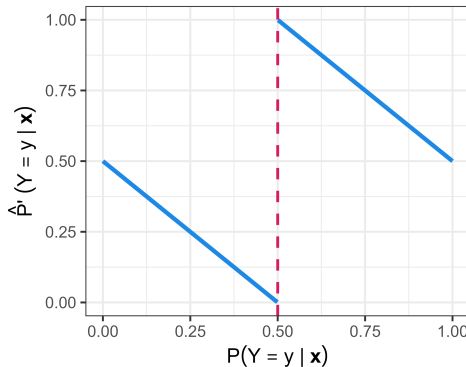


Figure 3.1: True class probabilities $\mathbb{P}(Y = y|\mathbf{x})$ and distorted probabilities $\hat{\mathbb{P}}'(Y = y|\mathbf{x})$. While both \mathbb{P} and $\hat{\mathbb{P}}'$ result in classifiers with identical accuracy, $\hat{\mathbb{P}}'$ provides poor probability estimates.

This manipulated model, $\hat{\mathbb{P}}'(Y = y|\mathbf{x})$, produces the same classification decisions as the perfectly calibrated model, $\hat{\mathbb{P}}(Y = y|\mathbf{x})$. This occurs because the decision boundary remains unchanged:

$$\hat{\mathbb{P}}(Y = y|\mathbf{x}) > 1/2 \text{ if and only if } \hat{\mathbb{P}}'(Y = y|\mathbf{x}) > 1/2.$$

As a result, both models achieve identical accuracy, but $\hat{\mathbb{P}}'$ distorts probabilities,

3.3. Parametric Approaches

shifting them toward 0.5 when certainty is high and away from 0.5 when uncertainty is greater, thus failing to quantify uncertainty properly.

Any model that shifts probabilities above 0.5 higher and those below 0.5 lower will achieve the same accuracy as $\widehat{\mathbb{P}}(Y = y|\mathbf{x})$. This limitation also affects metrics based solely on fixed-threshold classification decisions, such as the F1-score and balanced accuracy. Consequently, tuning models using these metrics can lead to poorly calibrated probabilities, distorting uncertainty. This issue is especially critical when reliable probabilistic rankings of observations are needed.

3.2 Probabilistic Classifiers

There is a plethora of methods to estimate $f(y|\mathbf{x})$ in classification problems: probabilistic classification's goal is to estimate $f(y|\mathbf{x})$. Many of the methods seen in Chapter 2 (such as the logistic regression) directly estimate such densities.

Regression can also be used to obtain probabilistic classifiers. Indeed, for a fixed i , consider the transformed variable $Z := \mathbb{I}(Y = i)$. Then, by construction, the regression of Z on \mathbf{x} is

$$\mathbb{E}[Z|\mathbf{x}] = \mathbb{P}(Y = i|\mathbf{x}) = f(i|\mathbf{x}).$$

Notice also that the mean squared error for estimating Z is the Brier Score for estimating $\mathbb{I}(Y = i)$ (recall Equation 3.2). This suggests that by using regression methods to $\mathbb{E}[Z|\mathbf{x}]$ one is effectively estimating $\mathbb{P}(Y = i|\mathbf{x})$ using the Brier Score to tune parameters and do model selection.

3.3 Parametric Approaches

Statistical models often imply a conditional density model. For instance, in a standard Gaussian linear regression model, the assumption is that

$$Y|\mathbf{x} \sim N(\boldsymbol{\beta}^\top \mathbf{x}; \sigma^2).$$

Generalized linear models (GLM; Nelder and Wedderburn 1972) extend this model by allowing the conditional density to be other members within the exponential family.

The parameters of such models can be estimated for instance via maximum likelihood estimation. Denoting by θ the parameters of the model, this corresponds to obtaining

$$\hat{\theta} = \arg \max_{\theta} \mathcal{L}(\theta; \mathcal{D}) = \arg \max_{\theta} \prod_{i=1}^n f_{\theta}(y_i | \mathbf{x}_i) f(\mathbf{x}_i) = \arg \max_{\theta} \prod_{i=1}^n f_{\theta}(y_i | \mathbf{x}_i),$$

where \mathcal{D} denotes the full dataset and we use the notation $f_{\theta}(y|\mathbf{x})$ to emphasize the dependency of the conditional model on θ . Once $\hat{\theta}$ is obtained, an estimate of the conditional density, $\hat{f}(y|\mathbf{x}) := f_{\hat{\theta}}(y|\mathbf{x})$, is readily available.

For instance, in the Gaussian linear model, the estimated conditional density is given by

$$\hat{f}(y|\mathbf{x}) = \frac{1}{\sqrt{2\pi\hat{\sigma}^2}} e^{-\frac{(y-\hat{\beta}^\top \mathbf{x})^2}{2\hat{\sigma}^2}},$$

where

$$\hat{\beta} = (\mathbb{X}^\top \mathbb{X})^{-1} \mathbb{X}^\top \mathbb{Y}, \quad (3.4)$$

is the least squares solution, with

$$\mathbb{X} = \begin{pmatrix} \mathbf{x}_1 \\ \vdots \\ \mathbf{x}_n \end{pmatrix}$$

being the design matrix, $\mathbb{Y} = (y_1, \dots, y_n)$, and

$$\hat{\sigma}^2 = \frac{1}{n} \sum_{i=1}^n (y_i - \hat{\beta}^\top \mathbf{x}_i)^2. \quad (3.5)$$

Of course, other estimators of β (such as the lasso described in Chapter 2) and σ^2 can also be used.

3.4. FlexCode

3.4 FlexCode

Be flexible, but stick to your principles.

Eleanor Roosevelt

FlexCode (Izbicki and Lee, 2017) is an acronym for *Flexible nonparametric conditional density estimation via regression*. It introduces a fully nonparametric approach to conditional density estimation by reframing the problem as an orthogonal series, where regression is utilized to estimate expansion coefficients. This strategy enables efficient estimation of conditional densities in high dimensions, leveraging the successes of high-dimensional regression.

For instance, in settings characterized by submanifold structures in the feature space, *FlexCode* adjusts to the intrinsic dimensionality of the data through the use of a carefully chosen regression method. Options include nearest neighbors, local linear, tree-based, or spectral series regression (Bickel and Li, 2007; Kpotufe and Dasgupta, 2012; Kpotufe, 2011; Lee and Izbicki, 2016). Similarly, when the number of relevant covariates (i.e., those influencing the distribution of Y) is small, *FlexCode* constructs effective conditional density estimators using regression techniques such as lasso, SAM, Rodeo, or other additive-based methods that perform variable selection (Lafferty and Wasserman, 2008; Meier et al., 2009; Tibshirani, 1996; Yang and Tokdar, 2015). The adaptability of *FlexCode* extends to handling different types of covariates, including discrete data, mixed data types, functional data, circular data, and more. These diverse data types often require specialized techniques (Di Marzio et al., 2016). An R implementation of *FlexCode* can be found at <https://github.com/rizbicki/FlexCoDE>, while a Python implementation can be found at <https://github.com/lee-group-cmu/FlexCode>.

For simplicity, we assume that Y lies in the interval $[0, 1]$. In cases where this assumption does not hold, we can map Y to this specified interval. We start by specifying an orthonormal basis $(\phi_i)_{i \in \mathbb{N}}$ in \mathbb{R} . This basis will be used to model the density $f(y|\mathbf{x})$ as a function of y . As we shall see, each coefficient in the expansion can be directly estimated via a regression. Note that there is a wide range of (orthogonal) bases one can choose from to capture any challenging shape of the density function of interest (Mallat, 1999). For example, when

dealing with reasonably smooth functions $f(z|\mathbf{x})$, the Fourier basis is a natural choice:

$$\phi_1(y) = 1; \quad \phi_{2i+1}(y) = \sqrt{2} \sin(2\pi iy), \quad i \in \mathbb{N}; \quad \phi_{2i}(y) = \sqrt{2} \cos(2\pi iy), \quad i \in \mathbb{N}$$

Alternatively, one can opt for wavelets or similar bases to effectively capture inhomogeneities in the density. In cases where the response is discrete, indicator functions may be a suitable choice (Izbicki and Lee, 2016, Sec. 4.2).

For fixed $\mathbf{x} \in \mathbb{R}^d$ and $f(\cdot|\mathbf{x}) \in \mathcal{L}^2(\mathbb{R})$, we express f as a series using the basis functions $(\phi_i)_{i \in \mathbb{N}}$ with coefficients $\beta_i(\mathbf{x})$:

$$f(y|\mathbf{x}) = \sum_{i \in \mathbb{N}} \beta_i(\mathbf{x}) \phi_i(y). \quad (3.6)$$

Since the basis functions $(\phi_i)_{i \in \mathbb{N}}$ are orthogonal, the expansion coefficients are determined by the inner product:

$$\beta_i(\mathbf{x}) = \langle f(\cdot|\mathbf{x}), \phi_i \rangle = \int_{\mathbb{R}} \phi_i(y) f(y|\mathbf{x}) dy = \mathbb{E}[\phi_i(Y)|\mathbf{x}]. \quad (3.7)$$

In other words, each $\beta_i(\mathbf{x})$ in Equation (3.6) is a regression function or conditional expectation. This implies that, for a fixed i , we can estimate $\beta_i(\mathbf{x})$ by regressing $\phi_i(y)$ on \mathbf{x} using the transformed sample $(\mathbf{X}_1, \phi_i(Y_1)), \dots, (\mathbf{X}_n, \phi_i(Y_n))$.

The *FlexCode* estimator for $f(y|\mathbf{x})$ is defined as follows:

$$\hat{f}(y|\mathbf{x}) := \sum_{i=1}^I \hat{\beta}_i(\mathbf{x}) \phi_i(y), \quad (3.8)$$

where the coefficients $\hat{\beta}_i(\mathbf{x})$ are obtained through regression:

$$\hat{\beta}_i(\mathbf{x}) = \hat{\mathbb{E}}[\phi_i(Y)|\mathbf{x}],$$

capturing how the density varies across the covariate space. The parameter I determines the series expansion cutoff and plays a crucial role in balancing the bias-variance tradeoff in the final density estimate. In general, a smaller value of I results in a smoother density. The optimal value for the tuning parameter I is determined through the validation set, utilizing the L_2 loss function for

3.4. FlexCode

estimation.

Notice that each β_i is fitted independently and does not depend on I . Thus, the optimal value of I can be chosen in a fast manner; one does not need to refit β_i 's for each I .

3.4.1 Normalization and Spurious Bumps

The estimated densities are not guaranteed to be valid density functions. To address this issue, FlexCode employs a renormalization procedure that adjusts the output to eliminate negative values and ensure the resulting function integrates to one, inspired by Efromovich (1999), Glad et al. (2003), and Hall and Murison (1993).

The procedure begins by defining a truncated function,

$$f_{\max}(y|\mathbf{x}) = \max\{0, \hat{f}(y|\mathbf{x})\}.$$

If the integral $\int f_{\max}(y|\mathbf{x}) dy$ satisfies $\int f_{\max}(y|\mathbf{x}) dy \geq 1$, then $\hat{f}(y|\mathbf{x})$ is adjusted to $\tilde{f}(y|\mathbf{x}) = \max\{0, \hat{f}(y|\mathbf{x}) - \xi\}$, where ξ is chosen such that $\int \tilde{f}(y|\mathbf{x}) dy = 1$. If the integral of $f_{\max}(y|\mathbf{x})$ is instead less than one, the function is rescaled as $\tilde{f}(y|\mathbf{x}) = f_{\max}(y|\mathbf{x}) / \int f_{\max}(y|\mathbf{x}) dy$.

To further refine the density estimate, FlexCode removes spurious bumps that may result from the Fourier series representation. Specifically, it identifies intervals $[a, b]$ where $\int_a^b \tilde{f}(y|\mathbf{x}) dy < \delta$ and eliminates them by treating δ as a tuning parameter. The optimal value of δ is selected to minimize the estimated risk.

3.4.2 Variable Importance

If the regression method used to estimate β_i provides variable importance metrics, these metrics can be directly utilized by FlexCode. Specifically, let $u_{i,j}$ denote a measure of importance of the j -th feature in estimating regression β_i . For instance, for random forests, $u_{i,j}$ may represent the mean decrease in the Mean Squared Error (Breiman, 2001b); for sparse additive models, $u_{i,j}$ may be value of the indicator function for the j -th summary statistic when estimating $\beta_i(\mathbf{x})$ (Ravikumar et al., 2009). We define an *importance measure* for the j -th

feature in estimating $f(y|\mathbf{x})$ according to

$$u_j := \frac{1}{I} \sum_{i=1}^I u_{i,j}. \quad (3.9)$$

This importance measures adds interpretability to FlexCode.

3.4.3 Theory

This section shows bounds and rates for *FlexCode* (Eq. 3.8). We use the notation $\hat{f}_I(z|\mathbf{x})$ to indicate its dependence on the cutoff I . Proofs and further details can be found in Izbicki and Lee (2017).

For every $s > \frac{1}{2}$ and $0 < c < \infty$, let $W_\phi(s, c) = \{f = \sum_{i \geq 1} \theta_i \phi_i : \sum_{i \geq 1} a_i^2 \theta_i^2 \leq c^2\}$, where $a_i \sim (\pi i)^s$, denote the Sobolev space. We assume that f belongs to a set of functions which are not too “wiggly”:

Assumption 1 (Smoothness in y direction). $\forall \mathbf{x} \in \mathcal{X}, f(y|\mathbf{x}) \in W_\phi(s_{\mathbf{x}}, c_{\mathbf{x}})$, where $f(y|\mathbf{x})$ is viewed as a function of y , and $s_{\mathbf{x}}$ and $c_{\mathbf{x}}$ are such that $\inf_{\mathbf{x}} s_{\mathbf{x}} \stackrel{\text{def}}{=} \beta > \frac{1}{2}$ and $\int_{\mathcal{X}} c_{\mathbf{x}}^2 d\mathbf{x} \stackrel{\text{def}}{=} C < \infty$.

We make the assumption that each function $\beta_i(\mathbf{x})$ is estimated using a regression method with a convergence rate of $O(n^{-\frac{2\alpha}{2\alpha+p}})$. Here, α typically represents a parameter associated with the smoothness of the $\beta_i(\mathbf{x})$ function, while p denotes either the number of relevant covariates or the intrinsic dimension of \mathbf{x} . To put it differently, we posit that each regression process is capable of adapting to the sparse structure inherent in the data. This formal assertion is explicitly presented as Assumption 2.

Assumption 2 (Regression convergence). For every $i \in \mathbb{N}$, there exists some $p \in \mathbb{N}$ and $\alpha > 0$ such that

$$\mathbb{E} \left[\int \left(\hat{\beta}_i(\mathbf{x}) - \beta_i(\mathbf{x}) \right)^2 d\mathbf{x} \right] = O(n^{-2\alpha/(2\alpha+p)})$$

Theorem 4. Under Assumptions 1 and 2, an upper bound on the risk of the CDE from Equation 3.8 is

$$\mathbb{E} \left[\iint \left(\hat{f}_I(y|\mathbf{x}) - f(y|\mathbf{x}) \right)^2 dy d\mathbf{x} \right] \leq IO \left(n^{-2\alpha/(2\alpha+p)} \right) + O(I^{-2\beta})$$

3.5. Mixture Models and Networks

Corollary 1. Under Assumptions 1 and 2, it is optimal to take $I \asymp n^{\frac{2\alpha}{(2\alpha+p)(2\beta+1)}}$, which yields the rate

$$O\left(n^{-\frac{2\beta}{2\beta+p\frac{2\beta+1}{2\alpha}+1}}\right)$$

for the FlexCode estimator.

In conclusion, the convergence rate of *FlexCode* solely depends on p , representing the "true" dimension of the problem. Notably, the rate approaches minimax efficiency concerning p . Indeed, in the isotropic scenario, where \mathbf{x} and y exhibit the same degree of smoothness ($\alpha = \beta$), the rate is given by

$$O\left(n^{-\frac{2\alpha}{2\alpha+p\frac{2\alpha+1}{2\alpha}+1}}\right),$$

which is close to the minimax rate $O\left(n^{-\frac{2\alpha}{(2\alpha+1+p)}}\right)$ of a conditional density estimator with p covariates (Izbicki and Lee, 2016). The difference lies in the multiplicative factor $\frac{2\alpha+1}{2\alpha}$ which approaches 1 as the function f becomes smoother. While *FlexCode*'s rate is marginally slower than the optimal rate, the estimator shows significantly greater speed of convergence compared to the standard minimax rate,

$$O\left(n^{-\frac{2\alpha}{(2\alpha+1+d)}}\right),$$

typical for nonparametric conditional density estimators in \mathbb{R}^d . Thus, despite the presence of d covariates, *FlexCode* mitigates the curse of dimensionality, effectively behaving as if only $p \ll d$ covariates were measured.

For a version of FlexCode for (dependent) time series data, see Grivol et al. (2024).

3.5 Mixture Models and Networks

In the context of conditional density estimation, mixture models (Benaglia et al., 2009; Quandt, 1958) assume that the conditional density $f(y|\mathbf{x})$ can be

written as a mixture of parametric densities,

$$f(y|\mathbf{x}) = \sum_{i=1}^m \alpha_i(\mathbf{x}) \phi(y|\theta_i(\mathbf{x})), \quad (3.10)$$

where $\alpha_i(\mathbf{x})$'s are nonnegative coefficients such that $\sum_{i=1}^m \alpha_i(\mathbf{x}) = 1$ and ϕ is the density of a predefined parametric distribution over y with parameters $\theta_i(\mathbf{x})$. For instance, $\phi(y|\theta_i(\mathbf{x}))$ can be the density of a gaussian distribution:

$$\phi(y|\theta_i(\mathbf{x})) = \frac{1}{\sqrt{2\pi\sigma_i^2(\mathbf{x})}} \exp\left\{-\frac{(y - \mu_i(\mathbf{x}))^2}{2\sigma_i^2(\mathbf{x})}\right\},$$

where $\theta_i(\mathbf{x}) = (\mu_i(\mathbf{x}), \sigma_i(\mathbf{x}))$. One then models each parameter by imposing a parametric relationship, such as

$$\mu_i(\mathbf{x}) = (\beta^{(i)})^t \mathbf{x} \text{ and } \sigma_i(\mathbf{x}) = \exp\left[(\gamma^{(i)})^t \mathbf{x}\right].$$

These parameters are typically fitted using the Expectation Maximization algorithm (EM; Dempster et al. 1977).

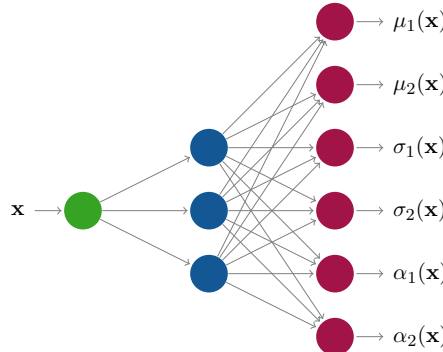


Figure 3.2: Example of a Gaussian mixture density network structure with input x , hidden layers, and outputs $\mu_1(x), \mu_2(x), \sigma_1(x), \sigma_2(x), \alpha_1(x)$, and $\alpha_2(x)$. The outputs are combined according to Equation 3.10 to give the estimated density.

Neural networks can also be used to parameterize mixture models. In particular, mixture density networks represent the functions $\alpha_i(\mathbf{x})$ and $\theta_i(\mathbf{x})$

3.6. Normalizing Flows

using neural networks (Bishop, 1994). These networks take \mathbf{x} as input and output pairs $(\alpha_i(\mathbf{x}), \theta_i(\mathbf{x}))_{i=1}^m$, where m is a user-defined parameter that shapes the output structure. For the output layers corresponding to $\alpha_i(\mathbf{x})$, a softmax function is typically applied to ensure these values lie on a probability simplex. Figure 3.2 shows an example of an architecture for estimating a mixture of two Gaussian distributions.

Rather than using the EM algorithm, this approach estimates network parameters using standard neural network techniques, often employing the cross-entropy loss function.

3.6 Normalizing Flows

I used to just live my life by going with the flow.

Jin

In this section, we assume $\mathbf{y} \in \mathbb{R}^m$, that is, the response can be multivariate. Normalizing flows model $f(\mathbf{y}|\mathbf{x})$ by creating a *bijective* transformation of \mathbf{y} ,

$$T^\mathbf{x} : \mathbb{R}^m \longrightarrow \mathbb{R}^m,$$

such that $T^\mathbf{x}(\mathbf{Y})|\mathbf{x}$ has density approximately $p_0(\cdot)^2$, where p_0 is chosen a priori. For instance, one may take p_0 to be a Normal($\mathbf{0}, \mathbf{I}_m$).

A key reason why this idea is useful is that $T^\mathbf{x}$ can be easily used to approximate $f(\mathbf{y}|\mathbf{x})$. Indeed, because $T^\mathbf{x}$ is bijective and $T^\mathbf{x}(\mathbf{Y})|\mathbf{x}$ has density approximately $p_0(\cdot)$, it follows that

$$f(\mathbf{y}|\mathbf{x}) \approx p_0(T^\mathbf{x}(\mathbf{y})) |\det J_{T^\mathbf{x}}(\mathbf{y})|, \quad (3.11)$$

where

$$J_{T^\mathbf{x}}(\mathbf{y}) = \begin{bmatrix} \frac{\partial T_1^\mathbf{x}}{\partial y_1} & \dots & \frac{\partial T_1^\mathbf{x}}{\partial y_m} \\ \vdots & \ddots & \vdots \\ \frac{\partial T_m^\mathbf{x}}{\partial y_1} & \dots & \frac{\partial T_m^\mathbf{x}}{\partial y_m} \end{bmatrix}$$

² $p_0(\cdot)$ may actually depend on \mathbf{x} so that, $p_0(\cdot|\mathbf{x})$

is the Jacobian matrix with all $m \times m$ partial derivatives of $T^{\mathbf{x}}$ with respect to \mathbf{y} . Thus, if a good $T^{\mathbf{x}}$ was known, the right-hand side of Equation 3.11 could be used to approximate $f(\mathbf{y}|\mathbf{x})$ – all of its terms are known.

Another feature of normalizing flows is that it is easy to sample from the estimated conditional density. Indeed, if $\mathbf{Z} \sim p_0(\cdot)$, then by construction $(T^{\mathbf{x}})^{-1}(\mathbf{Z})$ has approximately the same distribution as $\mathbf{Y}|\mathbf{x}$. Thus, one can sample from the estimated conditional density by sampling from the base distribution p_0 and then applying the inverse of the transformation that was learned.

In practice, to learn $T^{\mathbf{x}}$, this function is parameterized using a neural network with weights ϕ . This network takes \mathbf{x} and \mathbf{y} as inputs, and it outputs the vector $T^{\phi,\mathbf{x}}(\mathbf{y})$. Given a training sample $(\mathbf{X}_1, \mathbf{Y}_1), \dots, (\mathbf{X}_n, \mathbf{Y}_n)$, the weights ϕ are typically trained by minimizing the cross-entropy loss of the implied conditional density. That is, one searches for the weights ϕ that minimize

$$-\frac{1}{n} \sum_{i=1}^n \log \left[p_0 \left(T^{\phi,\mathbf{x}_i}(\mathbf{y}_i) \right) |\det J_{T^{\phi,\mathbf{x}_i}}(\mathbf{y}_i)| \right]$$

There are several approaches to parameterize $T^{\mathbf{x}}$ using neural networks. Modern methods focus on creating transformations that are both expressive, increasing the likelihood of approximating well the true density, and computationally efficient, ensuring that the Jacobians in Equation 3.11 are calculated with minimal cost. Typically, $T^{\mathbf{x}}$ is built using a composition of small building blocks, that is, $T^{\mathbf{x}} = S_B \circ \dots \circ S_2 \circ S_1$, where we omit \mathbf{x} from S 's to simplify the notation. Each S_b is a bijective transformation whose Jacobian is easy to compute. This approach is useful because

- (i) $T^{\mathbf{x}}$ is by construction bijective and its inverse can be easily computed as $S_1^{-1} \circ S_2^{-1} \circ \dots \circ S_B^{-1}$, and
- (ii) the determinant of its Jacobian can be computed using the chain rule:

$$\det J_{T^{\mathbf{x}}}(\mathbf{y}) = \det J_{S_B}(S_{B-1} \circ \dots \circ S_2 \circ S_1(\mathbf{y})) \dots \det J_{S_1}(\mathbf{y}).$$

Each S is parametrized using a neural network structure. In this way, the full network will consist of the nested layers $S_1 \rightarrow S_2 \rightarrow S_B$, as shown in Figure

3.7. The Ratio Trick

[3.3](#) for a setting with no features \mathbf{x} .

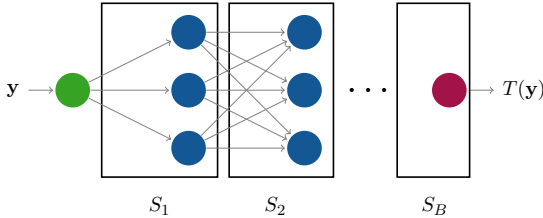


Figure 3.3: Pictorial representation of a simplified normalizing flow structure without features \mathbf{x} . The inputs are transformed through multiple stages of invertible transformations, S_1, S_2, \dots, S_B , leading to the output $T(\mathbf{y})$. Note that this illustration does not depict the exact transformations S .

An example of one of such building blocks S_b is the affine coupling layer ([Dinh et al., 2016](#)), which splits its input \mathbf{u} into two components, \mathbf{u}_1 and \mathbf{u}_2 and is given by

$$S(\mathbf{u}) = (\mathbf{u}_1, a(\mathbf{u}_1) \odot \mathbf{u}_2 + b(\mathbf{u}_1)).$$

Here, a and b are functions parametrized by the network: both take \mathbf{u}_1 as input and pass it through the layers of a neural network with weights that are estimated when training the normalizing flow. The symbol \odot represents the Hadamard (element-wise) product. This transformation remains bijective even if a and b are not.

Several such building blocks have been designed, such as invertible 1×1 convolutions, split priors ([Dinh et al., 2016](#)), masked autoregressive flows ([Papamakarios et al., 2017](#)), and neural autoregressive flows ([Huang et al., 2018](#)). See [Papamakarios et al. \(2021\)](#) for a comprehensive introduction to such models. See also [Wildberger et al. \(2024\)](#) for continuous normalizing flows.

3.7 The Ratio Trick

The ratio trick has appeared in very different fields and with different goals (e.g., [Cheng and Chu 2004](#); [Cranmer et al. 2015](#); [Cranmer et al. 2020](#); [Gutmann et al. 2018](#); [Qin 1998](#); [Sugiyama et al. 2010b](#)). Essentially, it converts the goal of estimating a quantity (usually a ratio between two densities) into the problem of estimating a classifier.

Here, we explore a version of this trick based on Dalmasso et al. (2020a) and Okuno and Polo (2021). In this context, the ratio tricks converts the problem of estimating the conditional density of a continuous vector \mathbf{y} given \mathbf{x} into the problem of estimating a probabilistic classifier.

Specifically, we start by generating a labeled sample $\mathcal{T} = \{(\mathbf{X}'_i, \mathbf{Y}'_i, S_i)\}_{i=1}^m$. This dataset contains all original training samples $(\mathbf{X}_1, \mathbf{Y}_1), \dots, (\mathbf{X}_n, \mathbf{Y}_n)$, and also additional artificial samples $(\tilde{\mathbf{X}}_1, \tilde{\mathbf{Y}}_1), \dots, (\tilde{\mathbf{X}}_{\tilde{n}}, \tilde{\mathbf{Y}}_{\tilde{n}})$, where each pair $(\tilde{\mathbf{X}}, \tilde{\mathbf{Y}})$ is drawn from $\tilde{\mathbf{X}} \sim U(\{\mathbf{X}_1, \dots, \mathbf{X}_n\})$ ³ and $\tilde{\mathbf{Y}}|\tilde{\mathbf{X}} = \tilde{\mathbf{x}} \sim g(\mathbf{y}|\mathbf{X} = \tilde{\mathbf{x}})$. Here, the conditional distribution $g(\mathbf{y}|\mathbf{x})$ is chosen by the user.

Define the odds at $(\mathbf{y}; \mathbf{x})$ as

$$\mathbb{O}(\mathbf{y}; \mathbf{x}) := \frac{\mathbb{P}(S = 1|\mathbf{x}, \mathbf{y})}{\mathbb{P}(S = 0|\mathbf{x}, \mathbf{y})}. \quad (3.12)$$

By construction, it holds that

$$\mathbb{O}(\mathbf{y}; \mathbf{x}) = \frac{f(\mathbf{x}, \mathbf{y}|S = 1)}{f(\mathbf{x}, \mathbf{y}|S = 0)} = \frac{f(\mathbf{y}|\mathbf{x})}{g(\mathbf{y}|\mathbf{x})}. \quad (3.13)$$

Thus,

$$f(\mathbf{y}|\mathbf{x}) = g(\mathbf{y}|\mathbf{x})\mathbb{O}(\mathbf{y}; \mathbf{x}).$$

This suggests we estimate f by using the plugin estimate

$$\hat{f}(\mathbf{y}|\mathbf{x}) := g(\mathbf{y}|\mathbf{x}) \frac{\widehat{\mathbb{P}}(S = 1|\mathbf{x}, \mathbf{y})}{\widehat{\mathbb{P}}(S = 0|\mathbf{x}, \mathbf{y})}, \quad (3.14)$$

where $\widehat{\mathbb{P}}(S = 1|\mathbf{x}, \mathbf{y})$ is obtained using any probabilistic classifier (such as those discussed in Chapter 2).

3.8 Other Conditional Density Estimators

In low-dimensional feature spaces, many conditional density estimators rely on the initial estimation of $f(y, \mathbf{x})$ and $f(\mathbf{x})$. A common practice involves using kernel density estimators, as pioneered by Rosenblatt (1969). The sub-

³One can also sample from the marginal distribution of \mathbf{x} , $f(\mathbf{x})$ if this is an option. This is the case on the LFI problem studied in Chapter 9.

3.8. Other Conditional Density Estimators

sequent combination of these estimates is expressed by $f(y|\mathbf{x}) = \frac{f(y,\mathbf{x})}{f(\mathbf{x})}$, often implemented through

$$\hat{f}(y|\mathbf{x}) = \frac{\sum_{i=1}^n K_{h_x}(\|\mathbf{x} - \mathbf{X}_i\|)K_{h_y}(y - Y_i)}{\sum_{i=1}^n K_{h_x}(\|\mathbf{x} - \mathbf{X}_i\|)},$$

where $K_h(t) = h^{-d}K(t/h)$ denotes a kernel with bandwidth h in d dimensions.

Several advancements have been made to enhance this approach. Notable works, such as those by Hyndman et al. (1996) and Ichimura and Fukuda (2010), introduce different criteria and shortcuts for parameter tuning, along with efficient implementations of these methods.

Alternative techniques for low-dimensional settings include locally polynomial regression (Fan et al., 1996), least squares approaches (Sugiyama et al., 2010a), and density estimation through quantile estimation (Takeuchi et al., 2009). Further exploration of these methods and others is available in the comprehensive review by Bertin et al. (2016).

Hall et al. (2004) presents a method for parameter tuning in kernel density estimators that automatically identifies relevant components of \mathbf{x} for $f(y|\mathbf{x})$. Similarly, Shiga et al. (Shiga et al., 2015) propose a conditional estimator that selects relevant components, assuming an additive structure in $f(y|\mathbf{x})$.

Efromovich (2010) introduces an orthogonal series estimator, offering automatic dimension reduction on \mathbf{x} when certain components are conditionally independent of the response. For high-dimensional feature spaces, Izbicki and Lee (2016) propose a spectral basis-based orthogonal series approach, while Inácio and Izbicki (2018) and Dalmasso et al. (2020b) present a version of FlexCode where $\beta_i(\mathbf{x})$ is estimated using neural networks.

Other neural network-based approaches have also gained prominence for conditional density estimation. Examples include conditional generative adversarial networks (cGANs; Mirza and Osindero 2014), conditional variational autoencoders (cVAEs; Sohn et al. 2015), diffusion models (Dhariwal and Nichol, 2021; Ho and Salimans, 2022; Ho et al., 2020; Nichol and Dhariwal, 2021; Sohl-Dickstein et al., 2015), and transformer-based generative models (Radford et al., 2019; Vaswani et al., 2017).

Additionally, some methods estimate the conditional cumulative distribution $F(y|\mathbf{x})$ directly, bypassing density estimation altogether (Kostic et al., 2024;

Li and Racine, 2008).

3.9 Quantile Regression

Quantile regression aims to estimate one property of the distribution of $Y|\mathbf{x}$: its *conditional quantiles*. Formally, the α -conditional quantile of Y at \mathbf{x} , $q_\alpha(\mathbf{x})$, is the function such that $\mathbb{P}(Y \leq q_\alpha(\mathbf{x})|\mathbf{X} = \mathbf{x}) = \alpha$ (we assume here that the distribution of $Y|\mathbf{x}$ is strictly continuous); see Figure 3.4 for an illustration. In other words, $q_\alpha(\mathbf{x}) = F^{-1}(\alpha|\mathbf{x})$, where F is the cumulative distribution of Y conditional on \mathbf{x} . Note that $q_{1/2}(\mathbf{x})$ is the conditional median.

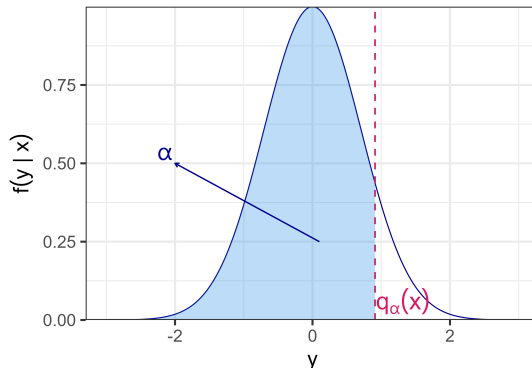


Figure 3.4: Illustration of the α -quantile. The shaded area represents the region where the cumulative probability equals α , with the quantile $q_\alpha(\mathbf{x})$ indicated by a vertical dashed line.

3.9.1 Pinball Loss

To assess the accuracy of an estimate of $q_\alpha(\mathbf{x})$, we will use the loss function called the *pinball loss*. Let $g : \mathcal{X} \rightarrow \mathbb{R}$ be an estimate of $q_\alpha(\mathbf{x})$. The pinball loss of g evaluated at (\mathbf{x}, y) is defined as

$$L_\alpha(g, \mathbf{x}, y) = (g(\mathbf{x}) - y)(\mathbb{I}(y \leq g(\mathbf{x})) - \alpha). \quad (3.15)$$

The risk derived from this loss function is minimized precisely by the

3.9. Quantile Regression

solution $g(\mathbf{x}) = q_\alpha(\mathbf{x})$:

$$\arg \min_g \mathbb{E}[L_\alpha(g, \mathbf{X}, Y)] = q_\alpha(\mathbf{x}).$$

This indicates that this loss function is suitable for evaluating estimates of $q_\alpha(\mathbf{x})$.

Figure 3.5 illustrates the behavior of this loss function as a function of $g(\mathbf{x})$ for $\alpha = 10\%$. According to it, underestimating y is less bad than overestimating this quantity.

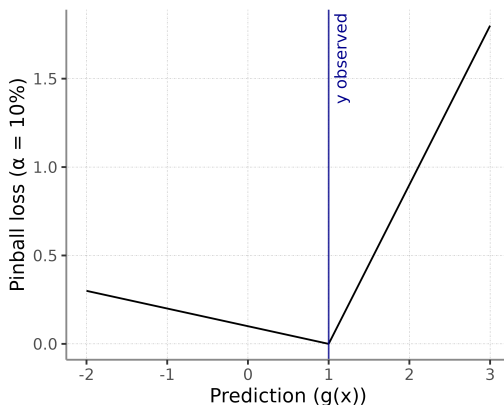


Figure 3.5: Pinball loss for $\alpha = 10\%$.

See Chung et al. (2021) and Feldman et al. (2021) for other loss functions that can be used for quantile regression that also encourage calibration.

3.9.1.1 Estimation the Quantile Function

In this section, we briefly describe a few ways to estimate the quantile regression.

- **[Parametric Methods]** One way to estimate $q_\alpha(\mathbf{x})$ is to assume that it depends linearly on the covariates. In other words, we can assume that

$$q_\alpha(\mathbf{x}) = \beta^t \mathbf{x}.$$

We can then search for

$$\arg \min_{\beta \in \mathbb{R}^d} \frac{1}{n} \sum_{i=1}^n L_\alpha(g_\beta, \mathbf{x}_i, y_i),$$

where $g_\beta(\mathbf{x}) := \beta^t \mathbf{x}$ (Koenker and Bassett Jr, 1978).

- **[KNN]** The idea of the k -nearest neighbors (KNN) method for estimating $q_\alpha(\mathbf{x})$ is to use the responses Y of the k -nearest neighbors to \mathbf{x} (Ma et al., 2016). Formally, we define

$$g(\mathbf{x}) = \hat{q}_\alpha(\{y_i\}_{i \in \mathcal{N}_\mathbf{x}}), \quad (3.16)$$

where $\hat{q}_\alpha(\mathcal{S})$ is the α -quantile of \mathcal{S} and $\mathcal{N}_\mathbf{x}$ is the set of the k nearest observations to \mathbf{x} , i.e.,

$$\mathcal{N}_\mathbf{x} = \left\{ i \in \{1, \dots, n\} : d(\mathbf{x}_i, \mathbf{x}) \leq d_\mathbf{x}^k \right\}$$

and $d_\mathbf{x}^k$ is the distance from \mathbf{x} to the k -th nearest neighbor of \mathbf{x} .

The tuning parameter k can be chosen through cross-validation using the pinball loss as the metric to be optimized.

- **[Random Forests]** Meinshausen and Ridgeway (2006) proposes estimating quantiles from an estimate of the conditional cumulative distribution. This estimate is a local version of the estimate given by the empirical cumulative distribution function:

$$\hat{F}(y|\mathbf{x}) = \sum_{i=1}^n w_i(\mathbf{x}) \mathbb{I}(y_i \leq y),$$

where $w_i(\mathbf{x})$ is a measure of similarity between \mathbf{x} and the i -th observation in the training set obtained through a random forest. Specifically, it is defined as follows: let $R_\mathbf{x}^b$ be the leaf where the observation \mathbf{x} falls in the b -th tree, and define the weight associated with that tree as

$$w_i(\mathbf{x}; b) = \frac{\mathbb{I}(\mathbf{x}_i \in R_\mathbf{x}^b)}{\sum_{j=1}^n \mathbb{I}(\mathbf{x}_j \in R_\mathbf{x}^b)}.$$

3.9. Quantile Regression

In other words, $w_i(\mathbf{x}; b)$ is the proportion of observations in the training set that fall in the same leaf as \mathbf{x} . The combined weight is then given by the average of these weights:

$$w_i(\mathbf{x}) = \frac{1}{B} \sum_{b=1}^B w_i(\mathbf{x}; b).$$

This method has several advantages over KNN. For example, random forests automatically perform variable selection, so the quantile estimates inherit this property and are therefore more robust in scenarios with many irrelevant variables. Additionally, random forests automatically take into account interactions and non-linearities of the covariates.

- **[Neural Networks]** A neural network can be trivially used to estimate quantile regression. To do this, simply use the pinball loss as the loss function of a network with a single output.

Figure 3.6 displays the 10th and 90th quantiles estimated by boosting, linear, and random forest quantile regression models for predicting life expectancy based on GDP per capita using the data described in Section 1.1. The code to generate this figure is available at the [Quantile Regression Notebook](#).

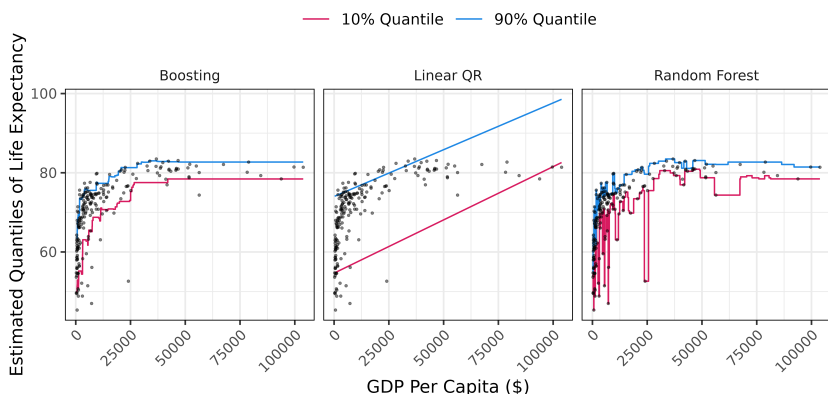


Figure 3.6: Comparison between boosting, linear, and random forest quantile regression models for Predicting Life Expectancy based on GDP per Capita, using 10th and 90th percentiles.

3.10 Simulated Example: Gaussian Distribution

Here, we compare various methods for CDE on a toy example which involves the creation of a multivariate dataset, where the conditional relationship between features and target variables is known. The data is generated according to:

$$\mathbf{X} \sim \mathcal{U}(0, 1)^d,$$

with $d = 50$, and

$$Y|\mathbf{x} \sim N(x_1, 1).$$

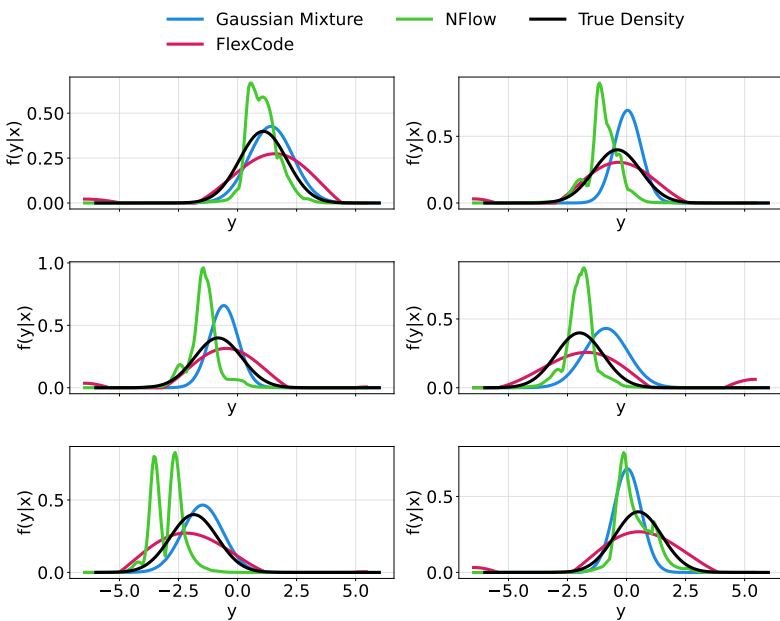


Figure 3.7: Comparison of estimated conditional density functions using FlexCode with random forest-based β estimates, Gaussian mixture density networks, and normalizing flows on a simulated Gaussian dataset. The true conditional density $Y|\mathbf{x} \sim N(x_1, 1)$ is shown for reference.

We compare FlexCode, where the β coefficients are estimated using random forests (Section 3.4), against a Gaussian mixture density network (Section 3.5) and normalizing flows (Section 3.6). The detailed implementation and code are available in the [CDE Notebook](#). Figure 3.7 illustrates the estimated

3.11. Example: Twitter Location Prediction

conditional densities at six test points. FlexCode consistently demonstrates superior performance over the other methods, as further supported by the L_2 loss values shown in Table 3.1.

Table 3.1: Estimated L_2 losses (with standard errors) for different CDE methods on a simulated Gaussian dataset. FlexCode, with random forest-based β estimates, outperforms the Gaussian mixture density network and normalizing flows.

Method	L_2 Loss (s.e.)
Gaussian Mixture	0.116 (0.012)
FlexCode	-0.266 (0.002)
NFlow	0.143 (0.008)

3.11 Example: Twitter Location Prediction

We leverage FlexCode to predict the geographical origin of tweets based on their content. By utilizing samples with known locations, we train our model to estimate the full conditional distribution of latitude and longitude $f(\mathbf{y}|\mathbf{x})$, where \mathbf{x} represents covariates extracted from tweets and $\mathbf{y} = (y_1, y_2)$ denotes the latitude/longitude pair.

Our dataset comprises approximately 8,000 tweets from the USA in July 2015 containing the keyword "beach". We extract 500 covariates using a bag-of-words method, focusing on the most frequent unigrams and bigrams (Manning, 2009). Given our anticipation that only a subset of the 500 covariates is pertinent to tweet location, we implement FlexCode through sparse additive models (Ravikumar et al., 2009). As the response is bivariate, we employ a tensor product of Fourier basis functions.

In Figure 3.8, two instances of estimated densities are illustrated. FlexCode successfully determines tweet locations even in ambiguous scenarios, such as the presence of Long Beach in both California and Connecticut (as depicted in the bottom right plot of Figure 3.8).

Notably, FlexCode-SAM, based on sparse additive models, allows us to identify the most relevant covariates for location prediction. In Figure 3.8 (left), the terms "beachin", "boardwalk", and "daytona" are present in at least

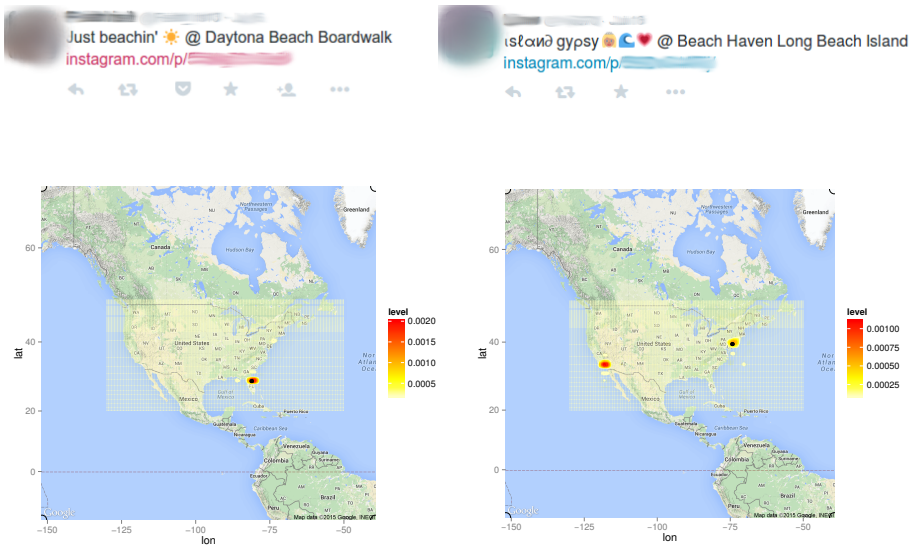


Figure 3.8: Top: Two tweets with the keyword “beach”. Bottom: Level sets of the estimated probability density of the tweet locations given the content of the tweets. The black dots indicate their true locations.

33% of the estimated regression functions. Conversely, for the example on the right, relevant covariates include “long beach”, “island”, “long”, and “haven”.

3.12 Summary

In this chapter, we introduced three metrics to compare the performance of estimators \hat{f} of the conditional density f : the L_2 loss, the cross-entropy loss, and CRPS. All loss functions are proper and can be easily estimated if an i.i.d. test dataset is available. We then covered how, in classification, f is estimated using probabilistic classifiers tuned with an appropriate loss function. In particular, we saw that accuracy, F1-score and related metrics are not appropriate for tuning probabilistic classifiers. We also explored several approaches to estimate this conditional density in a regression context, ranging from methods that leverage existing regression methods and probabilistic

3.12. Summary

classifiers (FlexCode and the Ratio trick) to methods that use modern neural network architectures (such as normalizing flows). Finally, we saw that specific quantiles of distribution $Y|\mathbf{x}$ maybe be directly estimated using quantile regression.

Chapter 4

Diagnostics and Recalibration



The Anatomy Lesson of Dr. Nicolaes Tulp. Rembrandt, 1632, Mauritshuis, The Hague.

4.1. PIT Values: Evaluating Calibration in Regression

A correct diagnosis is
three-fourths of the remedy.

Mahatma Gandhi

In Chapter 3, we covered various conditional density estimators and discussed different loss functions to help choose the best fit for a given dataset. However, these loss functions have limitations – they don't tell us if the best estimate we found, say \hat{f} , is actually good enough. They also don't provide guidance on how to improve \hat{f} or which specific data points (\mathbf{x} 's) need attention.

This chapter aims to address these practical questions that are crucial for trusting uncertainty quantification based on \hat{f} . We will focus on evaluating the overall quality of the estimate, figuring out how to enhance it, and identifying specific areas in the dataset that require improvement.

Sections 4.1 and 4.2 deal with regression problems, while Section 4.3 discusses usual techniques for classification calibration.

4.1 PIT Values: Evaluating Calibration in Regression

The standard way to address the question of whether \hat{f} is reasonable is to test the global consistency hypothesis:

Definition 2 (Global Consistency). *An estimate $\hat{f}(y|\mathbf{x})$ is globally consistent with the density $f(y|\mathbf{x})$ if the following null hypothesis holds:*

$$H_0 : \hat{f}(y|\mathbf{x}) = f(y|\mathbf{x}) \text{ for almost every } \mathbf{x} \in \mathcal{X} \text{ and } y \in \mathbb{R}. \quad (4.1)$$

This means that, under global consistency, the estimated conditional density $\hat{f}(y|\mathbf{x})$ accurately represents the true underlying density $f(y|\mathbf{x})$ across the entire feature space \mathcal{X} and output space \mathbb{R} . Notice that, in this hypothesis, we consider \hat{f} is a particular fixed conditional density estimate, that is, there is no randomness associated to it.

In a regression setting, one way of testing H_0 is by computing PIT values:

Definition 3 (PIT). Fix $\mathbf{x} \in \mathcal{X}$ and $y \in \mathbb{R}$. The probability integral transform of y at \mathbf{x} , as modeled by the conditional density estimate $\hat{f}(y|\mathbf{x})$, is

$$PIT(y; \mathbf{x}) := \int_{-\infty}^y \hat{f}(y'|\mathbf{x}) dy' =: \hat{F}(y|\mathbf{x}). \quad (4.2)$$

The PIT value therefore represents the cumulative probability, according to the estimated density \hat{f} , of observing a value less than or equal to y given the input \mathbf{x} . See Figure 4.1 for an illustration.

For implicit models of $\hat{f}(y|\mathbf{x})$ – generative models capable of sampling from \hat{f} but not evaluating it directly – the PIT values can be approximated through forward simulation. For a fixed $\mathbf{x} \in \mathcal{X}$ and $y \in \mathcal{Y}$, simulate $Y_1, \dots, Y_L \sim \hat{f}(\cdot|\mathbf{x})$. Then, approximate $PIT(y; \mathbf{x})$ using the cumulative average

$$PIT(y; \mathbf{x}) \approx \frac{1}{L} \sum_{i=1}^L \mathbb{I}(Y_i \leq y).$$

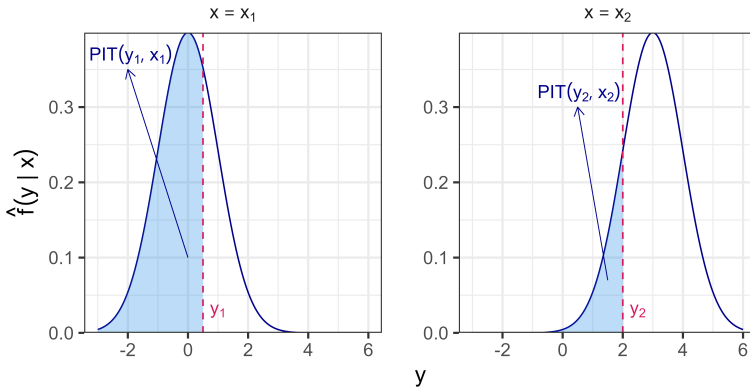


Figure 4.1: Illustration of the PIT values for two distributions, $\hat{f}(y|\mathbf{x}_1)$ and $\hat{f}(y|\mathbf{x}_2)$. The vertical dashed lines represent the true observed values $y = y_1$ and $y = y_2$, respectively, for each distribution. The highlighted areas indicate the regions of interest under the curves for the PIT values.

If the conditional density model $\hat{f}(y|\mathbf{x})$ is globally consistent with the true density $f(y|\mathbf{x})$, then the PIT values should be uniformly distributed over the interval $[0, 1]$. Specifically, if the null hypothesis H_0 (Equation 4.1) holds true,

4.1. PIT Values: Evaluating Calibration in Regression

the random variables $\text{PIT}(Y_1; \mathbf{X}_1), \dots, \text{PIT}(Y_n; \mathbf{X}_n)$ will be independent and identically distributed as $\text{Unif}(0, 1)$. Here, $(\mathbf{X}_1, Y_1), \dots, (\mathbf{X}_n, Y_n)$ represent a holdout set that was not used in the training of \hat{f} . This result follows from a fundamental property in probability theory: when you apply the cumulative distribution function of a random variable to the variable itself, the outcome is uniformly distributed on the interval $[0, 1]$. Therefore, if $\hat{f}(y|\mathbf{x})$ correctly models the true conditional density, the PIT values will reflect this uniformity.

This suggests that H_0 maybe be evaluated by checking if the PIT values are uniformly distributed. Indeed, the uniformity of PIT values is a widely used criterion for assessing the goodness-of-fit of unconditional (Dawid, 1984; Diebold et al., 1998; Gneiting and Katzfuss, 2014) and conditional density models in practice (Bordoloi et al., 2010; Cook et al., 2006; Tanaka et al., 2018). For example, practitioners often plot a histogram of the PIT values to visually inspect deviations from uniformity. Additionally, formal hypothesis tests, such as the Kolmogorov–Smirnov test, can be employed to evaluate whether the PIT values follow a uniform distribution statistically.

While these methods provide valuable insights, an estimate \hat{f} might pass the uniformity test even if it is not a good model. The following theorem illustrates this limitation:

Theorem 5 (Insensitivity to Covariate Transformations; Zhao et al. (2021)). Suppose there exists a function $g : \mathcal{X} \rightarrow \mathcal{Z}$, where $\mathcal{Z} \subseteq \mathbb{R}^k$ for some k , that satisfies

$$\hat{f}(y|\mathbf{x}) = f(y|g(\mathbf{x})). \quad (4.3)$$

Let $(\mathbf{X}, Y) \sim F_{\mathbf{X}, Y}$. Then $\text{PIT}(Y; \mathbf{X}) \sim \text{Unif}(0, 1)$.

Many models naturally lead to estimates that could satisfy the condition in Equation 4.3, even without being globally consistent. In fact, clearly misspecified models \hat{f} can yield uniform PIT values and “pass” an associated goodness-of-fit test regardless of the sample size. To illustrate, consider a scenario where $\hat{f}(y|\mathbf{x})$ is derived from a linear model. In this case, $\hat{f}(y|\mathbf{x})$ will depend on $\mathbf{x} \in \mathbb{R}^d$ solely through $g(\mathbf{x}) := \beta^T \mathbf{x}$, where $\beta \in \mathbb{R}^d$. Consequently, it is possible to have $\hat{f}(y|\mathbf{x}) = f(y|g(\mathbf{x}))$ even when $\hat{f}(y|\mathbf{x})$ substantially deviates from the true distribution $f(y|\mathbf{x})$.

As another example, consider a conditional density estimator incorporating

variable selection techniques (Dalmasso et al., 2020b; Izbicki and Lee, 2017; Shiga et al., 2015). Such an estimator could satisfy $\hat{f}(y|\mathbf{x}) = f(y|g(\mathbf{x}))$ with $g(\mathbf{x}) := (\mathbf{x})_S$, where $S \subset 1, \dots, d$ denotes a subset of covariates. Thus, a test of the overall uniformity of PIT values is no guarantee that we are correctly modeling the relationship between y and the predictors \mathbf{x} .

A test that overcomes this issue is given by Zhao et al. (2021) and described in Section 4.2. Before that, we discuss a formal calibration notion for CDE models that also involves the PIT values.

4.1.1 Probabilistic Calibration and Recalibration

There are several notions of calibration in CDE models for regression (Gneiting et al., 2007). Here we focus on *probabilistic calibration*, which essentially means that PIT values should be uniform.

Definition 4 (Probabilistic and Quantile Calibration; Dawid (1984) and Gneiting et al. (2007)). An estimator $\hat{f}(y|x)$ is said to be probabilistically calibrated if, for every $\alpha \in [0, 1]$,

$$\mathbb{P}(\text{PIT}(Y; \mathbf{X}) \leq \alpha) = \alpha,$$

where $\text{PIT}(Y; \mathbf{X}) = \hat{F}(Y|\mathbf{x})$ is its probability integral transform, as defined in Definition 3. This is equivalent to saying that

$$\mathbb{P}\left(Y \leq \hat{F}^{-1}(\alpha|\mathbf{X})\right) = \alpha,$$

which is often referred to as quantile calibration.

In simple terms, if a model is probabilistically calibrated, then, for example, 10% of the observed Y values should fall below the 10th percentile of the estimated conditional distribution, 50% should fall below the 50th percentile, and so forth. More generally, $(1 - \alpha)\%$ of the prediction intervals, $[\hat{F}^{-1}(\alpha/2|\mathbf{x}), \hat{F}^{-1}(1 - \alpha/2|\mathbf{x})]$, should contain the true Y values. (For a formal definition of marginal coverage and prediction sets, see Chapter 5.)

Probabilistic classification can be evaluated by analyzing the sample distribution of PIT values through histograms or P-P plots, as illustrated in Figure 4.2.

4.1. PIT Values: Evaluating Calibration in Regression

As discussed in Gneiting and Resin (2023) and in Theorem 5, probabilistic calibration primarily focuses on unconditional properties of the estimated densities. However, one can still attempt to improve the estimate \hat{f} by recalibrating it to move closer to probabilistic calibration.

Recalibration. One recalibration method is quantile recalibration (Bordoloi et al., 2010; Kuleshov et al., 2018). This method adjusts the estimated cumulative distribution function to correct deviations from uniformity in the PIT values. Formally, let

$$G(\alpha) = \mathbb{P}(\text{PIT}(Y; \mathbf{X}) \leq \alpha)$$

be the marginal cumulative distribution function of the PIT values, and let \hat{G} represent an estimate of G . This estimate can be derived, for instance, from the empirical CDF of the PIT values on a holdout set or by applying a kernel density estimator to that set. Once \hat{G} is obtained, the recalibrated CDF, denoted as \tilde{F} , is computed by transforming the original CDF \hat{F} using \hat{G} as follows:

$$\tilde{F}(y|\mathbf{x}) := \hat{G}\left(\hat{F}(y|\mathbf{x})\right).$$

By construction, if $\hat{G} = G$, then \tilde{F} is probabilistically calibrated. Indeed, for every $\alpha \in [0, 1]$, the recalibrated model satisfies:

$$\begin{aligned} \mathbb{P}\left(\tilde{F}(Y|\mathbf{X}) \leq \alpha\right) &= \mathbb{P}\left(\hat{G}\left(\hat{F}(Y|\mathbf{X})\right) \leq \alpha\right) = \mathbb{P}\left(\hat{F}(Y|\mathbf{X}) \leq \hat{G}^{-1}(\alpha)\right) \\ &= \mathbb{P}\left(\hat{F}(Y|\mathbf{X}) \leq G^{-1}(\alpha)\right) = G\left(G^{-1}(\alpha)\right) = \alpha. \end{aligned}$$

See Dheur and Taieb (2023), Dheur and Taieb (2024) and references therein for variations of these recalibration ideas, as well as other approaches to recalibrate CDEs. This recalibration techniques however focus on marginal aspects of the PIT distribution and do not address potential covariate dependencies.

4.1.2 Simulated Example: Gaussian Distribution Revisited

Figure 4.2 displays the histograms of the PIT for the three models discussed in Section 3.10. The code for this implementation is available in the [CDE Notebook](#). Under proper model calibration, these histograms should follow a

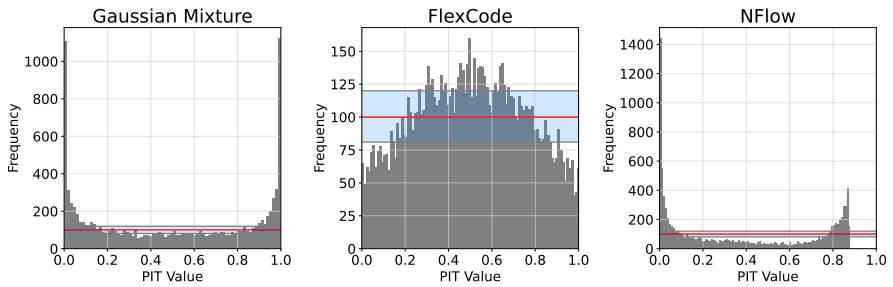


Figure 4.2: PIT histograms for the Gaussian Mixture, FlexCode, and NFlow models. Each panel shows the distribution of PIT values, with the red line representing the expected uniform distribution under proper calibration. The shaded region shows 95% confidence interval for the bar heights under the global consistency hypothesis.

uniform distribution, represented by the red line in each panel. The shaded region indicates the 95% confidence interval for the bar heights, assuming a uniform distribution. The plot suggests that although none of the models are fully calibrated, FlexCode demonstrates a better alignment with calibration.

4.2 Conditional PIT values

The primary objective of conditional PIT values is to overcome the limitations highlighted in Theorem 5 (Zhao et al., 2021). This approach is based on the following key result:

Theorem 6 (Local Consistency and Pointwise Uniformity). *Global consistency is achieved if and only if the distribution of $\text{PIT}(Y; \mathbf{x})$, given \mathbf{x} , is uniform over $(0, 1)$.*

Building on this result, Zhao et al. (2021) suggests testing H_0 by evaluating whether $\text{PIT}(Y; \mathbf{x})$, conditional on \mathbf{x} , follows a uniform distribution over $(0, 1)$. This testing problem is then reformulated as follows. For each $\gamma \in (0, 1)$, define the cumulative distribution function of the PIT at \mathbf{x} as

$$r^{\hat{f}}(\mathbf{x}; \gamma) := \mathbb{P}(\text{PIT}(Y; \mathbf{x}) < \gamma | \mathbf{x}). \quad (4.4)$$

Since $r^{\hat{f}}(\mathbf{x}; \gamma)$ represents the conditional cumulative distribution function of

4.2. Conditional PIT values

the PIT at \mathbf{x} , it follows that for each fixed \mathbf{x} ,

$$\begin{aligned}\widehat{f}(y|\mathbf{x}) &= f(y|\mathbf{x}) \text{ for almost every } y \in \mathcal{Y} \text{ if, and only if,} \\ r\widehat{f}(\mathbf{x}; \gamma) &= \gamma \text{ for every } \gamma \in (0, 1).\end{aligned}$$

In other words, global consistency holds if, and only if, $r\widehat{f}(\mathbf{x}; \gamma) = \gamma$ for every $\gamma \in (0, 1)$. This insight suggests that we can test H_0 by estimating $r\widehat{f}(\mathbf{x}; \gamma)$ and assessing its deviation from γ .

To estimate $r\widehat{f}$, note that this quantity can be interpreted as the regression of the indicator variable

$$W^\gamma := \mathbb{I}(\text{PIT}(Y; \mathbf{X}) < \gamma)$$

on \mathbf{X} . Therefore, $r\widehat{f}(\mathbf{x}; \gamma)$ can be estimated by calculating $W_i^\gamma := \mathbb{I}(\text{PIT}(Y_i; \mathbf{X}_i) < \gamma)$ and performing a regression of W on \mathbf{X} using the transformed dataset

$$\{(\mathbf{X}_1, W_1^\gamma), \dots, (\mathbf{X}_n, W_n^\gamma)\}.$$

Once $r\widehat{f}$ is estimated (for simplicity, we denote its estimate by $\widehat{r}(\mathbf{x}; \gamma)$), we can test H_0 using the test statistic

$$S := \frac{1}{n} \sum_{i=1}^n T(\mathbf{X}_i), \tag{4.5}$$

where

$$T(\mathbf{x}) := \frac{1}{|G|} \sum_{\alpha \in G} (\widehat{r}(\mathbf{x}; \alpha) - \alpha)^2 \tag{4.6}$$

quantifies the deviation of $\widehat{f}(y|\mathbf{x})$ from $f(y|\mathbf{x})$ at each point \mathbf{x} .

The distribution of T under the null hypothesis can be approximated using Monte Carlo sampling, leveraging the fact that under H_0 , $W \sim U(0, 1)$. Each Monte Carlo sample consists of $(\mathbf{X}_1, W_1^b), \dots, (\mathbf{X}_B, W_B^b)$, with $W_i^b \sim U(0, 1)$. The resulting test is referred to as the Global Consistency Test (GCT).

$T(\mathbf{x})$ can also be used as a test statistic to test *local consistency* at \mathbf{x} , which is defined as follows:

Definition 5 (Local Consistency). Fix $\mathbf{x} \in \mathcal{X}$. An estimate $\widehat{f}(y|\mathbf{x})$ is locally

consistent with the density $f(y|\mathbf{x})$ at fixed \mathbf{x} if the following null hypothesis holds:

$$H_0(\mathbf{x}) : \hat{f}(y|\mathbf{x}) = f(y|\mathbf{x}) \text{ for every } y \in \mathbb{R}. \quad (4.7)$$

Local consistency therefore means that, at the specific point \mathbf{x} , the estimated conditional density $\hat{f}(y|\mathbf{x})$ perfectly matches the true conditional density $f(y|\mathbf{x})$ for all possible values of y . In other words, the estimation is accurate at this particular location in the feature space.

The local null hypothesis $H_0(\mathbf{x})$ can be tested by using the test statistic $T(\mathbf{x})$ and Monte Carlo sampling to determine (an approximate) null distribution. We denote such test by Local Consistency Test (LCT).

Under certain conditions, LCT approximately controls the Type I error rate. Specifically, we require that the regression estimator used to construct \hat{r} is local in the following sense:

Assumption 3 (Local Regression Estimator). *There exists $\epsilon > 0$ such that the estimated regression at \mathbf{x} , denoted by $\hat{r}(\mathbf{x}, \gamma)$, only utilizes the sample points (\mathbf{X}_i, Y_i) for which \mathbf{X}_i lies within the ball $\mathcal{B}(\mathbf{x}; \epsilon)$, a neighborhood around \mathbf{x} with radius ϵ .*

This assumption ensures that the regression estimate $\hat{r}(\mathbf{x}, \gamma)$ at a point \mathbf{x} is influenced solely by the data points in the vicinity of \mathbf{x} , thus making the estimation highly localized.

Given this assumption, we can state the following theorem:

Theorem 7. *Fix $\epsilon \in \mathbb{R}$. Under the null hypothesis*

$$H_0^\epsilon(\mathbf{x}) : \hat{f}(y|\mathbf{x}) = f(y|\mathbf{x}) \text{ for almost every } y \in \mathcal{Y} \text{ and for all } \mathbf{x}' \in \mathcal{B}(\mathbf{x}; \epsilon),$$

and under Assumption 3, for any significance level $0 < \alpha < 1$,

$$\lim_{B \rightarrow \infty} \mathbb{P}(p(\mathbf{x}) \leq \alpha) = \alpha,$$

where $p(\mathbf{x})$ is the Monte Carlo p-value computed using $T(\mathbf{x})$ as the test statistic.

This theorem indicates that when the regression estimator is local, the LCT will control the Type I error rate at the specified level α asymptotically. In other words, the probability of incorrectly rejecting the null hypothesis $H_0^\epsilon(\mathbf{x})$ (which asserts that the estimated conditional density $\hat{f}(y|\mathbf{x})$ is consistent with

4.2. Conditional PIT values

the true density $f(y|\mathbf{x})$ within the neighborhood $B(\mathbf{x}; \epsilon)$) will approach α as the number of Monte Carlo samples B increases indefinitely.

4.2.1 Diagnostics

Conditional PIT values offer valuable insights into the nature of deviations between the estimated conditional density \hat{f} and the true conditional density f at any given location \mathbf{x} . One effective way to analyze these deviations is through the use of “amortized local P-P plots” (ALPs), which plot $\hat{r}_\alpha(\mathbf{x})$ against α .

P-P plots (Probability-Probability plots) traditionally serve as a diagnostic tool to compare the empirical CDF of a sample with a theoretical CDF (Gibbons and Chakraborti, 2014), helping to assess how well the model aligns with the expected distribution. In the context of ALPs, these plots allow us to visualize the agreement between the estimated conditional CDF and the uniform distribution, which is expected under the true model. The alignment, or lack thereof, reveals where and how the model’s performance may deviate from the true conditional density, providing detailed interpretive information about potential modes of deviation.

Figure 4.3 illustrates how these ALPs can highlight such deviations effectively. Importantly, these plots can be constructed without requiring knowledge of the true conditional density $f(y|\mathbf{x})$, making them a powerful tool for model diagnostics and interpretation.

4.2.2 Monotonic Neural Networks to Estimate the Regression Function

Dey et al. (2022) estimate $r^{\hat{f}}(\gamma; \mathbf{x})$ by improving upon Zhao et al., 2021. The key idea is to first augment the calibration data $(\mathbf{X}_1, Y_1), \dots, (\mathbf{X}_n, Y_n)$ by drawing multiple values $\gamma_{i,1}, \dots, \gamma_{i,K} \sim U(0, 1)$ for each data point ($i = 1, \dots, n$), and then regress the random variable

$$W_{i,j} := \mathbb{I}(\text{PIT}(Y_i; \mathbf{X}_i) \leq \gamma_{i,j})$$

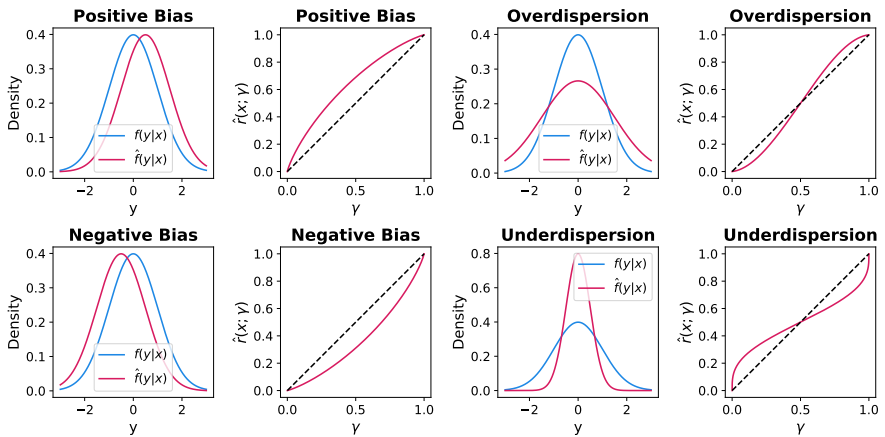


Figure 4.3: P-P plots assess the fit between a density model and actual data, revealing bias (left panel) and dispersion (right panel). “Amortized Local P-P Plots” (ALPs) compare conditional densities $\hat{f}(y|x)$ at any location x in the feature space \mathcal{X} .

on both \mathbf{X}_i and $\gamma_{i,j}$ using the augmented calibration sample $\{(\mathbf{X}_i, \gamma_{i,j}, W_{i,j})\}_{i,j}$, for $i = 1, \dots, n$ and $j = 1, \dots, K$. As $r^{\hat{f}}(\gamma; \mathbf{x})$ is a non-decreasing function of γ , Dey et al. (2022) use monotonic neural networks (Wehenkel and Louppe, 2019) for most applications with complex inputs, though any other suitable regression method may be used.

4.2.3 Handling Multivariate Responses

When the response \mathbf{Y} is multivariate, the random variable $F_{\mathbf{Y}|\mathbf{X}}(\mathbf{Y}|\mathbf{X})$ is no longer uniformly distributed (Genest and Rivest, 2001), making a direct generalization of PIT values to higher dimensions nontrivial. To address this, one approach is to evaluate the PIT statistic for univariate projections of \mathbf{Y} (Mucesh et al., 2021). Specifically, PIT values can be computed using the estimate $\hat{f}(h(\mathbf{Y})|\mathbf{x})$ induced by $\hat{f}(\mathbf{Y}|\mathbf{x})$, for a chosen projection function $h : \mathbb{R}^p \rightarrow \mathbb{R}$. The choice of h depends on the context. For instance, one could consider individual components, $h(\mathbf{y}) = y_j$, or use copPIT (Ziegel, Gneiting, et al., 2014), which creates a unidimensional projection encapsulating information about the joint distribution of \mathbf{Y} . While PIT and conditional PIT

4.2. Conditional PIT values

diagnostics on these projections cannot fully assess the fit to $f(\mathbf{Y}|\mathbf{x})$, they offer valuable insights and serve as useful goodness-of-fit checks.

An alternative diagnostic for \hat{f} is the highest predictive density (HPD) values (Dalmasso et al., 2020b; Harrison et al., 2015), defined as

$$\text{HPD}(\mathbf{y}; \mathbf{x}) = \int_{\{\mathbf{y}' : \hat{f}(\mathbf{y}'|\mathbf{x}) \geq \hat{f}(\mathbf{y}|\mathbf{x})\}} \hat{f}(\mathbf{y}'|\mathbf{x}) d\mathbf{y}';$$

see Figure 4.4 for an illustration. This measure reflects the plausibility of \mathbf{y} under $\hat{f}(\mathbf{y}|\mathbf{x})$, with smaller values indicating higher plausibility. In Bayesian contexts, where $y = \theta$ represents the parameter of interest, HPD values correspond to the complement of the e-value (Pereira and Stern, 1999). Like PIT values, HPD values are uniformly distributed under the global null hypothesis (Dalmasso et al., 2020b). However, standard goodness-of-fit tests based on HPD values, similar to those based on PIT, are insensitive to covariate transformations.

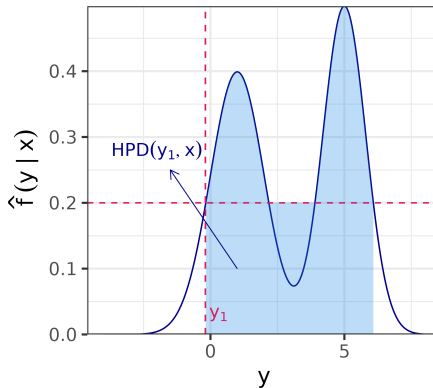


Figure 4.4: Illustration of the HPD value for a distribution, $\hat{f}(y|\mathbf{x})$. The vertical dashed lines represent the true observed values $y = y_1$. The highlighted areas indicate the regions of interest under the curves for the HPD value.

Fortunately, HPD values exhibit uniformity under the local consistency hypothesis:

Theorem 8 (Zhao et al., 2021). *For any $\mathbf{x} \in \mathcal{X}$, if the local null hypothesis $H_0(\mathbf{x}) : \hat{f}(\cdot|\mathbf{x}) = f(\cdot|\mathbf{x})$ holds, then the distribution of $\text{HPD}(\mathbf{Y}; \mathbf{x})$ given \mathbf{x} is uniform over*

$(0, 1)$.

This property enables the application of techniques from Section 4.2 to HPD values for assessing both global and local consistency in multivariate responses, including the construction of local P-P plots (Zhao et al., 2021).

The HPD statistic is particularly useful for constructing predictive regions with \hat{f} , as HPD values are intrinsically linked to highest predictive density sets (Example 5.1). Specifically, for the α -level HPD set $R_\alpha(\mathbf{x})$:

$$\text{HPD}(\mathbf{y}; \mathbf{x}) < \alpha \iff Y \in R_\alpha(\mathbf{x}).$$

Testing the local consistency of \hat{f} via HPD values thus directly evaluates the coverage of HPD sets. Moreover, HPD values are used the HPD-split conformal method (Section 5.3).

4.2.4 Example: Neural Density Inference for Galaxy Images

In this toy example, $\mathbf{x} \in \mathbb{R}^{400}$ represents an image of an elliptical galaxy generated by `GalSim`, an open-source toolkit for simulating realistic images of astronomical objects (Rowe et al., 2015). Our response variable is y , the galaxy's rotation angle with respect to the x-axis. For illustration, our data is simulated as a mixture of a larger population with $\lambda = 0.7$ (spheroidal galaxies), and a smaller population with $\lambda = 0.1$ (elongated galaxies). We then simulate a sample of images as follows: first, we draw λ and y from a prior distribution given by

$$\begin{aligned}\mathbb{P}(\lambda = 0.7) &= 1 - \mathbb{P}(\lambda = 0.1) = 0.9 \\ Y &\sim \text{Unif}(-\pi, \pi)\end{aligned}$$

Then we sample 20×20 galaxy images \mathbf{X} according to the data model $\mathbf{X} | \lambda, y \sim \text{GalSim}(a, \lambda)$, where

$$\begin{aligned}a | \lambda = 0.7 &\sim N(y, 0.05) \\ a | \lambda = 0.1 &\sim 0.5\text{Laplace}(y, 0.05) + 0.5\text{Laplace}(y, 0.0005).\end{aligned}$$

Finally, we fit a convolutional mixture density network (ConvMDN; see

4.2. Conditional PIT values

Section 3.5), which gives us an estimate of $f(y|\mathbf{x})$. We allow K , the number of mixture components, to vary. According to the KL divergence loss computed on a separate test sample with 1000 images, the best fit of $f(\theta|\mathbf{x})$ is achieved by a ConvMDN model with $K = 7$.

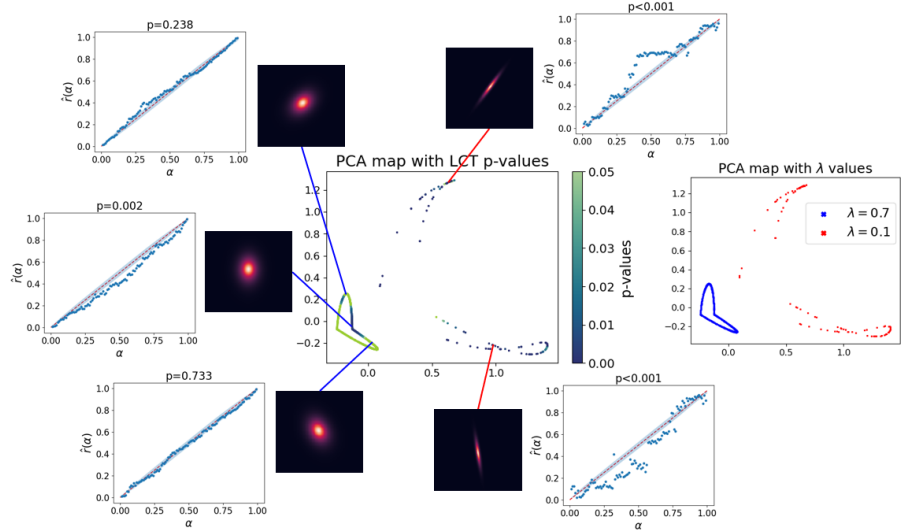


Figure 4.5: Diagnostics for conditional density estimation: Visualization of test galaxy points in \mathbb{R}^{400} using the first two components (center panel, "PCA map with LCT p-values"). ConvMDN's P-values indicate good fit for 90% of spheroidal galaxies ($\lambda = 0.7$) but poor fit for the 10% elongated galaxies ($\lambda = 0.1$). Local P-P plots reveal significant deviations in CDEs for the latter group, highlighting the need for improved density approximations.

Here, the ConvMDN model with the smallest KL loss fails the global test that uses the statistic in Equation 4.5 ($p < 0.001$), so we turn to the diagnostics described in Section 4 to understand why. Figure 4.5 plots the test galaxy images along their first two principal components. The local tests of Equation 4.6 show that the ConvMDN model generally fits the density well for the main population of spheroidal galaxies ($\lambda = 0.7$), but fails to properly model the smaller population of elongated galaxies ($\lambda = 0.1$). P-P plots at selected test points indicate severe bias in the density estimates for the $\lambda = 0.1$ population. These plots suggest that an effective way of obtaining a better approximation of the density is by improving the fit for the $\lambda = 0.1$ population (by obtaining

more data in that region of the feature space, using a different model class, etc). For instance, CDE models not based on mixtures could be more effective.

4.3 Calibration of Classification Models

Even though proper loss functions encourage $\mathbb{P}(Y = y|\mathbf{x})$ to be well estimated, this is not always achieved (Gneiting and Katzfuss, 2014; Vaicenavicius et al., 2019). Thus, in practice, it is common to check whether the probabilistic classifier is calibrated (Dawid, 1982; Gupta et al., 2020; Murphy and Epstein, 1967). In the context of binary classification, calibration is often defined as follows (see Gupta and Ramdas 2022; Widmann et al. 2019 for multi-class calibration):

Definition 6 (Marginal calibration). *A probabilistic binary classifier $g : \mathcal{X} \rightarrow [0, 1]$ is marginally calibrated if, and only if,*

$$\mathbb{P}(Y = 1|g(\mathbf{X})) = g(\mathbf{X}) \text{ (almost surely).} \quad (4.8)$$

Equation 4.8 is often referred to as *calibration* or *perfect calibration*. For instance, consider a classifier predicting whether a person has a disease: if the classifier is marginally calibrated, then for all individuals assigned a 70% probability of being sick, approximately 70% of them will indeed have the disease.

4.3.1 Evaluating Marginal Calibration

There are many ways to evaluate whether a probabilistic binary classifier is calibrated in the sense of Definition 6:

Calibration Plot (Reliability Diagram). A calibration plot, also known as reliability diagram (Zadrozny and Elkan, 2002), is a graphical tool that compares the estimated probabilities $g(\mathbf{x})$ with the actual outcomes on a holdout set. The predicted probabilities are partitioned into bins, and within each bin, the average predicted probability is compared with the observed frequency of the positive class. Formally, given a set of estimated probabilities $\{g(\mathbf{x}_i)\}_{i=1}^n$ evaluated on a holdout set not used for training, the steps are as follows:

4.3. Calibration of Classification Models

1. Sort the predicted probabilities $\{g(\mathbf{x}_i)\}_{i=1}^n$.
2. Divide the sorted probabilities into J contiguous bins.
3. For each bin B_j , calculate the observed proportion of sample points that fall into B_j :

$$\hat{o}_j = \frac{1}{|B_j|} \sum_{i \in B_j} y_i,$$

and the average estimated probability in B_j :

$$\hat{p}_j = \frac{1}{|B_j|} \sum_{i \in B_j} p_i.$$

4. Create a scatter plot of (\hat{p}_j, \hat{o}_j) .

By construction, \hat{o}_j is an estimate of $\mathbb{P}(Y = 1 | g(\mathbf{X}) \in B_j)$. Thus, if g is marginally calibrated, we expect that $\hat{p}_j \approx \hat{o}_j$ for all j . Deviations from the diagonal $\hat{p}_k = \hat{o}_k$ indicate miscalibration.

Figure 4.6 shows an example of a calibration plot generated from simulated data, where the estimated probabilities and the observed outcomes are compared across different probability bins. The dashed diagonal line represents perfect calibration, and deviations from this line illustrate areas where the model is miscalibrated.

Expected Calibration Error (ECE). The Expected Calibration Error is a summary statistic derived from the calibration plot that quantifies the difference between predicted probabilities and observed frequencies across bins:

$$ECE = \sum_{j=1}^J \frac{|B_j|}{n} |\hat{o}_j - \hat{p}_j|$$

A lower ECE indicates better calibration.

Maximum Calibration Error (MCE). The Maximum Calibration Error is a more conservative summary statistic, focusing on the worst-case deviation across all bins:

$$MCE = \max_{j=1, \dots, J} |\hat{o}_j - \hat{p}_j|.$$

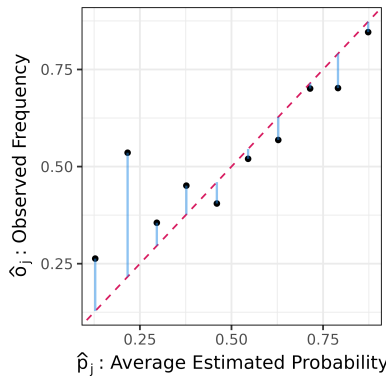


Figure 4.6: Example of calibration plot (a.k.a. reliability diagram) comparing estimated probabilities with observed frequencies in each bin.

Again, low MCE values indicate better calibration.

If one concludes that g is not calibrated, it can be recalibrated. The next section discusses ways to recalibrate g .

4.3.2 Recalibration of Probabilistic Classifiers

Several methods exist to recalibrate g to improve its marginal calibration. Below are a few approaches:

Platt scaling. Let $g : \mathcal{X} \rightarrow [0, 1]$ be a binary probabilistic classifier that outputs a score $g(\mathbf{x})$ for each input \mathbf{x} . Platt scaling (Platt et al., 1999) fits a logistic regression model to these scores, aiming to find a transformation that better reflects the true probabilities.

The recalibrated probabilities $g'(\mathbf{x})$ is given by:

$$g'(\mathbf{x}) = \frac{1}{1 + \exp(\alpha g(\mathbf{x}) + \beta)},$$

where α and β are parameters determined by fitting the logistic regression model on a labeled dataset $\{(g(\mathbf{x}_i), y_i)\}_{i=1}^n$.

Histogram binning. Histogram binning (Zadrozny and Elkan, 2001) is a non-parametric version of Platt scaling. The idea is to use the calibration plot

4.3. Calibration of Classification Models

(Section 4.3.1) to recalibrate g . Specifically, for each $\mathbf{x} \in \mathcal{X}$, the recalibrated version of g is given by

$$g'(\mathbf{x}) = \hat{p}_j,$$

where j is the bin B_j that contains \mathbf{x} .

Isotonic regression. Isotonic regression (Zadrozny and Elkan, 2002) fits a non-decreasing function to the estimated probabilities $g(\mathbf{x})$, ensuring that the recalibrated probabilities are better aligned with the observed frequencies of the positive class. Specifically, given a set of estimated probabilities $\{g(\mathbf{x}_i)\}_{i=1}^n$, isotonic regression recalibrates g by finding the function $g'(\mathbf{x})$ that minimizes the Brier Score:

$$\sum_{i=1}^n (\hat{g}(\mathbf{x}_i) - y_i)^2$$

subject to the constraint

$$g'(\mathbf{x}_{i+1}) \geq g'(\mathbf{x}_i) \text{ for all } i.$$

Temperature scaling. Temperature scaling is a simple recalibration technique used primarily with neural networks (Guo et al., 2017). It recalibrates $g(\mathbf{x})$ by rescaling its logit values by a constant factor. Specifically, let $\text{logit}(p) = \log(p/(1-p))$ be the logit of p . Temperature scaling recalibrates g according to

$$\text{logit}(g'(\mathbf{x})) = \frac{1}{T} \text{logit}(g(\mathbf{x})),$$

where T is the temperature parameter, typically chosen by minimizing the negative log-likelihood or the Brier Score on a validation set. $T > 1$ smooths the predicted probabilities, reducing overconfidence in the predictions. In particular, when $T \rightarrow \infty$, $g'(\mathbf{x}) = 1/2$. When $T = 1$, no transformation is made.

4.3.3 Limitations of Marginal Calibration

A classifier can be marginally calibrated even if it disregards information in \mathbf{x} . This parallels the scenario in regression (Theorem 5). In fact, g is calibrated

if and only if there exists a space \mathcal{Z} and a function $\lambda : \mathcal{X} \rightarrow \mathcal{Z}$ such that

$$\mathbb{P}(Y = 1 | \lambda(\mathbf{X})) = g(\mathbf{X}) \quad (\text{almost surely});$$

see Vaicenavicius et al. 2019, Proposition 1 and Gupta et al. 2020, Proposition 1. Thus, while $g(\mathbf{x}) = \mathbb{P}(Y = 1 | \mathbf{x})$ is calibrated, marginal calibration does not imply that g fully utilizes the information in \mathbf{x} . For example, $g(\mathbf{X}) := \mathbb{P}(Y = 1)$ is marginally calibrated. In other words, marginal calibration does not ensure that the *Bayes classifier*¹ is recovered, that is, $g(\mathbf{X})$ can be very different from $\mathbb{P}(Y = 1 | \mathbf{X})$. Moreover, it does not guarantee fairness; it is possible that $\mathbb{P}(Y = 1 | \mathbf{X} \in A, g(\mathbf{X})) \neq g(\mathbf{X})$, where $A \subset \mathcal{X}$ represents a subgroup of interest.

Therefore, we suggest that marginal calibration should be evaluated only after selecting the best probabilistic classifier based on a suitable proper loss function, as discussed in Section 3.1. Marginal calibration alone should not drive classifier selection, as it may not reflect the optimal exploitation of information in \mathbf{x} .

4.3.4 Example

In this toy example, we apply several calibration methods to a logistic regression model trained on synthetic data generated as follows:

1. The input features X were drawn from a standard normal distribution:

$$X_i \sim \mathcal{N}(0, 1) \quad \text{for } i = 1, 2, \dots, n.$$

2. The binary labels Y were generated according to a logistic model with a non-linear transformation of the input features. Specifically, the probability of the positive class was given by:

$$\mathbb{P}(Y_i = 1 | x_i) = \frac{\exp(x_i^3)}{1 + \exp(x_i^3)}.$$

The labels were then sampled as:

$$Y_i \sim \text{Bernoulli}(\mathbb{P}(Y_i = 1 | X_i)).$$

¹Here, $\mathbb{P}(Y = 1 | \mathbf{X})$ is referred to as the Bayes classifier.

4.3. Calibration of Classification Models

3. A logistic regression model was trained on the training set to predict the probability of the positive class $\mathbb{P}(Y = 1|x)$.

We trained the model on 1000 samples and used 2000 for recalibration and performance evaluation. While these same 2000 samples were used for both, the notebook ([Classification Calibration Notebook](#)) also includes evaluation on an independent test set, confirming that results are not biased by overfitting. Since the independent set results were similar, they are omitted here.

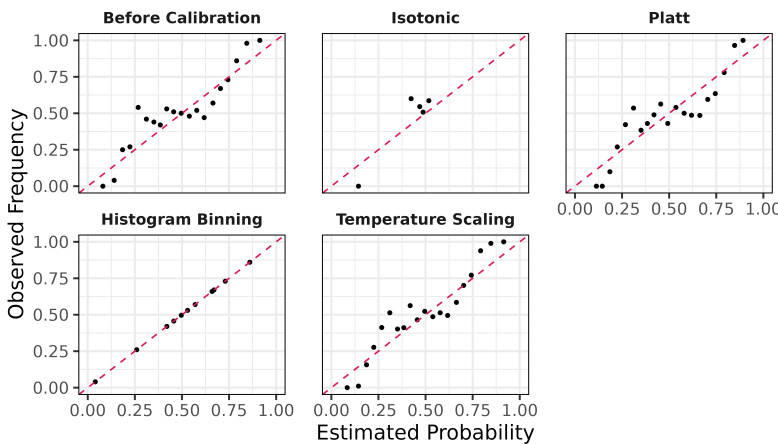


Figure 4.7: Calibration plots for different recalibration methods applied to a logistic regression model. Each plot compares the estimated probabilities against the observed frequencies on a validation set. The diagonal line represents perfect marginal calibration.

The calibration plots in Figure 4.7 and the metrics in Table 4.1 show that histogram binning is the only method that enhances both proper loss functions and marginal calibration. However, note that histogram binning inherently achieves perfect calibration because its recalibration is specifically designed to produce a perfect calibration plot. Additionally, while isotonic regression improves calibration, it worsens the loss functions. This happens because the calibration plot is non-monotonic, causing probabilities in the range of approximately 25% to 75% to be mapped to 50%.

4.4 Summary

In this chapter, we explored techniques for assessing and improving the accuracy of conditional density estimates and classification models. We began by introducing the concept of Probability Integral Transform values, a straightforward diagnostic tool used to evaluate whether a conditional density estimator, \hat{f} , is globally consistent with the true density f . While PIT values provide a useful first check – where uniformity suggests a good fit – we highlighted the limitations of this method. Specifically, we showed that even poorly specified models might pass the PIT uniformity test, making it an insufficient criterion for model validation.

Table 4.1: Comparison of Calibration Methods: Expected Calibration Error (ECE), Maximum Calibration Error (MCE), Negative Brier Score, and Log Loss for different calibration methods applied to a logistic regression model. Lower values indicate better performance.

Method	ECE	MCE	Brier Score	Log Loss
Before Calibration	0.085	0.272	0.196	0.566
Isotonic	0.027	0.177	0.250	0.694
Platt	0.096	0.225	0.198	0.575
Histogram Binning	0.000	0.000	0.185	0.531
Temperature Scaling	0.081	0.203	0.198	0.567

To address these shortcomings, we introduced *Conditional PIT values*. Unlike global PIT, which assesses uniformity across the entire dataset, Conditional PIT values focus on the distribution of PIT values given specific covariates. This more granular approach allows us to identify where the model deviates from the true conditional density, offering a clearer path to improvement.

In parallel, we examined calibration in classification models. Calibration is crucial for ensuring that the predicted probabilities from a classifier are reliable. We defined *marginal calibration* – where the predicted probability of an event closely matches the observed frequency – and presented several methods to assess and improve calibration, including *Platt scaling*, *Histogram binning*, *Isotonic regression*, and *Temperature scaling*. Through examples, we showed how these methods could be applied to recalibrate classifiers, improving both the model’s reliability and its predictive accuracy.

A key takeaway from this chapter is that *calibration* – whether in the con-

4.4. Summary

text of regression or classification – should be considered only after selecting the best model using appropriate loss functions. Calibration alone does not guarantee that a model fully captures the relationships within the data or that it leverages all available information. Therefore, it should be seen as the final step in the modeling process, ensuring that the selected model provides trustworthy predictions.

Chapter 5

From Conditional Densities to Prediction Regions



Color Study. Squares with Concentric Circles. Wassily Kandinsky, 1913,
Städtische Galerie im Lenbachhaus, Munich.

5.1. Optimal Prediction Regions

A good forecaster is not smarter than everyone else, he merely has his ignorance better organized.

Unknown Author

Oftentimes, the end goal of a supervised learning model is to provide prediction regions for new sample points. Prediction regions are sets of possible outcomes that reflect the range within which the true outcome is likely to fall, given a new sample point. These regions provide a more complete picture of the model's predictions by offering a range rather than a point estimate, thus incorporating uncertainty into the prediction process.

Formally, a prediction region is defined as follows:

Definition 7 (Prediction region). *A prediction region (or prediction set, or prediction band) is a function $R : \mathcal{X} \rightarrow \mathcal{P}(\mathcal{Y})$, where $\mathcal{P}(\mathcal{Y})$ is the set of the parts of \mathcal{Y} .*

In this chapter, we will begin by exploring the concept of optimal – also known as oracle – prediction regions derived from different loss functions. This understanding will lay the foundation for developing and assessing various methods for estimating prediction regions in practice. Next, we will examine techniques for estimating these regions, focusing on conformal methods, which offer guaranteed coverage, making them robust tools for uncertainty quantification.

5.1 Optimal Prediction Regions

To define optimal prediction regions, we start by introducing a loss function, denoted as

$$L : \mathcal{P}(\mathcal{Y}) \times \mathcal{X} \times \mathcal{Y} \longrightarrow \mathbb{R},$$

where $L(R; (\mathbf{X}, Y))$ quantifies the cost associated with a prediction region $R \subseteq \mathcal{Y}$ when the input \mathbf{X} and true output Y are observed.

The goal is to find an optimal prediction region that minimizes the overall

expected loss, also known as the risk. The risk function is defined as:

$$\begin{aligned}\mathcal{R} : (\mathcal{X} \longrightarrow \mathcal{P}(\mathcal{Y})) &\longrightarrow \mathbb{R}, \\ R &\longmapsto \mathcal{R}(R) := \mathbb{E}_{\mathbf{X}, Y}[L(R; (\mathbf{X}, Y))],\end{aligned}$$

where $\mathcal{R}(R)$ represents the expected loss or risk associated with a prediction region R over the joint distribution of \mathbf{X} and Y . The expectation is taken with respect to the distribution of both the input \mathbf{X} and the output Y , making the risk function a measure of how well the prediction region R performs on average.

Different choices of the loss function L lead to different forms of optimal prediction regions. For example, some loss functions might penalize regions that are too large or too small, while others might emphasize the inclusion of the true output Y within the region. The next examples will illustrate common types of prediction regions that arise from different loss functions, as shown in Figure 5.1. These examples show how varying the loss function influences the shape and properties of the optimal prediction region, reflecting different practical considerations. The optimal regions are also known as *oracle regions*, since they require knowledge of $f(y|\mathbf{x})$ or, at the very least, certain properties of it.

Example 5.1 (HPD Region). Consider a loss function defined as

$$L(R, (\mathbf{x}, y)) = \mathbb{I}(y \notin R) + \lambda \text{Vol}(R),$$

where $\mathbb{I}(y \notin R)$ is 1 if the true outcome y is not in the prediction region R , and 0 otherwise, and $\text{Vol}(R)$ represents the size of the region. This loss function combines two objectives:

- **Coverage term** ($\mathbb{I}(y \notin R)$): Penalizes the model when the true outcome y falls outside the predicted region R . This term encourages the region R to include y as often as possible.
- **Size term** ($\text{Vol}(R)$): Penalizes the model for making the prediction region R too large. A smaller region R is preferable for more precise predictions, but shrinking R too much may increase the likelihood of excluding the true outcome y .

5.1. Optimal Prediction Regions

The value $\lambda > 0$ balances the trade-off between including y in R and keeping R small. The prediction region that minimizes the risk associated to this loss is the *Highest Predictive Density Region* (HPD):

$$R(\mathbf{x}) = \{y \in \mathcal{Y} : f(y|\mathbf{x}) > \lambda\},$$

where $f(y|\mathbf{x})$ is the conditional density of y given \mathbf{x} . The HPD region includes the most likely values of y and balances accuracy with the region's size.

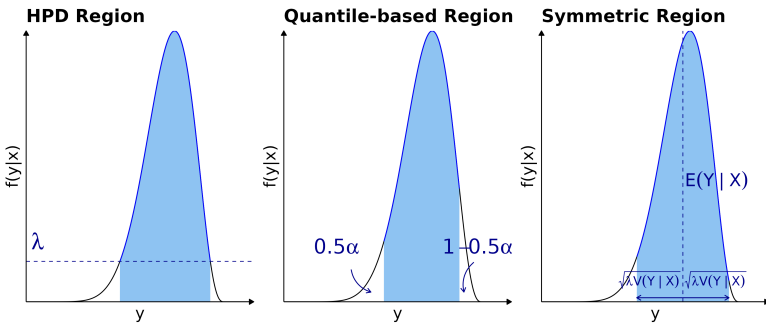


Figure 5.1: Illustration of the optimal prediction regions corresponding to different loss functions: the highest predictive density (HPD) region from Example 5.1, the quantile-based region from Example 5.2, and the symmetric region from Example 5.3. Each plot shows how the choice of loss function influences the shape and properties of the resulting prediction region.

HPD regions are applicable in both regression and classification settings. In regression, different loss functions can lead to various types of prediction regions.

Exemple 5.2 (Quantile-based Region). Consider the case where $\mathcal{Y} \subset \mathbb{R}$. Fix $\alpha \in (0, 1)$ and assume that the prediction region is an interval, $R(\mathbf{x}) = (a(\mathbf{x}), b(\mathbf{x}))$. The *interval loss* (Winkler, 1972) is defined by

$$L((a, b), (\mathbf{x}, y)) = \alpha \frac{b(\mathbf{x}) - a(\mathbf{x})}{2} + [(a(\mathbf{x}) - y)_+ + (y - b(\mathbf{x}))_+].$$

This loss function combines two components: the length of the prediction interval and a penalty for y falling outside the interval. The first term,

$\alpha \frac{b(\mathbf{x}) - a(\mathbf{x})}{2}$, reflects the length of the interval, weighted by α . The second term, $[(a(\mathbf{x}) - y) + + (y - b(\mathbf{x})) +]$, is a penalty that captures how far y lies from the interval. If y is inside $(a(\mathbf{x}), b(\mathbf{x}))$, this term equals zero, ensuring no penalty. However, if y lies outside the interval, the penalty grows proportionally to the distance between y and the nearest interval boundary.

The optimal prediction region that minimizes the risk for this loss function is the quantile-based interval:

$$R(\mathbf{x}) = (q_{\alpha/2}(\mathbf{x}), q_{1-\alpha/2}(\mathbf{x})),$$

where $q_\gamma(\mathbf{x}) = F^{-1}(\gamma|\mathbf{x})$ represents the γ -th conditional quantile of Y given \mathbf{x} . This interval captures the middle $1 - \alpha$ portion of the conditional distribution of Y .

Exemple 5.3 (Symmetric Region). Consider the case where $\mathcal{Y} \subset \mathbb{R}$. Fix $\lambda > 0$ and assume that the prediction region is an interval, $R(\mathbf{x}) = (a(\mathbf{x}), b(\mathbf{x}))$. The *symmetric interval loss* is defined by

$$L((a, b), (\mathbf{x}, y)) = \lambda \frac{b(\mathbf{x}) - a(\mathbf{x})}{2} + \left[y - \frac{a(\mathbf{x}) + b(\mathbf{x})}{2} \right] \frac{2}{b(\mathbf{x}) - a(\mathbf{x})}.$$

This loss function consists of two components: the width of the prediction interval and a penalty for y deviating from the center of the interval. The first term, $\lambda \frac{b(\mathbf{x}) - a(\mathbf{x})}{2}$, reflects the length of the interval, weighted by λ . The second term, $\left[y - \frac{a(\mathbf{x}) + b(\mathbf{x})}{2} \right] \frac{2}{b(\mathbf{x}) - a(\mathbf{x})}$, is a penalty that increases based on the distance of y from the midpoint of the interval. If y is equal to the midpoint, this term equals zero, ensuring no penalty. However, the further y deviates from the center, the greater the penalty.

The optimal prediction region that minimizes the risk for this loss function is the symmetric interval:

$$R(\mathbf{x}) = \mathbb{E}[Y|\mathbf{x}] \pm \sqrt{\lambda \mathbb{V}[Y|\mathbf{x}]},$$

where $\mathbb{E}[Y|\mathbf{x}]$ represents the conditional mean of Y given \mathbf{x} , and $\sqrt{\mathbb{V}[Y|\mathbf{x}]}$ represents the conditional standard deviation of Y given \mathbf{x} . This interval

5.2. Plug-in Prediction Regions

is centered around the expected value, with the width proportional to the standard deviation, scaled by the factor $\sqrt{\lambda}$.

Each prediction regions has its own strengths and weaknesses:

HPD Region: These regions are particularly effective for capturing the most probable outcomes, making them well-suited for skewed or multimodal distributions. However, they can result in irregularly shaped regions that are computationally challenging to handle/report.

Quantile-based Region: Quantile-based intervals are straightforward to compute and interpret, requiring only two numbers to represent the interval. However, these regions might lead to wide regions in multimodal cases.

Symmetric Region: Symmetric regions are easy to compute and are particularly effective for symmetric distributions, also needing just two numbers for representation. However, they can become large in skewed distributions.

5.1.1 Tuning Parameters and Notions of Coverage

In practice, tuning parameters in loss functions, such as λ in Example 5.1, are chosen to ensure the resulting prediction region achieves the desired coverage. Typically, λ is adjusted for each \mathbf{x} to theoretically achieve *conditional coverage*:

$$\mathbb{P}(Y \in R(\mathbf{X}) | \mathbf{X}) = 1 - \alpha \text{ (a.e.)}. \quad (5.1)$$

See Section 5.2 for more details. If $R(\mathbf{x})$ satisfies conditional coverage, *marginal coverage* is also achieved:

$$\mathbb{P}(Y \in R(\mathbf{X})) = 1 - \alpha. \quad (5.2)$$

In the next sections, we explore methods to approximate optimal regions.

5.2 Plug-in Prediction Regions

One straightforward approach to constructing prediction regions involves leveraging an initial estimate of the conditional density function, \hat{f} , and di-

rectly plugging it into the expression for the optimal region. For example, an estimated Highest Predictive Density (HPD) region can be obtained as:

$$\{y : \hat{f}(y|\mathbf{x}) \geq t_{1-\alpha}(\mathbf{x})\},$$

where the threshold $t_{1-\alpha}(\mathbf{x})$ is chosen such that:

$$\int_{\{y: \hat{f}(y|\mathbf{x}) \geq t_{1-\alpha}(\mathbf{x})\}} \hat{f}(y|\mathbf{x}) dy = 1 - \alpha.$$

Similarly, prediction regions can be derived without needing full knowledge of $f(y|\mathbf{x})$ by directly estimating critical quantities. For instance, a quantile regressor that provides estimates $\hat{q}_{\alpha/2}$ and $\hat{q}_{1-\alpha/2}$ can be used to construct the prediction region:

$$\{y : \hat{q}_{\alpha/2}(\mathbf{x}) < y < \hat{q}_{1-\alpha/2}(\mathbf{x})\}. \quad (5.3)$$

While these quantiles can also be derived using \hat{f} , this direct estimation offers a more practical approach in many scenarios.

Plug-in prediction regions are designed primarily to capture the aleatoric uncertainty inherent in the data. However, since the quantities such as the conditional density $f(y|\mathbf{x})$ or the quantiles $q_{\alpha/2}(\mathbf{x})$ are only estimated from data, the resulting prediction regions often do not achieve the correct coverage. In the next section, we will explore methods that build upon these estimates and also incorporate epistemic uncertainty, leading to prediction regions that more accurately reflect all uncertainty associated to Y , and that also achieve the desired coverage.

5.3 Conformal Regions

The main goal in conformal predictions is to use the data to obtain a valid prediction region (that is, a prediction region whose coverage matches its nominal coverage), $R(\mathbf{X}_{n+1})$, under very few assumptions. Indeed, typically, validity depends only the i.i.d. assumption (Angelopoulos, Bates, et al., 2023; Shafer and Vovk, 2008; Vovk et al., 2005).

A widely employed approach for constructing such prediction regions is

5.3. Conformal Regions

the split method (Lei et al., 2018; Papadopoulos et al., 2002; Vovk, 2012). In this method, the data is divided into two sets: the training set, \mathcal{D}_1 , and the calibration set, \mathcal{D}_2 . We assume that the size of the calibration set is $|\mathcal{D}_2| = n$. Typically, the calibration set can be much smaller than the training set; see Section 5.3.1 for some guidance on how to make such split.

After the data has been split, a non-conformity score $h : \mathcal{X} \times \mathcal{Y} \rightarrow \mathbb{R}$ is trained using \mathcal{D}_1 . The function $h(\mathbf{x}, y)$ is used to quantify the extent to which a given label value y aligns with the feature values \mathbf{x} of an instance. A high value of $h(\mathbf{x}, y)$ suggests that the appearance of label y in an instance characterized by features \mathbf{x} is improbable. In the context of regression, a few examples of non-conformity scores are:

- **[Regression-split]** $h(\mathbf{x}, y) = |y - \hat{r}(\mathbf{x})|$, where \hat{r} is an estimate of the regression of Y on \mathbf{x} (Lei et al., 2018). This measures the absolute difference between the observed value y and the predicted value $\hat{r}(\mathbf{x})$, indicating how far the actual outcome deviates from the regression prediction and is essentially the regression residual.
- **[Weighted]** $h(\mathbf{x}, y) = \frac{|y - \hat{r}(\mathbf{x})|}{\hat{\rho}(\mathbf{x})}$, where $\hat{\rho}(\mathbf{x})$ is any estimator of the conditional mean absolute deviation of $|Y - \hat{r}(\mathbf{X})||\mathbf{X} = \mathbf{x}$ (Lei et al., 2018). This score normalizes the absolute difference between y and the predicted value $\hat{r}(\mathbf{x})$ by the expected deviation around the prediction, making the non-conformity score relative to the aleatoric variability in the data.
- **[CD-split and variations]** $h(\mathbf{x}, y) = -\hat{f}(y|\mathbf{x})$ (Izbicki et al., 2020; Izbicki et al., 2022; Lei and Wasserman, 2014). This measures the nonconformity via the estimated conditional density of y given \mathbf{x} , meaning a lower density indicates a less likely outcome.
- **[HPD-split]** $h(\mathbf{x}, y) = -\int_{\{y' : \hat{f}(y'|\mathbf{x}) \leq \hat{f}(y|\mathbf{x})\}} \hat{f}(y'|\mathbf{x}) dy'$ (Izbicki et al., 2022). This score quantifies how far y is from the highest density regions by highlighting how unusual y is relative to other possible outcomes and is inspired by FBST's e-value (Pereira and Stern, 1999; Pereira and Stern, 2022).
- **[CQR]** $h(\mathbf{x}, y) = \max\{\hat{q}_{\alpha_1}(\mathbf{x}) - y, y - \hat{q}_{\alpha_2}(\mathbf{x})\}$, where $\hat{q}_{\alpha_1}, \hat{q}_{\alpha_2}$, $\alpha_1 < \alpha_2$, are quantile estimates (Romano et al., 2019). This measures how far y

is from the quantile estimates, capturing how much y deviates from the predicted lower and upper quantile boundaries for \mathbf{x} .

- **[CDF-split]** $h(\mathbf{x}, y) = |\widehat{F}(y|\mathbf{x}) - 1/2|$ where \widehat{F} is a CDF estimate (Chernozhukov et al., 2021). This measures the distance between the CDF value of y and 1/2, indicating how centered y is within the distribution of possible outcomes, with values near 1/2 being more typical.

Note that the non-conformity scores involving conditional densities can also be applied to classification tasks (see Section 5.3.5). For non-conformity scores that handle multivariate responses with mixed data types, refer to Dheur et al. (2024). Additionally, Manokhin (2022) provides a comprehensive list of papers on conformal predictions.

The conformal region has the shape

$$R(\mathbf{x}_{n+1}) = \{y : h(\mathbf{x}_{n+1}, y) \leq t\},$$

which means it consists of all y that are highly conformal to \mathbf{x} . The non-conformity score h determines the shape and properties of the prediction region.

For example, regression-split always leads to homoscedastic intervals centered around $\widehat{r}(\mathbf{x})$,

$$R(\mathbf{x}_{n+1}) = [\widehat{r}(\mathbf{x}_{n+1}) - t, \widehat{r}(\mathbf{x}_{n+1}) + t],$$

while the weighted approach can result in heteroscedastic symmetric intervals,

$$R(\mathbf{x}_{n+1}) = [\widehat{r}(\mathbf{x}_{n+1}) - \widehat{\rho}(\mathbf{x})t, \widehat{r}(\mathbf{x}_{n+1}) + \widehat{\rho}(\mathbf{x})t].$$

On the other hand, using $h(\mathbf{x}, y) = -\widehat{f}(y|\mathbf{x})$ can result in regions that are not necessarily intervals; they can be unions of intervals, for instance. CDF-split leads to prediction intervals around the median of $Y|\mathbf{x}$:

$$R(\mathbf{x}_{n+1}) = [\widehat{F}^{-1}(1/2 - t|\mathbf{x}_{n+1}), \widehat{F}^{-1}(1/2 + t|\mathbf{x}_{n+1})].$$

CQR, meanwhile, results in a calibrated version of quantile-based prediction

5.3. Conformal Regions

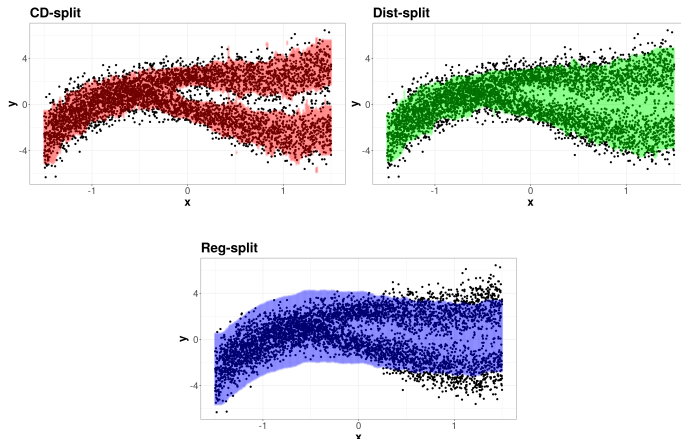


Figure 5.2: Prediction regions given by the following methods: CD-Split, which is based on $\hat{f}(y|\mathbf{x})$ (Izbicki et al., 2020), Dist-split, which is based on $\hat{F}(y|\mathbf{x})$ (Izbicki et al., 2020), and Regression-split, which is based on $\hat{r}(\mathbf{x})$ (Lei et al., 2018).

intervals (Equation 5.3):

$$R(\mathbf{x}_{n+1}) = [\hat{q}_{\alpha_1}(\mathbf{x}_{n+1}) - t, \hat{q}_{\alpha_2}(\mathbf{x}_{n+1}) + t],$$

that is, CQR expands or contracts the plugin regions $[\hat{q}_{\alpha_1}(\mathbf{x}_{n+1}), \hat{q}_{\alpha_2}(\mathbf{x}_{n+1})]$ to achieve the correct coverage. Some examples of prediction regions given by various non-conformity scores are shown in Figure 5.2.

After selecting the non-conformity score, the next step is to determine the cutoff t . The split conformal method proceeds as follows. First, we compute the random variable $U_i := h(\mathbf{X}_i, Y_i)$ for each sample point $(\mathbf{X}_i, Y_i) \in \mathcal{D}_2$. The cutoff t is then set to be

$$t := U_{[1-\alpha]},$$

the $\lceil n(1-\alpha) \rceil$ order statistic among U_1, \dots, U_n .

The next theorem shows that split conformal regions have the right marginal coverage:

Theorem 9. (Lei et al., 2018; Papadopoulos et al., 2002; Vovk, 2012) *If the data is*

i.i.d., the prediction region

$$R(\mathbf{X}_{n+1}) = \{y : h(\mathbf{X}_{n+1}, y) \leq U_{\lceil 1-\alpha \rceil}\}$$

is a marginally valid prediction region, that is,

$$\mathbb{P}(Y_{n+1} \in R(\mathbf{X}_{n+1})) \geq 1 - \alpha.$$

Proof. Because the data is i.i.d., the rank of U_{n+1} is uniform among $\{1, \dots, n+1\}$. It follows that

$$\begin{aligned} \mathbb{P}(Y_{n+1} \in R(\mathbf{X}_{n+1})) &= \mathbb{P}(Y_{n+1} \in \{y : h(\mathbf{X}_{n+1}, y) \leq U_{\lceil 1-\alpha \rceil}\}) \\ &= \mathbb{P}(h(\mathbf{X}_{n+1}, Y_{n+1}) \leq U_{\lceil 1-\alpha \rceil}) = \mathbb{P}(U_{n+1} \leq U_{\lceil 1-\alpha \rceil}) \geq 1 - \alpha. \end{aligned}$$

□

Remarkably, Theorem 9 does not assume that the non-conformity score needs to be correctly specified. For instance, the regression function $r(\mathbf{x})$ does not be well estimated if the score $h(\mathbf{x}, y) = |y - \hat{r}(\mathbf{x})|$ is used: marginal coverage will still be achieved.

If the non-conformity score is continuous, the coverage does not exceed $1 - \alpha$ by too much:

Theorem 10. (Lei et al., 2018) *If the data is i.i.d. and $h(\mathbf{X}, Y)$ is continuous, the prediction region*

$$R(\mathbf{X}_{n+1}) = \{y : h(\mathbf{X}_{n+1}, y) \leq U_{\lceil 1-\alpha \rceil}\}$$

is such that

$$\mathbb{P}(Y_{n+1} \in R(\mathbf{X}_{n+1})) \leq 1 - \alpha + \frac{1}{n+1}.$$

From a computational perspective, after training the non-conformity score, computing prediction bands becomes straightforward. The following R code shows this using the regression-split non-conformity score calculated with a K -Nearest Neighbor approach (Section 2.6.2) with $K = 10$. The conformal calibration of the prediction sets is performed in line 25. The code leads to the estimates shown in Figure 5.3.

5.3. Conformal Regions

```
1 # Load the necessary libraries
2 library(FNN)
3 library(dplyr)
4
5 # Example data
6 n <- 500
7 x <- runif(n)
8 y <- sin(2 * pi * x) + rnorm(n, sd = 0.1)
9 data <- data.frame(x = x, y = y)
10
11 # Split the data into training and calibration sets
12 train_indices <- sample(seq_len(n), size = 0.7 * n)
13 train_data <- data[train_indices, ]
14 calibration_data <- data[-train_indices, ]
15
16 # k-NN regression to define the non-conformity score
17 predictions <- FNN::knn.reg(
18   train = as.matrix(train_data$x),
19   test = as.matrix(calibration_data$x),
20   y = train_data$y, k = 10)
21
22 # Conformal calibration
23 t <- quantile(abs(predictions$pred - calibration_data$y), probs =
24   0.95)
25
26 # Generate a fine grid for the x-axis
27 grid_data <- data.frame(x_grid = seq(min(data$x), max(data$x),
28   length.out = 500))
29
30 # Evaluate predictions on the grid
31 grid_data <- grid_data %>%
32   mutate(y_pred = FNN::knn.reg(
33     train = as.matrix(train_data$x),
34     test = as.matrix(grid_data$x_grid),
35     y = train_data$y,
36     k = 10)$pred)
37
38 # prediction bands are then given by (y_pred-t, y_pred+t)
```

In this example, the marginal coverage of the intervals obtained for the spe-

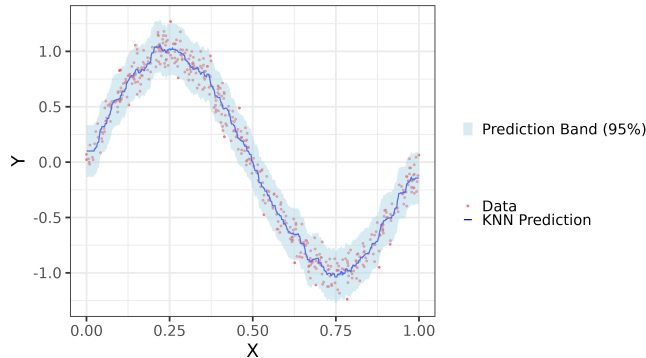


Figure 5.3: Conformal predictions with kNN regression. The light blue shaded area indicates the 95% prediction bands calculated using conformal inference, providing a measure of uncertainty around the predictions.

cific training and calibration data is 97.10% (see the full code at the [Conformal Notebook](#)). Notice that this value does *not* fall below $95\% + 1/(n+1) \approx 95.66\%$, as the upper bound in Theorem 10 seems to suggest. This is because the randomness in the probabilities involved in both Theorems 9 and 10 include the randomness over the calibration data. We discuss this in further details in the next section.

5.3.1 A Different Perspective on Conformal Regions: Tolerance Regions

The highest result of education is tolerance.

Helen Keller

If we examine the derivations of Theorems 9 and 10 more closely, we observe that the probability associated with the marginal coverage in these theorems is integrated over:

- The training sample used to construct the non-conformity score, \mathcal{D}_1 ,
- The calibration sample used to determine the cutoff t , \mathcal{D}_2 ,
- The new data point, $(\mathbf{X}_{n+1}, Y_{n+1})$.

5.3. Conformal Regions

Therefore, the interpretation of Theorem 9 is as follows: if one were to observe an infinite number of training and calibration datasets, and for each dataset assess whether a new observation Y_{n+1} falls within the prediction region $R(\mathbf{X}_{n+1})$, the coverage proportion would be at least $1 - \alpha$.

However, in practice, we have a single train and a single calibration dataset, and therefore ideally one would like to guarantee that $\mathbb{P}(Y_{n+1} \in R(\mathbf{X}_{n+1}) | \mathcal{D}_1, \mathcal{D}_2)$ to be larger than $1 - \alpha$. That is, the coverage probability would ideally be larger than $1 - \alpha$ given the observed data $\mathcal{D}_1, \mathcal{D}_2$. Although this does not hold, the next theorem shows that there is a high probability that the coverage will be large for a fixed $\mathcal{D}_1, \mathcal{D}_2$:

Theorem 11. (*Bian and Barber, 2023; Vovk, 2012*) Let $R(\cdot)$ be a split conformal prediction region with nominal level $1 - \alpha$. If the data is i.i.d., for any $\delta \in (0, 0.5]$,

$$\mathbb{P}\left(\beta(\mathcal{D}_1, \mathcal{D}_2) \geq 1 - \alpha - \sqrt{\frac{\log(1/\delta)}{2n}}\right) \geq 1 - \delta,$$

where $\beta(\mathcal{D}_1, \mathcal{D}_2) = \mathbb{P}(Y_{n+1} \in R(\mathbf{X}_{n+1}) | \mathcal{D}_1, \mathcal{D}_2)$ is the random variable that measures the probability of coverage for a given calibration and training sets, and $n = |\mathcal{D}_2|$ is the size of the calibration set.

Theorem 11 shows that, with high probability, the training and calibration set are such that a split conditional region has with marginal coverage not much smaller than the nominal value $1 - \alpha$. Technically, the split conformal approach leads to $(\alpha + \sqrt{\frac{\log(1/\delta)}{2n}}, \delta)$ -tolerance regions (Fraser and Guttman, 1956; Wilks, 1941). See Hulsman (2022) for additional relationships between tolerance regions and conformal methods.

Figure 5.4 shows, for various values of δ and n , the maximum distance of the true coverage $\beta(\mathcal{D}_1, \mathcal{D}_2)$ to $1 - \alpha$.

Interestingly, Theorem 11 also shows that if a split conformal method is trained with $\alpha' = \alpha - \sqrt{(2n)^{-1} \log(1/\delta)}$, then it will satisfy the stronger condition that

$$\mathbb{P}(\beta(\mathcal{D}_1, \mathcal{D}_2) \geq 1 - \alpha) \geq 1 - \delta.$$

This will of course come at the expense that the prediction regions will be larger.

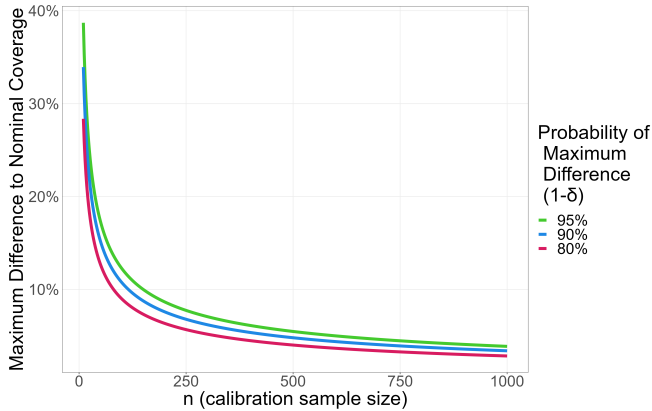


Figure 5.4: Maximum deviation of the nominal coverage $1 - \alpha$ from the true marginal coverage of conformal sets, expressed as a function of the probability δ and the calibration sample size n (see Theorem 11).

Theorem 11 can also be used to determine the size of the calibration set. Specifically, if one desires to have coverage at a distance of at most ϵ from $1 - \alpha$ with probability $1 - \delta$, one should take

$$n = \frac{\log(1/\delta)}{2\epsilon^2}.$$

5.3.2 Comparison to Prediction Sets from Linear Models

Under the standard linear model $Y|\mathbf{x} \sim N(\beta^\top \mathbf{x}, \sigma^2)$ (see Section 3.3) and assuming the data points are i.i.d., the traditional prediction interval for a new sample point \mathbf{x}_{n+1} is given by (Neter et al., 1996):

$$R(\mathbf{x}_{n+1}) = [\hat{r}(\mathbf{x}_{n+1}) - t_l, \hat{r}(\mathbf{x}_{n+1}) + t_l],$$

where $\hat{r}(\mathbf{x}_{n+1}) = \hat{\beta}^\top \mathbf{x}_{n+1}$, with $\hat{\beta}$ being the least squares estimate of β (Equation 2.9). The interval width is given by:

$$t_l(\mathbf{x}_{n+1}) = t_{(1-\alpha/2, n-d-1)} \times \sqrt{\hat{\sigma}^2 (1 + \mathbf{x}_{n+1}^\top (\mathbb{X}^\top \mathbb{X})^{-1} \mathbf{x}_{n+1})},$$

5.3. Conformal Regions

where

$$\hat{\sigma}^2 = \frac{1}{n-d-1} \sum_{i=1}^n \left(y_i - \hat{\beta}^\top \mathbf{x}_i \right)^2.$$

This prediction interval differs from the regression-split conformal interval $R(\mathbf{x}_{n+1}) = [\hat{r}(\mathbf{x}_{n+1}) - t, \hat{r}(\mathbf{x}_{n+1}) + t]$, even when the calibration set is large. Unlike regression-split intervals, which have constant length, the width of the standard linear prediction interval depends on \mathbf{x}_{n+1} through $\mathbf{x}_{n+1}^\top (\mathbb{X}^\top \mathbb{X})^{-1} \mathbf{x}_{n+1}$. The interval is wider for points \mathbf{x}_{n+1} that are farther from the bulk of the training data, which have larger epistemic uncertainty.

For this standard prediction interval to be valid, the assumptions of the linear model must hold. To illustrate this, we run simulations comparing this interval with conformal intervals obtained via regression-split using the same linear model. The full details are shown in the [Linear Prediction Sets Notebook](#).

In the simulations, features are generated as independent draws from a standard normal distribution with mean zero and variance one. Each sample consists of 150 features, and 300 sample points are used to train the linear model via least squares. We use 100 additional sample points to calibrate the conformal intervals.

The simulation scenarios are as follows:

- **Linear Homoskedastic:**

$$y_i = 2 \cdot x_{i,1} + \epsilon_i, \quad \epsilon_i \sim \mathcal{N}(0, \sigma^2),$$

where $\sigma = 0.3$.

- **Linear Heteroskedastic:**

$$y_i = 2 \cdot x_{i,1} + \frac{|x_{i,1}|}{2} \cdot \epsilon_i, \quad \epsilon_i \sim t_2,$$

where t_2 follows a Student's t-distribution with 2 degrees of freedom.

- **Nonlinear Heteroskedastic:**

$$y_i = \sin(5 \cdot x_{i,2}) + \frac{|x_{i,1}|}{2} \cdot \epsilon_i, \quad \epsilon_i \sim t_2.$$

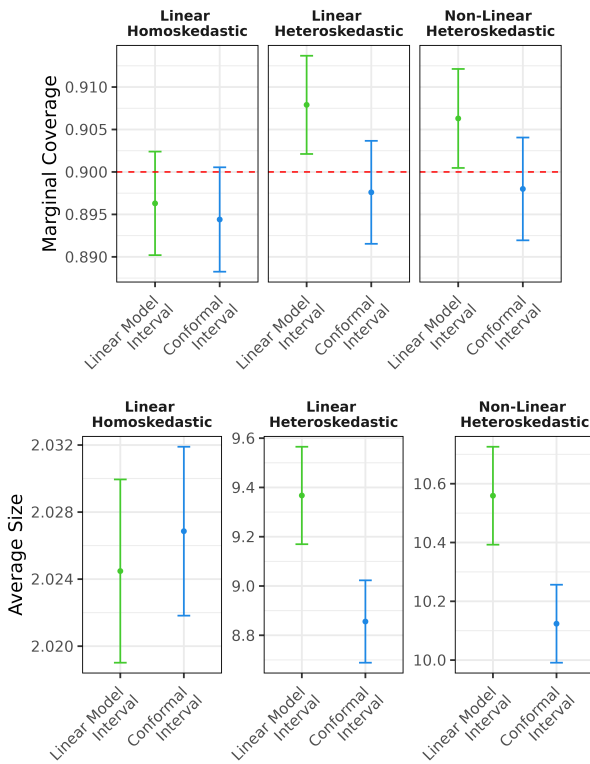


Figure 5.5: Top: Marginal coverage of conformal and linear prediction sets; red dashed line at 90% coverage. Bottom: Average size comparison. Linear models achieve 90% coverage only when specified correctly; conformal methods provide valid coverage even if misspecified.

Figure 5.5 compares the prediction sets from conformal methods and linear models across various data-generating schemes. The top panel shows that while linear models achieve the nominal 90% coverage (indicated by the red dashed line) when correctly specified, they tend to overcover when the model is misspecified. In contrast, conformal methods consistently provide valid coverage in all scenarios. The bottom panel shows that in misspecified settings, the linear model produces larger prediction intervals.

Figure 5.6 displays the fitted prediction intervals for data generated from

5.3. Conformal Regions

the model

$$y_i = \frac{1}{100} \cdot x_i + \epsilon_i, \quad \epsilon_i \sim \mathcal{N}(0, \sigma^2),$$

with $\sigma = 0.3$, as a function of x_i . The intervals derived from the linear model widen in regions with sparse training data, reflecting increased epistemic uncertainty due to a lack of sufficient information. In contrast, the intervals produced by regression-split remain homoscedastic, maintaining a constant width throughout.

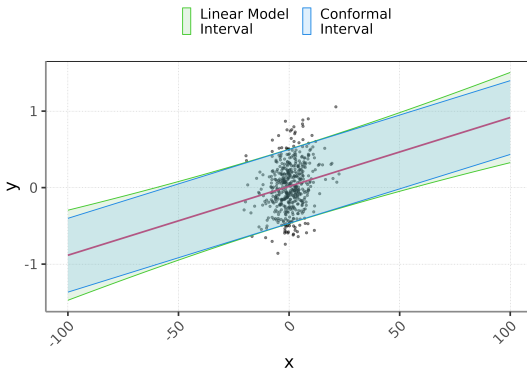


Figure 5.6: Comparison of prediction intervals from the conformal method (blue) and a linear model (green). Black points represent independent test data, and the red line is the least squares fit.

5.3.3 Achieving Asymptotic Conditional Coverage

Conformal methods do not control coverage conditional on \mathbf{x} (Equation 5.1). Indeed, it can be shown that exact conditional validity can be obtained only under strong assumptions about the distribution of (\mathbf{X}, Y) (Foygel Barber et al., 2021; Lei and Wasserman, 2014; Vovk, 2012).

However, under further assumptions about how the non-conformity score is computed, some non-conformity scores lead to prediction regions that also have other good properties such as asymptotic conditional validity. We illustrate this on HPD-split (Izbicki et al., 2022), which uses the non-conformity score

$$h(\mathbf{x}, y) = - \int_{\{y': \hat{f}(y'|\mathbf{x}) \leq \hat{f}(y|\mathbf{x})\}} \hat{f}(y'|\mathbf{x}) dy'.$$

This score is represented by the shaded in Figure 5.7.

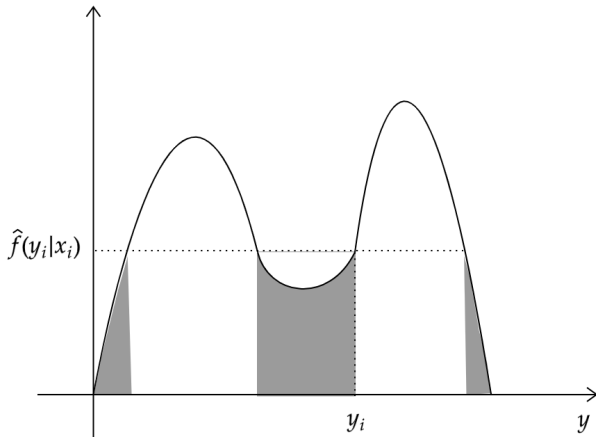


Figure 5.7: The HPD-split score of the sample point (\mathbf{x}_i, y_i) is given by the (negative) of the shaded area on the plot.

First, Y is assumed to belong to a bounded space:

Assumption 4. $Y \in \mathcal{Y}$, where \mathcal{Y} is bounded.

Second, $\hat{f}(y|\mathbf{x})$ is assumed to be consistent:

Assumption 5 (Consistency of \hat{f}). *There exist $\eta_n = o(1)$ and $\rho_n = o(1)$ s.t.*

$$\mathbb{P} \left(\mathbb{E} \left[\sup_{y \in \mathcal{Y}} \left(\hat{f}(y|\mathbf{X}) - f(y|\mathbf{X}) \right)^2 \middle| \hat{f} \right] \geq \eta_n \right) \leq \rho_n$$

Similarly, the conditional cumulative density function of $f(Y|\mathbf{X})$, which we denote by $H(z|\mathbf{x})$, needs to be assumed to be well behaved: it needs to be smooth (bounded density) and have no plateau close the α quantile:

Assumption 6. *For every \mathbf{x} , $H(u|\mathbf{x})$ is continuous, differentiable and $\frac{dH(u|\mathbf{x})}{du} \leq M_1$. Also $\frac{dH(u|\mathbf{x})}{du} \geq M_2 > 0$ in a neighborhood of $q_\alpha(\mathbf{x})$.*

Under the above assumptions HPD-split converges to the $1 - \alpha$ -level HPD Region (Example 5.1) and satisfies asymptotic conditional coverage:

5.3. Conformal Regions

Theorem 12 (Izbicki et al. (2022)). *Under Assumptions 4, 5, 6 and if the the data is i.i.d., the $1 - \alpha$ -level HPD-split region converges to the $1 - \alpha$ -level HPD set and there exist random sets, Λ_n , such that $\mathbb{P}(\mathbf{X}_{n+1} \in \Lambda_n | \Lambda_n) = 1 - o_{\mathbb{P}}(1)$ and*

$$\sup_{\mathbf{x}_{n+1} \in \Lambda_n} |\mathbb{P}(Y_{n+1} \in R(\mathbf{X}_{n+1}) | \mathbf{X}_{n+1} = \mathbf{x}_{n+1}) - (1 - \alpha)| = o(1).$$

Other scores that also satisfy asymptotic conditional validity are CD-split (Izbicki et al., 2020), Dist-Split (Izbicki et al., 2020), and CQR (Romano et al., 2019). Additionally, regression-split satisfies this property under more stringent assumptions, such as the condition that the distribution of $Y - r(\mathbf{X})$ is independent of \mathbf{X} . This assumption is not met for instance in the case of Figure 5.2, where the method undercovers Y for large values of \mathbf{x} .

5.3.3.1 Label-Conditional Conformal Regions

A second, often desired, type of conditional coverage is class-conditional (or label-conditional) coverage, defined as:

$$\mathbb{P}(Y_{n+1} \in R(\mathbf{X}_{n+1}) | Y_{n+1}) \geq 1 - \alpha \text{ (almost surely)}.$$

This criterion ensures that the predictive region $R(\mathbf{X}_{n+1})$ contains the true label with high probability, conditioned on the label itself. Class-conditional coverage becomes especially useful in settings involving dataset shift, where the joint distribution of (\mathbf{X}, Y) differs between the training and target domains (Masserano et al., 2024; Quiñonero-Candela et al., 2022).

In particular, class-conditional coverage is crucial under *prior probability shift*, a specific form of dataset shift where the conditional distribution $\mathbf{X}|Y$ remains stable, but the class prior $\mathbb{P}(Y = y)$ can vary across domains (Assunção et al., 2024; Forman, 2008; Podkopaev and Ramdas, 2021; Vaz et al., 2019). This is because a model trained to satisfy class-conditional coverage on the training set will continue to maintain this coverage in the target set, even when class distributions shift.

An approach to constructing conformal prediction sets that ensure class-conditional coverage in classification problems is to select a distinct conformal cutoff t for each class y (Sadinle et al., 2019; Vovk et al., 2005). Specifically, the

prediction sets take the form

$$R(\mathbf{x}_{n+1}) = \{y : h(\mathbf{x}_{n+1}, y) \leq t_y\},$$

where h is the conformal score function. Similar to the standard split conformal method, we first compute the random variable $U_i := h(\mathbf{X}_i, Y_i)$ for each sample point $(\mathbf{X}_i, Y_i) \in \mathcal{D}_2$. A separate cutoff t_y is determined for each class y by calculating the $1 - \alpha$ quantile of the set $\{U_i : Y_i = y\}$, meaning we only consider the scores of instances with label y .

See Ding et al. (2024) and references therein for other approaches to achieve label-conditional coverage. Also, see Section 5.3.5 for more on conformal methods for classification problems.

5.3.4 Local Conformal Regions

A different approach to get closer to control of conditional coverage is to first create a partition the feature space, say \mathcal{A} , and then apply the split conformal approach to each partition element $A \in \mathcal{A}$ separately (Boström and Johansson, 2020; Boström et al., 2021; Foygel Barber et al., 2021; Izbicki et al., 2022; Lei and Wasserman, 2014; Vovk, 2012). This yields methods that control local coverage, meaning that, for every $A \in \mathcal{A}$,

$$\mathbb{P}(Y_{n+1} \in C(\mathbf{X}_{n+1}) | \mathbf{X}_{n+1} \in A) \geq 1 - \alpha.$$

The choice of \mathcal{A} is crucial to guarantee that

$$\mathbb{P}(Y \in C(\mathbf{X}) | \mathbf{X} \in A) \approx \mathbb{P}(Y \in R(\mathbf{X}) | \mathbf{X} = \mathbf{x}),$$

that is, the local conformal regions $R(\mathbf{X})$ will not only have local coverage but will also be close to conditional coverage.

There are several ways to choose \mathcal{A} . For instance, while Lei and Wasserman, 2014 partitions the feature space by creating a hyper-rectangular mesh, Mondrian-based approaches (Boström and Johansson, 2020; Boström et al., 2021) define a partition with a predefined Mondrian taxonomy (Vovk et al., 2005). Here, we review Locart (Cabezas et al., 2025), which creates \mathcal{A} based on the following theorem:

5.3. Conformal Regions

Theorem 13 (The coarsest partition that controls conditional coverage; adapted from Cabezas et al. 2025). *Let \mathcal{A} be a partition of \mathcal{X} such that, for any $A \in \mathcal{A}$, $\mathbf{x}_1, \mathbf{x}_2 \in A$ if and only if $h(\mathbf{X}, Y) | \mathbf{X} = \mathbf{x}_1 \sim h(\mathbf{X}, Y) | \mathbf{X} = \mathbf{x}_2$, where $h(\mathbf{X}, Y)$ is any non-conformity score. Let $t_{1-\alpha}^*(\mathbf{x})$ be $(1 - \alpha)$ -quantile of the non-conformity scores. Then,*

1. *If $\mathbf{x}_1, \mathbf{x}_2 \in A$, then $t_{1-\alpha}^*(\mathbf{x}_1) = t_{1-\alpha}^*(\mathbf{x}_2)$ for every $\alpha \in (0, 1)$*
2. *If \mathcal{J} is another partition of \mathcal{X} such that, for any $J \in \mathcal{J}$, $\mathbf{x}_1, \mathbf{x}_2 \in J$ implies that $t_{1-\alpha}^*(\mathbf{x}_1) = t_{1-\alpha}^*(\mathbf{x}_2)$ for every $\alpha \in (0, 1)$, then*

$$\mathbf{x}_1, \mathbf{x}_2 \in J \implies \mathbf{x}_1, \mathbf{x}_2 \in A.$$

Cabezas et al. (2025) attempts to recover the partition described in this theorem. The key idea is to use a regression tree, which naturally partitions the feature space. Now, because regression trees are consistent estimators of conditional distributions (Meinshausen and Ridgeway, 2006), a regression tree that predicts the score $h(\mathbf{X}, Y)$ using \mathbf{x} as an input attempts to recover the partition described by Theorem 13, that is, the partition that groups features according to the conditional distribution of the residuals. This is, therefore, how Locart builds the partition \mathcal{A} . Concretely, once the non-conformity score h has been defined, Locart consists of the following steps:

1. Create the dataset $\{(\mathbf{X}_i, h(\mathbf{X}_i, Y_i))\}$ based on the calibration dataset, and split it into two disjoint sets I_{part} and I_{cut} .
2. Fit a regression tree on $\{(\mathbf{X}_i, h(\mathbf{X}_i, Y_i))\}_{i \in I_{\text{part}}}$ that predicts the non-conformity score h based on the features \mathbf{X} . This tree induces a partition \mathcal{A} of the feature space generated by its terminal nodes. Let $\mathcal{T} : \mathcal{X} \rightarrow \mathcal{A}$ be the function mapping an element of \mathcal{X} to the partition element it belongs.
3. Estimate $\hat{t}_{1-\alpha}(\mathbf{x}_{n+1})$ for a new instance \mathbf{x}_{n+1} by applying the conformal approach to all instances in $\{(\mathbf{X}_i, h(\mathbf{X}_i, Y_i))\}_{i \in I_{\text{cut}}}$ that fall into the same element of \mathcal{A} as \mathbf{x}_{n+1} does. That is, estimate $\hat{t}_{1-\alpha}(\mathbf{x}_{n+1})$ as

$$\hat{t}_{1-\alpha}(\mathbf{x}_{n+1}) = \hat{q}_{1-\alpha}(A(\mathbf{x}_{n+1})) \tag{5.4}$$

where

$$A(\mathbf{x}_{n+1}) = \{\hat{s}_i : \mathcal{T}(\mathbf{x}_i) = \mathcal{T}(\mathbf{x}_{n+1}), (\mathbf{X}_i, \hat{s}_i) \in \{(\mathbf{X}_i, \hat{s}_i)\}_{i \in I_{\text{cut}}}\}.$$

4. Using $\hat{t}_{1-\alpha}(\mathbf{x}_{n+1})$ from Equation 5.4, define the Locart prediction interval as

$$R(\mathbf{x}_{n+1}) = \{y : h(\mathbf{x}_{n+1}, y) \leq \hat{t}_{1-\alpha}(\mathbf{x})\}.$$

Cabezas et al. (2025) shows that this approach not only leads to local validity, but that under some assumptions it also satisfies asymptotic conditional validity. The paper also extends Locart to random forests.

5.3.5 Conformal Sets for Classification

In classification tasks, conformal prediction aims to produce sets of labels that include the true label with a predefined probability, $1 - \alpha$ (Angelopoulos et al., n.d.; Valle et al., 2023; Vovk et al., 2005). One of the most intuitive non-conformity scores for classification is based on class probability:

$$h(\mathbf{x}, y) = -\hat{f}(y|\mathbf{x}) = -\hat{\mathbb{P}}(Y = y|\mathbf{x}), \quad (5.5)$$

which serves as the classification analogue to the CD-split score discussed in Section 5.3. While this score ensures marginal coverage, it does not guarantee conditional coverage, even with large sample sizes. This limitation results in undercoverage for more challenging subgroups and overcoverage for easier ones.

A more robust alternative is adaptive prediction sets (APS; Romano et al. 2020), where the non-conformity score is defined as:

$$h(\mathbf{x}, y) = \sum_{y' \in \mathcal{Y}: \hat{\mathbb{P}}(Y = y'|\mathbf{x}) > \hat{\mathbb{P}}(Y = y|\mathbf{x})} \hat{\mathbb{P}}(Y = y'|\mathbf{x}).$$

This score is analogous to the HPD-split non-conformity score used in regression (Section 5.3), but is specifically designed for classification. Similar to the regression version HPD-split (Section 5.3.3), APS also achieves asymptotic conditional coverage.

5.3. Conformal Regions

Next, we apply APS (HPD-Split) and a localized version of the score in Equation 5.5 (CD-Split; see Izbicki et al. 2022 for details) to the MNIST dataset (LeCun et al., 1995). The data is divided into three sets: 9% for potential future samples, 70% for estimating $\mathbb{P}(y|\mathbf{x})$, and 21% for calculating split residuals. The conditional density, $\mathbb{P}(Y = y|\mathbf{x})$, is estimated using a convolutional neural network. Figure 5.8 presents six examples of images and their corresponding prediction sets. The top row displays examples where two labels were assigned to each data point. These cases typically appear ambiguous to humans. Both methods yield similar results.

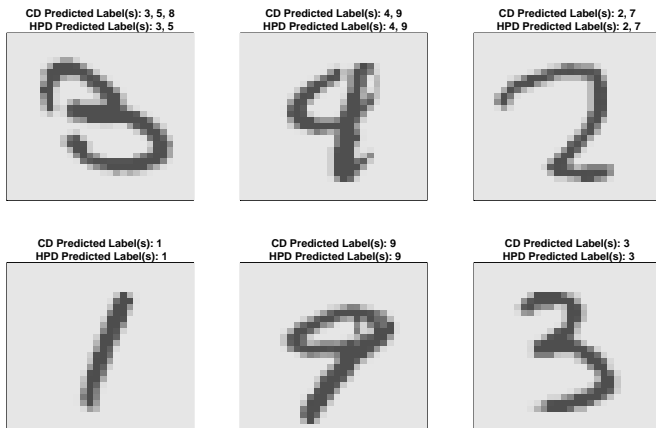


Figure 5.8: Prediction sets generated by CD-Split and APS (HPD-Split) for selected instances from the MNIST dataset.

5.3.6 Example: Photometric Redshift Prediction

We apply conformal methods to a key problem in cosmology: estimating a galaxy's redshift (y), a proxy for its distance from Earth, based on photometric features and r -magnitude (\mathbf{x}) derived from imaging data. Details about this problem can be found in Chapter 7.

Here, we construct prediction bands for redshifts using the Happy A dataset (Beck et al., 2017), specifically designed for comparing photometric redshift prediction algorithms. Happy A contains 74,950 galaxies from the Sloan Digital Sky Survey DR12. Our analysis employs 64,950 galaxies for

training, 5,000 for prediction, and an additional 5,000 for assessing the performance of conformal methods.

Within the training set, we apply random forests to fit the conformity of reg-split (Lei et al., 2018) and quantile-split (Romano et al., 2019). For density-based methods (HPD-split (Izbicki et al., 2022), CD-split+ (Izbicki et al., 2020), and Dist-split (Izbicki et al., 2020)), the non-conformity score is fitted using a Gaussian mixture density neural network (Section 3.5) with three components, one hidden layer, and 500 neurons. Using this mixture model, CD-split and HPD-split generate predictive regions as the union of at most three intervals. All methods adhere to a marginal coverage level of $1 - \alpha = 80\%$.

Table 5.1 details the local coverage and average size of prediction bands in two regions of the feature space: bright galaxies and faint galaxies, classified based on r -magnitude values. While all methods achieve local coverage close to the nominal 80% level for bright galaxies, this is not the case for faint galaxies. Nominal coverage for faint galaxies is only achieved by HPD-split and CD-split+, indicating superior control over conditional coverage in this context. Additionally, the table reveals that, except for reg-split, all methods produce regions of similar size. Reg-split yields smaller regions at the expense of worse local coverage among faint galaxies.

Table 5.1: Coverage and average size of the prediction bands for the photometric redshift prediction problem, along with their standard errors.

	Galaxy	HPD-split	CD-split+	Dist-split	Quantile-split	Reg-split
Coverage	Bright	0.800 (0.006)	0.795 (0.006)	0.802 (0.006)	0.808 (0.006)	0.807 (0.006)
	Faint	0.788 (0.018)	0.792 (0.018)	0.746 (0.019)	0.754 (0.019)	0.658 (0.021)
Average Size	Bright	0.050 (0.001)	0.049 (0.001)	0.050 (0.001)	0.051 (0.001)	0.044 (0.000)
	Faint	0.065 (0.001)	0.066 (0.001)	0.064 (0.002)	0.074 (0.002)	0.045 (0.000)

Figure 5.9 presents examples of the prediction regions for each method, with a horizontal line marking the true redshift for each instance. The size of all prediction regions increases for faint galaxies, which often exhibit multimodal densities (Kügler et al., 2016; Polsterer, 2016; Wittman, 2009). Specifically, in the selected instances of faint galaxies, the true redshift is either near 0.25 or 0.75, but never around 0.5. This multimodal behavior suggests that the central portion of the prediction intervals generated by Dist-split and quantile-split frequently includes unlikely estimates of the true redshift.

5.4. Comparing Linear, Bayesian, Conformal Methods, and Plug-in Approaches

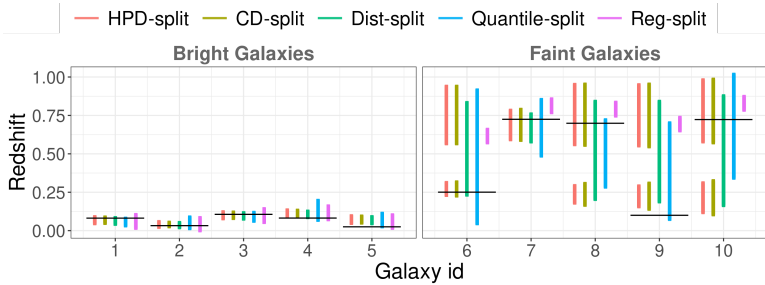


Figure 5.9: Prediction bands obtained for 5 bright and 5 faint galaxies from the test set. Horizontal lines indicate the true redshift of each galaxy.

5.4 Comparing Linear, Bayesian, Conformal Methods, and Plug-in Approaches

In this section, we compare the performance of several methods for constructing prediction intervals, emphasizing the key conceptual differences between them.

The data is generated using a homoscedastic linear Gaussian model, where the response variable y is generated as

$$y = 5x_1 + \epsilon, \quad \epsilon \sim \mathcal{N}(0, 1),$$

where x_1 is the first feature of \mathbf{x} . The features $\mathbf{X} \in \mathbb{R}^{65}$ are i.i.d. $\mathcal{N}(0, 1)$ random variables.

The methods compared are as follows:

- **Linear Model:** A standard linear regression model is fit using ordinary least squares. Prediction intervals are based on the assumption of normally distributed residuals, as detailed in Section 5.3.2.
- **Linear Model with Conformal Prediction:** This method applies the regression-split conformal approach to the predictions of the linear model, yielding prediction sets that provide coverage guarantees without making distributional assumptions.
- **Bayesian Regression (Bayes):** A Bayesian linear regression model is fit with a Gaussian prior on the regression coefficients. Prediction intervals

are derived from the posterior predictive distribution, as described in Section 6.1.

- **Bayesian Regression with Conformal Prediction (Bayes Conformal):** This method incorporates conformal prediction into the Bayesian linear model using the regression-split conformal approach, ensuring valid coverage without distributional assumptions.
- **Plug-in Method:** The plug-in method models $f(y|\mathbf{x})$ as a Gaussian distribution with mean $\hat{\beta}^\top \mathbf{x}$ and variance $\hat{\sigma}^2$, where $\hat{\sigma}^2$ is the maximum likelihood estimate (see Equation 3.5). The prediction interval is then the symmetric plug-in interval based on \hat{f} (Example 5.3).
- **Oracle:** These are the oracle symmetric intervals (see Example 5.3) using the true, but unknown in practice, values of β and σ^2 , assuming that $Y|\mathbf{x} \sim N(\beta^\top \mathbf{x}, \sigma^2)$. In this case, all the oracle regions discussed in Section 5.1 are the same because the Gaussian distribution is symmetric and unimodal.

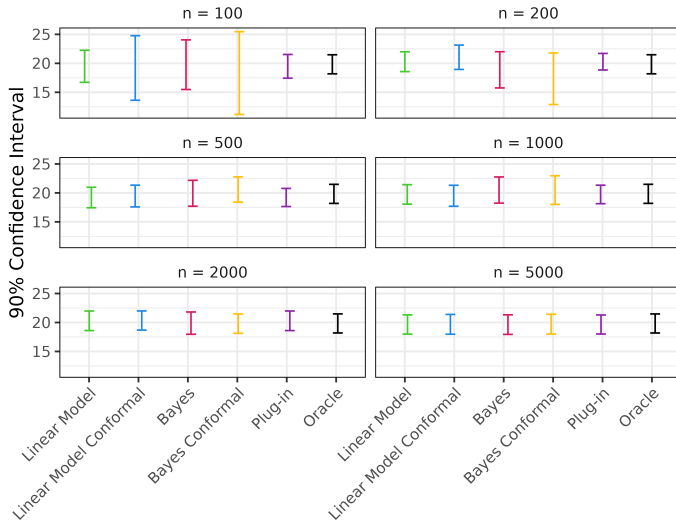
We simulate data with training sample sizes n , and for each sample size, we fit the models mentioned above. The prediction regions are calibrated to have nominal coverage of 90% (for the Bayesian region, we use the coverage according to the predictive distribution). The code is available at the [Predictive Intervals Comparison Notebook](#).

Figure 5.10 displays the prediction intervals for each method across the different training sample sizes for two new data points. When the training sample size is small, methods that account for epistemic uncertainty – namely the conformal intervals, the linear model, and Bayesian predictive sets – produce wider intervals than the oracle, reflecting their ability to capture the additional uncertainty from limited data. In contrast, the plug-in interval attempts to directly emulate the oracle, often showing similar or even narrower widths, but at the cost of reduced coverage, falling below the nominal level. As the sample size increases, all methods gradually converge toward the oracle's prediction intervals. Further insights into the role of the Bayesian predictive distribution in shaping prediction regions can be found in Section 1.2.

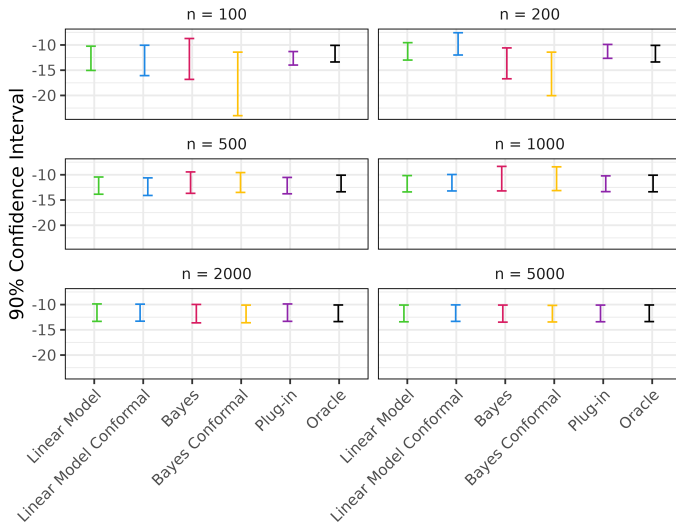
5.5. Summary

5.5 Summary

In this chapter, we explored various techniques for constructing prediction regions for the label of a new sample point. We began by deriving optimal regions according different loss functions, such as the HPD and the quantile-based regions. We then explored how estimates of the conditional density $f(y|\mathbf{x})$ can be directly used to provide an estimate of this optimal sets. These estimated regions however may not have the correct nominal coverage. To address this challenge, we introduced conformal prediction, a framework designed to generate prediction regions with guaranteed marginal coverage, assuming only that data points are exchangeable. We saw that different non-conformity scores yield regions with different properties. In particular some methods are constructed to ensure that, as the sample size increases, they approximate the optimal regions closely. Additionally, we examined conformal methods that are designed to achieve other properties, such as local conditional coverage. We will see another approach to construct prediction bands in Section 6.1.2.



(a) First sample point



(b) Second sample point

Figure 5.10: Prediction intervals for two data points across varying sample sizes. Methods accounting for epistemic uncertainty produce wider intervals for small sample sizes, while all methods converge toward the oracle as sample size increases.

5.5. Summary

Chapter 6

Capturing Epistemic Uncertainty through Bayesian and Ensemble Techniques



La Clairvoyance. René Magritte, 1936, Private Collection.

6.1. Bayesian Models

The greatest obstacle to discovery
is not ignorance – it is the illusion
of knowledge.

Daniel J. Boorstin

In Chapter 3, we explored how aleatoric uncertainty, the inherent variability in outcomes given the same input, can be captured through the conditional density $f(y|\mathbf{x})$, and we discussed several methods for estimating it. While epistemic uncertainty – our uncertainty about the model itself – can sometimes be directly quantified for specific conditional density estimation models like $\hat{f}(y|\mathbf{x})$, these approaches are often complex and difficult to work with (Calonico et al., 2018; Cheng and Chen, 2019). Instead, Chapter 5 shows that we can address epistemic uncertainty by incorporating it into the construction of predictive sets derived from $\hat{f}(y|\mathbf{x})$.

In this chapter, we explore how Bayesian models and ensemble techniques effectively model epistemic uncertainty around Y , offering a structured approach to quantify and incorporate it alongside aleatoric uncertainty. Additionally, we discuss the use of bootstrap techniques to assess epistemic uncertainty from a frequentist perspective.

For a broader overview of other related techniques, see Nemani et al. (2023).

6.1 Bayesian Models

In a Bayesian context, we need additional notation. As in the frequentist setting, the Bayesian model requires a family of distributions that model the aleatoric uncertainty of $Y|\mathbf{x}$. We will denote this class by

$$\mathcal{F} = \{f(y|\mathbf{x}, \theta) : \theta \in \Theta\}.$$

Θ may represent a parametric or a nonparametric space (that is, a space that cannot be mapped to \mathbb{R}^d). Additionally, the Bayesian model also poses a distribution over Θ (or, equivalently, over \mathcal{F}) which is named the *prior distribution*, which for simplicity we assume to have density $f(\theta)$ with respect to some

dominating measure. The prior distribution encodes the epistemic uncertainty about the data generating model.

Let $D = \{(\mathbf{X}_1, Y_1), \dots, (\mathbf{X}_n, Y_n)\}$ be the training data. As in most traditional regression models, in this section we assume that \mathbf{x}_i 's are fixed. Moreover, we assume that, given θ , the data points are independent, and that they all have the same conditional distribution $f(y|\mathbf{x}, \theta)$.

Prediction in Bayesian models is typically obtained by computing the predictive density

$$f(y|\mathbf{x}, D) = \int f(y|\mathbf{x}, D, \theta) f(\theta|\mathbf{x}, D) d\theta, \quad (6.1)$$

where (\mathbf{x}, y) represents a new sample point which we assume to be independent of D (given θ). This predictive distribution incorporates both the aleatoric and the epistemic uncertainty.

Under the assumptions that were made, the above expression can be simplified to

$$f(y|\mathbf{x}, D) = \int f(y|\mathbf{x}, \theta) f(\theta|D) d\theta,$$

$f(\theta|D)$ is the posterior distribution, while $f(y|\mathbf{x}, \theta)$ is simply the model for the aleatoric uncertainty. In words, the Bayesian method weights the different uncertainty models $f(y|\mathbf{x}, \theta)$ according to their posterior evidence $f(\theta|D)$. Thus, the Bayesian model naturally models the epistemic uncertainty, which in this context is the uncertainty regarding the true value of θ^* . For a deeper discussion on how these uncertainties are combined, see Section 6.1.1.

Important Warning! In the Bayesian framework, $f(y|\mathbf{x})$ does not represent the same conditional density discussed in Chapter 3. Instead, it refers to the *a priori* predictive density:

$$f(y|\mathbf{x}) = \int f(y|\mathbf{x}, \theta) f(\theta) d\theta.$$

In this context, the $f(y|\mathbf{x})$ we aim to estimate in Chapter 3 corresponds to $f(y|\mathbf{x}, \theta^*)$, where θ^* represents the true parameter value.

Many of the models that will be introduced in the following sections are

6.1. Bayesian Models

particular cases of the Bayesian approach to uncertainty quantification. We start with a simple example.

Example: Linear Gaussian Regression. To illustrate these principles, we now consider a practical example: the application of Bayesian methods to Gaussian linear regression. In this case, we take \mathcal{F} to represent a Gaussian linear regression model (as in Section 3.3):

$$Y|\mathbf{x}, \boldsymbol{\beta} \sim N(\boldsymbol{\beta}^\top \mathbf{x}, \sigma^2),$$

where for simplicity we assume σ^2 is known. Thus, in this case, $\theta = \boldsymbol{\beta}$. We can use the following prior distribution:

$$\boldsymbol{\beta} \sim N(\mathbf{0}, \Sigma_d),$$

where Σ_d is a $d \times d$ covariance matrix. This leads to the posterior distribution

$$\boldsymbol{\beta}|D \sim N\left(\frac{1}{\sigma^2} \left(\frac{1}{\sigma^2} \mathbb{X}^\top \mathbb{X} + \Sigma_d^{-1}\right)^{-1} \mathbb{X}^\top \mathbb{Y}, \left(\frac{1}{\sigma^2} \mathbb{X}^\top \mathbb{X} + \Sigma_d^{-1}\right)^{-1}\right),$$

where \mathbb{X} and \mathbb{Y} are defined in Section 3.3. Moreover, the predictive distribution, $f(y|\mathbf{x}, D)$, is given by

$$Y|\mathbf{x}, D \sim N\left(\left[\frac{1}{\sigma^2} \left(\frac{1}{\sigma^2} \mathbb{X}^\top \mathbb{X} + \Sigma_d^{-1}\right)^{-1} \mathbb{X}^\top \mathbb{Y}\right]^\top \mathbf{x}, \mathbf{x}^\top \left(\frac{1}{\sigma^2} \mathbb{X}^\top \mathbb{X} + \Sigma_d^{-1}\right)^{-1} \mathbf{x} + \sigma^2\right),$$

Interestingly, this expression reveals that the predictive distribution $Y|\mathbf{x}, D$ is centered around the ridge regression point estimate (discussed in Section 2.6.1), and the predictive variance naturally decomposes into two distinct components. The term $\mathbf{x}^\top \left(\frac{1}{\sigma^2} \mathbb{X}^\top \mathbb{X} + \Sigma_d^{-1}\right)^{-1} \mathbf{x}$ represents the epistemic uncertainty, which arises from our lack of knowledge about the regression coefficients $\boldsymbol{\beta}$. This uncertainty diminishes as we gather more data, making our estimates of $\boldsymbol{\beta}$ more precise. The second term, σ^2 , captures the aleatoric uncertainty, which represents the inherent noise in the data, independent of how well we estimate $\boldsymbol{\beta}$. As the sample size n increases, the epistemic uncertainty

term shrinks to zero, leaving only the aleatoric component. We further explore this in the next section.

6.1.1 Aleatoric vs. Epistemic Uncertainty Revisited

The Bayesian framework offers a clear decomposition of uncertainty into distinct sources. If we quantify a model's uncertainty by its variance, the law of total variance gives the following breakdown:

$$\mathbb{V}[Y|\mathbf{x}, D] = \mathbb{E}_{\theta \sim f(\theta|D)} [\mathbb{V}[Y|\mathbf{x}, \theta]] + \mathbb{V}_{\theta \sim f(\theta|D)} [\mathbb{E}[Y|\mathbf{x}, \theta]]. \quad (6.2)$$

This decomposition shows that the total uncertainty is the sum of the aleatoric uncertainty (the first term on the right-hand side, which represents the average intrinsic variability of the outcome Y) and epistemic uncertainty (the second term, capturing the variation in the prediction due to uncertainty about θ).

As the training sample size increases, the predictive distribution $f(y|\mathbf{x}, D)$ typically converges to the true conditional density $f(y|\mathbf{x}, \theta^*)$ (Schervish, 2012). This happens because, with sufficient data, the uncertainty due to model parameters (epistemic uncertainty) decreases, leaving only the inherent uncertainty of $Y|\mathbf{x}$ (aleatoric uncertainty). Figure 6.1 illustrates this behavior for a Gaussian example. For small sample sizes, $f(y|\mathbf{x}, D)$ is wider than $f(y|\mathbf{x}, \theta^*)$, reflecting greater epistemic uncertainty. However, as the sample size increases, the predictive distribution narrows and approaches the true conditional density, indicating that only aleatoric uncertainty remains. The code to construct this plot is available at the [Bayesian Density Notebook](#).

Since $f(y|\mathbf{x}, D)$ converges to $f(y|\mathbf{x}, \theta^*)$ as n grows, it can be used as an approximation of the true conditional density. This allows prediction regions to be constructed using $f(y|\mathbf{x}, D)$, similar to the oracle regions discussed in Section 5.1. However, these regions are usually wider than the plug-in regions from Section 5.2, as they account for both sources of uncertainty. In contrast, the conditional density estimation techniques described in Chapter 3 capture only aleatoric uncertainty, as seen in the numerical results from Section 5.4.

In the next section, we explore how plug-in regions based on $f(y|\mathbf{x}, D)$ can also be derived from a rigorous Bayesian decision-theoretic perspective.

6.1. Bayesian Models

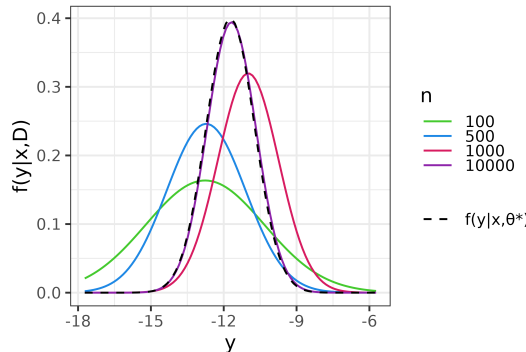


Figure 6.1: Colored lines represent the predictive distribution $f(y|x, D)$ for datasets D with different sample sizes n . The black dashed line is the true distribution $f(y|x, \theta^*)$, where θ^* is the true mean and variance. As n increases, the predictive distribution converges to $f(y|x, \theta^*)$.

6.1.2 Bayesian-Optimal Prediction Regions

The Bayesian framework to statistical inference offers a different approach to construct predictive regions. From a Bayesian decision-theoretic perspective, the Bayes risk of a predictive region R is defined as

$$\mathcal{R}^B(R) := \mathbb{E}[L(R; (\mathbf{X}, Y)) | D, \mathbf{X}].$$

The expectation is taken with respect to the predictive distribution of the new label Y , conditional on its features \mathbf{X} and the entire training set D (see Section 6.1, particularly Equation 6.1, for a detailed explanation of the predictive distribution).

The Bayes-optimal regions – that is, the regions that minimize \mathcal{R}^B – corresponding to the losses discussed in Examples 5.1–5.3 are:

- [HPD Region]

$$R(\mathbf{x}) = \{y \in \mathcal{Y} : f(y|\mathbf{x}, D) > \lambda\},$$

- [Quantile-based Region]

$$R(\mathbf{x}) = (q_{\alpha/2}(\mathbf{x}; D), q_{1-\alpha/2}(\mathbf{x}; D)),$$

where $q_\alpha(\mathbf{x}; D)$ denotes the α quantile of the predictive distribution $Y|\mathbf{x}, D$,

- [Symmetric Region]

$$R(\mathbf{x}) = \mathbb{E}[Y|\mathbf{x}, D] \pm \sqrt{\lambda \mathbb{V}[Y|\mathbf{x}, D]}.$$

In essence, the Bayesian counterpart to oracle prediction sets replaces the unknown quantity $f(y|\mathbf{x})$ with the predictive distribution $f(y|\mathbf{x}, D)$, which is known up to computational considerations. Thus, Bayesian regions can be computed directly. Furthermore, since $f(y|\mathbf{x}, D)$ generally converges to the true conditional density $f(y|\mathbf{x}, \theta^*)$, these regions tend to approach the oracle ones as the sample size grows.

6.2 Gaussian Process Regression

Gaussian processes can be used to describe the epistemic uncertainty about a regression function under a Bayesian framework. They are highly flexible and can be applied to model complex nonlinear regressions. Next, we explore two complementary but equivalent viewpoints on Gaussian processes: the feature space perspective (Section 6.2.1) and the kernel perspective (Section 6.2.2).

6.2.1 Feature Space Perspective

Let $\Phi : \mathbb{R}^d \longrightarrow \mathbb{R}^p$ be a fixed map from the feature space to \mathbb{R}^p . For instance, the map

$$\Phi(\mathbf{x}) = (x_1, \dots, x_d, x_1x_1, x_1x_2, \dots, x_dx_{d-1}, x_dx_d)$$

contains all two-order interactions of the original inputs. Φ is called a *feature map*. In its simplest form, a Gaussian process fits a Bayesian linear regression model (as that described in Section 6.1) to $\Phi(\mathbf{x})$. That is, the model assumes that

$$Y|\mathbf{x}, \boldsymbol{\beta} \sim N(\boldsymbol{\beta}^\top \Phi(\mathbf{x}), \sigma^2)$$

6.2. Gaussian Process Regression

and uses the following prior distribution:

$$\beta \sim N(\mathbf{0}, \Sigma_p),$$

where Σ_p is a $p \times p$ covariance matrix. The computations of the posterior and predictive distributions are the same as those derived for linear regression (Section 6.1), but with \mathbf{x} being replaced by $\Phi(\mathbf{x})$. Other assumptions about the likelihood function can also be made, and σ^2 may also be estimated from data (Gramacy, 2020).

Performing the feature map explicitly, however, can be time and memory-consuming. Fortunately, Gaussian processes can also be implemented using the kernel trick (Theodoridis and Koutroumbas, 2006). We describe this approach in what follows.

6.2.2 Kernel Perspective

Notice that the prior distribution over β 's in the last section induces a distribution over the space of all regression functions. For instance, for any $\mathbf{x}_1, \dots, \mathbf{x}_n$, the properties of the Gaussian distribution imply that the regression function evaluated at those points, $(\beta^\top \Phi(\mathbf{x}_1), \dots, \beta^\top \Phi(\mathbf{x}_n))$, has a multivariate Gaussian distribution *a priori*. The kernel perspective of Gaussian processes builds on this by directly placing a Gaussian distribution in the space of all regression functions.

Concretely, the kernel perspective views a Gaussian process as a distribution over functions (namely, the regression functions). Formally, a Gaussian process is a collection of random variables such that every finite collection of those random variables has a multivariate normal distribution (Williams and Rasmussen, 2006). Here we consider Gaussian processes over \mathcal{H} , the collection of all functions from the original feature space \mathbb{R}^d to \mathbb{R} . In this case, a Gaussian process is a distribution over \mathcal{H} that is uniquely characterized by its mean function, $m(\mathbf{x}) = \mathbb{E}[h(\mathbf{x})]$, and covariance function

$$K(\mathbf{x}, \mathbf{x}') = \mathbb{E} [(h(\mathbf{x}) - m(\mathbf{x})) (h(\mathbf{x}') - m(\mathbf{x}'))],$$

and is denoted by

$$h(\mathbf{x}) \sim \text{GP}(m(\mathbf{x}), K(\mathbf{x}, \mathbf{x}')).$$

If $h(\mathbf{x}) \sim \text{GP}(m(\mathbf{x}), K(\mathbf{x}, \mathbf{x}'))$ then, for any $\mathbf{x}_1, \dots, \mathbf{x}_n$,

$$(h(\mathbf{x}_1), \dots, h(\mathbf{x}_n)) \sim N(\mu, \Sigma),$$

where $\mu = (m(\mathbf{x}_1), \dots, m(\mathbf{x}_n))$ and Σ is a $n \times n$ covariance matrix whose (i, j) entrance is given by $K(\mathbf{x}_i, \mathbf{x}_j)$.

A common choice for the mean function $m(\mathbf{x})$, particularly when the response variable y has been rescaled to have a mean of zero, is the zero mean function, $m(\mathbf{x}) = 0$. For the covariance function, a commonly employed choice is the Gaussian (or Radial Basis Function) kernel, given by:

$$K(\mathbf{x}, \mathbf{x}') = \sigma_K^2 \exp\left(-\frac{\|\mathbf{x} - \mathbf{x}'\|^2}{2l^2}\right),$$

where σ_K^2 is the variance that scales the overall covariance and determines the concentration of the process around $m(\mathbf{x})$, and l is a length scale parameter controlling how quickly the covariance between function values decreases as the distance between input points increases. Figure 6.2 illustrates the effect of the Gaussian process hyperparameters on the shape of sampled functions. The prior variance σ_K^2 controls the concentration of the process around the mean value, while the length scale l determines the smoothness of the functions. Smaller length scales lead to more rapid fluctuations, while larger length scales yield smoother functions.

In the context of regression analysis, a Gaussian process is used to describe the epistemic uncertainty over the collection of regression functions \mathcal{H} by using $\text{GP}(m(\mathbf{x}), K(\mathbf{x}, \mathbf{x}'))$ as a prior distribution over \mathcal{H} . The data consists of the points $(\mathbf{X}_1, Y_1), \dots, (\mathbf{X}_n, Y_n)$, and it is typically assumed that, for each $h \in \mathcal{H}$,

$$Y_i | \mathbf{x}, h \sim N(h(\mathbf{x}_i), \sigma^2)$$

(see Gramacy 2020 for other assumptions and extensions to the case where σ^2 is unknown). This prior is then updated after the data has been observed. It turns out that the posterior distribution is also a Gaussian process, as is the

6.2. Gaussian Process Regression

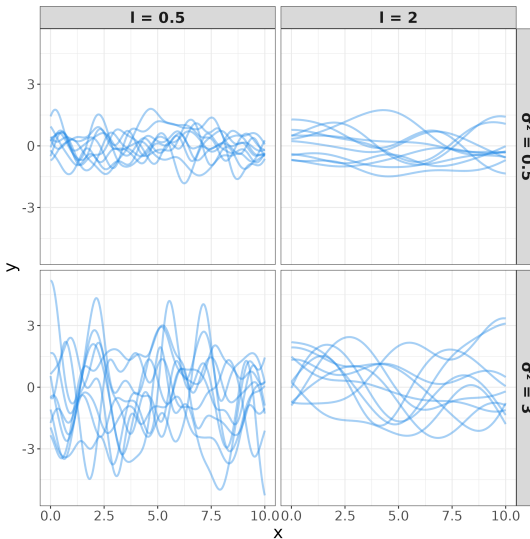


Figure 6.2: Gaussian process samples for different combinations of the prior variance (σ_K^2) and length scale (l) in a Gaussian kernel. Each panel shows ten sample functions generated from a Gaussian process with a zero mean function and a Gaussian covariance kernel.

predictive distribution.

Each kernel corresponds to a different feature space in the formulation of Section 6.2.1. Some of these feature maps may even have infinite components, which would make the perspective in Section 6.2.1 impossible to implement in practice. Indeed, in this case, the approach is fully nonparametric. Also, each feature space corresponds to a different kernel. For more details about this connection, see Williams and Rasmussen (2006).

Figure 6.3 presents a scatter plot of the data, the estimated regression line, the 95% credible interval around $r(\mathbf{x})$ from the posterior distribution $h(\mathbf{x})|\mathbf{x}, D$ (left panel), and the 95% prediction intervals from the predictive distribution of $Y|\mathbf{x}, D$ (right panel) for a simulated example. The code to construct this plot is available at the [Gaussian Process Notebook](#). The intervals widen in areas with less training data, indicating increased (epistemic) uncertainty about the regression function. This is also reflected on the width of the prediction sets.

The choice of prior, determined by the kernel in a Gaussian Process, plays

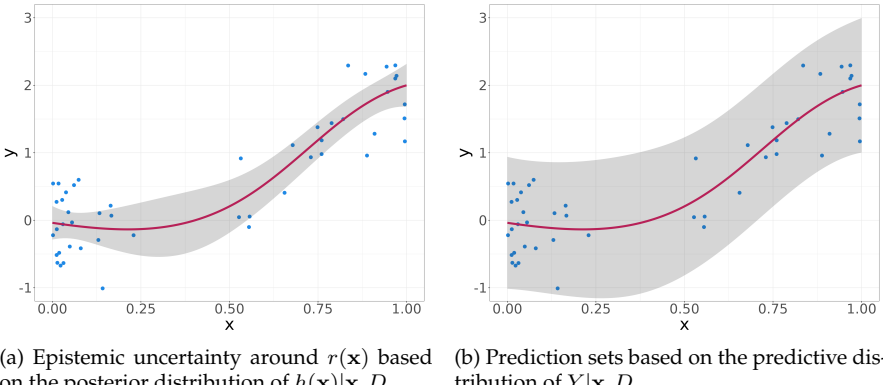


Figure 6.3: Gaussian Process Regression: The plot illustrates the original data points in blue, the estimated regression line in red, and the credible/prediction bands as the shaded area.

a critical role in shaping the regression estimates and the corresponding credible and prediction intervals. Figure 6.4 illustrates how different prior distributions, reflected in the selection of kernel correlation of the Gaussian kernel (determined by l), affect the example in Figure 1.3. The code to construct this plot is available at the [Gaussian Process Kernels](#). A larger correlation, which imposes a stronger smoothness assumption, leads to a smoother regression function that is less responsive to local variations. On the other hand, a smaller correlation, representing a weaker smoothness assumption, results in less smooth regression estimates that can capture more of the local variability in the data, but at the potential cost of overfitting to noise. In practice, hyperparameters from the prior distribution such as the length scale l , prior variance σ_K^2 , and noise variance σ^2 are often estimated using an empirical Bayes approach, where the marginal likelihood of the data (over h), also referred to as Type-II maximum likelihood, is maximized (Williams and Rasmussen, 2006). Concretely, the Type-II log-likelihood is given by

$$\log p(\mathbf{y}|\boldsymbol{\theta}) = -\frac{1}{2}\mathbf{y}^\top (\mathbf{K} + \sigma^2 \mathbf{I})^{-1} \mathbf{y} - \frac{1}{2} \log |\mathbf{K} + \sigma^2 \mathbf{I}| - \frac{n}{2} \log 2\pi,$$

where \mathbf{K} is the covariance matrix on the observed data computed from the

6.2. Gaussian Process Regression

kernel function $K(\mathbf{x}_i, \mathbf{x}_j)$, \mathbf{I} is the $n \times n$ identity matrix, $\mathbf{y} = (y_1, \dots, y_n)$, and θ are the hyperparameters. This likelihood is a function of the hyperparameters θ . By maximizing this log-likelihood, we obtain the Type-II maximum likelihood estimates of the hyperparameters.

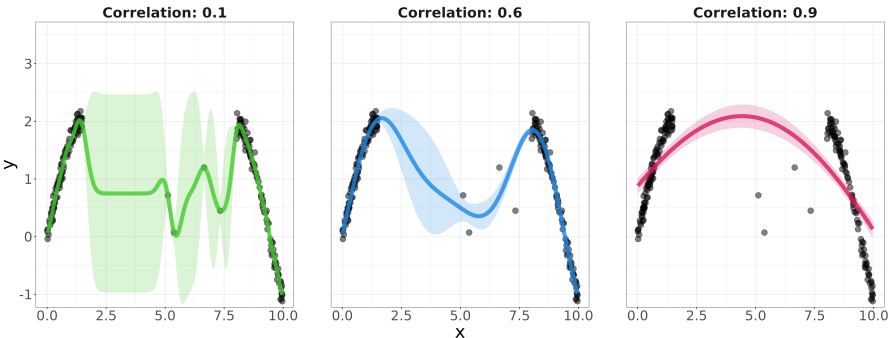


Figure 6.4: Gaussian Process Regression with Varying Bandwidths: The panels compare the predictions from Gaussian process models with different prior assumptions (small, moderate, and large bandwidths l). Shaded areas represent 95% credible intervals for the regression function (that is, the epistemic uncertainty around $r(\mathbf{x})$), illustrating how the prior influences both the flexibility of the model and the uncertainty regions.

Gaussian processes become computationally expensive for large datasets. This is primarily due to the need to invert an $n \times n$ covariance matrix, which requires $\mathcal{O}(n^3)$ time and $\mathcal{O}(n^2)$ memory (Williams and Rasmussen, 2006). However, they can be updated efficiently through rank-one updates, such as the Sherman–Morrison–Woodbury formula (Press, 2007), which avoids the need to recompute the entire inverse covariance matrix. This incremental updating capability makes Gaussian processes well-suited for sequential learning tasks. A key application is *Bayesian optimization*, where the goal is to find the global optimum of an unknown function with minimal evaluations – a topic discussed in the next section.

6.2.3 Bayesian Optimization and Gaussian Processes

Gaussian process regression is not only useful for quantifying aleatoric and epistemic uncertainty in prediction problem, but is also effective for optimiza-

tion problems, particularly in the context of Bayesian optimization. Bayesian optimization is widely used to optimize expensive-to-evaluate functions, common in fields like machine learning and engineering. It is designed to efficiently find the global optimum of functions where gradient-based methods are impractical or infeasible (Frazier, 2018; Gramacy, 2020).

In Bayesian optimization, the objective function is modeled as a Gaussian process prior, allowing us to use uncertainty estimates to guide the search for the optimal solution. This approach balances exploration (sampling where uncertainty is high) and exploitation (sampling where good results are expected based on previous evaluations).

Formally, let $h(\mathbf{x})$ represent the unknown objective function, with noisy observations:

$$Y_i = h(\mathbf{x}_i) + \epsilon,$$

where $\epsilon \sim N(0, \sigma^2)$ represents noise. The goal is to find \mathbf{x}^* that maximizes $h(\mathbf{x})$:

$$\mathbf{x}^* = \arg \max_{\mathbf{x}} h(\mathbf{x}).$$

For instance, in hyperparameter tuning for machine learning models, $h(\mathbf{x})$ could represent the negative mean squared error (MSE) of an XGBoost model, and \mathbf{x} could encode its hyperparameters (e.g., learning rate, tree depth, subsample ratio, and regularization parameters). Bayesian optimization would seek to maximize the negative validation MSE Y_i , an estimate of $h(\mathbf{x})$, while reducing computational cost, as each evaluation of the function requires refitting the XGBoost and is therefore expensive.

Given sequentially collected data $(\mathbf{X}_1, Y_1), \dots, (\mathbf{X}_n, Y_n)$ from previous evaluations of the noisy version $h(\mathbf{x})$, a GP is fitted to estimate the posterior distribution of $h(\mathbf{x})$. Specifically, let $\mu'(\mathbf{x})$ represent the posterior mean and $\sigma'(\mathbf{x})$ represent the posterior standard deviation of $h(\mathbf{x})$, given the observed data. The next point, \mathbf{x}_{next} , is chosen by maximizing an acquisition function that incorporates both the predicted mean and the uncertainty from the GP:

$$\mathbf{x}_{\text{next}} = \arg \max_{\mathbf{x}} \text{Acquisition}(\mathbf{x} | \text{data}).$$

Several acquisition functions are commonly used, including:

6.2. Gaussian Process Regression

- **Probability of Improvement (PI):** PI maximizes the likelihood that the next sampled point improves upon the current best guess of the maximum, $h' = \max_{\mathbf{x}} \mu'(\mathbf{x})$. The improvement at a new point \mathbf{x} is defined as $I(\mathbf{x}) = \max(h(\mathbf{x}) - h', 0)$, capturing the positive difference between the function value at \mathbf{x} and the current best value, or zero if there is no improvement. Since $h(\mathbf{x})$ is unknown, $I(\mathbf{x})$ is treated as a random variable, and the goal is to maximize the probability that it is greater than zero. The PI acquisition function computes the posterior probability that the improvement is positive:

$$\text{PI}(\mathbf{x}) := \mathbb{P}(I(\mathbf{x}) > 0 \mid \text{data}) = \mathbb{P}(h(\mathbf{x}) > h' \mid \text{data}),$$

that is, the probability that $h(\mathbf{x})$ exceeds h' . In standard GPs, this probability has a closed-form solution:

$$\text{PI}(\mathbf{x}) = \Phi\left(\frac{\mu'(\mathbf{x}) - h'}{\sigma'(\mathbf{x})}\right),$$

where Φ is the cumulative distribution function of the normal distribution. For other types of models, this probability can be approximated using Monte Carlo sampling.

- **Expected Improvement (EI):** EI extends PI by accounting for the magnitude of the improvement. It selects points that balance both the probability and size of the improvement:

$$\text{EI}(\mathbf{x}) = \mathbb{E}[I(\mathbf{x}) \mid \text{data}],$$

which, for standard GPs, has the closed form:

$$\text{EI}(\mathbf{x}) = (\mu'(\mathbf{x}) - h')\Phi\left(\frac{\mu'(\mathbf{x}) - h'}{\sigma'(\mathbf{x})}\right) + \sigma'(\mathbf{x})\phi\left(\frac{\mu'(\mathbf{x}) - h'}{\sigma'(\mathbf{x})}\right),$$

where ϕ is the normal PDF.

- **Upper Confidence Bound (UCB):** UCB explicitly balances exploration

and exploitation by selecting points that maximize:

$$\text{UCB}(\mathbf{x}) = \mu'(\mathbf{x}) + \lambda\sigma'(\mathbf{x}),$$

where λ controls the exploration-exploitation trade-off: higher λ encourages exploration, while lower values favor exploitation.

An alternative to the usual acquisition functions introduces a hyperparameter ξ into the improvement formula, allowing finer control over the balance between exploitation and exploration. The modified improvement function is:

$$I(\mathbf{x}; \xi) = \max(h(\mathbf{x}) - h' - \xi, 0),$$

where $\xi \geq 0$. When $\xi = 0$, we recover the original improvement formula. As ξ increases, the algorithm favors exploration by acting as if the current best value is higher than it actually is, encouraging sampling in less-explored regions. This is particularly useful for avoiding local maxima in the objective function h , as it pushes the search towards areas of high uncertainty, rather than solely refining around the current best-known point.

Figure 6.5 shows a GP model approximating a noisy objective function. The GP's posterior mean (red line) approximates the true function (black dashed line) using five blue data points, with the gray region indicating uncertainty. The other subplots visualize three acquisition functions – PI, EI, and UCB – guiding the next evaluation. We use 5 standard deviations in UCB. The location of the observed data points is displayed as vertical lines. Higher acquisition values highlight more promising points. Each function balances exploration and exploitation differently, guiding the optimizer to uncertain areas or near the current maximum. The code to obtain this plot is available at the [Bayesian Optimization Notebook](#).

Next, we sequentially apply Bayesian optimization to maximize the objective function using all the previously discussed acquisition functions – EI, PI, UCB – alongside Random Sampling for comparison. Unlike the other methods, Random Sampling selects points without considering uncertainty or past evaluations. Figure 6.6 shows the best value of the objective function identified at each step. In this case, UCB yields the best performance, while PI struggles, often getting trapped in the suboptimal local maximum of the objective func-

6.3. Bayesian Additive Regression Trees (BART)

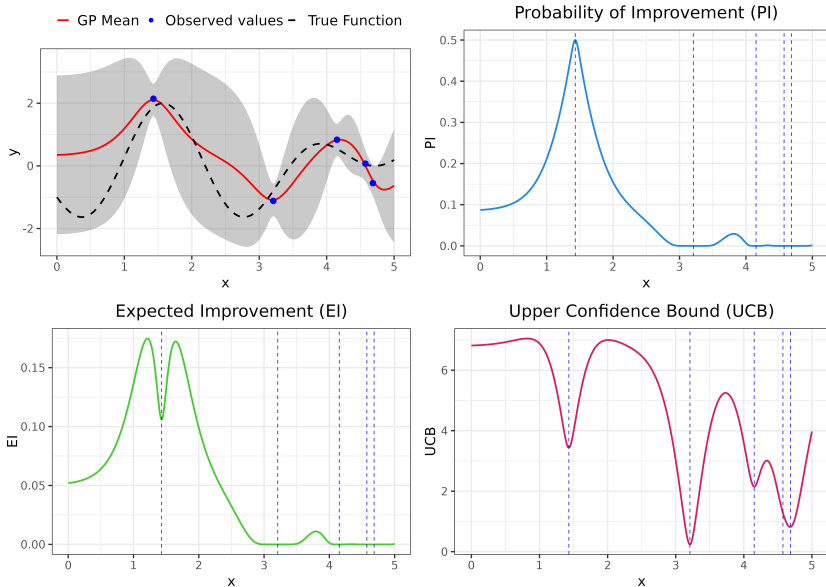


Figure 6.5: Bayesian optimization with Gaussian Processes using three acquisition functions: PI, EI, and UCB. The top-left plot shows the GP posterior mean, uncertainty (gray), true objective (dashed), and observed points (blue). The remaining plots show PI, EI, and UCB guiding the search for the optimum. Vertical lines show the locations of the observed data.

tion. The code used for this analysis can be found in the [Bayesian Optimization Sequence Notebook](#).

6.3 Bayesian Additive Regression Trees (BART)

In its simplest form, BART (Chipman et al., 2012) assumes that

$$Y = h(\mathbf{x}) + \epsilon = \sum_{b=1}^B g_b(\mathbf{x}) + \epsilon,$$

where $\epsilon \sim N(0, \sigma^2)$. Each $g_b(\mathbf{x})$ is assumed to be constant across hyperrectangles defined over the feature space. Specifically, $g_b(\mathbf{x})$ takes the form of a regression tree. Let T_b represent the topology of the regression tree associated

with g_b , and let $\boldsymbol{\mu}_b = \{\mu_{b,1}, \dots, \mu_{b,|T_b|}\}$ be the outputs of this tree associated with each of the $|T_b|$ leaves of T_b . We define

$$g_b(\mathbf{x}) := g(\mathbf{x}; T_b; \boldsymbol{\mu}_b) := \mu_{b,i},$$

where $\mu_{b,i}$ is the output of T_b associated with \mathbf{x} .

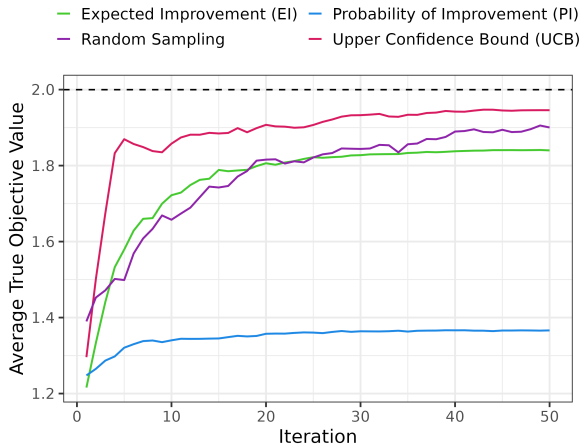


Figure 6.6: Comparison of acquisition functions in Bayesian optimization: EI, PI, UCB, and Random Sampling. The plot shows how performance improves as new data is collected over 50 iterations. The dashed line represents the true maximum of the objective function.

The BART model thus assumes that the regression function is a sum of the outputs of each regression tree,

$$\mathbb{E}[Y|\mathbf{x}] = \sum_{b=1}^B g_b(\mathbf{x}) = \sum_{b=1}^B g(\mathbf{x}; T_b; \boldsymbol{\mu}_b).$$

The parameters of the model are therefore $\theta = (T_1, \boldsymbol{\mu}_1, \dots, T_B, \boldsymbol{\mu}_B, \sigma)$. The prior for θ is chosen such that the following conditional independences hold:

$$f(\theta) = f(\sigma) \prod_{b=1}^B f(T_b) f(\boldsymbol{\mu}_b | T_b),$$

6.3. Bayesian Additive Regression Trees (BART)

and

$$f(\boldsymbol{\mu}_b | T_b) = \prod_{i=1}^{|T_b|} f(\mu_{b,i} | T_b).$$

Each of these components is chosen as follows:

- The prior distribution $f(T_j)$ is defined following Chipman et al. (1998). Concretely, the probability that a node at depth d is not a leaf is given by $\alpha(1+d)^{-\beta}$, where $\alpha \in (0, 1)$ and $\beta \geq 0$ are hyperparameters. Additionally, the prior distribution for selecting the splitting variable at each node is uniform, as is the prior distribution for the threshold used to split that variable.
- The prior distribution for each $\mu_{b,i}$ is assumed to be Gaussian. For details on the selection of its hyperparameters, refer to Chipman et al. (1998).
- The prior distribution for σ^2 is taken to be the inverse chi-square distribution. Again, see Chipman et al. (1998) for guidance on selecting its hyperparameter.

Chipman et al. (2012) shows how MCMC can be performed to sample from the posterior distribution induced by this prior and model.

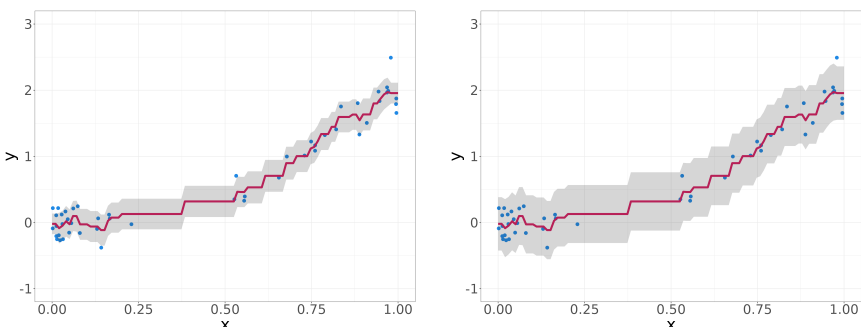


Figure 6.7: Bayesian Additive Regression Trees: The plot illustrates the original data points in blue, the estimated regression line in red, and the credible/prediction bands as the shaded area.

Figure 6.7 presents a scatter plot of the data, the estimated regression line, the 95% credible interval around $r(\mathbf{x})$ from the posterior distribution $f(\mathbf{x})|\mathbf{x}, D$ (left panel), and the 95% prediction intervals from the predictive distribution of $Y|\mathbf{x}, D$ (right panel) for the same simulated example as Figure 6.3. The model was fitted to this data using the *BART* package in R (Sparapani et al., 2021); see the full code at the [BART Notebook](#).

See Hill et al. (2020) and Tan and Roy (2019) and references therein for extensions of this model. These extensions, for instance, allow for different distributions for ϵ .

6.4 Monte Carlo Dropout

Monte Carlo dropout is a technique originally designed to avoid overfitting of a neural network (Srivastava et al., 2014), but that can also be used to measure the uncertainty around point predictions in such networks. This section provides a succinct overview of this technique.

Recall that, in a regression context, a feed-forward neural network outputs an estimate with the shape (Section 2.6.6)

$$g(\mathbf{x}) = a \circ \mathbb{H}_H \dots \tilde{a} \circ \mathbb{H}_1 \cdot \tilde{a} \circ \mathbb{H}_0 \cdot \tilde{\mathbf{x}},$$

where $\tilde{\mathbf{x}} = (1, \mathbf{x})$ and $\tilde{a}(\mathbf{y}) = (1, a(\mathbf{y}))$. In a network with dropout, the output (at training time) is instead given by

$$g(\mathbf{x}) = a \circ \mathbb{H}_H (\mathbf{b}_H \odot \dots \tilde{a} \circ \mathbb{H}_1 \cdot (\mathbf{b}_1 \odot \tilde{a} \circ \mathbb{H}_0 \cdot (\mathbf{b}_0 \odot \tilde{\mathbf{x}}))),$$

where \odot denotes the Hadamard product, and each \mathbf{b}_i is a vector in which the first component is one, and the remaining ones are independent Bernoulli random variables with some predefined parameter p . A different set of \mathbf{b}_i 's is drawn at each training iteration. In words, dropout randomly sets the activation function of each node to be zero with probability p . Intuitively, dropout decreases how much a network depends on each parameter, thus preventing overfitting. Indeed, it can be shown that it effectively performs stochastic gradient descent on a regularized version of the loss function (Wager et al., 2013).

6.4. Monte Carlo Dropout

If used during prediction time, dropout induces a distribution over the possible outputs of a fitted network. This randomness can be used to quantify the uncertainty around the predictions. Specifically, consider a fixed network with estimated parameters $\mathbb{H}_0, \dots, \mathbb{H}_H$. Let θ denote the network parameters that determine its output (that is, the output is a function of \mathbf{x} and θ). The randomness on the Bernoulli random variables in dropout \mathbf{b}_i 's induces a distribution over θ , say $q(\theta)$. It has been shown that, under some conditions, $q(\theta)$ approximates the posterior distribution over θ given by a specific Bayesian deep Gaussian process (Gal and Ghahramani, 2016). More precisely, $q(\theta)$ is the distribution that has smallest Kullback-Leibler divergence to the true posterior $p(\theta|D)$, where D represents the training data, among a specific family of tractable distributions over θ . Thus, if a model for the aleatoric uncertainty, $Y|\mathbf{x}, \theta$, is available, we can approximate the Bayesian predictive distribution via

$$f(y|\mathbf{x}, D) \approx \int f(y|\mathbf{x}, \theta) q(\theta) d\theta.$$

In particular, we can effectively sample from the predictive distribution by:

- (i) Sampling θ from $q(\theta)$. This can be done by using Monte Carlo dropout on the network.
- (ii) Sampling from $Y|\mathbf{x}, \theta$ using the model for the aleatoric uncertainty.

The aleatoric uncertainty can be modeled, for example, using a Gaussian distribution $Y|\mathbf{x} \sim N(\mu(\mathbf{x}), \sigma^2)$, where $\mu(\mathbf{x})$ is estimated by the neural network. The variance σ^2 can either be estimated as a second output of the network or calculated separately. Alternatively, a heteroscedastic model can be used, where the variance depends on the input, $Y|\mathbf{x} \sim N(\mu(\mathbf{x}), \sigma^2(\mathbf{x}))$, with both $\mu(\mathbf{x})$ and $\sigma^2(\mathbf{x})$ estimated by the network.

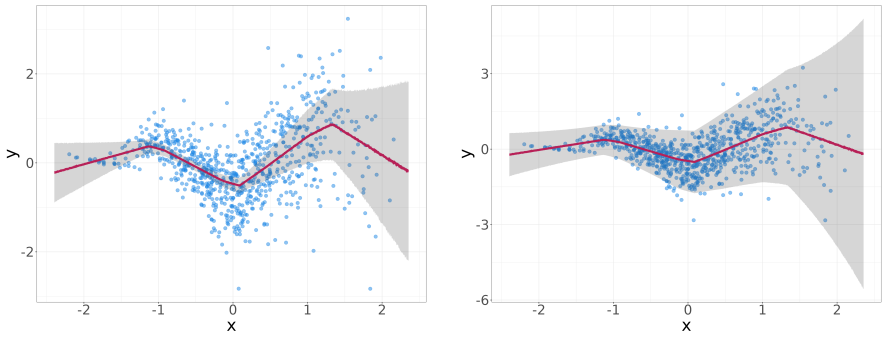
In practice, given a sample of outputs $\theta_1, \dots, \theta_B$ from a dropout network after passing \mathbf{x} through it B times, the aleatoric variance at \mathbf{x} , defined as $\mathbb{E}_{\theta \sim f(\theta|D)} [\mathbb{V}[Y|\mathbf{x}, \theta]]$, can be approximated by:

$$\frac{1}{B} \sum_{b=1}^B \mathbb{V}[Y|\mathbf{x}, \theta_b].$$

Similarly, the epistemic variance, defined as $\mathbb{V}_{\theta \sim f(\theta|D)} [\mathbb{E}[Y|\mathbf{x}, \theta]]$, can be esti-

mated from the variance of the values $\mathbb{E}[Y|\mathbf{x}, \theta_1], \dots, \mathbb{E}[Y|\mathbf{x}, \theta_B]$. Finally, the aleatoric and epistemic variances can be combined using Equation 6.2.

Figure 6.8 shows Monte Carlo dropout results for a neural network regression model on simulated data. The right panel combines total uncertainty (epistemic and aleotoric), while the left focuses on epistemic uncertainty around $\mathbb{E}[Y|\mathbf{x}]$. Scatter points represent observed data, the red line is the estimated regression, and shaded regions indicate 95% uncertainty intervals. Areas with more data have lower epistemic uncertainty. Full code is available in the [Monte Carlo Dropout Notebook](#).



(a) Epistemic uncertainty around the estimated mean (b) Total uncertainty around the predictions of Y

Figure 6.8: Monte Carlo Dropout: The plots illustrate the model predictions with uncertainty bands. The right plot shows total uncertainty (including both aleatoric and epistemic), while the left plot isolates epistemic uncertainty around the regression function. The blue points represent the original data, the red line shows the predicted mean, and the shaded areas represent uncertainty.

See Kendall and Gal (2017) and Valdenegro-Toro and Mori (2022) for variations and further details, and Folgoc et al. (2021) for a critique of this approximation.

6.5 Batch Normalization

Batch normalization, initially devised to make training of neural networks faster and more stable (Ioffe and Szegedy, 2015), has also been discovered

6.6. Deep Ensembles

to serve as an implicit regularizer for standard network solutions (Luo et al., 2018), akin to the effects observed with Monte Carlo dropout (Section 6.4). Moreover, Teye et al. (2018) indicates its utility in quantifying uncertainty surrounding point predictions within these networks. This section shows a concise summary of the technique.

During training, batch normalization renormalizes the input of each node, say h , according to

$$\tilde{h} = \frac{h - \mu_B}{\sigma_B},$$

where μ_B and σ_B represent the mean and standard deviation of the batch size being used, $B \subset \{1, \dots, n\}$. Because the batch being used during training changes, this process induces a randomness in the output of the network. Specifically, let θ denote the network parameters that determine its output (that is, the output is a function of \mathbf{x} and θ). The randomness on B induces a distribution over θ , say $q(\theta)$. It has been shown that, under some conditions, $q(\theta)$ approximates the posterior distribution over θ given by a specific Bayesian process (Teye et al., 2018). More precisely, $q(\theta)$ is the distribution that has smallest Kullback-Leibler divergence to the true posterior $p(\theta|D)$, where D represents the training data, among a specific family of tractable distributions over θ . Thus, as in Monte Carlo dropout, if a model for the aleatoric uncertainty, $Y|\mathbf{x}, \theta$, is available, we can approximate the Bayesian predictive distribution via

$$f(y|\mathbf{x}, D) \approx \int f(y|\mathbf{x}, \theta) q(\theta) d\theta.$$

6.6 Deep Ensembles

Deep ensembles (Lakshminarayanan et al., 2017) are inspired by Random Forests (Section 2.6.3). In this approach, one trains B neural networks that model the aleatoric uncertainty $f(y|\mathbf{x})$. However, instead of training these networks on bootstrap samples of the original dataset, the full dataset is always used. Instead, the initial weights for each network are independently selected at random, and the dataset is randomly shuffled for each training iteration. Moreover, the authors suggest the use of adversarial training to smooth the estimated densities (Goodfellow et al., 2014; Szegedy et al., 2013).

Each network gives a different estimate of $f(y|\mathbf{x})$, say $\hat{f}_b(y|\mathbf{x})$. The estimated distribution that measures both the aleatoric and the epistemic uncertainty is then defined to be the mixture

$$\frac{1}{B} \sum_{b=1}^B \hat{f}_b(y|\mathbf{x}).$$

Hoffmann and Elster (2021) show that this corresponds to an approximation of the Bayesian predictive density $\hat{f}(y|\mathbf{x}, D)$ for a specific prior. See Rahaman et al. (2021) for criticisms to this approach.

6.7 The Bootstrap

Confidence is what you have
before you understand the
problem.

Woody Allen

The bootstrap (Efron and Tibshirani, 1994) is a flexible tool for constructing frequentist confidence sets. In the context of regression models, it can be used to quantify epistemic uncertainty about the regression function. Specifically, for a fixed $\mathbf{x} \in \mathcal{X}$, the goal of the bootstrap is to create an interval, $(L_{\mathbf{x}}(D), U_{\mathbf{x}}(D))$, such that

$$\mathbb{P}(L_{\mathbf{x}}(D) \leq r(\mathbf{x}) \leq U_{\mathbf{x}}(D)) \approx 1 - \alpha,$$

where $D = \{(\mathbf{X}_1, Y_1), \dots, (\mathbf{X}_n, Y_n)\}$ is the training data, and $r(\mathbf{x})$ is the true regression function.

There are several variants of the bootstrap method to achieve this goal (see, e.g., Shalizi 2013; Wasserman 2006 and references therein). A simple version, applicable when a method for estimating $r(\mathbf{x})$ is available, proceeds as follows:

- 1. Resampling:** Generate B bootstrap samples, $D_1^*, D_2^*, \dots, D_B^*$, by randomly sampling with replacement from the original dataset D . Each bootstrap sample D_b^* contains n points.

6.7. The Bootstrap

2. **Estimate the Regression Function:** For each bootstrap sample D_b^* , compute the estimate $\hat{r}_b(x)$ of the regression function using the same method applied to the original data. This results in B estimates: $\hat{r}_1(x), \dots, \hat{r}_B(x)$.
3. **Construct Confidence Intervals:** For each x , construct a confidence interval for $r(x)$ by taking the $\alpha/2$ and $1 - \alpha/2$ quantiles of the distribution of $\hat{r}_b(x)$ across the B bootstrap samples.

In addition to confidence sets, the bootstrap can also be used to create prediction sets by resampling from the original data, as discussed in Davison and Hinkley (1997). This allows for the capture of both aleatoric and epistemic uncertainties. However, the bootstrap requires several assumptions to be valid, and its performance is asymptotic in the sample size n (Hall, 1992).

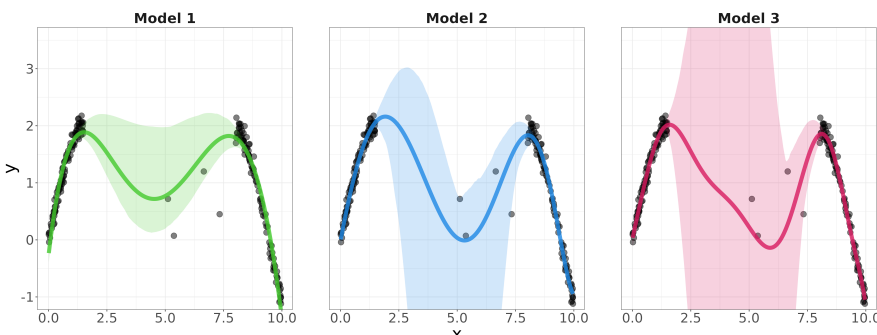


Figure 6.9: Bootstrap predictions for three polynomial regression models. The solid lines represent the mean predicted regression function, while the shaded areas indicate 95% bootstrap confidence intervals. Wider intervals reflect increased epistemic uncertainty, especially in areas with sparse data.

Figure 6.9 shown an application of the bootstrap procedure to construct confidence intervals around a regression function; the code to obtain this plot is available at the [Bootstrap Notebook](#). Three polynomial models (as in Example 2.1), with degrees 5, 8, and 10, were fitted to a dataset containing dense regions at the extremes of the x range and sparse data in the middle. The solid lines represent the predicted mean function for each model, while the shaded areas depict the 95% bootstrap confidence intervals. The varying width of the confidence intervals across the x values illustrates the epistemic

uncertainty captured by the bootstrap – the intervals are wider in regions with sparse data, where uncertainty is higher. Notably, the degree of uncertainty is also influenced by the choice of model, with each polynomial producing different levels of uncertainty.

6.8 Summary

In this chapter, we discussed several techniques for quantifying both aleatoric and epistemic uncertainties in machine learning models.

Bayesian models offer a structured way to incorporate both types of uncertainty through the posterior predictive distribution, $f(y|\mathbf{x}, D)$. We showed that using $f(y|\mathbf{x}, D)$ in oracle sets is sound from a Bayesian decision-theoretic perspective.

We explored different models that produce variations of $f(y|\mathbf{x}, D)$. Gaussian processes provide a flexible, nonparametric approach to capturing uncertainty in complex, nonlinear settings. BART, with its tree-based structure, offers a more interpretable model, making it particularly useful when transparency is important. Techniques like Monte Carlo Dropout and Batch Normalization, initially developed to improve neural network training, repurpose their randomness to estimate uncertainty and approximate Bayesian models. Finally, Deep Ensembles leverage multiple neural networks with random initialization to capture model uncertainty. Finally, bootstrap methods provide a frequentist approach to measuring epistemic uncertainty by refitting models on variations of the original dataset.

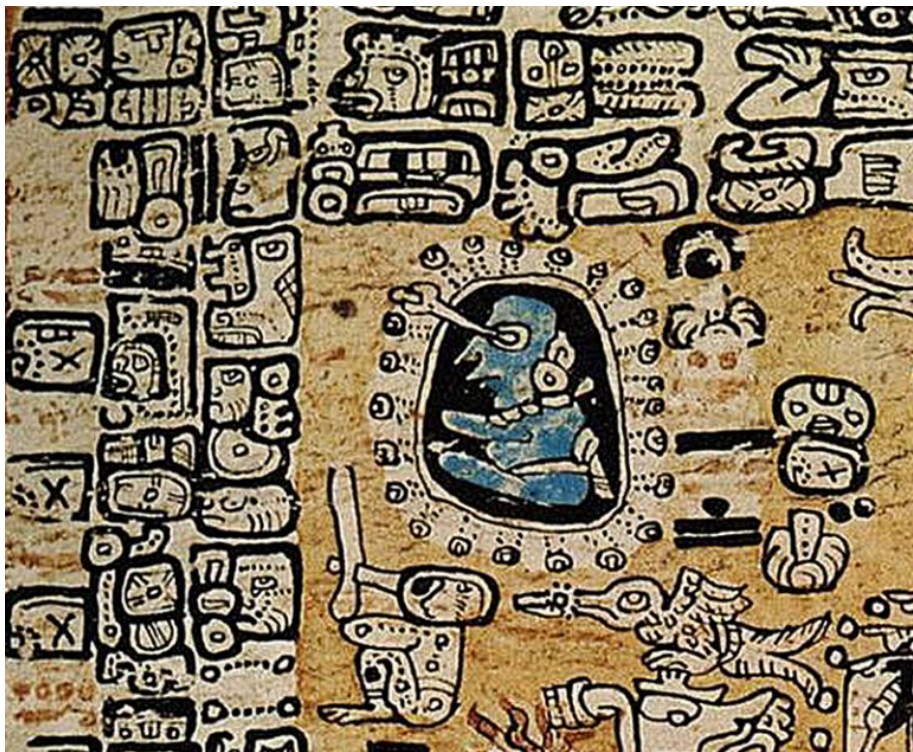
6.8. Summary

Part II

Applications

Chapter 7

Photometric Redshift Prediction



Mayan astronomer depicted in the Madrid Codex, page 34; Mexico, 15th century.

7.1. *Vera C. Rubin Observatory*

To confine our attention to terrestrial matters would be to limit the human spirit.

Stephen Hawking

This chapter provides applications of UQ techniques to the problem of photometric redshift estimation, a crucial task in astrophysics. Redshift, which measures how much the wavelength of light from a galaxy has been stretched due to the expansion of the universe, is essential for determining the distance to galaxies and for inferring cosmological parameters. While spectroscopy provides precise redshift measurements, it is resource-intensive and impractical for large-scale sky surveys. Consequently, photometry is used as a faster alternative. This technique records the radiation from astronomical objects through approximately 5-10 broad-band filters, providing quicker measurements that are less detailed than those obtained from spectroscopy.

In photometric redshift estimation, often referred to as the photo- z problem, the aim is to predict the redshift (y) of an object based on its observed photometric covariates (x), using a dataset of galaxies with spectroscopically confirmed redshifts. Due to degeneracies – where galaxies at different distances have similar photometric colors due to overlapping filter effects – and observational noise, probability densities ($f(y|x)$) are better suited to describe the relationship between x and y than traditional regression ($\mathbb{E}[Y|x]$) (Almosallam et al., 2016; Beck et al., 2016; Benitez, 2000; Dalmasso et al., 2020b; Dey et al., 2021; Malz and Hogg, 2022; Mandelbaum et al., 2008; Zhou et al., 2021).

In Section 7.1 we apply some of the techniques presented in the last chapters to estimate the redshift of galaxies simulated by the photo- z collaboration from the Vera C. Rubin Observatory. Then, in Section 7.2, we predict the redshift from quasars observed by the Southern Photometric Local Universe Survey.

7.1 Vera C. Rubin Observatory

In this section, based on Schmidt et al. (2020), we leverage data generated from the Rubin Observatory’s Legacy Survey of Space and Time (LSST)-Dark

Energy Science Collaboration photo- z data challenge to conduct a comparative analysis of $f(y|x)$ estimates.

For our calibration set, we use the "training set" detailed in Schmidt et al. (2020), comprising approximately 44,000 instances. The Buzzard-highres-v1.0 simulation, based on the Chinchilla-400 N-body dark matter simulation, provides a mock catalogue of 238 million galaxies. Although the redshift range extends from 0 to 8.7, a color correction issue limits it to 0-2.0. The dataset, designed to simulate LSST observations, includes photometry in six bands (ugrizy) with added Gaussian noise. Our test set contains 399,356 galaxies.

Table 7.1 provides an overview of the estimators for $f(y|x)$ that were compared. In this table, *ML* refers to estimators that rely on the training data, while *template* refers to methods that match observed photometry with a set of idealized photometric data for various galaxy types across different redshifts. Template methods are grounded in the underlying physics of the problem, while ML methods solely use the available training data.

Table 7.1: List of conditional density estimators applied to the LSST-DESC Photo-z Data Challenge.

Code	Type	Paper	Website
BPZ	template	Benitez (2000)	http://www.stsci.edu/~dcoe/BPZ/
EAZY	template	Brammer et al. (2008)	https://github.com/gbrammer/eazy-photoz
LePHARE	template	Arnouts et al. (1999)	http://www.cfht.hawaii.edu/~arnouts/lephare.html
ANN22	ML	Sadeh et al. (2016)	https://github.com/IftachSadeh/ANNZ
DELIGHT	ML/template	Leistedt and Hogg (2017)	https://github.com/ixkael/Delight
FLEXZBOOST	ML	Izbicki and Lee (2017)	https://github.com/tospisi/flexcode; https://github.com/lee-group-cmu/FlexCode
GPz	ML	Almosallam et al. (2016)	https://github.com/OxfordML/GPz
METAPHoR	ML	Cavuoti et al. (2017)	http://dame.dsfs.unina.it
CMNN	ML	Graham et al. (2018)	-
Skynet	ML	Graff et al. (2014)	http://ccforge.cse.rl.ac.uk/gf/project/skynet/
TPZ	ML	Carrasco Kind and Brunner (2013)	https://github.com/mgckind/MLZ
TRAINZ	N/A		

TRAINZ provides a simple estimate of the marginal distribution of redshifts, whereas FLEXZBoost represents a specialized adaptation of FlexCode (Section 3.4) designed for this problem. In particular, we employ xgboost (Chen and Guestrin, 2016) as the regression method to estimate the expansion coefficients, leveraging its scalability for large datasets. Additionally, we introduce a tuning parameter to sharpen the density estimates $\hat{f}(y|x)$, modifying them as $\tilde{f}(y|x) \propto \hat{f}(y|x)^\alpha$. FlexCode is particularly interesting for this application because it enables *lossless compression* of photo- z estimates. Specifically, $\tilde{f}(y|x)$ can be reconstructed at any resolution using only the first 35 coefficients of a Fourier

7.1. *Vera C. Rubin Observatory*

basis $\phi_i(y)_i$ for this data. This feature sets it apart from most other estimators, which rely on lossy compression methods, such as binning the redshift space, to store the estimated distributions in photometric dataset catalogs that are used in downstream analyses.

Table 7.2 presents a comparison of the performance of various estimators of $f(y|x)$ using the L^2 loss metric (Section 3.1.1). FLEXZBoost achieves the lowest L^2 loss among the methods evaluated, indicating better performance. As anticipated, TRAINZ exhibits significantly poorer results.

Table 7.2: Comparison with methods benchmarked in the LSST-DESC Photo-z Data Challenge (Schmidt et al., 2020). In terms of L_2 loss, FLEXZBoost has the best performance.

Photo- z Algorithm	L^2 Loss
ANNz2	-6.88
BPZ	-7.82
Delight	-8.33
EAZY	-7.07
FlexZBoost	-10.60
GP z	-9.93
LePhare	-1.66
METAPhOR	-6.28
CMNN	-10.43
SkyNet	-7.89
TPZ	-9.55
trainZ	-0.83

Figure 7.1 shows a comparison of goodness-of-fit diagnostics for the estimated conditional density functions $f(y|x)$ across different models. Each pair of panels provides insights into model calibration and predictive performance. The top panel of each pair combines a Quantile-Quantile (QQ) plot (in red) and a histogram of PIT values (in blue). Although TRAINZ is a naive estimate lacking specific information about individual redshifts, it performs well according to the figure’s metrics, which are widely used in the photo- z literature. This behavior is explained by Theorem 5, as these metrics assess only marginal coverage, and confirms that looking at goodness-of-fit only is not a good strategy to compare estimators. FLEXZBoost also yields descent diagnostics, but in some cases, the PIT values are exactly zero or one, suggesting

that the estimated densities are overly narrow in these instances.

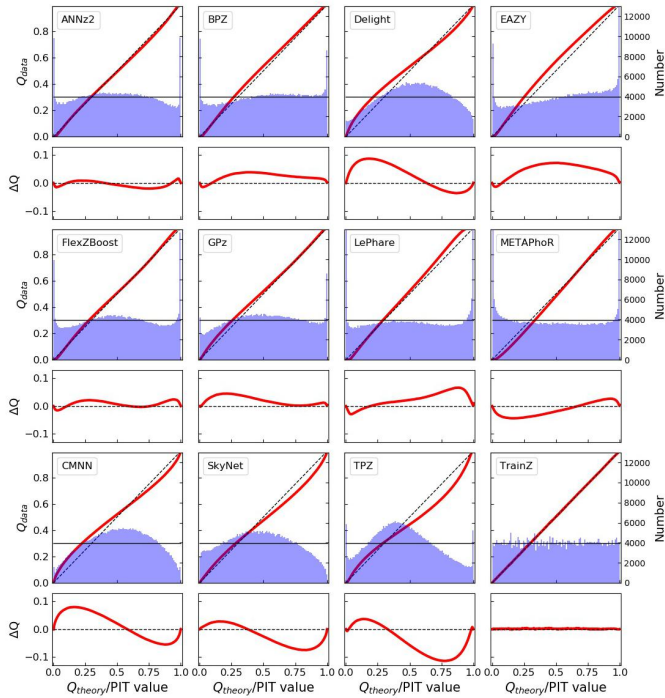


Figure 7.1: Goodness-of-fit for all $f(y|x)$ estimates. The top panel shows the Quantile-Quantile (QQ) plot (red) and PIT histogram (blue). Ideally, the QQ plot aligns with the dashed diagonal, and the PIT histogram matches the uniform distribution (thin black line). The bottom panel highlights deviations of QQ quantiles from the diagonal. Adapted from Schmidt et al. (2020).

7.2 Southern Photometric Local Universe Survey (S-PLUS)

S-PLUS (Southern Photometric Local Universe Survey; Mendes de Oliveira et al. 2019) is an extensive sky survey aiming to cover approximately 9300 square degrees of the Southern Sky using an optical system composed of twelve filters. These filters include five broad bands (ugriz), similar to those

7.2. Southern Photometric Local Universe Survey (S-PLUS)

used in the Sloan Digital Sky Survey (SDSS), as well as seven narrow bands. In addition to its intrinsic data, S-PLUS integrates photometric data from other surveys such as GALEX and WISE, extending the wavelength range and further improving photometric redshift predictions.

In this section, based on Nakazono et al. (2024), we evaluate the value of adding narrow bands to the photometric set of covariates in the prediction of quasar redshifts. Specifically, we compare two sets of features:

- **broad+GALEX+WISE**: $u-r, g-r, r-i, r-z, FUV-r, NUV-r, r-W1, r-W2$
- **broad+GALEX+WISE+narrow**: the above eight broad-band colors extended with the same seven narrow-band colors as in the first case.

We use 33,151 labeled quasars. Further details about the analysis can be found in Nakazono et al. (2024).

We estimate the distribution over redshifts for each quasar using FlexCode (Section 3.4) and a Bayesian Mixture Density Network (BMDN). The latter integrates a Mixture Density Network (Section 3.5) with Bayesian Neural Networks (Bishop, 1997), estimating both epistemic and aleatoric uncertainties.

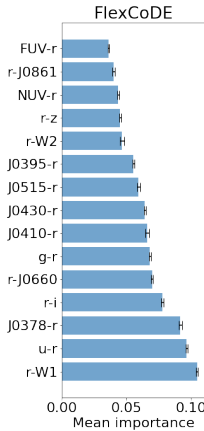


Figure 7.2: Average feature importances for FlexCoDE in the SDSS data.

Figure 7.2 highlights FlexCode’s top features, $r-W1$ and $u-r$, which cap the Spectral Energy Distribution (SED) shape across broad wavelengths. The L_2 loss values for FlexCode are -2.88 (with narrow bands) and -1.32 (without

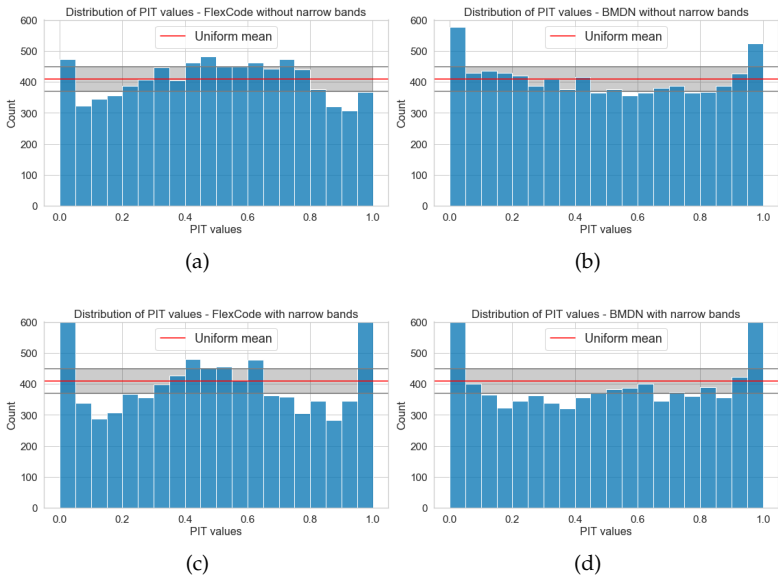


Figure 7.3: PIT distribution for: (a) FlexCode without narrow bands; (b) BMDN without narrow bands; (c) FlexCode with narrow bands; and (d) BMDN with narrow bands. Calibration is indicated by closeness to the uniform distribution (red line).

narrow bands). For BMDN, these values are -2.85 (with narrow bands) and -1.46 (without narrow bands). Thus, narrow bands improve both models. Moreover, the FlexCode model trained with narrow bands produced the best photo-z's PDF, as evidenced by having the lowest L_2 loss.

Figure 7.3 presents PIT histograms (Section 4.1) for BMDN and FlexCode models, trained with and without narrow bands, showing under-dispersed PDFs that suggest room for improvement with alternative methods. Figure 7.4 compares estimated PDFs, highlighting that for $z_{\text{spec}} < 3.5$ and $r < 21.3$, primary peaks align with true redshifts, reflecting the spectroscopic sample. FlexCode yields sharper PDFs with narrow bands, indicating more precise estimates, while BMDN shows improvements for specific cases. For $z > 5$, redshifts are underestimated due to SDSS pipeline errors. SDSS J022737.70-011927.0 exemplifies color-redshift degeneracy, with FlexCode assigning higher probability to the true redshift than BMDN.

7.2. Southern Photometric Local Universe Survey (S-PLUS)

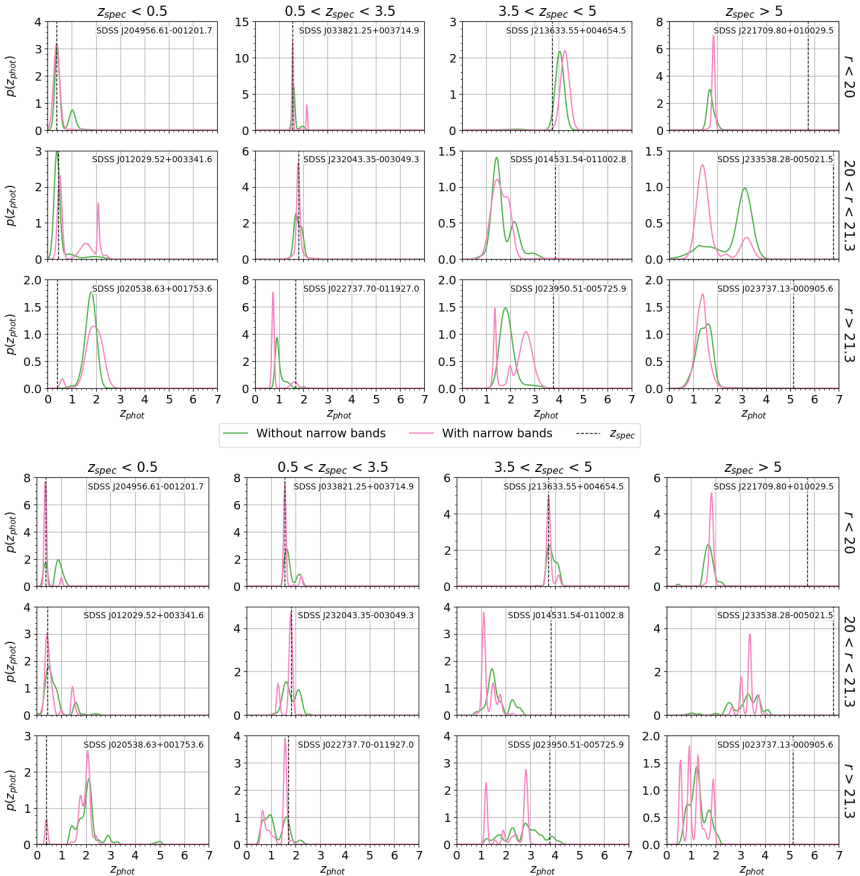


Figure 7.4: Redshift density estimates from BMDN (top) and FlexCode (bottom) for 12 quasars. Dashed lines show spectroscopic redshifts. Green curves use broad+GALEX+WISE; pink include narrow bands.

Chapter 8

Disease Surveillance: Dengue and COVID-19



The Plague of Flies. James Tissot, circa 1896-1902, Jewish Museum, New York.

8.1. Dengue Nowcasting

An ounce of prevention is worth a pound of cure.

Benjamin Franklin

8.1 Dengue Nowcasting

Dengue remains a significant public health challenge, especially in tropical regions where the *Aedes aegypti* mosquito is common. The disease affects millions each year, with symptoms that can range from mild to severe. Since there is no specific treatment for dengue, predicting and managing outbreaks quickly is crucial to reduce its impact on communities (Lancet, 2024).

Traditional dengue surveillance systems are essential but often suffer from delays in reporting, which can slow down the response to outbreaks (Bastos et al., 2019). These delays make it harder for health authorities to act quickly, which is why nowcasting – predicting the current situation using real-time data – is so important. Nowcasting helps provide the most up-to-date information, allowing for better decision-making and more effective control measures.

However, prediction alone is insufficient. Equally important is quantifying the uncertainty in these predictions. This chapter demonstrates how Dengue-tracker (<https://diseasesurveillance.github.io/>) incorporates uncertainty quantification into dengue nowcasting (Xiao et al., 2024). By including UQ, the system not only provides estimates of dengue cases but also prediction bands that indicate the possible range of outcomes. These prediction bands are crucial for helping health authorities assess risks and make informed decisions (Codeço et al., 2016).

8.1.1 Prediction Model

The core idea behind Dengue-tracker is that during a dengue outbreak, the number of searches for dengue-related terms in search engines increases. Thus, we use Google Trends data as covariates to estimate the actual dengue cases, even when official reports are delayed.

To model this relationship, we selected specific search terms that are highly correlated with dengue outbreaks. These terms are "Dengue" and "Sintomas Dengue" (Dengue Symptoms). The choice of these terms was guided by historical analysis, where we observed consistent spikes in search volumes corresponding with reported dengue cases.

Our nowcasting model can be formally described as follows. Let $Y_{l,t}$ represent the count of new dengue cases in location l during week t . Assume we are currently in week $t = t_0$. Due to reporting delays, $Y_{l,t}$ may be unreliable for weeks close to t_0 . To correct these estimates, we assume that $Y_{l,t}$ is reliable for $t \leq t_0 - K$ (where we set $K = 4$ in our case, based on empirical evidence that suggests that most reporting delays typically do not exceed four weeks in most locations).

To predict $Y_{l,t}$ for recent weeks, we utilize Google Trends search data, denoted as $X_{k,l,t}$, where $X_{k,l,t}$ represents the volume of searches on Google Trends for term k in location l and week t . Our model is specified as

$$Y_{l,t} = \beta_{0,l} + \sum_{k=1}^K \beta_{k,l} \cdot X_{k,l,t} + \epsilon_{l,t},$$

where $\epsilon_{l,t}$ is an error term with zero mean and zero variance. This linear model posits that dengue cases in a particular location and week are approximately proportional to the search activity for relevant terms.

To account for regional variations, we fit the model independently for each location l , using all available data up to $t \leq t_0 - K$. We employ standard least squares estimation (Equation 3.4) to obtain the coefficients $\hat{\beta}_{0,l}$ and $\hat{\beta}_{k,l}$, which are then used to predict $Y_{l,t}$ for more recent weeks:

$$Y_{l,t} = \hat{\beta}_{0,l} + \sum_{k=1}^K \hat{\beta}_{k,l} \cdot X_{k,l,t}.$$

8.1.2 Uncertainty Quantification for the Number of Cases

To account for the uncertainty in the predictions provided by the Dengue-tracker, we evaluate three different methods for building 90% prediction intervals:

8.1. Dengue Nowcasting

- **Linear Model:** We use the standard prediction intervals derived from the Gaussian linear model used to generate the point predictions. These intervals are detailed in Section 5.3.2.
- **Linear Quantile Regression:** We apply linear quantile regression (Section 3.9) to model the conditional quantiles of Y_t given X_t . This method estimates the $\alpha/2$ and $1 - \alpha/2$ quantiles of $f(y_t|x_t)$ using all available data up to $t_0 - K$.
- **Conformalized Quantile Regression (CQR):** We enhance the quantile regression approach by applying split-Conformalized Quantile Regression (CQR; Romano et al. 2019). This method uses the conformal score $h(\mathbf{x}, y) = \max\{\hat{q}_{\alpha/2}(\mathbf{x}) - y, y - \hat{q}_{1-\alpha/2}(\mathbf{x})\}$, where $\hat{q}_{\alpha/2}$ and $\hat{q}_{1-\alpha/2}$ are the estimated quantiles. Although CQR is primarily designed for i.i.d. data, split-conformal has shown robust performance in practice, provided that $f(y_t|x_t)$ is stationary and exhibits weak dependence (Oliveira et al., 2024).

8.1.3 Results

The official data used in this analysis comes from the Notifiable Diseases Information System (SINAN; Sistema de Informação de Agravos de Notificação (SINAN) 2024), a critical component of Brazil's public health infrastructure managed by the Brazilian Ministry of Health. SINAN collects, processes, and disseminates data on notifiable diseases, including dengue, across the country. For our analysis, we specifically model state-level data to capture regional variations in dengue incidence. While SINAN provides a comprehensive dataset that is crucial for monitoring disease trends and guiding public health responses, the inherent delays in reporting and data entry can create a lag in the availability of real-time information. This lag highlights the importance of nowcasting techniques to supplement and enhance the insights derived from SINAN data.

Figure 8.1 presents the estimated curves for dengue cases in three Brazilian states: Rio de Janeiro, Pernambuco and São Paulo. We fit a different model independently for each state. Each plot includes the 90% prediction bands obtained via CQR alongside the officially reported case numbers. We compare our approach to InfoDengue, which uses a Bayesian hierarchical model to

nowcast events by analyzing temporal, spatial, and delay-related variability by evaluating weekly updating patterns (Codeço et al., 2016). The results show that the model provides accurate, timely estimates of dengue cases.

Table 8.1: Mean and standard error (in parentheses) of coverage probabilities for different models across Brazilian states. Nominal coverage is 90%.

State	Linear Model	Linear QR	Conformal
AC	0.5 (<0.001)	0.875 (0.006)	0.875 (0.006)
AL	0 (<0.001)	1 (<0.001)	1 (<0.001)
AM	0.751 (0.012)	0.875 (0.006)	0.875 (0.006)
AP	0.25 (<0.001)	0.875 (0.006)	0.875 (0.006)
BA	0.625 (0.006)	1 (<0.001)	1 (<0.001)
BR	0 (<0.001)	1 (<0.001)	1 (<0.001)
CE	0.125 (0.006)	0.125 (0.006)	0.125 (0.006)
DF	0.249 (0.012)	1 (<0.001)	1 (<0.001)
ES	0.125 (0.006)	0.5 (<0.001)	0.5 (<0.001)
GO	0.625 (0.006)	0.75 (<0.001)	0.75 (<0.001)
MA	0.75 (<0.001)	1 (<0.001)	1 (<0.001)
MG	0.625 (0.006)	1 (<0.001)	1 (<0.001)
MS	0.375 (0.006)	0.75 (<0.001)	0.75 (<0.001)
MT	0.375 (0.006)	1 (<0.001)	1 (<0.001)
PA	0.25 (<0.001)	0.875 (0.006)	0.875 (0.006)
PB	0.125 (0.006)	1 (<0.001)	1 (<0.001)
PE	0.125 (0.006)	0.25 (<0.001)	0.25 (<0.001)
PI	0.125 (0.006)	1 (<0.001)	1 (<0.001)
PR	0.875 (0.006)	1 (<0.001)	1 (<0.001)
RJ	0.125 (0.006)	1 (<0.001)	1 (<0.001)
RN	0 (<0.001)	0.25 (<0.001)	0.25 (<0.001)
RO	0.125 (0.006)	1 (<0.001)	1 (<0.001)
RR	0.75 (<0.001)	0.75 (<0.001)	0.75 (<0.001)
RS	0.125 (0.006)	1 (<0.001)	1 (<0.001)
SC	0.625 (0.006)	1 (<0.001)	1 (<0.001)
SE	0.375 (0.006)	1 (<0.001)	1 (<0.001)
SP	0 (<0.001)	1 (<0.001)	1 (<0.001)
TO	1 (<0.001)	1 (<0.001)	1 (<0.001)

Table 8.1 presents the mean and standard error of these coverage probabilities for the three UQ models. The conformal model consistently shows coverage probabilities closer to the nominal 90% value across most states compared to the standard linear model. However, it does not deviate much from

8.1. Dengue Nowcasting

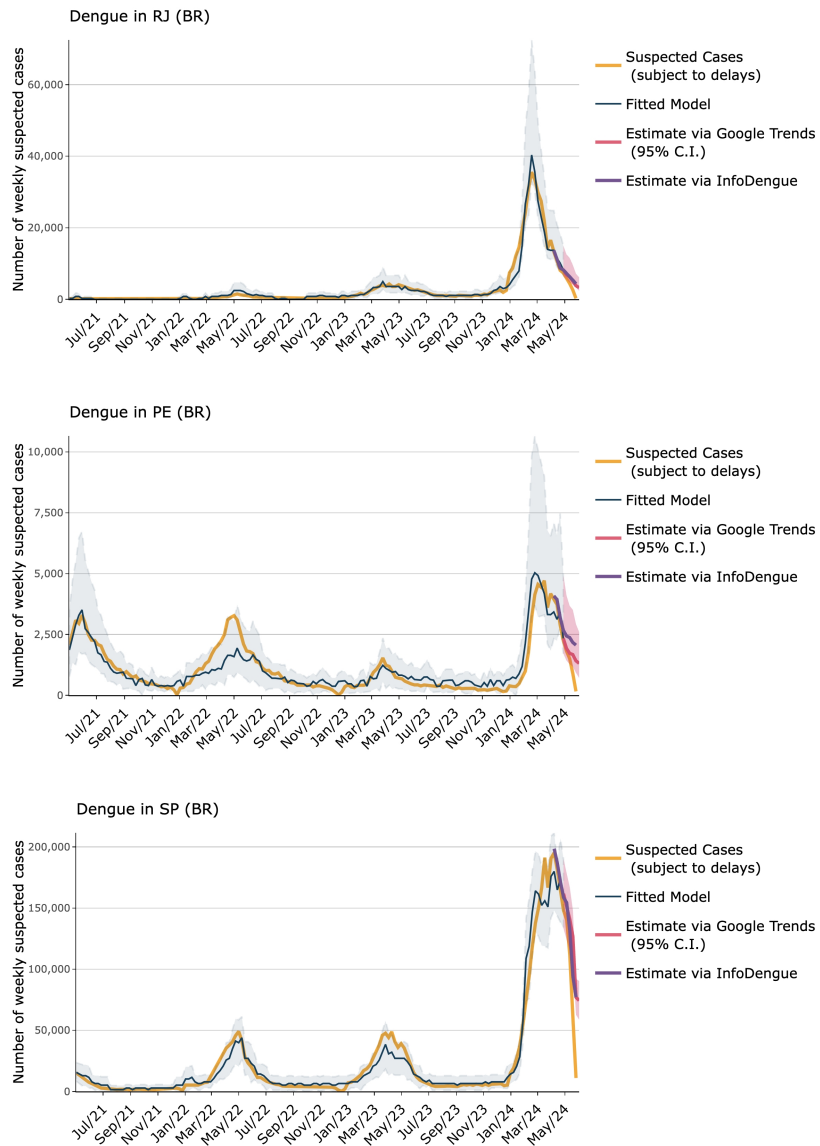


Figure 8.1: Estimated dengue case curves for Rio de Janeiro, Pernambuco and São Paulo. The plots feature 90% prediction bands obtained via CQR and the official reported case numbers, illustrating the model's accuracy in estimating dengue cases without delays.

the quantile regression approach, which already has good coverage. Indeed, in all states the correction factor from CQR was $t < 0.001$, indicating that the prediction sets from CQR and quantile regression are almost identical.

8.2 COVID-19 Hospitalizations and Vaccination Impact

The COVID-19 pandemic overwhelmed healthcare systems globally due to a surge in hospitalizations. Vaccination campaigns, initiated in late 2020, significantly reduced severe cases and hospital admissions. Understanding the scale of this reduction helps quantify the impact of vaccinations on public health. In this section, we use methods similar to those applied in the dengue nowcasting section, to estimate the number of hospitalizations prevented by COVID-19 vaccinations in São Paulo, Brazil, by May 17, 2021.

To carry out this estimation, we used data from the Brazilian Ministry of Health's SIVEP-Gripe database, which tracks severe acute respiratory illness (SARI) cases, including those caused by COVID-19. By constructing a counterfactual model, we aim to predict how many hospitalizations would have occurred in the elderly population (aged 65 and above) if they had not been vaccinated.

8.2.1 Prediction Model for Avoided Hospitalizations

To assess the reduction in hospitalizations due to COVID-19 vaccination, we develop a counterfactual model to estimate what would have occurred if vaccination had not taken place. Specifically, we focused on predicting hospitalizations among the elderly (aged 65 and above) in São Paulo without the vaccine. We follow Izbicki et al. (2021) and use synthetic control methods (Abadie et al., 2010) by modelling the counterfactual using hospitalization data from younger age groups.

Denote by $Y_{t,f}$ the number of hospitalized COVID-19 patients in age group f ($f = 1, \dots, F$) on day t ($t = 1, \dots, T$). The potential outcomes, representing the hypothetical results of different interventions (either receiving the vaccine or not), are denoted by $Y_{t,f}(v)$, where $v = 1$ corresponds to the number of

8.2. COVID-19 Hospitalizations and Vaccination Impact

hospitalizations if that group had been offered the vaccine at time t , and $v = 0$ corresponds to this number if the group had not been offered the vaccine. Note that only one of $Y_{t,f}(0)$ or $Y_{t,f}(1)$ is observed, never both.

We assume that the intervention (the vaccination) for the group of interest (denoted by $f = 1$) took place at time t_0 , while the other groups, $f = 2, \dots, F$ were not offered the vaccine until the study concluded.

Let $\mathbf{Y}_t^{-1}(v) = (Y_{t,2}(v), \dots, Y_{t,F}(v))$. These will be our control groups, as they had not been offered the vaccine at the time this data was collected. In this analysis we assume that

$$Y_{t,f}(0) = \beta_0 + \boldsymbol{\beta}^t \mathbf{Y}_t^{-1}(0) + \epsilon_{t,f}, \quad t = 1, \dots, T \quad (8.1)$$

where $(\epsilon_{t,f})_{t,f} \stackrel{i.i.d.}{\sim} N(0, \sigma^2)$. Since $Y_{t,f} = Y_{t,f}(0)$ for all f and for $t < t_0$ (no group was offered the vaccine before time t_0), Equation 8.1 implies that

$$Y_{t,1} = \beta_0 + \boldsymbol{\beta}^t \mathbf{Y}_t^{-1} + \epsilon_{t,1}, \quad t = 1, \dots, T_0 - 1$$

which suggests that we can estimate the model parameters (β_0 , $\boldsymbol{\beta}$, and σ^2) via ordinary least squares regression using the data collected up to t_0 .

Furthermore, since $Y_{t,f} = Y_{t,f}(0)$ for all $t \geq T_0$ and $f > 1$ (the unvaccinated groups), we observe $Y_{t,f}(1)$ for $t \geq T_0$ and $f > 1$, allowing us to estimate the counterfactual for group 1 as:

$$\hat{Y}_{t,1}(0) := \hat{\beta}_0 + \hat{\boldsymbol{\beta}}^t \mathbf{Y}_t^{-1}(0), \quad t = T_0, \dots, T.$$

Finally, as we observe $Y_{t,1}(1)$ for $t \geq t_0$, we can then estimate the effect of the intervention at each point in time by computing $Y_{t,1}(1) - \hat{Y}_{t,1}(0)$.

This counterfactual analysis relies on three key assumptions:

- If the vaccination campaign had not begun, the relationship between hospitalizations in the elderly and younger groups would have remained consistent after February 8, as it was before that date;
- Vaccination did not have a significant impact on the younger group prior to May 17;
- The linear model provides a reasonable approximation.

For this analysis, we used the population aged 55-62 as the sole control group, as they had not been vaccinated during the study period and exhibited similar behavioral patterns to the elderly. Moreover, we take t_0 to be February 8, 2021, which is when the vaccination campaign started in Brazil.

To quantify uncertainty, we constructed 90% prediction intervals for the counterfactual hospitalizations using linear regression, quantile regression, and conformalized quantile regression, as described in Section 8.1.2.

8.2.2 Results

Figure 8.2 shows the observed number of hospitalizations, the counterfactual curve predicting hospitalizations if vaccination had not started, and the 90% prediction intervals for the counterfactual model, derived using three uncertainty quantification methods. The vertical lines indicate the start of vaccination for different age groups. The observed data consistently falls below the counterfactual predictions, suggesting that the vaccination campaign significantly reduced hospitalizations. Moreover, all UQ methods yield similar prediction regions. A closer inspect shows that the correction factor from CQR was $t < 0.001$, indicating that the prediction sets from CQR and quantile regression are almost identical.

The most pronounced difference between observed and counterfactual hospitalization rates occurred on May 17, 2021, with a reduction of approximately 60.0% (95% CI: 57.1%, 62.2% for the linear prediction sets; similar results were obtained with other methods). By analyzing the area under the curves, we estimate that vaccination prevented around 18,000 hospitalizations in São Paulo by that date. Given the 45% mortality rate for hospitalized individuals over 65 years old with Sars Covid-19 in the region, this likely saved about 8,100 lives. Additionally, considering hospitalization costs estimated in Miethke-Morais et al. (2020), approximately US\$220 million was saved – enough to cover the purchase of 22 million COVID-19 vaccine doses at US\$10 per dose.

8.2. COVID-19 Hospitalizations and Vaccination Impact

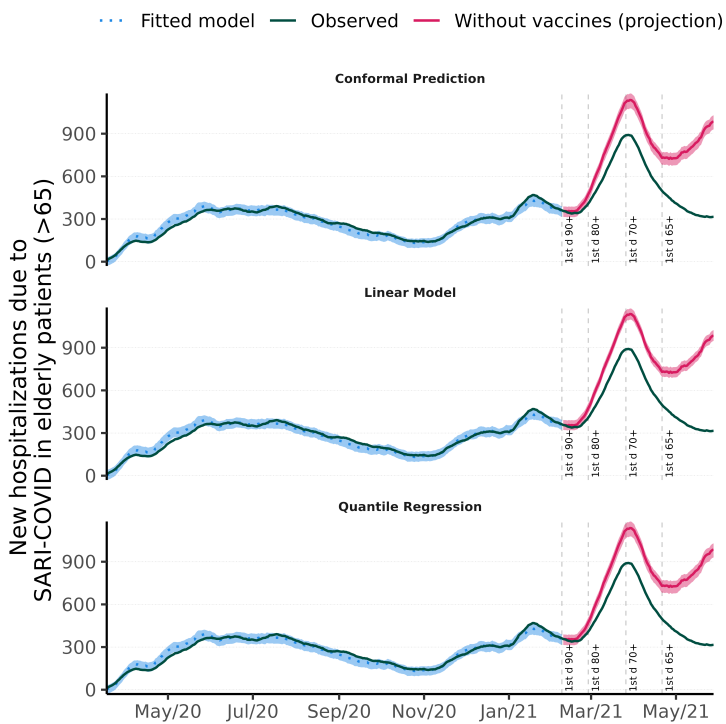


Figure 8.2: Number of hospitalizations due to SARI-COVID in elderly patients (dark green), fitted pre-vaccination model (blue) and estimated counterfactual curve for the setting without vaccines (red). The plot compared various methods for obtaining 90% prediction bands.

Chapter 9

Likelihood-Free Inference (LFI)



Las Meninas. Diego Velázquez, 1656, Museo del Prado, Madrid.

Truth is much too complicated to
allow anything but
approximations.

John von Neumann

In many statistical inference problems within the sciences, establishing the relationship between the parameters of interest and observable data is often complicated. However, it is often feasible to create computational forward models that simulate realistic data. These models take the parameters values θ as inputs, and output observable data x from that model at θ . Examples of this occur in genetics (Beaumont, 2010; Estoup et al., 2012), astronomy (Cameron and Pettitt, 2012; Ho et al., 2019; Weyant et al., 2013), high-energy physics (Kieseler et al., 2022), and many other science fields. In such scenarios, the complexity of the data generation process often hinders the derivation of an analytically precise form for the likelihood function. Thus, one cannot use standard Bayesian or frequentist tools as no tractable form for the posterior distribution or the likelihood function is available.

These challenges have sparked a recent surge in interest in "likelihood-free inference" methods, often called Simulation-Based Inference (SBI), or Simulator-Based Inference. This category includes approaches such as "Approximate Bayesian Computation" (ABC) (Marin et al., 2012; Marin et al., 2016), amortized likelihood estimators (Fasiolo et al., 2018; Gutmann and Corander, 2016; Izbicki et al., 2014; Järvenpää et al., 2021; Lueckmann et al., 2019; Papamakarios et al., 2019; Picchini et al., 2020; Wood, 2010), and amortized posterior estimators (Greenberg et al., 2019a; Lueckmann et al., 2017; Papamakarios and Murray, 2016). See Cranmer et al. (2020) for an overview.

We begin by describing the approach introduced by Izbicki et al. (2019), which leverages conditional density estimators (CDEs) to estimate posterior distributions (Section 9.1). This discussion highlights the utility of this approach and outlines the necessary adaptations for naive CDEs. While the emphasis is on FlexCode, the concepts and methods discussed are broadly applicable to any CDE. Then, we discuss the LF2I (Likelihood-Free Frequentist Inference) framework introduced by Dalmasso et al. (2020a) and Dalmasso

et al. (2024) (Section 9.3).

In this chapter, we assume we have a parametric model F_θ , $\theta \in \Theta$, that models observable data $\mathbf{X} \in \mathcal{X}$, that is, $\mathbf{X} \sim F_\theta$. Our goal is to recover θ that generated the true observed data \mathbf{x}_o . We assume we are able to generate from F_θ for any given θ , even if the likelihood function induced by F_θ is not analytically tractable. We assume Θ is continuous, even though several of the methods discussed here can be used if it is discrete.

9.1 Approximate Bayesian Computation via Conditional Density Estimation (ABC-CDE)

Given a prior distribution over Θ , $f(\theta)$, the posterior distribution $f(\theta|\mathbf{x})$ is simply the conditional density of θ on \mathbf{x} . Examining LFI through a conditional density estimation framework provides a systematic approach to tackle the following three challenges:

- (i) how to efficiently estimate the posterior density $f(\theta|\mathbf{x}_o)$, where \mathbf{x}_o is the observed sample; in particular, in settings with complex, high-dimensional data and costly simulations,
- (ii) selecting appropriate tuning parameters and evaluating the performance of ABC and related methods solely based on simulations and observed data; that is, without knowing the true posterior distribution, and
- (iii) how to best choose summary statistics for ABC and related methods when given a very large number of candidate summary statistics.

9.1.1 Estimating the Posterior Density via CDE

One way to estimate $f(\theta|\mathbf{x}_o)$ via CDE methods is to generate an i.i.d. sample $\mathcal{T} = \{(\theta_i, \mathbf{x}_i)\}$ by sampling $\theta \sim f(\theta)$ and then $\mathbf{x} \sim f(\mathbf{x}|\theta)$ for each pair. Applying the chosen CDE method to \mathcal{T} yields an estimated density $\hat{f}(\theta|\mathbf{x})$. However, this naive approach may yield suboptimal results because some \mathbf{x} values are distant from the observed data \mathbf{x}_o . In ABC applications, the focus is often solely on estimating $f(\theta|\mathbf{x})$ for \mathbf{x}_o , not all possible \mathbf{x} .

9.1. Approximate Bayesian Computation via Conditional Density Estimation (ABC-CDE)

In these cases, one can instead estimate $f(\theta|x)$ by training on a set \mathcal{T} comprising samples x near x_o . This training set is created by using a basic ABC rejection sampling algorithm (see Algorithm 1) with a fixed distance function $d(x, x_o)$ (possibly based on summary statistics) and tolerance level ϵ .

Algorithm 1: Training set for CDE via Rejection ABC

Input: Tolerance level ϵ , number of desired samples B , distance function d , sample x_0
Output: Training set \mathcal{T} which approximates the joint distribution of (θ, \mathbf{X}) in a neighborhood of x_0

```

 $\mathcal{T} \leftarrow \{\};$ 
while  $|\mathcal{T}| < B$  do
    Sample  $\theta \sim f(\theta);$ 
    Sample  $x \sim f(x|\theta);$ 
    if  $d(x, x_0) < \epsilon$  then
         $\mathcal{T} \leftarrow \mathcal{T} \cup \{(\theta, x)\};$ 
    end
end
return  $\mathcal{T};$ 

```

We use our conditional density estimator on the new training set \mathcal{T} and evaluate it at $x = x_o$. This acts as an ABC post-processing step (Marin et al., 2012): the initial ABC posterior approximation comes from the sample $\theta_1, \dots, \theta_B$ (approximating $f(\theta|d(\mathbf{X}, x_o) < \epsilon)$). We then refine this by estimating the conditional density at $x = x_o$.

In what follows, we assume for simplicity that we are interested in estimating the posterior distribution of a single parameter $\theta \in \mathbb{R}$, even if there are several parameters in the problem.¹

9.1.2 Method Selection: Comparing Different Estimators of the Posterior

Surrogate Loss. Ultimately, we need to be able to decide which approach is best for approximating $f(\theta|x_o)$ without knowledge of the true posterior.

¹Most inference problems can be expressed as the computation of unidimensional quantities. Say one is interested in estimating m functions of parameters of the model θ , g_1, \dots, g_m . One can then (i) use ABC to obtain a single simulation set $\mathcal{T} = \{(\theta_1, \mathbf{x}_1), \dots, (\theta_B, \mathbf{x}_B)\}$ (ii) for each function g_i , compute $\mathcal{T}^{g_i} = \{(g_i(\theta_1), \mathbf{x}_1), \dots, (g_i(\theta_B), \mathbf{x}_B)\}$, and (iii) fit a (univariate) conditional density estimator to \mathcal{T}^{g_i} to estimate $f(g_i(\theta)|x_o)$.

Ideally, we seek an estimator $\hat{f}(\theta|\mathbf{x}_o)$ minimizing the L_2 loss at \mathbf{x}_o :

$$L_{\mathbf{x}_o}(\hat{f}, f) = \int (\hat{f}(\theta|\mathbf{x}_o) - f(\theta|\mathbf{x}_o))^2 d\theta. \quad (9.1)$$

However, since $L_{\mathbf{x}_o}$ relies on the true $f(\theta|\mathbf{x}_o)$, which is unknown, method selection becomes challenging. To address this, we instead use a *surrogate* loss function:

$$L_{\mathbf{x}_o}^\epsilon(\hat{f}, f) = \int \int (\hat{f}(\theta|\mathbf{x}) - f(\theta|\mathbf{x}))^2 \frac{f(\mathbf{x}) \mathbb{I}(d(\mathbf{x}, \mathbf{x}_o) < \epsilon)}{\mathbb{P}(d(\mathbf{X}, \mathbf{x}_o) < \epsilon)} d\theta d\mathbf{x},$$

This surrogate loss ensures a close fit within an ϵ -neighborhood of \mathbf{x}_o . The denominator $\mathbb{P}(d(\mathbf{X}, \mathbf{x}_o) < \epsilon)$ is the constant that makes $\frac{f(\mathbf{x}) \mathbb{I}(d(\mathbf{x}, \mathbf{x}_o) < \epsilon)}{\mathbb{P}(d(\mathbf{X}, \mathbf{x}_o) < \epsilon)}$ a proper density in \mathbf{x} .

The advantage of the above definition is that we can directly *estimate* $L_{\mathbf{x}_o}^\epsilon(\hat{f}, f)$ from the ABC posterior sample. Indeed, $L_{\mathbf{x}_o}^\epsilon(\hat{f}, f)$ can be written as

$$\mathbb{E}_{\mathbf{X}'} \left[\int \hat{f}^2(\theta|\mathbf{X}') d\theta \right] - 2\mathbb{E}_{(\theta', \mathbf{X}')} \left[\hat{f}(\theta'|\mathbf{X}') \right] + K_f, \quad (9.2)$$

where (θ', \mathbf{X}') is a random vector with distribution induced by a sample generated according to the ABC rejection procedure in Algorithm 1; and K_f is a constant that does not depend on the estimator $\hat{f}(\theta|\mathbf{x}_o)$. Thus, given a sample of size B' of the ABC algorithm, $(\theta'_1, \mathbf{x}'_1), \dots, (\theta'_B, \mathbf{x}'_B)$, we can estimate $L_{\mathbf{x}_o}^\epsilon(\hat{f}, f)$ (up to the constant K_f) via

$$\hat{L}_{\mathbf{x}_o}^\epsilon(\hat{f}, f) = \frac{1}{B'} \sum_{k=1}^{B'} \int \hat{f}^2(\theta|\mathbf{x}'_k) d\theta - 2 \frac{1}{B'} \sum_{k=1}^{B'} \hat{f}(\theta'_k|\mathbf{x}'_k). \quad (9.3)$$

When given a set of estimators $\mathcal{F} = \{\hat{f}_1, \dots, \hat{f}_m\}$, we select the method with the smallest estimated surrogate loss,

$$\hat{f} := \arg \min_{\hat{f} \in \mathcal{F}} \hat{L}_{\mathbf{x}_o}^\epsilon(\hat{f}, f).$$

Next, we investigate the conditions under which the estimated surrogate loss is close to the true loss; the proofs for all results can be found in Izbicki

9.1. Approximate Bayesian Computation via Conditional Density Estimation (ABC-CDE)

et al. (2019).

The following theorem states that, if $(\hat{f}(\theta|\mathbf{x}) - f(\theta|\mathbf{x}))^2$ is a smooth function of \mathbf{x} , then the (exact) surrogate loss $L_{\mathbf{x}_o}^\epsilon$ is close to $L_{\mathbf{x}_o}$ for small values of ϵ .

Theorem 14. Assume that, for every $\theta \in \Theta$, $g_\theta(\mathbf{x}) := (\hat{f}(\theta|\mathbf{x}) - f(\theta|\mathbf{x}))^2$ satisfies the Hölder condition of order β with a constant K_θ ² such that $K_H := \int K_\theta d\theta < \infty$. Then $|L_{\mathbf{x}_o}^\epsilon(\hat{f}, f) - L_{\mathbf{x}_o}(\hat{f}, f)| \leq K_H \epsilon^\beta = O(\epsilon^\beta)$.

The next theorem shows that the estimator $\hat{L}_{\mathbf{x}_o}^\epsilon$ in Equation 9.3 does indeed converge to the true loss $L_{\mathbf{x}_o}(\hat{f}, f)$.

Theorem 15. Let K_f be as in Equation 9.2. Under the assumptions of Theorem 14, $|\hat{L}_{\mathbf{x}_o}^\epsilon(\hat{f}, f) + K_f - L_{\mathbf{x}_o}(\hat{f}, f)| = O(\epsilon^\beta) + O_P(1/\sqrt{B'})$.

Under some additional conditions, it is also possible to guarantee that not only the estimated surrogate loss is close to the true loss, but that the result holds uniformly for a finite class of estimators of the posterior distribution. This is formally stated in the following theorem.

Theorem 16. Let $\mathcal{F} = \{\hat{f}_1, \dots, \hat{f}_m\}$ be a set of estimators of $f(\theta|\mathbf{x}_o)$. Assume there exists M such that $|\hat{f}_i(\theta|\mathbf{x})| \leq M$ for every \mathbf{x}, θ , and $i = 1, \dots, m$.³ Moreover, assume that for every $\theta \in \Theta$, $g_{i,\theta}(\mathbf{x}) := (\hat{f}_i(\theta|\mathbf{x}) - f(\theta|\mathbf{x}))^2$ satisfies the Hölder condition of order β with constants K_θ such that $K_H := \int K_\theta d\theta < \infty$. Then, for every $\nu > 0$,

$$\mathbb{P}\left(\max_{\hat{f} \in \mathcal{F}} |\hat{L}_{\mathbf{x}_o}^\epsilon(\hat{f}, f) + K_f - L_{\mathbf{x}_o}(\hat{f}, f)| \geq K_\epsilon \epsilon^\beta + \nu\right) \leq 2me^{-\frac{B'\nu^2}{2(M^2+2M)^2}}.$$

Finally, the next corollary shows that the procedure we propose in this section, with high probability, picks an estimate of the posterior density that has a true loss that is close to the true loss of the best method in \mathcal{F} .

Corollary 2. Let $\hat{f}^* := \arg \min_{\hat{f} \in \mathcal{F}} \hat{L}_{\mathbf{x}_o}^\epsilon(\hat{f}, f)$ be the best estimator in \mathcal{F} according to the estimated surrogate loss, and let $f^* = \arg \min_{\hat{f} \in \mathcal{F}} L_{\mathbf{x}_o}(\hat{f}, f)$ be the best estimator in \mathcal{F} according to the true loss. Then, under the assumptions from Theorem 16, with probability at least $1 - 2me^{-\frac{B'\nu^2}{2(M^2+2M)^2}}$, $L_{\mathbf{x}_o}(\hat{f}^*, f) \leq L_{\mathbf{x}_o}(f^*, f) + 2(K_H \epsilon^\beta + \nu)$.

²That is, there exists a constant K_θ such that for every $\mathbf{x}, \mathbf{y} \in \mathbb{R}^d$ $|g_\theta(\mathbf{x}) - g_\theta(\mathbf{y})| \leq K_\theta(d(\mathbf{x}, \mathbf{y}))^\beta$.

³Such assumptions hold if the \hat{f}_i 's are obtained via FlexCode with bounded basis functions (e.g., Fourier basis) or a kernel density estimator on the ABC samples.

9.1.3 Summary Statistics Selection

In a standard ABC framework, the variable \mathbf{x} does not represent the raw data but instead consists of many summary statistics. Using all these statistics together can be difficult, especially when some of them provide little useful information about the model parameters (Blum, 2010).

We can use FlexCode (Section 3.4) as a method for either (i) directly estimating $f(\theta|\mathbf{x}_o)$ in scenarios involving a large number of summary statistics, or (ii) assigning an importance measure to each summary statistic. This measure can then be employed for variable selection in Approximate Bayesian Computation (ABC) and related procedures.

Two versions of FlexCode are especially useful for these purposes: FlexCode-SAM⁴ and FlexCode-RF⁵. These versions of FlexCode can adapt dynamically to the number of relevant covariates. As a result, both FlexCode-SAM and FlexCode-RF can automatically identify the important summary statistics needed to estimate the posterior distribution of θ . This removes the need for manual pre-selection of summary statistics, as FlexCode-SAM and FlexCode-RF automatically discard irrelevant covariates.

In a broader context, FlexCode offers a tool for calculating an importance measure for summary statistics, applicable not only within the FlexCode framework but also in other procedures. In the context of LFI, one can infer the relevance of the j -th summary statistic *in posterior estimation* from its relevance in estimating the I first *regression* functions in FlexCode (recall Section 3.4.2) – even if we do not use FlexCode for estimating the posterior using the technique discussed in Equation 3.9. We can use these values to select variables for estimating $f(\theta|\mathbf{x}_o)$ via other ABC methods. For example, one approach is to choose all summary statistics such that $u_j > t$, where the threshold value t is defined by the user.

⁴FlexCode with expansion coefficients estimated through Sparse Additive Models (Ravikumar et al., 2009).

⁵FlexCode with expansion coefficients estimated via Random Forests.

9.2. Examples

9.2 Examples

9.2.1 Examples with Known Posteriors

We begin with examples featuring well-known and computable posterior distributions:

1. Mean of Gaussian with Known Variance: $X_1, \dots, X_{20} | \mu \stackrel{iid}{\sim} \mathcal{N}(\mu, 1)$, $\mu \sim \mathcal{N}(0, \sigma_0^2)$. Experiments are repeated for σ_0 in a grid of ten values from 0.5 to 100.

2. Precision of Gaussian with Unknown Precision: $X_1, \dots, X_{20} | (\mu, \tau) \stackrel{iid}{\sim} \mathcal{N}(\mu, 1/\tau)$, $(\mu, \tau) \sim \text{Normal-Gamma}(0, 1, \alpha_0, \beta_0)$. Experiments are conducted with α_0 and β_0 to ensure $\mathbb{E}[\tau] = 1$ and $\sqrt{\mathbb{V}[\tau]}$ spans a grid of ten values from 0.1 to 5.

In these examples, observed data \mathbf{x}_o are drawn from a $N(0, 1)$ distribution. We run each experiment 200 times, that is, with 200 different values of \mathbf{x}_o . The training set \mathcal{T} , which is used to build conditional density estimators, is constructed according to Algorithm 1 with $B = 10,000$ and a tolerance level ϵ that corresponds to an acceptance rate of 1%. For the distance function $d(\mathbf{x}, \mathbf{x}_o)$, we choose the Euclidean distance between minimal sufficient statistics normalized to have mean zero and variance 1; these statistics are \bar{x} for scenario 1 and (\bar{x}, s) for scenario 2.

We compare the following methods:

- ABC: Utilizing the rejection ABC method with minimal sufficient statistics. This involves applying a kernel density estimator to the θ coordinate of \mathcal{T} , with the bandwidth determined through cross-validation.
- FlexCode_Raw-NN* Employing the FlexCode estimator with Nearest Neighbors regression.
- FlexCode_Raw-Series: Utilizing the FlexCode estimator with Spectral Series regression as described by (Lee and Izbicki, 2016).
- FlexCode_Raw-RF: Applying the FlexCode estimator with Random Forest regression.

The three FlexCode estimators (indicated by "Raw") are directly applied to the sorted values of the original covariates $X_{(1)}, \dots, X_{(20)}$, without using minimal sufficient statistics or other summary statistics. To evaluate the performance of each method, we calculate the true loss $L_{\mathbf{x}_o}$ for each \mathbf{x}_o . Additionally, we estimate the surrogate loss $L_{\mathbf{x}_o}^\epsilon$ using Equation 9.3 with an additional sample of size $B' = 10,000$ from Algorithm 1.

9.2.1.1 CDE and Method Selection

Figures 9.1 and 9.2,(left) show the effectiveness of methods in estimating posterior density for Settings 1-2. Panels (a) show the proportion of instances where each method yields optimal results based on true loss from Equation 9.1. Generally, FlexCode-based methods outperform ABC, especially with larger prior variances. FlexCode with Nearest Neighbors regression excels in this context, while FlexCode with expansion coefficients via Spectral Series regression is also competitive, as supported by Panels (c) displaying average true loss with standard errors.

Figures 9.1 and 9.2, right, summarizes our method selection algorithm's performance. Panels (b) show the agreement between the true loss $L_{\mathbf{x}_o}(\hat{f}, f)$ and the estimated loss (Equation 9.3) in method selection. Two algorithm variations are presented: one including all data (triangles) and another excluding cases with inconclusive confidence intervals (circles). The baseline represents random method selection. The plots consistently show similar conclusions between true and estimated losses. Additional scatterplots (Panels d) illustrate differences between true and estimated losses for specific settings, confirming agreement between surrogate and true losses in identifying the best method for posterior density estimation.

9.2.1.2 Summary Statistic Selection

In this section, we assess the performance of FlexCode-RF for summary statistics selection (Sec. 9.1.3). For this purpose, the following summary statistics were used: The **mean** is the average of the data points. The **median** represents the central value of the data points. For **mean1**, we calculate the average of the first half of the data points, while **mean1** is the average of the

9.2. Examples

latter half. The **SD** is the standard deviation of the data points , while **IQR** is the difference between the 75th and 25th percentiles. The **Quantile1** is the first quartile of the data. Lastly, we consider 43 independent random variables $\sim N(0, 1)$, which are by construction not informative about the parameter value.

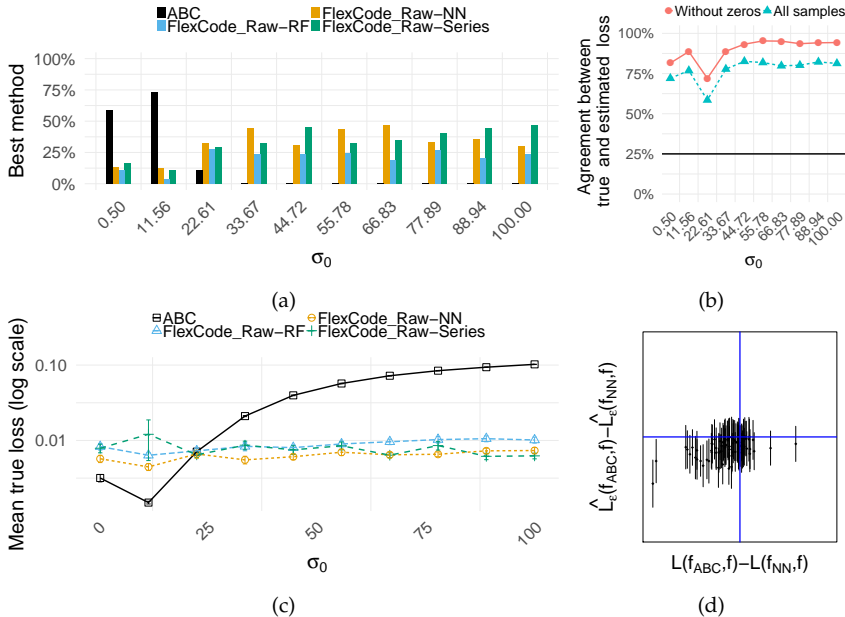


Figure 9.1: CDE and method selection for scenario 1. *Left:* Rejection ABC excels with small σ_0 , while NN and Series FlexCode perform better for moderate and large σ_0 . *Right:* Surrogate loss estimation guides method choice; horizontal line in (b) represents random selection.

Figures 9.3 and 9.4 present results from applying FlexCode-RF and ABC across different scenarios using various summary statistics. Panels (a) show the true loss as the number of statistics increases. FlexCode-RF remains robust to the inclusion of irrelevant statistics, while standard ABC’s performance deteriorates as noise or nuisance statistics are added. Panels (b) display the average importance of each statistic, as defined by Equation 3.9, where $u_{i,j}$ represents the mean decrease in the Gini index. FlexCode-RF assigns high importance to sufficient statistics or those strongly correlated with them. For

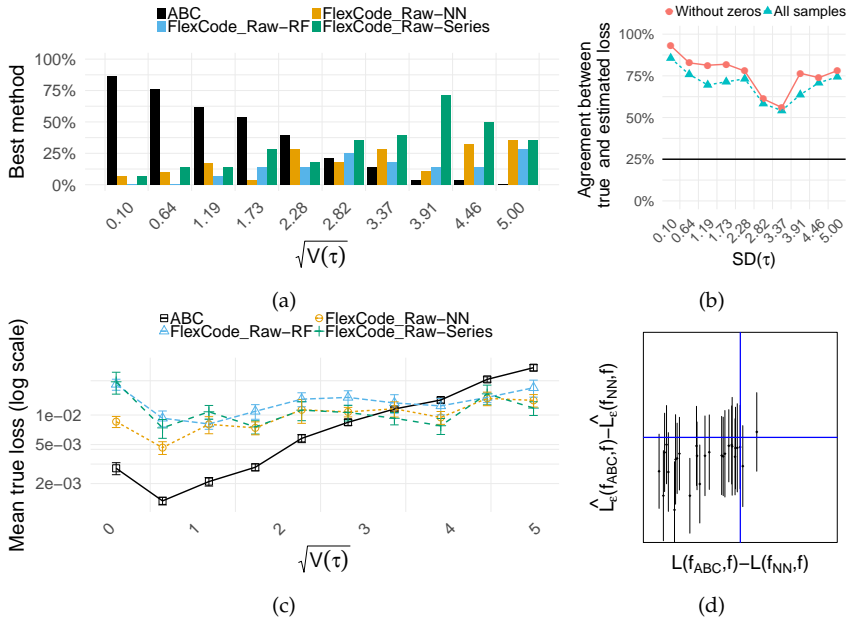


Figure 9.2: CDE and method selection for scenario 2. *Left:* Rejection ABC excels with small σ_0 , while NN and Series FlexCode perform better for moderate and large σ_0 . *Right:* Surrogate loss estimation guides method choice; horizontal line in (b) represents random selection.

instance, in Figure 9.3, location measures receive higher importance, whereas in Figure 9.4, dispersion measures are more significant. FlexCode-RF consistently assigns zero importance to random noise statistics, indicating that the summary statistic selection method effectively identifies relevant statistics for accurate posterior estimation, $f(\theta|x_o)$.

9.2.2 Application: Estimating a Galaxy's Dark Matter Density Profile

We extend our analysis to more complex simulations under the Λ CDM framework, the standard cosmological model describing a universe dominated by dark energy and cold dark matter. Specifically, we focus on the dark matter distribution in galaxies using the Navarro-Frenk-White (NFW) profile

9.2. Examples

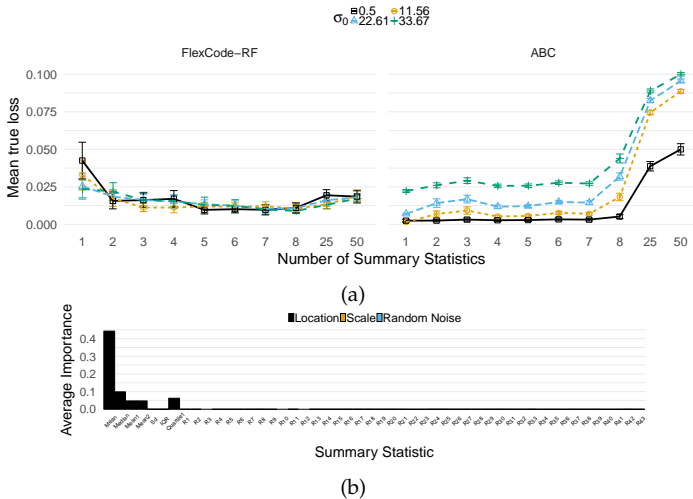


Figure 9.3: Summary statistics selection in scenario 1 (mean of a Gaussian with known variance). ABC sensitivity to noise is clear in (a) (entries 8-51), with FlexCode-RF showing robustness. FlexCode-RF identifies location statistics in (b) (entries 1-5).

([Navarro, 1996](#)), a widely used model for describing the density profile of dark matter halos. Our goal is to constrain the NFW parameters for the Sculptor dwarf spheroidal galaxy, starting with the critical energy E_c ([Strigari et al. 2017](#), Equation 15), while keeping other parameters fixed at standard values.

The observed data \mathbf{x}_0 include velocities and positions of 200 stars, simulated based on the NFW model ([Liu et al., 2018](#)). We employ ABC, defining the distance metric as the L^2 norm between kernel density estimates of the joint distribution of velocity and position. This distance metric is applied consistently across FlexCode-NN and FlexCode-Series. For functional data, we use FlexCode-Functional, which employs functional kernel regression for coefficient estimation ([Ferraty and Vieu, 2006](#)).

To evaluate the performance of the CDE methods, we generate 1000 test observations, with each ABC sample containing 1000 accepted observations (acceptance rate of 0.1). The prior for E_c is uniformly distributed over $U(0.01, 1.0)$.

[Figure 9.5](#) illustrates the true losses for various methods. The left panel shows that FlexCode estimators outperform ABC for certain scenarios with

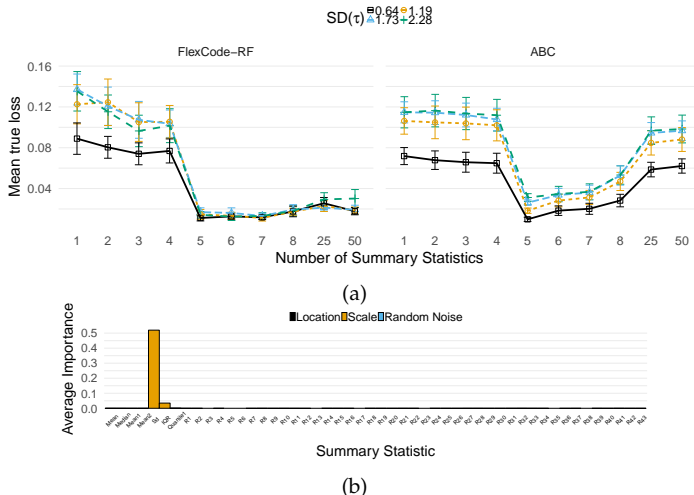


Figure 9.4: Summary statistics selection in scenario 2 (precision of a Gaussian with unknown precision). ABC sensitivity to noise is clear in (a) (entries 8–51), with FlexCode-RF showing robustness. FlexCode-RF identifies location statistics in (b) (entries 1–5) and emphasizes dispersion statistics (e.g., entry 5).

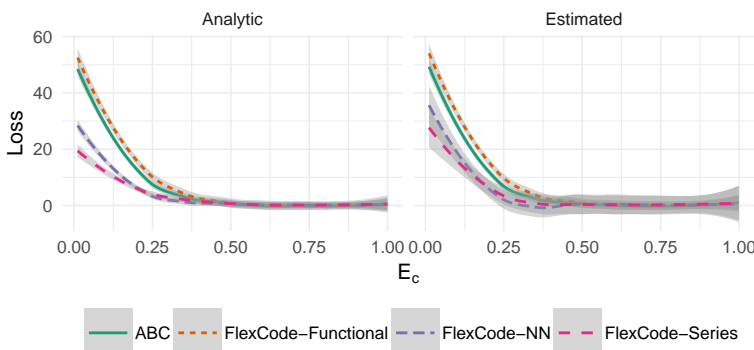


Figure 9.5: *Left:* True loss in various parameter regions. *Right:* The estimated surrogate loss (here shifted with a constant for easier comparison) can be used to identify improvements upon the ABC estimates.

9.3. Likelihood Free Frequentist Inference (LF2I)

low true E_c . The right panel, which compares estimated surrogate losses, supports similar findings, corroborating that the surrogate loss serves as a practical substitute for the unavailable true loss.

9.3 Likelihood Free Frequentist Inference (LF2I)

The goal of Likelihood Free Frequentist Inference (LF2I; Dalmasso et al. 2020a; Dalmasso et al. 2024) is to construct a set $R(\mathbf{X})$ such that

$$\mathbb{P}_{\mathbf{X}|\theta}(\theta \in R(\mathbf{X})) = 1 - \alpha, \quad (9.4)$$

where $\alpha \in (0, 1)$, regardless of the true value of the unknown parameter $\theta \in \Theta$. That is, $R(\mathbf{X})$ needs to be a frequentist set – it needs to control conditional coverage. In this section, we describe how LF2I achieves this. The full process is illustrated in Figure 9.6.

9.3.1 Confidence Sets via Neyman Inversion

The starting point of LF2I is Neyman confidence sets, which are based on Neyman's inversion of hypothesis test (Neyman, 1937). Specifically, Neyman's confidence sets have the shape

$$R(\mathbf{X}) := \{\theta \in \Theta \mid \tau(\mathbf{X}; \theta) \geq C_\theta\}, \quad (9.5)$$

where $\tau(\mathbf{X}; \theta)$ measures how plausible it is that \mathbf{X} was generated from θ (formally, it is a test statistic for null hypothesis that the data was generated from θ ; see Section 9.3.2), and C_θ is chosen so that conditional coverage holds (Equation 9.4). From a hypothesis test perspective, C_θ is the rejection cutoff that leads to type I error control. In other words, $R(\mathbf{x})$ contains plausible values for θ (according to the metric τ) given data \mathbf{x} .

The challenges of using Neyman's confidence sets in an LFI context are that:

- Most standard techniques for constructing τ require knowledge of an analytical expression for the likelihood function. This is the case of the Likelihood Ratio Test, for instance.

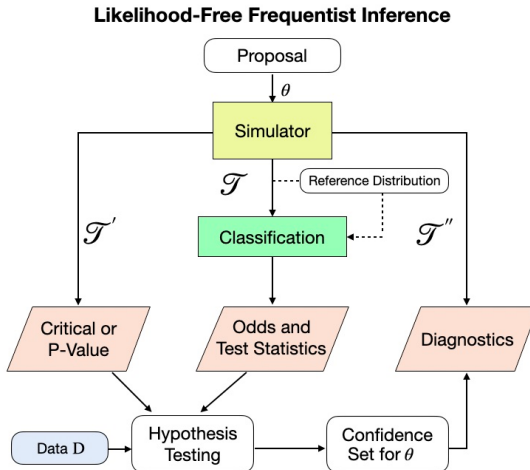


Figure 9.6: The three-branch modular framework for likelihood-free frequentist inference (LF2I). The middle branch is used to construct a test statistic; the left branch calibrates cutoffs to test hypotheses and thus generated confidence sets. The right branch provides independent diagnostics to test if the constructed sets have the right coverage.

- The standard derivation of C_θ either uses asymptotic derivations that only work if the sample size is large and for certain test statistics, or uses Monte Carlo simulations that are each fixed θ , which is too expensive for larger dimensional spaces.

In what follows, we discuss how to address these challenges using some of the Uncertainty Quantification techniques we have introduced before. We also discuss how to check whether the confidence regions given by LF2I have the correct conditional coverage. Code to implement LF2I in Python can be found at <https://github.com/lee-group-cmu/lf2i>.

9.3.2 Choosing a Test Statistic

Any test statistic τ can be used in LF2I as long as it can be computed. In this section, we show some examples of statistics that can be used. Some of these statistics are influenced by Bayesian methods, although we apply them in a frequentist context.

9.3. Likelihood Free Frequentist Inference (LFI)

9.3.2.1 Likelihood-Based Statistics

Many traditional test statistics rely on the likelihood function $f(\mathbf{x}|\theta)$. Here, we will discuss two of them, and then discussed how they can be used in a LFI setting.

The first one is the likelihood ratio (LR) statistic, which tests $H_0 : \theta = \theta_0$ using

$$\lambda(\mathbf{x}; \theta_0) = \frac{f(\mathbf{x}|\theta_0)}{\sup_{\theta \in \Theta} f(\mathbf{x}|\theta)}. \quad (9.6)$$

The second one is the Bayes Factor (BF), which essentially changes the maximization in the LR statistic by an integration with respect to a prior distribution $f(\theta)$:

$$\beta(\mathbf{x}; \theta_0) \equiv \frac{f(\mathbf{x}|H_0)}{f(\mathbf{x}|H_1)} = \frac{f(\mathbf{x}|\theta_0)}{\int_{\Theta} f(\mathbf{x}|\theta) df(\theta)}. \quad (9.7)$$

In an LFI setting, $f(\mathbf{x}|\theta)$ cannot be evaluated, and therefore these statistics cannot be computed. Thus, they need to be estimated. In order to do that, consider a proposal distribution $\pi(\theta)$ over the parameter space. We can use the forward simulator to generate $(\theta_1, \mathbf{X}_1), \dots, (\theta_B, \mathbf{X}_B)$, where each $(\theta, \mathbf{X}) \sim \pi(\theta) f(\mathbf{x}|\theta)$. By construction, the conditional density of $\mathbf{X}|\theta$ is $f(\mathbf{x}|\theta)$, and thus this quantity can be estimated using the conditional density estimators discussed in Chapter 3.

Dalmasso et al. (2020a) and Dalmasso et al. (2024) in particular estimate the likelihood function using the ratio trick (Section 3.7). Notice that the notation of that section corresponds to the choice $y := \mathbf{x}$ and $\mathbf{x} =: \theta$. Dalmasso et al. (2024) takes $g(\mathbf{x}|\theta)$ in Equation 3.13 to be $g(\mathbf{x})$, that is, a distribution that does not depend on θ . In this way,

$$\mathbb{O}(\mathbf{x}; \theta) = \frac{f(\mathbf{x}|\theta)}{g(\mathbf{x})},$$

that is, $\mathbb{O}(\mathbf{x}; \theta)$ is, up to $g(\mathbf{x})$, the likelihood function. Now, because $g(\mathbf{x})$ is constant in θ , this implies that the $\mathbb{O}(\mathbf{x}; \theta)$ is a version of the likelihood function, and therefore can be used in the LR statistic or the BF without the needs of applying the correction $g(\mathbf{x}|\theta)$ from Equation 3.14 (Izbicki et al., 2014). In other words, the LR statistic can be estimated by

$$\widehat{\lambda}(\mathbf{x}; \theta_0) = \frac{\widehat{\mathbb{O}}(\mathbf{x}; \theta_0)}{\sup_{\theta \in \Theta} \widehat{\mathbb{O}}(\mathbf{x}; \theta)},$$

and the Bayes Factor by

$$\widehat{\beta}(\mathbf{x}; \theta_0) = \frac{\widehat{\mathbb{O}}(\mathbf{x}; \theta_0)}{\int_{\theta \in \Theta} \widehat{\mathbb{O}}(\mathbf{x}; \theta) d\pi(\theta)},$$

where

$$\widehat{\mathbb{O}}(\mathbf{x}; \theta) := \frac{\widehat{\mathbb{P}}(Y = 1 | \mathbf{x}, \theta)}{\widehat{\mathbb{P}}(Y = 0 | \mathbf{x}, \theta)}.$$

Moreover, if $g(\mathbf{x}) := \int f(\mathbf{x} | \theta) d\pi(\theta) = f(\mathbf{x})$ (that is, if g is chosen to be the marginal distribution of \mathbf{x} with respect to the prior $\pi(\theta)$), the odds becomes the Bayes factor itself, and thus, in this special case,

$$\widehat{\beta}(\mathbf{x}; \theta_0) = \widehat{\mathbb{O}}(\mathbf{x}; \theta_0).$$

See Cranmer et al. (2020), Heinrich (2022), and Thomas et al. (2022) for variations of these statistics and how to estimate them based on data from the simulator.

9.3.2.2 Waldo

An alternative test statistic that can be used to construct confidence sets is the Waldo statistic (Masserano et al., 2023), which is given by

$$\omega(\mathbf{x}; \theta_0) = (\mathbb{E}[\theta | \mathbf{x}] - \theta_0)^t \mathbb{V}[\theta | \mathbf{x}]^{-1} (\mathbb{E}[\theta | \mathbf{x}] - \theta_0), \quad (9.8)$$

where $\mathbb{E}[\theta | \mathbf{x}]$ and $\mathbb{V}[\theta | \mathbf{x}]$ represent the posterior mean and variance of θ given data \mathbf{x} . Waldo is a Bayesian version of the Wald test statistic (Wald, 1943).

Similar to the likelihood-based statistics, Waldo cannot be directly computed in an LF2I setting. However, it can be approximated by

$$\widehat{\omega}(\mathbf{x}; \theta_0) = (\widehat{\mathbb{E}}[\theta | \mathbf{x}] - \theta_0)^t \widehat{\mathbb{V}}[\theta | \mathbf{x}]^{-1} (\widehat{\mathbb{E}}[\theta | \mathbf{x}] - \theta_0), \quad (9.9)$$

where $\widehat{\mathbb{E}}[\theta | \mathbf{x}]$ and $\widehat{\mathbb{V}}[\theta | \mathbf{x}]$ are estimates of $\mathbb{E}[\theta | \mathbf{x}]$ and $\mathbb{V}[\theta | \mathbf{x}]$ obtained using the

9.3. Likelihood Free Frequentist Inference (LF2I)

data from the simulator, $(\theta_1, \mathbf{X}_1), \dots, (\theta_B, \mathbf{X}_B) \sim \pi(\theta)f(\mathbf{x}|\theta)$. These can be obtained in two ways:

- Using an estimate of the posterior distribution, $\hat{f}(\theta|\mathbf{x})$, which can be obtained using e.g. the ABC-CDE approach discussed in Section 9.1. For instance, if $\theta \in \mathbb{R}$, this corresponds to taking $\mathbb{E}[\theta|\mathbf{x}] := \int \theta \hat{f}(\theta|\mathbf{x})d\theta$ and $\mathbb{V}[\theta|\mathbf{x}] := \int \theta^2 \hat{f}(\theta|\mathbf{x})d\theta - \mathbb{E}^2[\theta|\mathbf{x}]$.
- Directly estimating both $\mathbb{E}[\theta|\mathbf{x}]$ and $\mathbb{V}[\theta|\mathbf{x}]$ via regression/supervised learning. Concretely, $\mathbb{E}[\theta|\mathbf{x}]$ is the regression of θ on \mathbf{x} , and $\mathbb{V}[\theta|\mathbf{x}] = \mathbb{E}[\theta^2|\mathbf{x}] - \mathbb{E}^2[\theta|\mathbf{x}]$ is the difference between the regression of θ^2 on \mathbf{x} and the first regression (squared) that was already estimated.

Masserano et al. (2023) shows that the Waldo statistic leads to larger power/tighter (frequentist) confidence sets than the Wald statistic in regions where $\pi(\theta)$ places large mass.

9.3.3 Calibrating the Cutoffs

After selecting the test statistic, denoted as $\tau(\mathbf{X}; \theta)$, the next step is to estimate C_θ for constructing the confidence set described in Equation 9.5. The estimated confidence set will then be

$$\hat{R}(\mathbf{X}) := \left\{ \theta \in \Theta \mid \tau(\mathbf{X}; \theta) \geq \hat{C}_\theta \right\}.$$

To ensure that this set achieves a confidence level of $1 - \alpha$, it is necessary to define C_θ as follows:

$$C_\theta = F_{\tau(\mathbf{X}; \theta)|\theta}^{-1}(\alpha),$$

where $F_{\tau(\mathbf{X}; \theta)|\theta}$ represents the cumulative distribution function of the random variable $\tau(\mathbf{X}; \theta)$ conditioned on the parameter θ . In other words, C_θ is the α conditional quantile of $\tau(\mathbf{X}; \theta)$ on θ . Again, in an LFI setting we do not know this distribution, but we can estimate it. There are a few ways of doing it:

- **[Monte Carlo]** Use the simulator to generate a sufficiently large Monte Carlo sample consisting of $\mathbf{X}_1, \dots, \mathbf{X}_B$, all sampled at the same θ . Then, estimate C_θ by computing the α quantile of the values

$$\{\tau(\mathbf{X}_1; \theta), \dots, \tau(\mathbf{X}_B; \theta)\}.$$

Notice however that, to compute confidence sets, it is necessary to estimate C_θ for a fine grid of θ values. This approach can therefore be expensive, especially when dealing with a parameter space of large dimensions.

- **[Quantile Regression]** Dalmasso et al. (2020a) and Dalmasso et al. (2024) use quantile regression to regress $\tau(\mathbf{X}; \theta)$ on θ . Specifically, they (i) use the simulator to obtain a training set $(\theta_1, \mathbf{X}_1), \dots, (\theta_B, \mathbf{X}_B)$, (ii) compute the transformed data $(\theta_1, \tau(\mathbf{X}_1; \theta_1)), \dots, (\theta_B, \tau(\mathbf{X}_B; \theta_B))$, and (iii) use one of the techniques of Section 3.9 to α -quantile regress $\tau(\mathbf{X}; \theta)$ on θ .
- **[Partition-based Regression (TRUST)]** TRUST (Cabezas et al., 2024) is inspired by conformal methods (Section 5.3) and estimates the distribution of $\tau(\mathbf{X}; \theta)$ conditional on θ by partitioning Θ . It achieves this by fitting a regression tree to simulated data $(\theta_1, \mathbf{X}_1), \dots, (\theta_B, \mathbf{X}_B)$. The steps are as follows:
 1. Using the modified training data $(\theta_1, \tau(\mathbf{X}_1; \theta_1)), \dots, (\theta_B, \tau(\mathbf{X}_B; \theta_B))$, fit a regression tree to predict τ based on θ . This tree partitions the parameter space Θ into disjoint regions A_1, A_2, \dots, A_K , where each region corresponds to a leaf of the tree.
 2. For a given $\theta \in \Theta$, determine the leaf A_k that contains θ . Let $\mathcal{I}_k = \{b \in \{1, \dots, B\} : \theta_b \in A_k\}$ denote the indices of the simulated pairs (θ_b, \mathbf{X}_b) that fall within the same partition. The empirical CDF of $\tau(\mathbf{X}; \theta)$ within A_k is

$$H_B(t | \theta) = \frac{1}{|\mathcal{I}_k|} \sum_{b \in \mathcal{I}_k} \mathbb{I}(\tau(\mathbf{X}_b; \theta_b) \leq t),$$

where $\mathbb{I}(\cdot)$ is the indicator function.

3. The cutoff C_θ for θ is estimated as the α -quantile of the values $\{\tau(\mathbf{X}_b; \theta_b) : b \in \mathcal{I}_k\}$, that is, $\hat{C}_\theta = H_B^{-1}(\alpha | \theta)$, where $H_B^{-1}(\alpha | \theta)$ is the generalized inverse of H_B .

TRUST confidence sets $\hat{R}(\mathbf{X})$ have finite-sample local coverage:

$$\mathbb{P}\left(\theta \in \hat{R}(\mathbf{X}) | \theta \in A\right) = 1 - \alpha,$$

9.3. Likelihood Free Frequentist Inference (LF2I)

where A is a subset of Θ designed to approximate the conditional coverage: $\mathbb{P}\left(\theta \in \widehat{R}(\mathbf{X}) \mid \theta\right) \approx \mathbb{P}\left(\theta \in \widehat{R}(\mathbf{X}) \mid \theta \in A\right)$. Additionally, the method achieves B -asymptotic conditional coverage, even for small observed datasets:

$$\lim_{B \rightarrow \infty} \mathbb{P}\left(\theta \in \widehat{R}(\mathbf{X}) \mid \theta\right) = 1 - \alpha.$$

That is, TRUST coverage is correct as long as the number of simulations is large. Cabezas et al. (2024) also introduces TRUST++, is an extension of TRUST that employs random forests.

9.3.4 Evaluating Coverage and UQ over the Confidence Sets

Once the test statistic is selected and cutoffs are determined, we construct a confidence via $\widehat{R}(\mathbf{X}) := \left\{\theta \in \Theta \mid \tau(\mathbf{X}; \theta) \geq \widehat{C}_\theta\right\}$. Notice that $\widehat{R}(\mathbf{X})$ may not be a valid confidence set for every $\theta \in \Theta$ due to the fact that \widehat{C}_θ is an estimate of C_θ . That is, the constructed confidence set may not achieve the correct coverage. To assess the adequacy of such estimates, LF2I examines their quality by estimating the coverage probability as a function of θ . This evaluation helps ensure that the confidence set provides reliable coverage across Θ .

In order to check coverage, LF2I uses the fact that

$$\mathbb{P}_{\mathbf{X}|\theta}\left(\theta \in \widehat{R}(\mathbf{X})\right) = \mathbb{E}[Z|\theta],$$

where $Z := \mathbb{I}(\theta \in R(\mathbf{X}))$ and (θ, \mathbf{X}) is drawn from the simulator. In other words, the coverage probability is the regression of Z on θ . Thus, LF2I (i) uses the simulator to obtain a training set $(\theta_1, \mathbf{X}_1), \dots, (\theta_B, \mathbf{X}_B)$, (ii) compute the transformed data $(\theta_1, Z_1), \dots, (\theta_B, Z_B)$, where $Z_i = \mathbb{I}(\theta_i \in R(\mathbf{X}_i))$ and (iii) use e.g. one of the techniques of Chapter 2 to regress Z on θ (equivalently, fit a probabilistic classifier). By checking whether such estimates are far from $1 - \alpha$ for all θ 's, one can determine the adequacy of coverage for $\widehat{R}(\mathbf{X})$ and pinpoint regions that require improvement for specific θ values. Subsequently, adjustments can be made to reestimate C_θ in those identified areas.

TRUST provides an alternative approach to evaluate the accuracy of the estimated confidence sets $\widehat{R}(\mathbf{X})$: it estimates the uncertainty around the true $R(\mathbf{X})$. For each $\theta \in \Theta$, TRUST constructs a confidence set $(\widehat{C}_\theta^L, \widehat{C}_\theta^U)$ for C_θ using standard quantile-based methods (Hahn and Meeker, 2011), and propagates

this uncertainty to compute:

$$\begin{aligned}\mathcal{I}(\mathbf{X}) &= \{\theta \in \Theta \mid \tau(\mathbf{X}; \theta) \geq \hat{C}_\theta^U\}, \quad \mathcal{O}(\mathbf{X}) = \{\theta \in \Theta \mid \tau(\mathbf{X}; \theta) \leq \hat{C}_\theta^L\}, \\ \mathcal{U}(\mathbf{X}) &= \{\theta \in \Theta \mid \hat{C}_\theta^L \leq \tau(\mathbf{X}; \theta) \leq \hat{C}_\theta^U\}.\end{aligned}$$

Here, $\mathcal{I}(\mathbf{X})$ contains parameters confidently inside the interval, $\mathcal{O}(\mathbf{X})$ those confidently outside, and $\mathcal{U}(\mathbf{X})$ those with uncertain status. Following 3-way hypothesis testing (Berg, 2004; Esteves et al., 2016; Izbicki et al., 2023), these correspond to acceptance, rejection, and agnostic regions. If $\mathcal{U}(\mathbf{X})$ is large, increasing the number of simulations B can improve the estimate of $R(\mathbf{X})$.

9.3.5 Example: Two Moons

We compare the methods for calibrating cutoffs in LF2I described in Section 9.3.3 using the following implementations:

- **[Monte Carlo]** Simulates n_{MC} statistics over an equally spaced grid of Θ . The $(1 - \alpha)$ -quantile of these simulations at the nearest grid point estimates C_θ . For multi-dimensional Θ , the grid combines equally spaced one-dimensional grids for each coordinate. The grid size ensures comparability across methods by maintaining the simulation budget B proportional to $d = \dim \Theta$, with $n_{MC} = 500$.
- **[Quantile Regression via Boosting]** Estimate C_θ through the $(1 - \alpha)$ conditional quantile of $\tau(\mathbf{X}, \theta)$ given θ , implemented using *scikit-learn*'s boosting.
- **[TRUST++]** Applies the tuned version of TRUST++ described in Cabezas et al. (2024).

For this example, $\mathbf{x} = (x_1, x_2) \in \mathbb{R}^2$, and $\theta \in \mathbb{R}^2$. The model is given by the two moons model (Greenberg et al., 2019b), in which the posterior exhibits a bimodal moon-shaped structure. The prior $\theta_i \sim U(-1, 1)$ is used to estimate τ over $\Theta = (-1, 1)^2$. We use normalizing flows (Section 3.6) to approximate the posterior. Further details are in Cabezas et al. (2024).

Figure 9.7 illustrates the confidence regions for a realization of the two moons example. Both TRUST++ and boosting closely approximate the oracle

9.3. Likelihood Free Frequentist Inference (LF2I)

region (that is, the region that has the correct coverage), whereas the Monte Carlo method underestimates its size. While TRUST++ and boosting produce similar regions, TRUST++ offers an additional layer of uncertainty quantification, providing insights into oracle information constrained by the simulation budget.

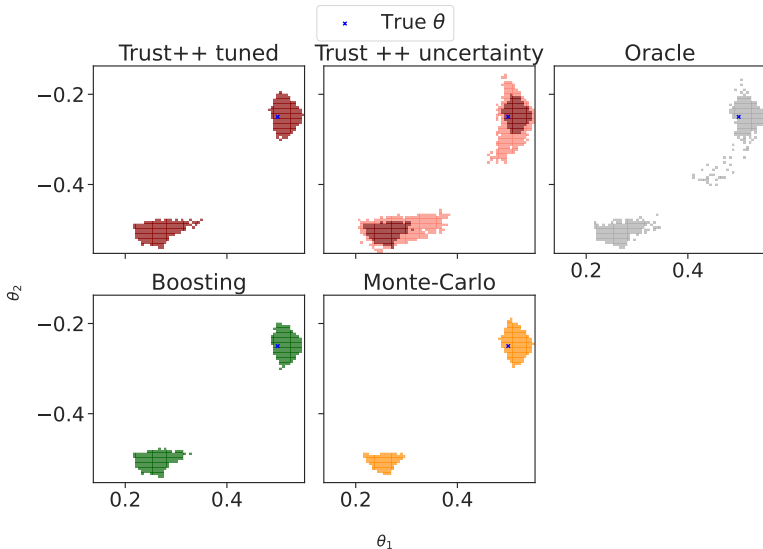


Figure 9.7: Visualization of 95% confidence regions and TRUST++ uncertainty for the two moons example. Maroon areas indicate high confidence from TRUST++, while salmon areas highlight uncertainty.

9.3.6 Nuisance Parameters

The parameters θ can often be decomposed into $\theta = (\mu, \nu)$, where $\mu \in M$ are parameters of interest and $\nu \in N$ are nuisance. In this case, one only cares about constructing confidence sets for μ . In this setting, Neyman confidence sets then have the shape

$$R(\mathbf{X}) := \{\mu \in M \mid \tau(\mathbf{X}; \mu) \geq C_\mu\},$$

where $\tau(\mathbf{X}; \mu)$ measures how plausible it is that \mathbf{X} was generated from μ . We now discuss how to design both $\tau(\mathbf{X}; \mu)$ and C_μ .

One way to create a test statistic $\tau(\mathbf{X}; \mu)$ is to use the techniques from Section 9.3.2 to design a statistic that tests the hypothesis

$$H_0 : \mu = \mu_0 \text{ and } \nu = \nu_0.$$

Denote this statistic by $\tau(\mathbf{X}; (\mu_0, \nu_0))$. This statistic can then be integrated over ν to produce $\tau(\mathbf{X}; \mu)$ in a Bayesian context: $\tau(\mathbf{X}; \mu) = \int \tau(\mathbf{X}; (\mu, \nu)) dP(\nu)$. Alternatively, in a frequentist vain, one may take its maximum value: $\tau(\mathbf{X}; \mu) = \sup_{\nu \in N} \tau(\mathbf{X}; (\mu, \nu))$. Furthermore, certain statistics automatically manage nuisance parameters without additional adjustments. This is the case of Waldo (Section 9.3.2.2):

$$\omega(\mathbf{x}; \mu_0) = (\mathbb{E}[\mu|\mathbf{x}] - \mu_0)^t \mathbb{V}[\mu|\mathbf{x}]^{-1} (\mathbb{E}[\mu|\mathbf{x}] - \mu_0).$$

Once the test statistic is defined, the cutoffs C_μ need to be chosen. One way of doing that in order to guarantee that $R(\mathbf{X})$ has coverage $1 - \alpha$ is to set C_μ to be

$$C_\mu = \inf_{\nu \in N} F_{\tau(\mathbf{X}; \mu)|\mu, \nu}^{-1}(\alpha),$$

where $F_{\tau(\mathbf{X}; \mu)|\mu, \nu}$ represents the cumulative distribution function of the random variable $\tau(\mathbf{X}; \mu)$ conditioned on all parameters (μ, ν) . Of course, such cumulative distribution must be estimated, which can be done in the same way as described in Section 9.3.3. Computing the infimum is computationally expensive of N is high-dimensional. In TRUST and TRUST++ however the problem is simplified because \hat{H}_B is computed using a partition of Θ . This means that the minimization only requires evaluating $\hat{H}_B^{-1}(1 - \alpha|\mu, \nu)$ for a finite number of ν values, one for each element of the partition that covers μ . For example, in the case of TRUST, this approach only requires minimization over the leaves associated with the given μ .

An alternative approach to handle nuisance parameters is to integrate $F_{\tau(\mathbf{X}; \mu)|\mu, \nu}^{-1}(\alpha)$ with respect to ν , although this procedure does not have coverage guarantees (Dalmasso et al., 2024). See also Masserano et al. (2024) for a different way to handle nuisance parameters that also controls coverage, and Dalmasso et al. (2024) for alternative approximations such as profiling.

9.3. Likelihood Free Frequentist Inference (LF2I)

9.3.7 Example: Muon energy estimation

In this section, we follow Dalmasso et al. (2024) to estimate muon energy using a high-granularity calorimeter in a particle collider experiment. Muons are particles similar to electrons but significantly heavier. They are key to studying the subatomic world and testing the predictions of the Standard Model of particle physics – a theory that describes how fundamental particles and forces interact. Despite its strong predictive power, the Standard Model leaves important questions unanswered, making precise measurements, such as muon energy, essential for uncovering potential physics beyond its scope.

In the experiment, each data point is represented as a 3D image, \mathbf{x} , with a dimensionality of approximately 50,000. These images represent the detailed pattern and magnitude of energy deposits in a finely segmented calorimeter as muons pass through it. A calorimeter is a detector designed to measure the energy of particles by recording the energy they lose as they interact with its material. The dataset consists of $n = 1$ with a total of 886,716 3D inputs, each corresponding to a scalar muon energy θ . These data are generated through simulations using GEANT4 (Agostinelli et al., 2003), a widely used simulator for accurately modeling particle interactions under the Standard Model. The dataset is publicly available at Kieseler et al., 2021.

The primary objective is to determine whether a high-granularity calorimeter provides tighter constraints on muon energy compared to detectors that measure only total energy. We investigate three levels of energy measurement: (i) a 1D input representing the sum of calorimeter cells for muons with energy $E > 0.1 \text{ GeV}$; (ii) 28 custom features extracted from spatial and energy information of calorimeter cells (see Kieseler et al., 2022); and (iii) the full calorimeter data, $\mathbf{x} \in \mathbb{R}^{51,200}$. For each data point, LF2I confidence sets are constructed using the estimated Bayes Factor (Equation 9.7). A convolutional neural network classifier, as described in Kieseler et al., 2022, is used to estimate the odds function for the full calorimeter data, while critical values are obtained via quantile gradient boosted trees. For the 1D and 28D datasets, a gradient boosting classifier is employed to learn the odds function. Around 83% of the data ($B = 738,930$) is used for training, with 14% allocated to estimate critical values ($B' = 123,155$). For comparison, SMC-ABC (Sisson et al., 2007), another likelihood-free inference (LFI) algorithm, is applied to all simulated datasets,

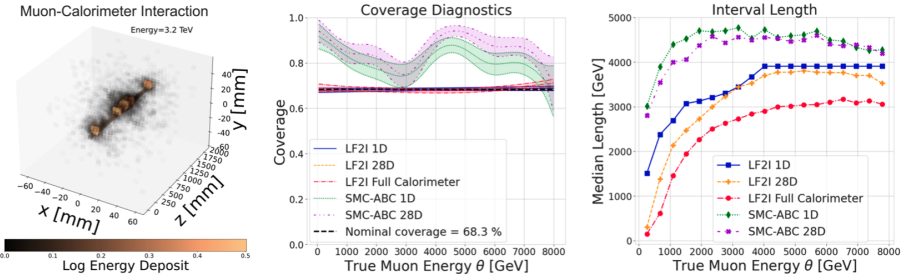


Figure 9.8: LF2I outperforms SMC-ABC with nominal coverage and tighter intervals. Left: Example muon data at $\theta \approx 3.2$ TeV in a $32 \times 32 \times 50$ cell calorimeter. Center: LF2I (blue, orange, red) maintains 68.3% coverage, while SMC-ABC (green, purple) consistently over-covers. Right: Median interval lengths. SMC-ABC, despite computational intensity, lacks constraining power. Full calorimeter data for SMC-ABC is omitted due to computational constraints.

utilizing the same total of $B + B' = 862,085$ samples. The remaining data ($B'' = 24,631$) is reserved for validation and diagnostics.

Figure 9.8 (center) shows that LF2I with the Bayes Factor test statistic achieves nominal coverage of 68.3% across all datasets. In contrast, SMC-ABC produces overly conservative credible intervals, leading to over-coverage. In terms of interval length (constraining power), Figure 9.8 (right) indicates that SMC-ABC intervals are significantly wider than LF2I confidence sets for both the 1D and 28D datasets. Due to computational limitations, running SMC-ABC on the full 51,200-dimensional calorimeter data was not feasible. Notably, the information in the data directly influences the size of LF2I confidence sets: the full calorimeter results in noticeably smaller intervals, and therefore leads to higher constraining power.

9.4 Summary

This chapter explored Likelihood-Free Inference in statistical models where the likelihood function is intractable. We focused on two methodologies: Approximate Bayesian Computation via Conditional Density Estimation (ABC-CDE) and Likelihood-Free Frequentist Inference (LF2I).

ABC-CDE was presented as an approach for estimating posterior distribu-

9.4. Summary

tions using conditional density estimation, providing an efficient solution from a Bayesian perspective. LF2I was introduced as a framework for constructing frequentist confidence sets that ensure proper coverage, regardless of the true parameter values. Its modular design allows for the integration of various test statistics and calibration techniques, making it adaptable to a wide range of applications.

Chapter 10

Optimizing Construction Schedules: Mitigating Weather-Related Delays



Frustrated Workers. Designed with the help of IA.

The best way to predict the future
is to create it.

Peter Drucker

Construction delays can stem from various factors, including the incompetence of involved parties, material and equipment shortages, and adverse weather conditions (Durdyev et al., 2020; Sanni-Anibire and Egbu, 2022; Sepasgozar et al., 2019). These delays negatively impact both owners and contractors, leading to contractual penalties and reduced resource productivity. Among these factors, weather events stand out as a significant source of uncertainty due to their direct effect on productivity (Assaf and Al-Hejji, 2006; Schuldt et al., 2021). Modeling delays caused by weather is particularly challenging, as these events vary not only in time and location but also in the specific weather conditions required for different construction tasks. Consequently, effective project management must accurately account for these conditions for each task to minimize potential negative impacts on productivity and deadlines.

This chapter illustrates how the tools presented in previous chapters can estimate the uncertainty in a project's completion time taking into account weather conditions. Specifically, we aim to estimate the probability distribution of Z , the project's duration in days, relying exclusively on historical meteorological data. Table 10.1 illustrates part of the meteorological dataset. We denote such distribution as $f(z|i,y)$, where j is the day of year and y the year of project implementation.

Table 10.1: Example of historical data from weather stations, including daily mean temperature, precipitation, and minimum temperature.

Weather Station	Date	T_{mean} (°C)	P (mm)	T_{min} (°C)	...
1	2020-01-31	5	0	1	...
1	2020-02-01	-2	0	-10	...
:	:	:	:	:	...
2	2022-06-01	7	8	1	...
2	2022-06-02	3	24	-5	...
2	2022-06-03	4	17	-6	...
...

The construction time will depend on a construction schedule. This schedule outlines the tasks needed to produce the deliverables, including their sequence, durations, and resource requirements (Edition, 2008). Figure 10.1 provides an example of a fictitious schedule with tasks carried out sequentially, without accounting for weather-related delays. We assume this schedule is known.

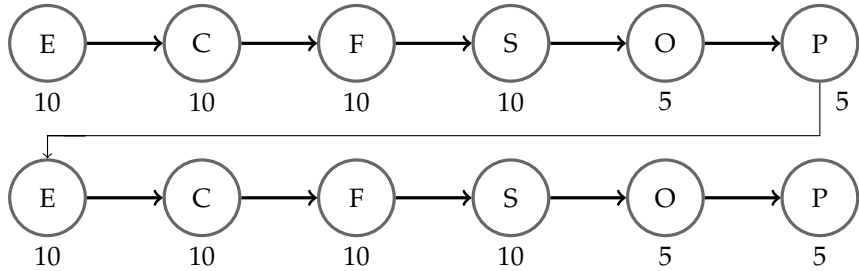


Figure 10.1: Construction schedule represented by a finite network of arcs, where the nodes represent the activities of earthworks (E), concrete (C), formwork (F), steelwork (S), outdoor painting (O), and pavements (P). For each task, a planned duration is associated below the node.

We assume the climatic conditions for each task are known. Table 10.2, adapted from Ballesteros-Pérez et al. (2017), lists an example of thresholds defining when tasks cannot proceed. For instance, "earthworks" are halted if the average daily temperature falls below 0°C. We assume task limits apply only to the specific day and do not affect subsequent days.

Table 10.2: Weather limits for type of tasks: earthworks (E), concrete (C), formwork (F), steelwork (S), outdoor painting (O), and pavements (P). "x" denotes conditions under which the task cannot be performed.

Weather variable	E	C	F	S	O	P
Minimum temperature $\leq 0^{\circ}\text{C}$		x			x	
Average temperature $\leq 0^{\circ}\text{C}$	x			x	x	
Maximum temperature $\geq 40^{\circ}\text{C}$		x		x		x
Precipitation $\geq 1 \text{ mm}$					x	x
Precipitation $\geq 10 \text{ mm}$	x	x			x	x
Precipitation $\geq 30 \text{ mm}$	x	x		x	x	x
Wind gusts $\geq 30 \text{ knots}$	x	x	x	x	x	

10.1. Estimating the Distribution

Having these components, we are now ready to describe our estimator of $f(z|i, y)$.

10.1 Estimating the Distribution

Consider a project composed of a set of p tasks, represented by $t = \{1, \dots, p\}$. The schedule of Figure 10.1 contains $p = 12$ tasks. Although the tasks do not overlap in this schedule, the method can be easily applied when they do intersect. The project execution time, Z , is defined as the number of days until all p tasks are completed, taking delays into account. The objective is to model the distribution of Z by considering the execution time of each task, including delays due to climate factors.

To achieve this, let the random variable $X_{i,y}^{(t)}$ indicate whether task t could be executed on day i of year y considering climatic factors:

$$X_{i,y}^{(t)} = \begin{cases} 1 & \text{if task } t \text{ was executed on day } i \text{ of year } y, \\ 0 & \text{otherwise.} \end{cases}$$

Our model assumes $X_{i,y}^{(t)} \sim \text{Bernoulli}(\theta_i^{(t)})$, where $\theta_i^{(t)}$ is the probability of completing task t on the i -day of a given year, with $X_{i,y}^{(t)}$'s independent for each fixed t .

Notice that, given a starting day and year, Z is a deterministic function of $X_{i,y}^{(t)}$'s. Therefore, after $\theta^{(t)} = (\theta_1^{(t)}, \dots, \theta_{365}^{(t)})$ have been estimated, Z can be sampled from this model by using Monte Carlo simulation to sample $X_{i,y}^{(t)}$'s with the estimated parameters. This method easily incorporates task dependencies. For multiple tasks on the same day, each task is checked independently.

The Monte Carlo samples are implicitly defining an estimate $\hat{f}(z|i, y)$, which can then be used to approximate α -quantiles and the mean of Z , as well as to compute prediction sets or any of the other tools developed in previous chapters.

The parameters $\theta^{(t)}$ can be estimated using historical weather data in various

ways. For instance, we can use a KNN-like estimate:

$$\hat{\theta}_i^{(t)} = \frac{1}{N} \sum_{y=1}^Y \sum_{m \in \mathcal{N}(l)} \sum_{j \in \mathcal{N}(i)} Y_{t,m,j,y}, \quad (10.1)$$

where $\mathcal{N}(l)$ is the set of K_l locations closest to the location where the construction will be performed, $\mathcal{N}(i)$ is the set of K_i days closest to i ,¹ $N = Y \times |\mathcal{N}(i)| \times |\mathcal{N}(l)|$, and $Y_{t,l,i,y}$ is the indicator that task t could be performed on location l on the i -th day of year y . For other approaches to estimate this parameter, see Comito et al. (2025).

10.2 Model Selection

Suppose we temporally split our dataset into two parts: training and validation. Using the training set, we create I estimates for $f(z|j,y)$:

$$f_1(z|j,y), \dots, f_I(z|j,y),$$

where j is the day of the year and y the year of project implementation. Each estimate can come from different configurations of tuning parameters of a given model, or entirely different models.

Our goal in this section is to select the model that best approximates the true f . To achieve this, we first create variations of the validation datasets, denoted by $(Z_1, I_1, Y_1), \dots, (Z_m, I_m, Y_m)$, using various temporal splits of the original validation dataset. Specifically, we randomly choose different starting dates (I_k, Y_k) . The Z_k values are then obtained by applying the construction schedule to data after the chosen start date, reflecting actual observed weather conditions on the weather datasets.

Given a loss function L , we can estimate the risk of an estimate \hat{f} via

$$\hat{R}(f, \hat{f}) = \frac{1}{m} \sum_{k=1}^m L(Z_k, \hat{f}(z|I_k, Y_k)).$$

¹Notice that “day of the year” is a circular variable, so instead of the Euclidean distance we use e.g. $d(i,j) = \min\{|i-j|, 365 - |i-j|\}$.

10.2. Model Selection

Next, we discuss choices of loss functions.

10.2.1 CDE loss

Inspired by the L^2 loss for continuous problems (Equation 3.1), we consider the Brier Score

$$L(Z_k, \hat{f}(z|i_k, y_k)) = \sum_z \hat{f}^2(z|i, y) - 2\hat{f}(Z_k|i, y).$$

Up to a constant that does not depend on \hat{f} , L is a good estimator of the L^2 distance

$$\sum_z \left(f(z|i, y) - \hat{f}(z|i, y) \right)^2.$$

10.2.2 Weighted pinball loss

If we are primarily interested in accurately estimating certain quantiles of $f(z|j, y)$, we can utilize the pinball loss (Section 3.9.1).

Here, we extend the standard pinball loss by combining multiple α values to assess model uncertainty. This is done using a weighting function $w(\alpha)$ to assign weights to each α . The weighted loss is defined as:

$$L^w(Z_k, f(z|i_k, y_k)) = \int w(\alpha) L_\alpha(Z_k, Q(\alpha|i_k, y_k)) d\alpha$$

where $Q(\alpha|i_k, y_k)$ is the α -quantile of $\hat{f}(y|i_k, y_k)$ and L_α is the α -pinball loss (Equation 3.15).

The weighting function $w(\alpha)$ can be tailored to emphasize different parts of the distribution based on the specific application. For example, in construction projects, accurately estimating the upper tails of $f(z)$ is critical to ensure the observed value lies within the density with high probability. Therefore, it is appropriate to weight the right tail more heavily, such as with $w(\alpha) \propto \alpha^2$, making higher α values more significant. Alternatively, other weights can shift the focus to different quantiles. For instance, the left tail can be emphasized using $w(\alpha) \propto (1 - \alpha)^2$, or both tails can be equally weighted with $w(\alpha) \propto (\alpha - 0.5)^2$.

10.3 Example

To illustrate the application of the model, we used daily meteorological data from the UK, following criteria similar to those of Ballesteros-Pérez et al. (2017). The MIDAS dataset ([Met Office MIDAS Open: UK Land Surface Stations Data \(1853-current\) 2019](#)) includes daily records of precipitation, temperature, and wind speed from 1985 to 2020. We applied comparable inclusion and exclusion criteria for weather stations, imputing missing values with a 7-day moving average if at least three observations were available. Stations with significant data gaps in the validation and test sets were excluded, resulting in the selection of 68 stations for analysis. The model was trained on years 1985-2012, and the years 2013-2016 were used to select its tuning parameters.

We used the schedule from Figure 10.1 and the climatic limits from Table 10.2. The project duration was fixed at 160 days, disregarding regional climatic conditions. We estimated the probability of workable days using only days with complete data for all selected variables.

Figure 10.2 demonstrates a byproduct of our estimates $\hat{f}(z|i, y)$ as a function of its proposing starting day i for a specific location (station 908). The results highlight the model's effectiveness in providing accurate and actionable insights for project scheduling. The comparison between the model's estimates and the actual project durations, represented by the observed lines at the bottom, underscores the method's precision and reliability.

10.3. Example

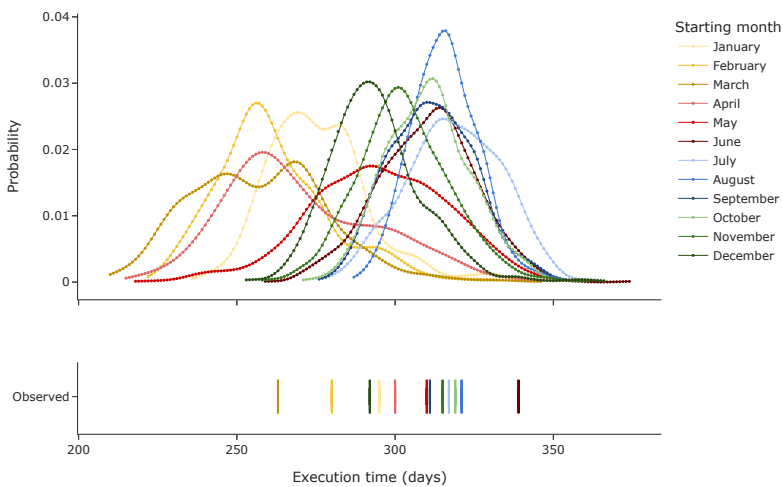
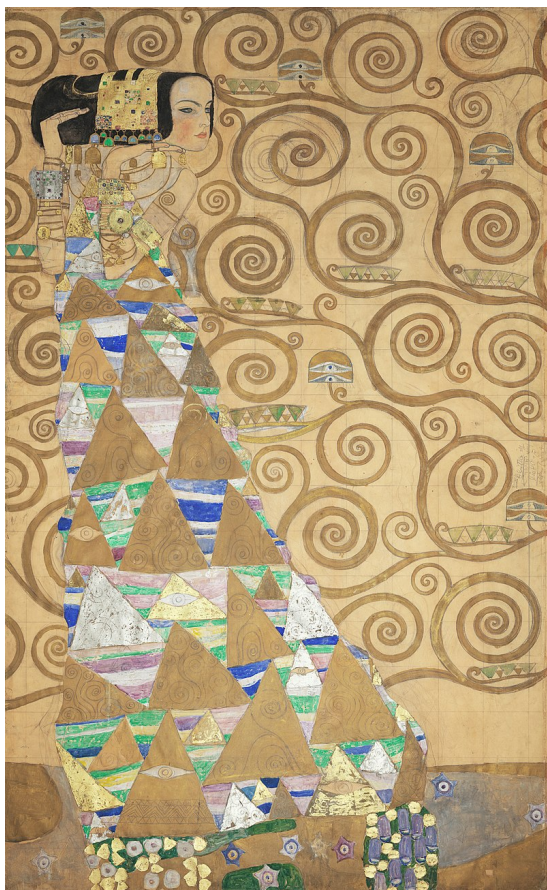


Figure 10.2: Illustrative application of the method using real-world data: the model estimates the distribution of project durations as a function of its starting date, providing valuable insights for optimal project scheduling. The observed lines at the bottom represent actual project durations, demonstrating the high accuracy of the model's estimates.

Chapter 11

Closing Thoughts



Expectation. Gustav Klimt, 1905–1909, MAK - Museum of Applied Arts, Vienna.

11.1. Summary of Key Concepts

Doubt is not a pleasant condition,
but certainty is absurd.

Voltaire

11.1 Summary of Key Concepts

This book has explored a variety of tools for Uncertainty Quantification in machine learning, focusing on how different types of uncertainty – aleatoric and epistemic – appear in both theoretical and applied settings. Aleatoric uncertainty refers to the inherent variability in the data, which cannot be reduced even with an infinite amount of data points. It is driven by randomness in the system being modeled and is captured by the conditional distributions of Y given \mathbf{x} , which is the $f(y|\mathbf{x})$ in regression and $\mathbb{P}(Y = y|\mathbf{x})$ in classification. In contrast, epistemic uncertainty arises from a lack of knowledge of the true data generating process $f(y|\mathbf{x})$ due to insufficient data. While aleatoric uncertainty can only be reduced by gathering additional features for the sample points, epistemic uncertainty, in principle, can be diminished as more data is collected, assuming the model effectively captures the true underlying process.

We saw several approaches to quantify aleatoric uncertainty by estimating conditional densities. In classification problems, probabilistic classifiers automatically estimate $f(y|\mathbf{x})$ as long as a proper loss function is used to train and choose parameters. For regression problems, we saw techniques that include parametric models, kernel-based approaches, and flexible nonparametric models like FlexCode, mixture models, and normalizing flows. After the conditional density has been estimated, we saw that prediction sets can be constructed to account for both aleatoric and epistemic uncertainties. These sets can be derived directly from the conditional density estimates, or quantities derived from them, such as quantiles, means, and variances. Notably, conformal methods provide a flexible and increasingly popular framework for constructing prediction sets with guaranteed marginal coverage as long as the data is i.i.d.

Although conformal methods are straightforward to apply and can be

adapted to a wide range of models, they do not guarantee conditional coverage. As a result, they may over- or under-cover certain subgroups of the data. To mitigate this limitation, we explored enhancements to conformal prediction that improve conditional coverage properties, ensuring better reliability across various regions of the feature space.

An alternative approach to modeling both aleatoric and epistemic uncertainty is through Bayesian methods, which inherently combine these uncertainties. Indeed, the posterior predictive distribution $f(y|\mathbf{x}, D)$, where D represents the training data, captures aleatoric uncertainty via the model's conditional distribution and epistemic uncertainty through the posterior over model parameters. This distribution can then be directly used to construct Bayesian prediction sets. These sets can also be further refined with conformal prediction techniques to ensure valid coverage. However, Bayesian models often rely on computationally intensive methods such as Markov Chain Monte Carlo (MCMC), limiting scalability for large or complex datasets.

Neural networks, when combined with techniques such as dropout and deep ensembles, provide an alternative practical tool for managing epistemic uncertainty. Although these methods may initially seem ad-hoc, they can be understood as approximations to Bayesian solutions under specific priors. For instance, Monte Carlo dropout approximates Bayesian posteriors by sampling from the model's uncertainty during both training and prediction. Deep ensembles, which aggregate predictions from multiple neural networks with different initializations, offer another way to capture model uncertainty. However, it remains unclear whether these approximations are sufficiently accurate or if the chosen priors are appropriate, especially in complex models. This is crucial since the prior selection directly influences the estimation of epistemic uncertainty.

We also saw that the bootstrap as a tool to evaluate epistemic uncertainties under a frequentist perspective. The bootstrap can be applied to any model, but its coverage guarantees are asymptotic and require assumptions to be met.

Calibration is another important aspect of UQ. It ensures that probabilistic predictions reflect actual observed frequencies, making it essential in both regression and classification tasks. However, calibration alone is not sufficient. While many models may be calibrated, some can be dull and fail to fully utilize

11.2. Limitations of UQ Approaches

the predictive power of the available data. For this reason, calibration techniques should only be applied after selecting the best model using appropriate proper loss functions, such as the Brier score, cross-entropy loss or the L_2 loss. In this context, calibration serves as a fine-tuning step, rather than as the primary criterion for model selection.

11.2 Limitations of UQ Approaches

While uncertainty quantification is a powerful tool for improving model reliability, it also comes with limitations. In this section we explore some of them.

11.2.1 Assumptions and Ontological Uncertainties

UQ methods often rely on assumptions about the underlying data distribution and the correctness of the models being used. For example, Bayesian UQ methods assume that the prior distributions adequately reflect the one's uncertainty about model parameters. However, poorly chosen priors or models that fail to capture the true data-generating process can lead to misleading uncertainty estimates. This issue is particularly pronounced in high-dimensional spaces, where defining sensible priors becomes increasingly challenging.

Even though often referred to as "distribution-free", standard conformal methods rely on the i.i.d. assumption to achieve marginal coverage. As we have seen, achieving asymptotic conditional coverage or other desirable properties requires even stricter assumptions that may not be met in real-world scenarios.

In real-world applications, the distribution of training data frequently differs from that observed during deployment. This shift can compromise the reliability of uncertainty quantification if not adequately addressed. Techniques like domain adaptation, transfer learning, and importance weighting have been developed to adjust models and improve alignment with new data distributions (Gibbs and Candes, 2021; Izbicki et al., 2017; Kasa et al., 2024; Masserano et al., 2024; Tibshirani et al., 2019; Vaz et al., 2019). However, these methods often rely on strong assumptions for effective correction or may only optimize against specific criteria, such as marginal validity (Gibbs and Candès,

2024).

Despite these advancements, there remain limits to what can be anticipated, leading to uncertainties that lie beyond the model's assumptions – referred to as ontological uncertainty, or “unknown unknowns” (Frank et al., 2024; Gansch and Adee, 2020; Zhang et al., 2020). Unlike *known* dataset shifts, which can be mitigated through adaptation, ontological uncertainty arises from unforeseen changes – such as new regulations, disruptive technologies, or rare global events – that fall outside the model’s predictive scope.

11.2.2 Overconfidence

A consequence of the assumptions discussed earlier is that UQ methods can become overly confident in the model’s predictive abilities, particularly when they fail to address model misspecification or account for deeper, ontological uncertainties arising from gaps in knowledge. While some techniques aim to provide calibrated uncertainty estimates, they inherently rely on the assumption that the model is capable of capturing the true underlying data structure given sufficient data. This assumption can lead to *overconfidence*, even when the uncertainty appears well-quantified.

As a result, UQ methods should be interpreted carefully, especially in critical or fast-changing situations where the model’s limitations are not fully clear.

11.2.3 Uncertainty Cannot Address All Risks

Finally, UQ doesn’t cover all types of risk in decision-making. For instance, ethical challenges or societal consequences might not be reflected in a model’s numerical uncertainties. In decisions with significant consequences, it is crucial to recognize the limits of UQ and consider other factors. For instance, even if an autonomous vehicle’s machine learning models provide accurate uncertainty estimates about potential collisions, they cannot capture ethical dilemmas, such as deciding how to prioritize the safety of passengers versus pedestrians in unavoidable crash scenarios. These ethical risks lie beyond the scope of UQ.

Human interpretation of uncertainty also presents risks that UQ cannot

11.3. Practical Recommendations for Using UQ in Machine Learning

address. Even with well-calibrated predictions, decision-makers may misinterpret or misuse uncertainty estimates due to cognitive biases or lack of domain expertise. In important areas like national security or finance, poor decisions can happen based on how uncertainty is handled, no matter how good the UQ is. Relying too much on models without considering the bigger picture can make these problems worse.

11.3 Practical Recommendations for Using UQ in Machine Learning

We end the book by offering practical guidelines for practitioners implementing UQ methods in their machine learning models. Here are some recommendations:

1. **Understand the Type of Uncertainty:** Distinguishing between aleatoric and epistemic uncertainty is essential. Epistemic uncertainty, which arises from limited knowledge about the data-generating process, can be reduced by acquiring additional data. In contrast, aleatoric uncertainty, which reflects inherent variability in the data, can only be minimized by measuring additional covariates that capture this variability.
2. **Incorporate Domain Knowledge:** When developing a model, leverage available domain knowledge to inform the choice of priors and model structure. Integrating expert insights can help reduce uncertainty, especially when data is limited.
3. **Avoid Improper Scores Like Accuracy for UQ:** Scores like accuracy can lead to misleading UQ. Instead, use proper scoring rules. Always verify the default scoring settings in the implementation you are using, as many default to improper scores.
4. **Model Calibration:** Calibration is essential for good UQ. However, calibration techniques should only be applied after choosing the best model using proper loss functions like Brier score, cross-entropy loss, or L_2 loss. Calibration alone is insufficient if the model fails to fully utilize the data.

5. **Flexible Techniques are Not Always Appropriate:** While flexible models like deep learning and nonparametric approaches offer adaptability, they may not suit all applications due to the risk of overfitting, especially with limited data. Many times simple parametric models are more effective: in simpler tasks, conventional models, like linear or generalized linear models, may provide better performance.
6. **Sensitivity Analysis:** Conduct sensitivity analyses by trying different approaches, hyperparameter settings, and priors. Compare results across these variations to assess the robustness and reliability of your uncertainty estimates. This practice can help identify weaknesses in your model and guide improvements.
7. **Handling Dataset Shifts:** In real-world applications, dataset shifts are common. If you expect shifts in your problem, use models that account for them through techniques like domain adaptation, transfer learning, or importance weighting to prevent misleading uncertainty estimates. Alternatively, test your model's robustness to shifts by adjusting the training data to simulate different scenarios.
8. **Beware of Overconfidence:** UQ methods often assume that the model is capable of capturing the true underlying structure of the data. This assumption can lead to overconfidence, especially in the presence of model misspecification or when faced with ontological uncertainties that fall outside the model's predictive scope.

11.3. Practical Recommendations for Using UQ in Machine Learning

Index

L_2 loss function, 47

ABC, 175

Accuracy, 16

Activation function, 36

Approximate Bayesian
Computation, 175

Artificial neural networks, 35

Backpropagation, 40

Bagging, 32

BART, 142

Batch normalization, 147

Bayesian Additive Regression
Trees, 142

Bayesian decision theory, 132

Bayesian models, 128

Bayesian optimization, 138

Boosting, 34

Bootstrap, 149

Brier score, 48

Calibration plot, 89

Class-conditional conformal
region, 116

Classification, 14

Conditional coverage, 102

Conditional PIT values, 81

Conformal classification, 119

Conformal Inference, 103

Conformal Predictions, 103

Conformal Regions, 103

Continuous ranked probability
score, 50

Coverage, 102

Cross-entropy, 48

Cross-validation, 19

CRPS, 50

Data splitting, 19

Deep ensembles, 148

Dropout, 41, 145

Early stopping, 40

Expected calibration error, 90

Feature map, 133

FlexCode, 56

Gaussian process regression, 133

Highest Predictive Density
Region, 100

Histogram binning, 91

HPD region, 99

Isotonic regression, 92

K-Nearest Neighbors, 28

Kernel estimators, 65

KNN, 28

Kullback-Leibler divergence, 49

Label-conditional conformal
region, 116

Lasso, 26

LFI, 173

Likelihood-free Inference, 173

Logistic regression, 27

Loss function, 15

Marginal coverage, 102

Maximum calibration error, 90

Mixture Density Networks, 60

Mixture Models, 60

Monte Carlo Dropout, 145

Negative loglikelihood, 48

Neural networks, 35

Neyman confidence sets, 186

Normalizing flows, 62

Oracle intervals, 98

Oracle regions, 98

Pinball loss, 67

PIT values, 76

Platt scaling, 91

Prediction band, 98

Prediction intervals, 98

Prediction region, 98

Prediction regions, 98

Prediction set, 98

Probabilistic calibration, 79

Probability Integral
Trasformation, 76

Quantile calibration, 79

Quantile regression, 67

Quantile-based region, 100

Random Forests, 32

Ratio trick, 64

Recalibration of CDEs, 80

Regression, 14

Reliability diagram, 89

Ridge regression, 27

Risk, 15

SGD, 40

Simulator-based Inference, 173

Smoothing kernels, 65

Stochastic Gradient Descent, 40

Symmetric Region, 101

Temperature scaling, 92

Test set, 19

Training set, 19

Tuning parameters, 25

Validation set, 19

Bibliography

- Abadie, A., Diamond, A., & Hainmueller, J. (2010). Synthetic control methods for comparative case studies: Estimating the effect of California's tobacco control program. *Journal of the American Statistical Association*, 105(490), 493–505.
- Afrasiabi, M., Mohammadi, M., Rastegar, M., Stankovic, L., Afrasiabi, S., & Khazaei, M. (2020). Deep-based conditional probability density function forecasting of residential loads. *IEEE Transactions on Smart Grid*, 11(4), 3646–3657.
- Agostinelli, S., Allison, J., Amako, K. a., Apostolakis, J., Araujo, H., Arce, P., Asai, M., Axen, D., Banerjee, S., Barrand, G., et al. (2003). Geant4—a simulation toolkit. *Nuclear instruments and methods in physics research section A: Accelerators, Spectrometers, Detectors and Associated Equipment*, 506(3), 250–303.
- Almosallam, I. A., Jarvis, M. J., & Roberts, S. J. (2016). GPz: Non-stationary Sparse Gaussian Processes for Heteroscedastic Uncertainty Estimation in Photometric Redshifts. *MNRAS*, 462, 726–739. <https://doi.org/10.1093/mnras/stw1618>
- Angelopoulos, A. N., Bates, S., et al. (2023). Conformal prediction: A gentle introduction. *Foundations and Trends® in Machine Learning*, 16(4), 494–591.
- Angelopoulos, A. N., Bates, S., Jordan, M., & Malik, J. (n.d.). Uncertainty sets for image classifiers using conformal prediction. *International Conference on Learning Representations*.

- Arnouts, S., Cristiani, S., Moscardini, L., Matarrese, S., Lucchin, F., Fontana, A., & Giallongo, E. (1999). Measuring and modelling the redshift evolution of clustering: the Hubble Deep Field North., *310*, 540–556.
- Assaf, S. A., & Al-Hejji, S. (2006). Causes of delay in large construction projects. *International Journal of Project Management*, *24*(4), 349–357.
- Assunção, G. O., Izicki, R., & Prates, M. O. (2024). Is augmentation effective in improving prediction in imbalanced datasets? *Journal of Data Science*, 1–16.
- Ballesteros-Pérez, P., Rojas-Céspedes, Y. A., Hughes, W., Kabiri, S., Pellicer, E., Mora-Melià, D., & del Campo-Hitschfeld, M. L. (2017). Weather-wise: A weather-aware planning tool for improving construction productivity and dealing with claims. *Automation in construction*, *84*, 81–95.
- Bastos, L. S., Economou, T., Gomes, M. F., Villela, D. A., Coelho, F. C., Cruz, O. G., Stoner, O., Bailey, T., & Codeço, C. T. (2019). A modelling approach for correcting reporting delays in disease surveillance data. *Statistics in medicine*, *38*(22), 4363–4377.
- Beaumont, M. A. (2010). Approximate bayesian computation in evolution and ecology. *Annual review of ecology, evolution, and systematics*, *41*, 379–406.
- Beck, R., Lin, C.-A., Ishida, E., Gieseke, F., de Souza, R., Costa-Duarte, M., Hattab, M., Krone-Martins, A., & Collaboration, C. (2017). On the realistic validation of photometric redshifts. *Monthly Notices of the Royal Astronomical Society*, *468*(4), 4323–4339.
- Beck, R., Dobos, L., Budavári, T., Szalay, A. S., & Csabai, I. (2016). Photometric redshifts for the SDSS Data Release 12. *Monthly Notices of the Royal Astronomical Society*, *460*(2), 1371–1381.
- Bejani, M. M., & Ghatee, M. (2021). A systematic review on overfitting control in shallow and deep neural networks. *Artificial Intelligence Review*, *54*(8), 6391–6438.
- Benaglia, T., Chauveau, D., Hunter, D. R., & Young, D. S. (2009). Mixtools: An r package for analyzing finite mixture models. *Journal of Statistical Software*, *32*(6), 1–29.
- Benedetti, J. K. (1977). On the nonparametric estimation of regression functions. *Journal of the Royal Statistical Society. Series B (Methodological)*, 248–253.

- Benitez, N. (2000). Bayesian Photometric Redshift Estimation. *The Astrophysical Journal*, 536(2), 571–583. <https://doi.org/10.1086/308947>
- Berg, N. (2004). No-decision classification: An alternative to testing for statistical significance. *the Journal of socio-Economics*, 33(5), 631–650.
- Bertin, K., Lacour, C., & Rivoirard, V. (2016). Adaptive pointwise estimation of conditional density function. *Annales de l'Institut Henri Poincaré, Probabilités et Statistiques*, 52(2), 939–980.
- Bian, M., & Barber, R. F. (2023). Training-conditional coverage for distribution-free predictive inference. *Electronic Journal of Statistics*, 17(2), 2044–2066.
- Bickel, P. J., & Li, B. (2007). Local polynomial regression on unknown manifolds. In *Ims lecture notes-monograph series, complex datasets and inverse problems* (pp. 177–186, Vol. 54). Institute of Mathematical Statisitcs.
- Bishop, C. M. (1994). Mixture density networks.
- Bishop, C. M. (1997). Bayesian neural networks. *J. Braz. Comput. Soc.*, 4(1).
- Blum, M. G. (2010). Approximate bayesian computation: A nonparametric perspective. *Journal of the American Statistical Association*, 105(491), 1178–1187.
- Bordoloi, R., Lilly, S. J., & Amara, A. (2010). Photo-z performance for precision cosmology. *Monthly Notices of the Royal Astronomical Society*, 406(2), 881–895.
- Boström, H., & Johansson, U. (2020). Mondrian conformal regressors. *Conformal and Probabilistic Prediction and Applications*, 114–133.
- Boström, H., Johansson, U., & Löfström, T. (2021). Mondrian conformal predictive distributions. *Conformal and Probabilistic Prediction and Applications*, 24–38.
- Bowman, A. W. (1985). A comparative study of some kernel-based nonparametric density estimators. *Journal of Statistical Computation and Simulation*, 21(3-4), 313–327.
- Brammer, G. B., van Dokkum, P. G., & Coppi, P. (2008). EAZY: A Fast, Public Photometric Redshift Code., 686, Article 1503-1513, 1503–1513. <https://doi.org/10.1086/591786>
- Breiman, L. (2001a). Statistical modeling: The two cultures. *Statistical Science*, 16(3), 199–231.

- Breiman, L. (2001b). Random forests. *Machine Learning*, 45(1), 5–32.
- Brier, G. W. (1950). Verification of forecasts expressed in terms of probability. *Monthly weather review*, 78(1), 1–3.
- Cabezas, L. M. C., Soares, G. P., Ramos, T. R., Stern, R. B., & Izbicki, R. (2024). Distribution-free calibration of statistical confidence sets. *arXiv preprint arXiv:2411.19368*. <https://arxiv.org/pdf/2411.19368>
- Cabezas, L. M., Otto, M. P., Izbicki, R., & Stern, R. B. (2025). Regression trees for fast and adaptive prediction intervals. *Information Sciences*, 121369.
- Calonico, S., Cattaneo, M. D., & Farrell, M. H. (2018). On the effect of bias estimation on coverage accuracy in nonparametric inference. *Journal of the American Statistical Association*, 113(522), 767–779.
- Cameron, E., & Pettitt, A. (2012). Approximate bayesian computation for astronomical model analysis: A case study in galaxy demographics and morphological transformation at high redshift. *Monthly Notices of the Royal Astronomical Society*, 425(1), 44–65.
- Campos, M., Farinhas, A., Zerva, C., Figueiredo, M. A., & Martins, A. F. (2024). Conformal prediction for natural language processing: A survey. *Transactions of the Association for Computational Linguistics*, 12, 1497–1516.
- Carrasco Kind, M., & Brunner, R. J. (2013). Tpz: Photometric redshift pdfs and ancillary information by using prediction trees and random forests. *MNRAS*, 432(2), 1483–1501.
- Carvutoi, S., Amaro, V., Brescia, M., Vellucci, C., Tortora, C., & Longo, G. (2017). Metaphor: A machine-learning-based method for the probability density estimation of photometric redshifts., 465(2), 1959–1973. <https://doi.org/10.1093/mnras/stw2930>
- Chen, T., & Guestrin, C. (2016). Xgboost: A scalable tree boosting system. *Proceedings of the 22nd ACM SIGKDD international conference on knowledge discovery and data mining*, 785–794.
- Cheng, G., & Chen, Y.-C. (2019). Nonparametric inference via bootstrapping the debiased estimator. *Electronic Journal of Statistics*, 13, 2194–2256.
- Cheng, K. F., & Chu, C.-K. (2004). Semiparametric density estimation under a two-sample density ratio model. *Bernoulli*, 10(4), 583–604.

- Cherian, J. J., Gibbs, I., & Candès, E. J. (2024). Large language model validity via enhanced conformal prediction methods. *arXiv preprint arXiv:2406.09714*.
- Chernozhukov, V., Wüthrich, K., & Zhu, Y. (2021). Distributional conformal prediction. *Proceedings of the National Academy of Sciences*, 118(48).
- Chipman, H. A., George, E. I., & McCulloch, R. E. (1998). Bayesian cart model search. *Journal of the American Statistical Association*, 93(443), 935–948.
- Chipman, H. A., George, E. I., & McCulloch, R. E. (2012). Bart: Bayesian additive regression trees. *Annals of Applied Statistics*, 6(1), 266–298.
- Chung, Y., Neiswanger, W., Char, I., & Schneider, J. (2021). Beyond pinball loss: Quantile methods for calibrated uncertainty quantification. *Advances in Neural Information Processing Systems*, 34, 10971–10984.
- Clark, C., Kinder, S., Egemen, D., Befano, B., Desai, K., Ahmed, S. R., Singh, P., Rodriguez, A. C., Jeronimo, J., De Sanjose, S., et al. (2024). Conformal prediction and monte carlo inference for addressing uncertainty in cervical cancer screening. *International Workshop on Uncertainty for Safe Utilization of Machine Learning in Medical Imaging*, 205–214.
- Codeço, C. T., Cruz, O. G., Riback, T. I., Degener, C. M., Gomes, M. F., Villela, D., Bastos, L., Camargo, S., Saraceni, V., Lemos, M. C. F., et al. (2016). Infodengue: A nowcasting system for the surveillance of dengue fever transmission. *BioRxiv*, 046193.
- Comito, M. B., Izbicki, R., do Canto Hubert Junior, P., & Moura, F. (2025). Improving decision-making in construction: Nonparametric modeling of weather-induced delays [in prep.].
- Cook, S. R., Gelman, A., & Rubin, D. B. (2006). Validation of software for bayesian models using posterior quantiles. *Journal of Computational and Graphical Statistics*, 15(3), 675–692.
- Cramér, H. (1928). On the composition of elementary errors: First paper: Mathematical deductions. *Scandinavian Actuarial Journal*, 1928(1), 13–74.
- Cranmer, K., Brehmer, J., & Louppe, G. (2020). The frontier of simulation-based inference. *Proceedings of the National Academy of Sciences*, 117(48), 30055–30062.
- Cranmer, K., Pavéz, J., & Louppe, G. (2015). Approximating likelihood ratios with calibrated discriminative classifiers. *arXiv:1506.02169*.

- Csillag, D., Paes, L. M., Ramos, T., Romano, J. V., Schuller, R., Seixas, R. B., Oliveira, R. I., & Orenstein, P. (2023). Amnioml: Amniotic fluid segmentation and volume prediction with uncertainty quantification. *Proceedings of the AAAI Conference on Artificial Intelligence*, 37(13), 15494–15502.
- Dalmasso, N., Izbicki, R., & Lee, A. (2020a). Confidence sets and hypothesis testing in a likelihood-free inference setting. *International Conference on Machine Learning*, 2323–2334.
- Dalmasso, N., Masserano, L., Zhao, D., Izbicki, R., & Lee, A. B. (2024). Likelihood-free frequentist inference: Bridging classical statistics and machine learning for reliable simulator-based inference. *Electronic Journal of Statistics*, 18(2), 5045–5090.
- Dalmasso, N., Pospisil, T., Lee, A. B., Izbicki, R., Freeman, P. E., & Malz, A. I. (2020b). Conditional density estimation tools in Python and R with applications to photometric redshifts and likelihood-free cosmological inference. *Astronomy and Computing*, 100362.
- Davison, A. C., & Hinkley, D. V. (1997). *Bootstrap methods and their application*. Cambridge university press.
- Dawid, A. P. (1982). The well-calibrated bayesian. *Journal of the American Statistical Association*, 77(379), 605–610.
- Dawid, A. P. (1984). Present position and potential developments: Some personal views statistical theory the prequential approach. *Journal of the Royal Statistical Society: Series A (General)*, 147(2), 278–290.
- Dempster, A. P., Laird, N. M., & Rubin, D. B. (1977). Maximum likelihood from incomplete data via the em algorithm. *Journal of the royal statistical society: series B (methodological)*, 39(1), 1–22.
- Dey, B., Andrews, B. H., Newman, J. A., Mao, Y.-Y., Rau, M. M., & Zhou, R. (2021). Photometric Redshifts from SDSS Images with an Interpretable Deep Capsule Network, Article arXiv:2112.03939.
- Dey, B., Zhao, D., Newman, J. A., Andrews, B. H., Izbicki, R., & Lee, A. B. (2022). Calibrated predictive distributions via diagnostics for conditional coverage. *arXiv:2205.14568*.
- Dhariwal, P., & Nichol, A. Q. (2021). Diffusion models beat gans on image synthesis. In M. Ranzato, A. Beygelzimer, Y. N. Dauphin, P. Liang, & J. W.

- Vaughan (Eds.), *Advances in neural information processing systems 34: Annual conference on neural information processing systems 2021, neurips 2021, december 6-14, 2021, virtual* (pp. 8780–8794).
- Dheur, V., Bosser, T., Izbicki, R., & Ben Taieb, S. (2024). Distribution-free conformal joint prediction regions for neural marked temporal point processes. *Machine Learning*, 1–48.
- Dheur, V., & Taieb, S. B. (2023). A large-scale study of probabilistic calibration in neural network regression. *International Conference on Machine Learning*, 7813–7836.
- Dheur, V., & Taieb, S. B. (2024). Probabilistic calibration by design for neural network regression. *International Conference on Artificial Intelligence and Statistics*, 3133–3141.
- Di Marzio, M., Fensore, S., Panzera, A., & Taylor, C. C. (2016). A note on nonparametric estimation of circular conditional densities. *Journal of Statistical Computation and Simulation*, 1–10.
- Diebold, F. X., Gunther, T. A., & Tay, A. S. (1998). Evaluating density forecasts with applications to financial risk management, international economic re) view, vol. 39, no. 4. *Symposium on Forecasting and Empirical Methods in Macroeconomics and Finance*, 863.
- Ding, T., Angelopoulos, A., Bates, S., Jordan, M., & Tibshirani, R. J. (2024). Class-conditional conformal prediction with many classes. *Advances in Neural Information Processing Systems*, 36.
- Dinh, L., Sohl-Dickstein, J., & Bengio, S. (2016). Density estimation using Real NVP. *arXiv:1605.08803*.
- Durdyev, S., Hosseini, M. R., Baroudi, B., & Roshanaei, M. (2020). Causes of delay in residential building construction projects: A case study of azerbaijan. *Journal of Engineering, Design and Technology*, 18(3), 659–672.
- Edition, F. (2008). *A guide to the project management body of knowledge (pmbok guide)*. Project Management Institute.
- Efromovich, S. (1999). *Nonparametric curve estimation: Methods, theory and application*. Springer.
- Efromovich, S. (2010). Dimension reduction and adaptation in conditional density estimation. *Journal of the American Statistical Association*, 105(490), 761–774.

- Efron, B., & Tibshirani, R. J. (1994). *An introduction to the bootstrap*. Chapman; Hall/CRC.
- England, J. R., & Viscarra Rossel, R. A. (2018). Proximal sensing for soil carbon accounting. *Soil*, 4(2), 101–122.
- Esteves, L. G., Izbicki, R., Stern, J. M., & Stern, R. B. (2016). The logical consistency of simultaneous agnostic hypothesis tests. *Entropy*, 18(7), 256.
- Estoup, A., Lombaert, E., MARIN, J.-M., Guillemaud, T., Pudlo, P., Robert, C. P., & CORNUET, J.-M. (2012). Estimation of demo-genetic model probabilities with approximate bayesian computation using linear discriminant analysis on summary statistics. *Molecular ecology resources*, 12(5), 846–855.
- Fan, J., Yao, Q., & Tong, H. (1996). Estimation of conditional densities and sensitivity measures in nonlinear dynamical systems. *Biometrika*, 83(1), 189–206.
- Fasiolo, M., Wood, S. N., Hartig, F., & Bravington, M. V. (2018). An extended empirical saddlepoint approximation for intractable likelihoods. *Electron. J. Statist.*, 12(1), 1544–1578.
- Feldman, S., Bates, S., & Romano, Y. (2021). Improving conditional coverage via orthogonal quantile regression. *Advances in neural information processing systems*, 34, 2060–2071.
- Ferraty, F., & Vieu, P. (2006). *Nonparametric functional data analysis: Theory and practice*. Springer Science & Business Media.
- Folgoc, L. L., Baltatzis, V., Desai, S., Devaraj, A., Ellis, S., Manzanera, O. E. M., Nair, A., Qiu, H., Schnabel, J., & Glocke, B. (2021). Is mc dropout bayesian? *arXiv:2110.04286*.
- Forman, G. (2008). Quantifying counts and costs via classification. *Data Mining and Knowledge Discovery*, 17, 164–206.
- Foygel Barber, R., Candes, E. J., Ramdas, A., & Tibshirani, R. J. (2021). The limits of distribution-free conditional predictive inference. *Information and Inference: A Journal of the IMA*, 10(2), 455–482.
- Frank, M., Fuchs, C., & Zeller-Plumhoff, B. (2024). Helmholtz UQ dictionary [Accessed: 2024-09-09]. https://dictionary.helmholtz-uq.de/content/landing_page.html

- Fraser, D. A., & Guttman, I. (1956). Tolerance regions. *The Annals of Mathematical Statistics*, 27(1), 162–179.
- Frazier, P. I. (2018). A tutorial on bayesian optimization. *arXiv:1807.02811*.
- Fröhlich, A., Ramos, T., Cabello, G., Buzatto, I., Izbicki, R., & Tiezzi, D. (2024). Personalizedus: Interpretable breast cancer risk assessment with local coverage uncertainty quantification. *arXiv:2408.15458*.
- Gal, Y., & Ghahramani, Z. (2016). Dropout as a bayesian approximation: Representing model uncertainty in deep learning. *International Conference on Machine Learning*, 1050–1059.
- Gansch, R., & Adee, A. (2020). System theoretic view on uncertainties. *2020 Design, Automation & Test in Europe Conference & Exhibition (DATE)*, 1345–1350.
- Genest, C., & Rivest, L.-P. (2001). On the multivariate probability integral transformation. *Statistics & probability letters*, 53(4), 391–399.
- Gibbons, J. D., & Chakraborti, S. (2014). *Nonparametric statistical inference: Revised and expanded*. CRC press.
- Gibbs, I., & Candes, E. (2021). Adaptive conformal inference under distribution shift. *Advances in Neural Information Processing Systems*, 34, 1660–1672.
- Gibbs, I., & Candès, E. J. (2024). Conformal inference for online prediction with arbitrary distribution shifts. *Journal of Machine Learning Research*, 25(162), 1–36.
- Glad, I. K., Hjort, N. L., & Ushakov, N. G. (2003). Correction of density estimators that are not densities. *Scandinavian Journal of Statistics*, 30(2), 415–427.
- Gneiting, T., Balabdaoui, F., & Raftery, A. E. (2007). Probabilistic forecasts, calibration and sharpness. *Journal of the Royal Statistical Society Series B: Statistical Methodology*, 69(2), 243–268.
- Gneiting, T., & Katzfuss, M. (2014). Probabilistic forecasting. *Annual Review of Statistics and Its Application*, 1, 125–151.
- Gneiting, T., & Resin, J. (2023). Regression diagnostics meets forecast evaluation: Conditional calibration, reliability diagrams, and coefficient of determination. *Electronic Journal of Statistics*, 17(2), 3226–3286.
- Goodfellow, I., Bengio, Y., & Courville, A. (2016). *Deep learning*. MIT press.

- Goodfellow, I. J., Shlens, J., & Szegedy, C. (2014). Explaining and harnessing adversarial examples. *arXiv:1412.6572*.
- Graff, P., Feroz, F., Hobson, M. P., & Lasenby, A. (2014). Skynet: An efficient and robust neural network training tool for machine learning in astronomy., 441(2), 1741–1759. <https://doi.org/10.1093/mnras/stu642>
- Graham, M. L., Connolly, A. J., Ivezić, Ž., Schmidt, S. J., Jones, R. L., Jurić, M., Daniel, S. F., & Yoachim, P. (2018). Photometric Redshifts with the LSST: Evaluating Survey Observing Strategies., 155, Article 1, 1. <https://doi.org/10.3847/1538-3881/aa99d4>
- Gramacy, R. B. (2020). *Surrogates: Gaussian process modeling, design, and optimization for the applied sciences*. Chapman; Hall/CRC.
- Greenberg, D., Nonnenmacher, M., & Macke, J. (2019a). Automatic posterior transformation for likelihood-free inference. In K. Chaudhuri & R. Salakhutdinov (Eds.), *Proceedings of the 36th international conference on machine learning* (pp. 2404–2414, Vol. 97). PMLR.
- Greenberg, D., Nonnenmacher, M., & Macke, J. (2019b). Automatic posterior transformation for likelihood-free inference. *International Conference on Machine Learning*, 2404–2414.
- Grivol, G., Izbicki, R., Okuno, A. A., & Stern, R. B. (2024). Flexible conditional density estimation for time series. *Brazilian Journal of Probability and Statistics*, 38(2).
- Guo, C., Pleiss, G., Sun, Y., & Weinberger, K. Q. (2017). On calibration of modern neural networks. *Proceedings of the 34th International Conference on Machine Learning-Volume 70*, 1321–1330.
- Gupta, C., Podkopaev, A., & Ramdas, A. (2020). Distribution-free binary classification: Prediction sets, confidence intervals and calibration. *Advances in Neural Information Processing Systems*, 33, 3711–3723.
- Gupta, C., & Ramdas, A. (2022). Top-label calibration and multiclass-to-binary reductions. *International Conference on Learning Representations*.
- Gutmann, M. U., & Corander, J. (2016). Bayesian optimization for likelihood-free inference of simulator-based statistical models. *Journal of Machine Learning Research*, 17(125), 1–47.
- Gutmann, M. U., Dutta, R., Kaski, S., & Corander, J. (2018). Likelihood-free inference via classification. *Statistics and Computing*, 28, 411–425.

- Hahn, G. J., & Meeker, W. Q. (2011). *Statistical intervals: A guide for practitioners* (Vol. 92). John Wiley & Sons.
- Hall, P., Racine, J. S., & Li, Q. (2004). Cross-validation and the estimation of conditional probability densities. *Journal of the American Statistical Association*, 99, 1015–1026.
- Hall, P. (1987). On kullback-leibler loss and density estimation. *The Annals of Statistics*, 1491–1519.
- Hall, P. (1992). On bootstrap confidence intervals in nonparametric regression. *The Annals of Statistics*, 695–711.
- Hall, P., & Murison, R. D. (1993). Correcting the negativity of high-order kernel density estimators. *Journal of Multivariate Analysis*, 47(1), 103–122.
- Harrison, D., Sutton, D., Carvalho, P., & Hobson, M. (2015). Validation of Bayesian posterior distributions using a multidimensional Kolmogorov Smirnov test. *Monthly Notices of the Royal Astronomical Society*, 451(3), 2610–2624. <https://doi.org/10.1093/mnras/stv1110>
- Heinrich, L. (2022). Learning optimal test statistics in the presence of nuisance parameters. *arXiv:2203.13079*.
- Hill, J., Linero, A., & Murray, J. (2020). Bayesian additive regression trees: A review and look forward. *Annual Review of Statistics and Its Application*, 7, 251–278.
- Ho, J., Jain, A., & Abbeel, P. (2020). Denoising diffusion probabilistic models. *CoRR, abs/2006.11239*. <https://arxiv.org/abs/2006.11239>
- Ho, J., & Salimans, T. (2022). Classifier-free diffusion guidance. *CoRR, abs/2207.12598*. <https://doi.org/10.48550/arXiv.2207.12598>
- Ho, M., Rau, M. M., Ntampaka, M., Farahi, A., Trac, H., & Póczos, B. (2019). A robust and efficient deep learning method for dynamical mass measurements of galaxy clusters. *The Astrophysical Journal*, 887(1), 25.
- Hoerl, A. E., & Kennard, R. W. (1970). Ridge regression: Biased estimation for nonorthogonal problems. *Technometrics*, 12(1), 55–67.
- Hoffmann, L., & Elster, C. (2021). Deep ensembles from a bayesian perspective. *arXiv:2105.13283*.
- Horta, A., Malone, B., Stockmann, U., Minasny, B., Bishop, T., McBratney, A., Pallasser, R., & Pozza, L. (2015). Potential of integrated field spec-

- troscopy and spatial analysis for enhanced assessment of soil contamination: A prospective review. *Geoderma*, 241, 180–209.
- Huang, C.-W., Krueger, D., Lacoste, A., & Courville, A. (2018). Neural autoregressive flows. *International Conference on Machine Learning*, 2078–2087.
- Hüllermeier, E., & Waegeman, W. (2021). Aleatoric and epistemic uncertainty in machine learning: An introduction to concepts and methods. *Machine Learning*, 110, 457–506.
- Hulsman, R. (2022). Distribution-free finite-sample guarantees and split conformal prediction. *arXiv:2210.14735*.
- Hyndman, R. J., Bashtannyk, D. M., & Grunwald, G. K. (1996). Estimating and visualizing conditional densities. *Journal of Computational & Graphical Statistics*, 5, 315–336.
- Ichimura, T., & Fukuda, D. (2010). A fast algorithm for computing least-squares cross-validations for nonparametric conditional kernel density functions. *Computational Statistics Data Analysis*, 54(12), 3404–3410.
- Inácio, M. d. A., & Izbicki, R. (2018). Conditional density estimation using fourier series and neural networks. *Anais do VI Symposium on Knowledge Discovery, Mining and Learning*, 41–48.
- Ioffe, S., & Szegedy, C. (2015). Batch normalization: Accelerating deep network training by reducing internal covariate shift. *International conference on machine learning*, 448–456.
- Izbicki, R., Lee, A., & Schafer, C. (2014). High-dimensional density ratio estimation with extensions to approximate likelihood computation. *Journal of Machine Learning Research (AISTATS Track)*, 420–429.
- Izbicki, R., Bastos, L. S., Izbicki, M., Lopes, H. F., & Santos, T. M. d. (2021). How many hospitalizations has the COVID-19 vaccination already prevented in São Paulo? *Clinics*, 76, e3250.
- Izbicki, R., Cabezas, L. M. C., Colugnatti, F. A. B., Lassance, R. F. L., de Souza, A. A. L., & Stern, R. B. (2023). React to nhst: Sensible conclusions to meaningful hypotheses. <https://arxiv.org/abs/2308.09112>
- Izbicki, R., & Lee, A. B. (2016). Nonparametric conditional density estimation in a high-dimensional regression setting. *Journal of Computational and Graphical Statistics*, 25(4), 1297–1316.

- Izbicki, R., & Lee, A. B. (2017). Converting high-dimensional regression to high-dimensional conditional density estimation. *Electronic Journal of Statistics*, 11(2), 2800–2831.
- Izbicki, R., Lee, A. B., & Freeman, P. E. (2017). Photo- z estimation: An example of nonparametric conditional density estimation under selection bias. *The Annals of Applied Statistics*, 11(2), 698–724.
- Izbicki, R., Lee, A. B., & Pospisil, T. (2019). ABC-CDE: Toward approximate bayesian computation with complex high-dimensional data and limited simulations. *Journal of Computational and Graphical Statistics*, 28(3), 481–492.
- Izbicki, R., Shimizu, G., & Stern, R. B. (2022). CD-split and HPD-split: Efficient conformal regions in high dimensions. *Journal of Machine Learning Research*.
- Izbicki, R., Shimizu, G. T., & Stern, R. B. (2020). Distribution-free conditional predictive bands using density estimators. *Proceedings of Machine Learning Research (AISTATS Track)*.
- James, G., Witten, D., Hastie, T., Tibshirani, R., et al. (2013). *An introduction to statistical learning* (Vol. 112). Springer.
- Järvenpää, M., Gutmann, M. U., Vehtari, A., & Marttinen, P. (2021). Parallel Gaussian process surrogate Bayesian inference with noisy likelihood evaluations. *Bayesian Anal.*, 16(1), 147–178.
- Kasa, K., Zhang, Z., Yang, H., & Taylor, G. W. (2024). Adapting conformal prediction to distribution shifts without labels. *arXiv:2406.01416*.
- Ke, G., Meng, Q., Finley, T., Wang, T., Chen, W., Ma, W., Ye, Q., & Liu, T.-Y. (2017). Lightgbm: A highly efficient gradient boosting decision tree. *Advances in neural information processing systems*, 3146–3154.
- Kendall, A., & Gal, Y. (2017). What uncertainties do we need in bayesian deep learning for computer vision? *Advances in neural information processing systems*, 30.
- Kieseler, J., Strong, G. C., Chiandotto, F., Dorigo, T., & Layer, L. (2022). Calorimetric measurement of multi-TeV muons via deep regression. *The European Physical Journal C*, 82(1), 1–26.

- Kieseler, J., Strong, G. C., Chiandotto, F., Dorigo, T., & Layer, L. (2021). Preprocessed dataset for "calorimetric measurement of multi-tev muons via deep regression". URL <https://doi.org/10.5281/zenodo.5163817>.
- Koenker, R., & Bassett Jr, G. (1978). Regression quantiles. *Econometrica: journal of the Econometric Society*, 33–50.
- Kostic, V. R., Turri, G., Novelli, P., Lounici, K., et al. (2024). Neural conditional probability for uncertainty quantification. *The Thirty-eighth Annual Conference on Neural Information Processing Systems*.
- Kpotufe, S., & Dasgupta, S. (2012). A tree-based regressor that adapts to intrinsic dimension. *Journal of Computer and System Sciences*, 78(5), 1496–1515.
- Kpotufe, S. (2011). K-NN regression adapts to local intrinsic dimension. *Advances in Neural Information Processing Systems*, 729–737.
- Kügler, S. D., Gianniotis, N., & Polsterer, K. L. (2016). A spectral model for multimodal redshift estimation. *2016 IEEE Symposium Series on Computational Intelligence (SSCI)*, 1–8.
- Kuleshov, V., Fenner, N., & Ermon, S. (2018). Accurate uncertainties for deep learning using calibrated regression. *International conference on machine learning*, 2796–2804.
- Lafferty, J., & Wasserman, L. (2008). Rodeo: Sparse, greedy nonparametric regression. *The Annals of Statistics*, 36(1), 28–63.
- Lakshminarayanan, B., Pritzel, A., & Blundell, C. (2017). Simple and scalable predictive uncertainty estimation using deep ensembles. *Advances in neural information processing systems*, 30.
- Lancet, T. (2024). Dengue: The threat to health now and in the future.
- LeCun, Y., Jackel, L., Bottou, L., Brunot, A., Cortes, C., Denker, J., Drucker, H., Guyon, I., Muller, U., Sackinger, E., et al. (1995). Comparison of learning algorithms for handwritten digit recognition. *International conference on artificial neural networks*, 60, 53–60.
- Lee, A. B., & Izbicki, R. (2016). A spectral series approach to high-dimensional nonparametric regression. *Electronic Journal of Statistics*, 10(1), 423–463.
- Lei, J., G'Sell, M., Rinaldo, A., Tibshirani, R. J., & Wasserman, L. (2018). Distribution-free predictive inference for regression. *Journal of the American Statistical Association*, 113(523), 1094–1111.

- Lei, J., & Wasserman, L. (2014). Distribution-free prediction bands for nonparametric regression. *Journal of the Royal Statistical Society: Series B (Statistical Methodology)*, 76(1), 71–96.
- Leistedt, B., & Hogg, D. W. (2017). Data-driven, Interpretable Photometric Redshifts Trained on Heterogeneous and Unrepresentative Data., 838, Article 5, 5. <https://doi.org/10.3847/1538-4357/aa6332>
- Li, Q., & Racine, J. S. (2008). Nonparametric estimation of conditional CDF and quantile functions with mixed categorical and continuous data. *Journal of Business & Economic Statistics*, 26(4), 423–434.
- Liu, M.-S., Fragkiadaki, K., & Walker, M. (2018). *Likelihood-free inference of for-
nax dark matter density profile* (Data Analysis Project). Carnegie Mellon University, Machine Learning Department. <https://www.ml.cmu.edu/research/dap-papers/S18/dap-liu-mao-sheng.pdf>
- Lueckmann, J.-M., Bassetto, G., Karaletsos, T., & Macke, J. H. (2019). Likelihood-free inference with emulator networks. *Symposium on Advances in Approximate Bayesian Inference*, 32–53.
- Lueckmann, J.-M., Goncalves, P. J., Bassetto, G., Öcal, K., Nonnenmacher, M., & Macke, J. H. (2017). Flexible statistical inference for mechanistic models of neural dynamics. In I. Guyon, U. V. Luxburg, S. Bengio, H. Wallach, R. Fergus, S. Vishwanathan, & R. Garnett (Eds.), *Advances in neural information processing systems 30* (pp. 1289–1299). Curran Associates, Inc. <http://papers.nips.cc/paper/6728-flexible-statistical-inference-for-mechanistic-models-of-neural-dynamics.pdf>
- Luo, P., Wang, X., Shao, W., & Peng, Z. (2018). Towards understanding regularization in batch normalization. *arXiv:1809.00846*.
- Ma, X., He, X., & Shi, X. (2016). A variant of k nearest neighbor quantile regression. *Journal of Applied Statistics*, 43(3), 526–537.
- Mallat, S. (1999). *A wavelet tour of signal processing*. Academic press.
- Malz, A. I., & Hogg, D. W. (2022). How to Obtain the Redshift Distribution from Probabilistic Redshift Estimates. *The Astrophysical Journal*, 928(2), Article 127, 127. <https://doi.org/10.3847/1538-4357/ac062f>
- Mandelbaum, R., Seljak, U., Hirata, C. M., Bardelli, S., Bolzonella, M., Bon-
giorno, A., Carollo, M., Contini, T., Cunha, C. E., Garilli, B., Iovino,
A., Kampczyk, P., Kneib, J. .-, Knobel, C., Koo, D. C., Lamareille, F.,

- Le Fèvre, O., Le Borgne, J. .-, Lilly, S. J., ... Tasca, L. (2008). Precision photometric redshift calibration for galaxy-galaxy weak lensing. *Monthly Notices of the Royal Astronomical Society*, 386(2), 781–806. <https://doi.org/10.1111/j.1365-2966.2008.12947.x>
- Manning, C. D. (2009). *An introduction to information retrieval*. Cambridge university press.
- Manokhin, V. (2022). *Awesome conformal prediction* (Version v1.0.0). Zenodo. <https://doi.org/10.5281/zenodo.6467205>
- Marin, J.-M., Pudlo, P., Robert, C. P., & Ryder, R. J. (2012). Approximate bayesian computational methods. *Statistics and computing*, 22(6), 1167–1180.
- Marin, J.-M., Raynal, L., Pudlo, P., Ribatet, M., & Robert, C. (2016). ABC random forests for Bayesian parameter inference. *Bioinformatics (Oxford, England)*, 35. <https://doi.org/10.1093/bioinformatics/bty867>
- Marques, L., & Berenson, D. (2024). Quantifying aleatoric and epistemic dynamics uncertainty via local conformal calibration. *arXiv:2409.08249*.
- Masserano, L., Dorigo, T., Izbicki, R., Kuusela, M., & Lee, A. (2023). Simulator-based inference with waldo: Confidence regions by leveraging prediction algorithms and posterior estimators for inverse problems. *International Conference on Artificial Intelligence and Statistics*, 2960–2974.
- Masserano, L., Shen, A., Doro, M., Dorigo, T., Izbicki, R., & Lee, A. B. (2024). Classification under nuisance parameters and generalized label shift in likelihood-free inference. *International Conference on Machine Learning*.
- Matheson, J. E., & Winkler, R. L. (1976). Scoring rules for continuous probability distributions. *Management science*, 22(10), 1087–1096.
- McAllister, R. T., Gal, Y., Kendall, A., Van Der Wilk, M., Shah, A., Cipolla, R., & Weller, A. (2017). Concrete problems for autonomous vehicle safety: Advantages of bayesian deep learning.
- McCulloch, W. S., & Pitts, W. (1943). A logical calculus of the ideas immanent in nervous activity. *The bulletin of mathematical biophysics*, 5(4), 115–133.
- Meier, L., Van de Geer, S., & Bühlmann, P. (2009). High-dimensional additive modeling. *The Annals of Statistics*, 37(6B), 3779–3821.
- Meinshausen, N., & Ridgeway, G. (2006). Quantile regression forests. *Journal of machine learning research*, 7(6).

- Mendes de Oliveira, C., Ribeiro, T., Schoenell, W., Kanaan, A., Overzier, R. A., Molino, A., Sampedro, L., Coelho, P., Barbosa, C. E., Cortesi, A., Costa-Duarte, M. V., Herpich, F. R., Hernandez-Jimenez, J. A., Placco, V. M., Xavier, H. S., Abramo, L. R., Saito, R. K., Chies-Santos, A. L., Ederoclite, A., . . . Zaritsky, D. (2019). The Southern Photometric Local Universe Survey (S-PLUS): improved SEDs, morphologies, and redshifts with 12 optical filters. *Monthly Notices of the Royal Astronomical Society*, 489(1), 241–267.
- Met office midas open: Uk land surface stations data (1853-current). (2019).
- Mian, Z., Deng, X., Dong, X., Tian, Y., Cao, T., Chen, K., & Al Jaber, T. (2024). A literature review of fault diagnosis based on ensemble learning. *Engineering Applications of Artificial Intelligence*, 127, 107357.
- Miethke-Morais, A., Cassenote, A., Piva, H., Tokunaga, E., Cobello, V., Rodrigues Gonçalves, F. A., dos Santos Lobo, R. A., Trindade, E., Carneiro D'Albuquerque, L. A., & de Paiva Haddad, L. B. (2020). Unraveling COVID-19-related hospital costs: The impact of clinical and demographic conditions. *MedRxiv*, 2020–12.
- Mirza, M., & Osindero, S. (2014). Conditional generative adversarial nets. *CoRR*, *abs/1411.1784*. <http://arxiv.org/abs/1411.1784>
- Mucesh, S., Hartley, W. G., Palmese, A., Lahav, O., Whiteway, L., Bluck, A., Alarcon, A., Amon, A., Bechtol, K., Bernstein, G., et al. (2021). A machine learning approach to galaxy properties: Joint redshift–stellar mass probability distributions with Random Forest. *Monthly Notices of the Royal Astronomical Society*, 502(2), 2770–2786.
- Murphy, A. H., & Epstein, E. S. (1967). Verification of probabilistic predictions: A brief review. *Journal of Applied Meteorology and Climatology*, 6(5), 748–755.
- Nakazono, L., R Valen  a, R., Soares, G., Izbicki, R., Ivezi  ,   ., R Lima, E., T Hirata, N., Sodr   Jr, L., Overzier, R., Almeida-Fernandes, F., et al. (2024). The quasar catalogue for s-plus dr4 (qucats) and the estimation of photometric redshifts. *Monthly Notices of the Royal Astronomical Society*, 531(1), 327–339.
- Navarro, J. F. (1996). The structure of cold dark matter halos. *Symposium international astronomical union*, 171, 255–258.

- Nelder, J. A., & Wedderburn, R. W. (1972). Generalized linear models. *Journal of the Royal Statistical Society Series A: Statistics in Society*, 135(3), 370–384.
- Nemani, V., Biggio, L., Huan, X., Hu, Z., Fink, O., Tran, A., Wang, Y., Zhang, X., & Hu, C. (2023). Uncertainty quantification in machine learning for engineering design and health prognostics: A tutorial. *Mechanical Systems and Signal Processing*, 205, 110796.
- Neter, J., Kutner, M. H., Nachtsheim, C. J., & Wasserman, W. (1996). Applied linear statistical models.
- Neyman, J. (1937). Outline of a theory of statistical estimation based on the classical theory of probability. *Philosophical Transactions of the Royal Society of London. Series A, Mathematical and Physical Sciences*, 236(767), 333–380.
- Nichol, A. Q., & Dhariwal, P. (2021). Improved denoising diffusion probabilistic models. In M. Meila & T. Zhang (Eds.), *Proceedings of the 38th international conference on machine learning, ICML 2021, 18-24 july 2021, virtual event* (pp. 8162–8171, Vol. 139). PMLR. <http://proceedings.mlr.press/v139/nichol21a.html>
- Okuno, A. A., & Polo, F. M. (2021). Ocde: Odds conditional density estimator. *arXiv:2107.04118*.
- Oliveira, R. I., Orenstein, P., Ramos, T., & Romano, J. V. (2024). Split conformal prediction and non-exchangeable data. *Journal of Machine Learning Research*, 25(225), 1–38.
- Padarian, J., Minasny, B., & McBratney, A. (2022). Assessing the uncertainty of deep learning soil spectral models using monte carlo dropout. *Geoderma*, 425, 116063.
- Papadopoulos, H., Proedrou, K., Vovk, V., & Gammerman, A. (2002). Inductive confidence machines for regression. *European Conference on Machine Learning*, 345–356.
- Papamakarios, G., & Murray, I. (2016). Fast ε -free inference of simulation models with bayesian conditional density estimation. *Advances in neural information processing systems*, 29.
- Papamakarios, G., Nalisnick, E., Rezende, D. J., Mohamed, S., & Lakshminarayanan, B. (2021). Normalizing flows for probabilistic modeling

- and inference. *The Journal of Machine Learning Research*, 22(1), 2617–2680.
- Papamakarios, G., Pavlakou, T., & Murray, I. (2017). Masked autoregressive flow for density estimation. *Advances in neural information processing systems*, 30.
- Papamakarios, G., Sterratt, D., & Murray, I. (2019). Sequential neural likelihood: Fast likelihood-free inference with autoregressive flows. *The 22nd International Conference on Artificial Intelligence and Statistics*, 837–848.
- Pereira, C. A. d. B., & Stern, J. M. (1999). Evidence and credibility: Full bayesian significance test for precise hypotheses. *Entropy*, 1(4), 99–110.
- Pereira, C. A. d. B., & Stern, J. M. (2022). The e-value: A fully bayesian significance measure for precise statistical hypotheses and its research program. *São Paulo Journal of Mathematical Sciences*, 16(1), 566–584.
- Picchini, U., Simola, U., & Corander, J. (2020). Adaptive MCMC for synthetic likelihoods and correlated synthetic likelihoods. *arXiv:2004.04558*.
- Platt, J., et al. (1999). Probabilistic outputs for support vector machines and comparisons to regularized likelihood methods. *Advances in large margin classifiers*, 10(3), 61–74.
- Podkopaev, A., & Ramdas, A. (2021). Distribution-free uncertainty quantification for classification under label shift. *Uncertainty in artificial intelligence*, 844–853.
- Polsterer, K. L. (2016). Dealing with uncertain multimodal photometric redshift estimations. *Proceedings of the International Astronomical Union*, 12(S325), 156–165.
- Press, W. H. (2007). *Numerical recipes 3rd edition: The art of scientific computing*. Cambridge university press.
- Prokhorenkova, L., Gusev, G., Vorobev, A., Dorogush, A. V., & Gulin, A. (2018). Catboost: Unbiased boosting with categorical features. *Advances in neural information processing systems*, 6638–6648.
- Qin, J. (1998). Inferences for case-control and semiparametric two-sample density ratio models. *Biometrika*, 85(3), 619–630.
- Quandt, R. E. (1958). The estimation of the parameters of a linear regression system obeying two separate regimes. *Journal of the american statistical association*, 53(284), 873–880.

- Quiñonero-Candela, J., Sugiyama, M., Schwaighofer, A., & Lawrence, N. D. (2022). *Dataset shift in machine learning*. Mit Press.
- Radford, A., Wu, J., Child, R., Luan, D., Amodei, D., & Sutskever, I. (2019). Language models are unsupervised multitask learners.
- Rahaman, R., et al. (2021). Uncertainty quantification and deep ensembles. *Advances in Neural Information Processing Systems*, 34, 20063–20075.
- Ravikumar, P., Lafferty, J., Liu, H., & Wasserman, L. (2009). Sparse additive models. *Journal of the Royal Statistical Society, Series B*, 71(5), 1009–1030.
- Ray, E. L., & Reich, N. G. (2018). Prediction of infectious disease epidemics via weighted density ensembles. *PLoS computational biology*, 14(2), e1005910.
- Romano, Y., Patterson, E., & Candès, E. (2019). Conformalized quantile regression. In *Advances in neural information processing systems* (pp. 3543–3553, Vol. 32). Curran Associates, Inc.
- Romano, Y., Sesia, M., & Candes, E. (2020). Classification with valid and adaptive coverage. *Advances in Neural Information Processing Systems*, 33, 3581–3591.
- Rosenblatt, F. (1958). The perceptron: A probabilistic model for information storage and organization in the brain. *Psychological review*, 65(6), 386.
- Rosenblatt, M. (1969). Conditional probability density and regression estimators. In P. Krishnaiah (Ed.), *Multivariate analysis ii*.
- Rowe, B. T., Jarvis, M., Mandelbaum, R., Bernstein, G. M., Bosch, J., Simet, M., Meyers, J. E., Kacprzak, T., Nakajima, R., Zuntz, J., et al. (2015). Galsim: The modular galaxy image simulation toolkit. *Astronomy and Computing*, 10, 121–150.
- Sadeh, I., Abdalla, F. B., & Lahav, O. (2016). ANNz2: Photometric Redshift and Probability Distribution Function Estimation using Machine Learning. *PASP*, 128(968), 104502. <https://doi.org/10.1088/1538-3873/128/968/104502>
- Sadinle, M., Lei, J., & Wasserman, L. (2019). Least ambiguous set-valued classifiers with bounded error levels. *Journal of the American Statistical Association*, 114(525), 223–234.

- Sanni-Anibire, M. O., & Egbu, C. (2022). Causes of delay in construction projects: A review of literature. *Built Environment Project and Asset Management*, 12(1), 28–46.
- Schervish, M. J. (2012). *Theory of statistics*. Springer Science & Business Media.
- Schervish, M. J., & DeGroot, M. H. (2014). *Probability and statistics* (Vol. 563). Pearson Education London, UK:
- Schmidt, S. J., Malz, A. I., Soo, J. Y. H., Almosallam, I. A., Brescia, M., Cavuoti, S., Cohen-Tanugi, J., Connolly, A. J., DeRose, J., Freeman, P. E., Graham, M. L., Iyer, K. G., Jarvis, M. J., Kalmbach, J. B., Kovacs, E., Lee, A. B., Longo, G., Morrison, C. B., Newman, J. A., . . . LSST Dark Energy Science Collaboration. (2020). Evaluation of probabilistic photometric redshift estimation approaches for The Rubin Observatory Legacy Survey of Space and Time (LSST). *Monthly Notices of the Royal Astronomical Society*, 499(2), 1587–1606.
- Schuldt, S., Moerschell, J., Kim, J.-W., & Fang, D. (2021). Weather and construction: A preliminary study on the impact of weather events on productivity. *Journal of Construction Engineering and Management*, 147(6), 04021058.
- Searle, R., McBratney, A., Grundy, M., Kidd, D., Malone, B., Arrouays, D., Stockman, U., Zund, P., Wilson, P., Wilford, J., et al. (2021). Digital soil mapping and assessment for australia and beyond: A propitious future. *Geoderma Regional*, 24, e00359.
- Selvan, R., Faye, F., Middleton, J., & Pai, A. (2020). Uncertainty quantification in medical image segmentation with normalizing flows. *Machine Learning in Medical Imaging: 11th International Workshop, MLMI 2020, Held in Conjunction with MICCAI 2020, Lima, Peru, October 4, 2020, Proceedings* 11, 80–90.
- Sepasgozar, A., Samad M Eshtehardian, Shirowzhan, S., Nadoushani, Z. M., & Foroozanfa, M. (2019). Delay causes and emerging digital tools: A novel model of delay analysis and risk mitigation. *International Journal of Project Management*, 37(7), 941–961.
- Shafer, G., & Vovk, V. (2008). A tutorial on conformal prediction. *Journal of Machine Learning Research*, 9(3).
- Shalizi, C. (2013). Advanced data analysis from an elementary point of view.

- Shiga, M., Tangkaratt, V., & Sugiyama, M. (2015). Direct conditional probability density estimation with sparse feature selection. *Machine Learning*, 100(2), 161–182. <https://doi.org/10.1007/s10994-014-5472-x>
- Sisson, S. A., Fan, Y., & Tanaka, M. M. (2007). Sequential monte carlo without likelihoods. *Proceedings of the National Academy of Sciences*, 104(6), 1760–1765.
- Sistema de Informação de Agravos de Notificação (SINAN). (2024). Dengue, chikungunya e zika - sinan portal [Accessed: 2024-09-03]. <https://portalsinan.saude.gov.br/sinan-dengue-chikungunya>
- Sohl-Dickstein, J., Weiss, E. A., Maheswaranathan, N., & Ganguli, S. (2015). Deep unsupervised learning using nonequilibrium thermodynamics. *CoRR, abs/1503.03585*. <http://arxiv.org/abs/1503.03585>
- Sohn, K., Lee, H., & Yan, X. (2015). Learning structured output representation using deep conditional generative models. *Advances in neural information processing systems*, 28.
- Sparapani, R., Spanbauer, C., & McCulloch, R. (2021). Nonparametric machine learning and efficient computation with bayesian additive regression trees: The bart r package. *Journal of Statistical Software*, 97, 1–66.
- Srivastava, N., Hinton, G., Krizhevsky, A., Sutskever, I., & Salakhutdinov, R. (2014). Dropout: A simple way to prevent neural networks from overfitting. *The journal of machine learning research*, 15(1), 1929–1958.
- Stone, C. J. (1977). Consistent nonparametric regression. *The annals of statistics*, 595–620.
- Stone, M. (1974). Cross-validatory choice and assessment of statistical predictions. *Journal of the Royal Statistical Society: Series B (Methodological)*, 36(2), 111–133.
- Strigari, L. E., Frenk, C. S., & White, S. D. (2017). Dynamical models for the sculptor dwarf spheroidal in a Λ cdm universe. *The Astrophysical Journal*, 838(2), 123.
- Sugiyama, M., Takeuchi, I., Suzuki, T., Kanamori, T., Hachiya, H., & Okanohara, D. (2010a). Conditional density estimation via least-squares density ratio estimation. *Proceedings of the Thirteenth International Conference on Artificial Intelligence and Statistics*, 781–788.

- Sugiyama, M., Suzuki, T., & Kanamori, T. (2010b). Density ratio estimation: A comprehensive review (statistical experiment and its related topics). *Kulib Repository*, 1703, 10–31.
- Szegedy, C., Zaremba, W., Sutskever, I., Bruna, J., Erhan, D., Goodfellow, I., & Fergus, R. (2013). Intriguing properties of neural networks. *arXiv:1312.6199*.
- Székely, G. J., & Rizzo, M. L. (2013). Energy statistics: A class of statistics based on distances. *Journal of statistical planning and inference*, 143(8), 1249–1272.
- Székely, G. (2003). *E-statistics: Energy of statistical samples* (Technical Report No. 03-05) ((also technical reports by same title, from 2000–2003 and NSA Grant # MDA 904-02-1-0091 (2000–2002))). Bowling Green State University, Department of Mathematics and Statistics.
- Takeuchi, I., Nomura, K., & Kanamori, T. (2009). Nonparametric conditional density estimation using piecewise-linear solution path of kernel quantile regression. *Neural Computation*, 21(2), 533–559.
- Tan, Y. V., & Roy, J. (2019). Bayesian additive regression trees and the general bart model. *Statistics in medicine*, 38(25), 5048–5069.
- Tanaka, M., Coupon, J., Hsieh, B.-C., Mineo, S., Nishizawa, A. J., Speagle, J., Furusawa, H., Miyazaki, S., & Murayama, H. (2018). Photometric redshifts for hyper suprime-cam subaru strategic program data release 1. *Publications of the Astronomical Society of Japan*, 70(SP1). <https://doi.org/10.1093/pasj/psx077>
- Teye, M., Azizpour, H., & Smith, K. (2018). Bayesian uncertainty estimation for batch normalized deep networks. *International Conference on Machine Learning*, 4907–4916.
- Theodoridis, S., & Koutroumbas, K. (2006). *Pattern recognition*. Elsevier.
- Thomas, O., Dutta, R., Corander, J., Kaski, S., & Gutmann, M. U. (2022). Likelihood-free inference by ratio estimation. *Bayesian Analysis*, 17(1), 1–31.
- Tibshirani, R. (1996). Regression shrinkage and selection via the lasso. *Journal of the Royal Statistical Society. Series B (Methodological)*, 267–288.
- Tibshirani, R. J., Foygel Barber, R., Candès, E., & Ramdas, A. (2019). Conformal prediction under covariate shift. *Advances in neural information processing systems*, 32.

- Vaicenavicius, J., Widmann, D., Andersson, C., Lindsten, F., Roll, J., & Schön, T. (2019). Evaluating model calibration in classification. *The 22nd International Conference on Artificial Intelligence and Statistics*, 3459–3467.
- Valdenegro-Toro, M., & Mori, D. S. (2022). A deeper look into aleatoric and epistemic uncertainty disentanglement. *2022 IEEE/CVF Conference on Computer Vision and Pattern Recognition Workshops (CVPRW)*, 1508–1516.
- Valle, D., Haneda, L., Izbicki, R., Kamimura, R., Azevedo, B., Gomes, S., Sanchez, A., & Almeida, D. (2024a). Nonparametric quantification of uncertainty in multistep upscaling approaches: A case study on estimating forest biomass in the brazilian amazon [To appear]. *Science of Remote Sensing*.
- Valle, D., Leite, R., Izbicki, R., Silva, C., & Haneda, L. (2024b). Local uncertainty maps for land-use/land-cover classification without remote sensing and modeling work using a class-conditional conformal approach. *International Journal of Applied Earth Observation and Geoinformation*.
- Valle, D., Izbicki, R., & Leite, R. V. (2023). Quantifying uncertainty in land-use land-cover classification using conformal statistics. *Remote Sensing of Environment*, 295, 113682.
- Vaswani, A., Shazeer, N., Parmar, N., Uszkoreit, J., Jones, L., Gomez, A. N., Kaiser, L., & Polosukhin, I. (2017). Attention is all you need. In I. Guyon, U. von Luxburg, S. Bengio, H. M. Wallach, R. Fergus, S. V. N. Vishwanathan, & R. Garnett (Eds.), *Advances in neural information processing systems 30: Annual conference on neural information processing systems 2017, december 4-9, 2017, Long Beach, CA, USA* (pp. 5998–6008).
- Vaz, A. F., Izbicki, R., & Stern, R. B. (2019). Quantification under prior probability shift: The ratio estimator and its extensions. *Journal of Machine Learning Research*, 20(79), 1–33.
- Vazquez, J., & Facelli, J. C. (2022). Conformal prediction in clinical medical sciences. *Journal of Healthcare Informatics Research*, 6(3), 241–252.
- Vovk, V. (2012). Conditional validity of inductive conformal predictors. *Asian conference on machine learning*, 475–490.
- Vovk, V., Gammerman, A., & Shafer, G. (2005). *Algorithmic learning in a random world* (Vol. 29). Springer.

- Wager, S., Wang, S., & Liang, P. S. (2013). Dropout training as adaptive regularization. *Advances in neural information processing systems*, 26.
- Wald, A. (1943). Tests of statistical hypotheses concerning several parameters when the number of observations is large. *Transactions of the American Mathematical society*, 54(3), 426–482.
- Wasserman, L. (2006). *All of nonparametric statistics*. Springer Science & Business Media.
- Wehenkel, A., & Louppe, G. (2019). Unconstrained monotonic neural networks. *Advances in neural information processing systems*, 32.
- Weyant, A., Schafer, C., & Wood-Vasey, W. M. (2013). Likelihood-free cosmological inference with type ia supernovae: Approximate bayesian computation for a complete treatment of uncertainty. *The Astrophysical Journal*, 764(2), 116.
- Widmann, D., Lindsten, F., & Zachariah, D. (2019). Calibration tests in multi-class classification: A unifying framework. *Advances in neural information processing systems*, 32.
- Wildberger, J., Dax, M., Buchholz, S., Green, S., Macke, J. H., & Schölkopf, B. (2024). Flow matching for scalable simulation-based inference. *Advances in Neural Information Processing Systems*, 36.
- Wilks, S. S. (1941). Determination of sample sizes for setting tolerance limits. *The Annals of Mathematical Statistics*, 12(1), 91–96.
- Williams, C. K., & Rasmussen, C. E. (2006). *Gaussian processes for machine learning* (Vol. 2). MIT press Cambridge, MA.
- Winkler, R. L. (1972). A decision-theoretic approach to interval estimation. *Journal of the American Statistical Association*, 67(337), 187–191.
- Wittman, D. (2009). What lies beneath: Using p (z) to reduce systematic photometric redshift errors. *The Astrophysical Journal Letters*, 700(2), L174.
- Wood, S. (2010). Statistical inference for noisy nonlinear ecological dynamic systems. *Nature*, 466, 1102–4.
- Wu, J. T., Leung, K., & Leung, G. M. (2020). Nowcasting and forecasting the potential domestic and international spread of the 2019-ncov outbreak originating in wuhan, china: A modelling study. *The lancet*, 395(10225), 689–697.

- Xiao, Y., Soares, G., Bastos, L., Izbicki, R., & Moraga, P. (2024). Dengue nowcasting in brazil by combining official surveillance data and google trends information. *medRxiv*. <https://doi.org/10.1101/2024.09.02.24312934>
- Yang, Y., & Tokdar, S. T. (2015). Minimax-optimal nonparametric regression in high dimensions. *The Annals of Statistics*, 43(2), 652–674.
- Zadrozny, B., & Elkan, C. (2001). Obtaining calibrated probability estimates from decision trees and naive bayesian classifiers. *Icml*, 1, 609–616.
- Zadrozny, B., & Elkan, C. (2002). Transforming classifier scores into accurate multiclass probability estimates. *Proceedings of the eighth ACM SIGKDD international conference on Knowledge discovery and data mining*, 694–699.
- Zhang, A., Lipton, Z. C., Li, M., & Smola, A. J. (2021). Dive into deep learning. *arXiv:2106.11342*.
- Zhang, H., Zimmerman, J., Nettleton, D., & Nordman, D. J. (2020). Random forest prediction intervals. *The American Statistician*.
- Zhao, D., Dalmasso, N., Izbicki, R., & Lee, A. B. (2021). Diagnostics for conditional density models and bayesian inference algorithms. *Uncertainty in Artificial Intelligence*, 1830–1840.
- Zhou, R., Newman, J. A., Mao, Y.-Y., Meisner, A., Moustakas, J., Myers, A. D., Prakash, A., Zentner, A. R., Brooks, D., Duan, Y., Landriau, M., Levi, M. E., Prada, F., & Tarle, G. (2021). The clustering of DESI-like luminous red galaxies using photometric redshifts. *Monthly Notices of the Royal Astronomical Society*, 501(3), 3309–3331.
- Ziegel, J. F., Gneiting, T., et al. (2014). Copula calibration. *Electronic journal of statistics*, 8(2), 2619–2638.

About the Book

Designed for practitioners and researchers with a solid mathematical foundation, this book provides a detailed exploration of uncertainty quantification in supervised machine learning. It addresses both aleatoric and epistemic uncertainties, equipping readers with tools to enhance prediction reliability across applications such as cosmology and infectious disease forecasting. Combining theoretical insights with practical examples, the book helps readers move beyond point predictions to build models that effectively communicate uncertainty. Hands-on examples are available in the accompanying GitHub repository.

About the Author

Rafael Izbicki is a faculty member in the Statistics Department at the Federal University of São Carlos (UFSCar) in Brazil. He holds a bachelor's and a master's degree in Statistics from the University of São Paulo and a Ph.D. in Statistics from Carnegie Mellon University. Rafael's research focuses on uncertainty quantification, statistical theory, foundations of statistics, and machine learning, with applications across fields like cosmology, epidemiology, and biology. He has published numerous papers in leading journals and has held a CNPq Research Fellowship since 2017. For more information, visit rafaelizbicki.com.